ICMAR'2000

Novosibirsk, Russia

Proceedings
Part II

NOVOSIBIRSK-TOMSK, RUSSIA

9 - 16 July, 2000

International Conference on the Methods of Aerophysical Research

REPORT DOCUMENTATION PAGE

Form Approved OMB No. 0704-0188

1. AGENCY USE ONLY (Leave blank)	2. REPORT DATE	3. REPORT TYPE AND DATES COVERED
	28 August 2000	Conference Proceedings

4. TITLE AND SUBTITLE

International Conferences on Methods of Aerophysical Research (ICMAR'2000), *Part II*

5. FUNDING NUMBERS

F61775-00-WF022

6. AUTHOR(S)

Conference Committee

7. PERFORMING ORGANIZATION NAME(S) AND ADDRESS(ES)

Institute of Theoretical and Applied Mechanics
Institutskaya 4/1
Novosibirsk 630090
Russia

8. PERFORMING ORGANIZATION REPORT NUMBER

N/A

9. SPONSORING/MONITORING AGENCY NAME(S) AND ADDRESS(ES)

EOARD
PSC 802 BOX 14
FPO 09499-0200

10. SPONSORING/MONITORING AGENCY REPORT NUMBER

CSP 00-5022

11. SUPPLEMENTARY NOTES

Two volumes. *Part I*

12a. DISTRIBUTION/AVAILABILITY STATEMENT

Approved for public release; distribution is unlimited.

12b. DISTRIBUTION CODE

A

13. ABSTRACT (Maximum 200 words)

The Final Proceedings for International Conferences on Methods of Aerophysical Research (ICMAR'2000), 9 July 2000 - 15 July 2000

This is an interdisciplinary conference. Topics include 'Problems of Modeling at Sub/Trans/Super/Hypersonic Velocities'; 'Methods of Flow Diagnostics'; 'Instrumentation in Aerophysical Experiments'; 'Verification of Computational Fluid Dynamics (CFD) Models and Methods'.

14. SUBJECT TERMS

EOARD, Hypersonic Flow, Diagnostics, Computational Fluid Dynamics (CFD)

15. NUMBER OF PAGES

244, 228

16. PRICE CODE

N/A

17. SECURITY CLASSIFICATION OF REPORT	18. SECURITY CLASSIFICATION OF THIS PAGE	19. SECURITY CLASSIFICATION OF ABSTRACT	20. LIMITATION OF ABSTRACT
UNCLASSIFIED	UNCLASSIFIED	UNCLASSIFIED	UL

INTERNATIONAL CONFERENCE ON THE METHODS
OF AEROPHYSICAL RESEARCH

9 – 16 July, 2000
Novosibirsk – Tomsk, Russia

Proceedings
Part II

AQ F00-12-3864

RESEARCH OF HEAT EXCHANGE OF A SUPERSONIC JET OF A RECTANGULAR SECTION WITH A SURFACE FOR COLD GASDYNAMIC SPRAYING

A.P. Alkhimov, S.V. Klinkov, V.F. Kosarev

Institute of Theoretical and Applied Mechanics SB RAS
630090, Novosibirsk, Russia

The study of heat exchange of a jet with a substrate under conditions of gas-dynamic spraying process is important both from scientific and practical point of view. At first, the processes of adhesive fixing of particles on a surface, as well as for thermal coating, essentially depend on the surface temperature [1, 2]. Besides, in many technological processes of coating it is important to control the temperature of the coated workpiece to ensure a required spraying mode and conditions of the workpiece surface. The use of exothermal effect of reactions of interaction of coating components immediately on the spray surface in a cold-spray process can be rather effective. One of the perspective synthesized materials is nickel aluminide – intermetallide compound that has high wear hardness and thermal resistance. It is known that to initialize the synthesis reaction of this intermetallide compound it is necessary to heat the mixture of initial components up to a temperature of $\sim 600\,°C$. The research of possibilities and conditions of obtaining such a temperature in a spray spot is also an important problem.

For rather small concentration of particles ($\varphi \leq 10^{-6}$) ordinarily used in the cold-spray process, the heat exchange between the particles and the surface is small compared to the gas/surface heat exchange. Therefore, in the estimate of the surface temperature, the greatest significance has the account of heat exchange processes between the jet and the surface.

For the measurement of heat exchange efficiency, a calorimetric probe inserted into a slab of thermoinsulator material flash-mounted with the surface was used. In Fig. 1, a schematic flow of a plane supersonic jet on a substrate with the indication of coordinate axes and main geometric sizes of the problem considered is shown.
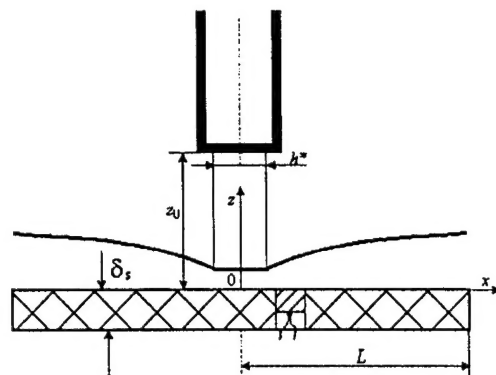
Fig. *1*. Schematic flow of a plane supersonic jet on an substrate.

As an example, in Fig. 2,*a* the experimental results of the temperature registered by the probe versus time are shown. In Fig. 2,*b*, the same data are represented in the coordinates $\ln((T_0(x) - T_s(x))/T_0(x))$, t together with approximating lines passing through experimental points. The heat-transfer coefficients for these cases calculated by the slope of these lines are also shown.
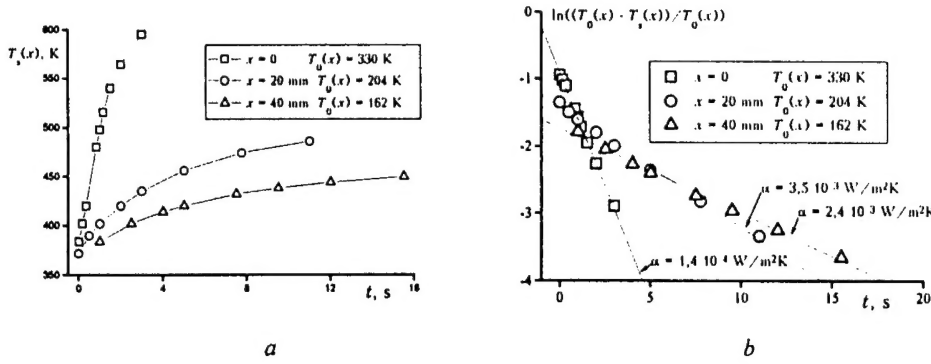
Fig. 2. Dependence of temperature on time for the flow of a plane supersonic isobaric air jet. $p_0 = 1{,}45$ MPa, $T_0^* = 330$ K, $h^* = 3$ mm is the thickness of the jet on the nozzle edge, $z_0 = 15$ mm.

The behavior of the relative stagnation temperature in the near-wall jet is represented in Fig. 3.
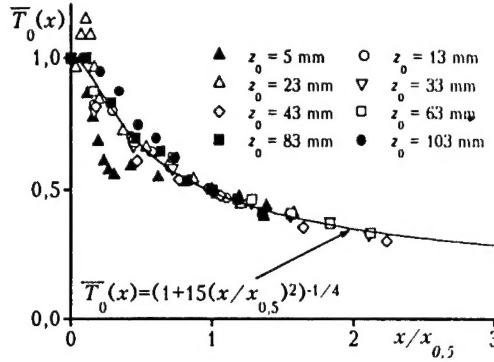
Fig. 3. Stagnation temperature in the near-wall jet, for normal flow of the air jet on the substrate,

$$\overline{T}_0(x) = \frac{T_0(x) - T_a}{T_0^* - T_a} , \ T_0^* = 550 \text{ K}, \ T_a = 300 \text{ K is the ambient temperature.}$$

It is visible that in a wide range of z_0 the data are satisfactorily approximated by the function

$$f(x/x_{0,5}) = \left(1 + 15(x/x_{0,5})^2\right)^{-0,25} .$$

A similar distribution is preserved for a flow around a non-insulated (for example, metal) surface because the heat exchange between the air jet and the substrate surface makes a rather small part of the total transferable heat (typical values of the Stanton number are St $\sim 0{,}01$). Thus, mixing of the ambient air in the wall jet mainly determines the decreasing in the stagnation temperature along the surface.

The heat transfer coefficient at the stagnation point does not depend (in the researched range) on the jet stagnation temperature at the nozzle exit. The maximum value of the heat transfer coefficient is obtained at some distance $z_0/h^* = 5 - 7$ and then its decrease is observed.

The dependence of the experimentally measured (Δ) Nusselt number on the Reynolds number Re_x, calculated by the distance from the stagnation point along the coordinate x, is shown in Fig. 4,a.

4

Fig. 4. Dependence of the Nusselt (a) and Stanton (b) numbers on the Reynolds number.

$z_0/h^* = 5$; $Re_{0,5} = 6,8 \cdot 10^4$;
$Nu(0) = \alpha(0)h^*/\lambda_0 = 980$;
$\lambda_0 \approx 0,04$ W/m·K, $\eta = Re_x/Re_{0,5}$.

It is visible that the dependence of the Nusselt number proportional to the heat transfer coefficient is approximated by the formula
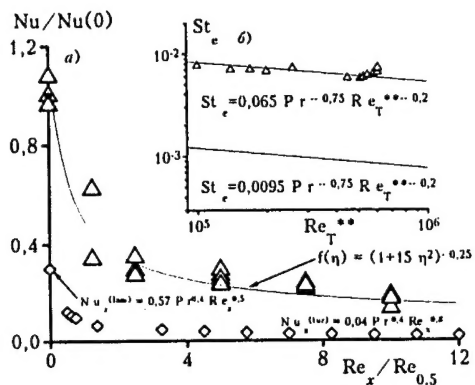
$$\frac{Nu(x)}{Nu(0)} = \left(1 + 15\left(\frac{Re_x}{Re_{0,5}}\right)^2\right)^{-0,25} ,$$

which includes the entire range of x, including damping far from the stagnation point in a subsonic part of the near-wall jet, where $Nu \sim 1/x^{0,5}$ according to [3].

For comparison, the dependence of the heat transfer coefficient on Re_x is calculated using experimental distributions of the parameters on the external boundary of the near-wall jet $M_e^2(x)$, $u_e(x)$ [4] and $T_{0e}(x)$, by applying the formula from [5, 6]

$$\alpha = 0,04\,Pr^{-0,6}\,Re_{xe}^{-0,2}\,\rho_e u_e c_p \left(T_w/T_r\right)^{-0,16} \tag{4}$$

where ρ_e, u_e are the density and velocity of the near-wall jet in the external boundary.

The factor $\left(T_w/T_r\right)^{-0,16}$ (T_w, T_r are the temperatures of the substrate surface and recovery in the near-wall jet) makes minor influence (for conditions of our experiments, the maximum single-error correction will make about 1,1); therefore, it was not taken into account. This formula is obtained from the theory of a turbulent boundary layer, a similar formula is obtained in [7].

In the vicinity of the stagnation point, the heat transfer coefficient was calculated using the theory of a laminar boundary layer for flow of a jet on a substrate with allowance for velocity distributions in the vicinity of the stagnation point $u = \beta x$ [10]:

$$\alpha = 0,57/Pr^{0,6}\sqrt{\rho_0\beta\mu_0 c_p^2} . \tag{5}$$

A typical value for conditions of our experiment was obtained by calculation according to formula (5), $\alpha = (3,8 - 4,2)\cdot 10^3$ W/m²K at the stagnation point for $\beta = 2a_k/h^* = (2,4 - 3)\cdot 10^5$ s^{-1}.

Figure 4,a indicates the data calculated by (4), (5) designated by rhombs. It is visible that the calculated values appear much below than the experimental results. This difference can be explained by the influence of velocity fluctuations in vicinity of the stagnation point and in the near-wall jet. For example, in [8] the influence of velocity fluctuations and other parameters is

5

taken into account by the formula $\text{Nu}_\text{T}(0) = \text{Nu}(0)(1 + 0.75b^{0.54})$, $b = 0.18\varepsilon v \cdot \sqrt{\rho_0/\beta\mu_0}$, where $\text{Nu}(0)$ is the Nusselt number calculated disregarding turbulent oscillations, $\varepsilon = \sqrt{v'^2}/v\cdot$ is the turbulence level, ρ_0 is the density at the stagnation point, and μ_0 is the viscosity calculated by the stagnation temperature of the flow. For the results calculated by this formula to become equal to the experimental ones, it is necessary to accept $\varepsilon = 0.25$. This value appears in the range (0.04 - 0.5) of ε, measured experimentally by independent methods [9].

In Fig. *4,b* the values of the Stanton number $\text{St}_e = \alpha/\rho_e u_e c_p$ are represented depending on the Reynolds number constructed by the energy loss thickness $\delta_T^{\bullet\bullet}$, which is calculated using to the energy equation for a turbulent boundary layer.

As follows from Fig. *4,b* in this case the experimental values appear to be greater than the calculated ones. It shows that for the flow under study it is impossible to calculate heat exchange by (4) and (5) and, apparently, the model of calculation of heat exchange offered in works [7, 8] is more correct and promising. However, there are difficulties in calculation and experimental measurement of velocity fluctuations, and this problem in many cases appears much more difficult than direct measurement of heat transfer coefficient.

The experimental results obtained allowed one to determine the temperature on the surface and inside the substrate. Distribution of temperature in a substrate of length $2L$ and thickness δ_s is calculated by the joint solution of the stationary heat conduction equation

$$\frac{\partial^2 T(x,z)}{\partial x^2} + \frac{\partial^2 T(x,z)}{\partial z^2} = 0$$

($T(x, z)$ is the temperature in the substrate) and the law of conservation of heat in a steady-state case $\int_0^L \alpha(x)(T_0(x) - T(x,0))dx = 0$, using experimental data on the stagnation temperature and heat transfer coefficient in the near-wall jet. The solution was sought as $T(x,z) = T_s(x) + a(x)z + b(x)z^2$. The boundary conditions on the surfaces $z = 0$ and $z = -\delta_s$ result in the relationships

$$\lambda\frac{\partial T(x,z)}{\partial z}\bigg|_{z=0} = \alpha(x)(T_0(x) - T_s(x)) \Rightarrow a(x) = \frac{\alpha(x)}{\lambda}(T_0(x) - T_s(x)),$$

$$\lambda\frac{\partial T(x,z)}{\partial z}\bigg|_{z=-\delta_s} = 0 \Rightarrow b(x) = \frac{a(x)}{2\delta_s} = \frac{\alpha(x)(T_0(x) - T_s(x))}{2\delta_s\lambda}.$$

Finally, we have

$$T(x,z) = T_s(x) + \frac{\alpha(x)}{\lambda}(T_0(x) - T_s(x))\left(z + \frac{z^2}{2\delta_s}\right). \tag{7}$$

By substituting (7) into the heat conduction equation and performing necessary calculations, we obtain the equation for calculation of the temperature of the substrate surface.

$$\frac{\partial^2 T_s(x)}{\partial x^2} = \frac{\alpha(x)}{\delta_s}(T_0(x) - T_s(x)).$$

6

Solving it together with the integral heat conservation equation, we obtain the temperature distribution on the substrate surface for $0 \leq x \leq L$. Then, using the known $T_s(x)$, we find the temperature distribution in the substrate.

The results of calculation for the case $L = 100 \cdot 10^{-3}$ m, $T_0^* = 1200$ K, $\delta_s = 3$ mm are presented in Fig. 5. Figure 5,a represents the surface temperature of substrate made of various materials.
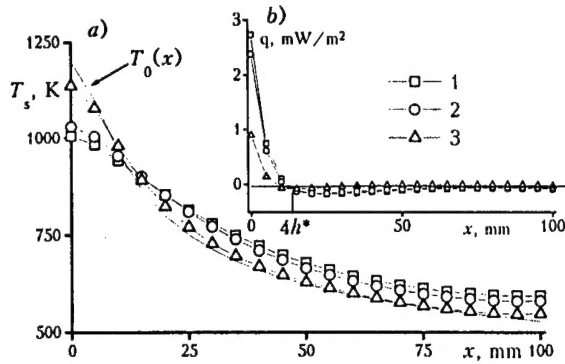

Fig. 5. Distribution of the surface temperature (a) and heat flux (b) on various substrates. 1 – Cu ($\lambda = 350$ W/m·K), 2 – Al ($\lambda = 250$ W/m·K), 3 – Steel ($\lambda = 40$ W/m·K).

The calculation shows that noticeable decreases in the surface temperature in the vicinity of the stagnation point (for materials with $\lambda \geq 40$ W/m·K) in comparison with the stagnation temperature of the incoming jet occurs because of redistribution of heat inside the substrate. As is visible from Fig. 5,b, at the initial stage ($0 \leq x \leq 4h^*$) the heat enters the substrate, at longer distances, the process is converted – heat goes away from the substrate to the near-wall jet.

Based on (7) it is possible to estimate ΔT_{max}, the maximum difference of surface temperatures for $z = 0$ and $z = - \delta_s$

$$\Delta T_{max} = \frac{\alpha(0)\delta_s}{2\lambda} \left(T_0(0) - T_s(0)\right) \approx 20 \text{ K}$$

for the condition of calculation represented in Fig. 6,a. That is, the surfaces temperatures of $z = 0$ and $z = -\delta_s$ practically do not differ.

Using the calculation data a dependence of the surface temperature on the substrate length in the spray spot ($x = 0$) for various versus of substrate thickness δ_s is plotted in Fig. 6.
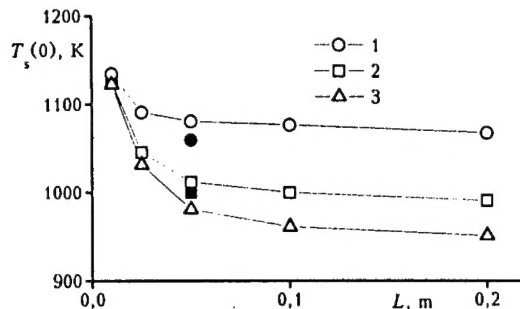

Fig. 6. Dependence of copper substrate surface temperature in the spray spot ($x = 0$) on its length. 1 – $\delta_s = 1$ mm, 2 – $\delta_s = 3$ mm, 3 – $\delta_s = 5$ mm.

7

It is seen that, with an increase in the substrate length up to $(15-20) \cdot h^*$, the surface temperature at the center decreases noticeably. And the greater the size δ_s, the greater the decrease. A further increase in the substrate length practically does not influence the surface temperature at the center. The experimental verification (solid circle and square symbols) shows good agreement of the measured data on the surface temperature near the stagnation point with those obtained by calculation, which proves the assumption made and allows one to use the proposed model of heat exchange in practical evaluations.

Thus, the distributions of the stagnation temperature and heat transfer coefficient in the near-wall jet for various stand-off distances from the edge of a supersonic nozzle of a rectangular section to an substrate are experimentally obtained. It is shown that the experimental data on the heat transfer coefficient are much higher than the calculated ones, and this difference can be explained by velocity fluctuations in the vicinity of the stagnation point and in the near-wall jet.

Using experimental data of the stagnation temperature and heat transfer coefficient, in the stationary case the substrate temperature is calculated. It is shown that at the expense of redistribution of heat inside the substrate for heat-conductive materials ($\lambda \geq 40$ W/m·K), a decrease in the surface temperature in a spray spot in comparison with the stagnation temperature is observed. This effect should be taken into account for improvement of spraying regimes with excitation of synthesis reactions immediately on the surface, because in this case the temperature is a major parameter influencing the initiation of the reaction.

References

1. **Kudinov V.V., Pekshev P.Y., Belashenko V.E.** et al. Plasma Spraying. M.: Nauka, 1990. 407 p. (in Russian).
2. **Shorshorov M.H., Harlamov Y.A.** Physico-Chemical Fundamentals of Detonation Spraying. M.: Nauka, 1978 (in Russian).
3. **Yudaev B.N., Michailov M.S., Savin V.K.** Heat Exchange at Jet – Obstacle Interaction. – M.: Mashinostroenie, 1977 (in Russian).
4. **Alkhimov A.P., Klinkov S.V., and Kosarev V.F.** Impingement of the Supersonic Jet of the Rectangular Section on the Flat Obstacle // Thermophysics and Aeromechanics, 2000, vol. 7, № 2.
5. **Belov I.A., Pamadi B.N.** Jet impingement upon flat plate // IIT-AERO-TN – Bombay Inst. of Technology. 1970. № 3. P. 89.
6. **Belov I.A., Ginzburg I.G., Zasimko V.A., Terpigorev V.S.** Influence of Jet Turbulence on Heat Exchange with an Obstacle // In: Heat and Mass Transfer. – Minsk, ITMO. 1969. Vol. 2. p. 167 – 183 (in Russian).
7. **Gubanova O.I., Lunev V.V., Plastinina L.I.** About Central Burbling Zone in Interaction of an Underexpanded Supersonic Jet with a Flat Plate // Izv. Russian Akad. Nauk, Mekh. Zhid. Gasa. 1971. № 2. p. 135 - 138 (in Russian).
8. **Belov I.A.** Interaction of Irregular Flows with Obstacles. Leningrad: Mashinostroenie, 1983 (in Russian).
9. **Kalghatgi G.T., Hunt B.L.** The occurrence of stagnation bubbles in supersonic jet impingement flows // Aeronaut. Quarterly. 1976. Vol. 27. P. 169 - 185.
10. **Volchkov E.P., Semenov S.V.** Fundamentals of Boundary Layer Theory. Novosibirsk: Institute of Thermophysics SB RAS, 1994 (in Russian).

THE FEATURES OF ACCELERATION OF PARTICLES IN SUPERSONIC NOZZLES OF A RECTANGULAR CUT FOR COLD GAS DYNAMIC SPRAYING

A.P. Alkhimov, V.F. Kosarev and S.V. Klinkov
Institute of Theoretical and Applied Mechanics SB RAS
630090, Novosibirsk, Russia

This paper presents the peculiarities of the supersonic nozzle design for the cold gas-dynamic spraying. Solution procedure of the problem how to produce the high particle velocity due to correct choice of the geometrical dimensions of the applied accelerating nozzles is described. Numerical and experimental research of wedge-shaped nozzles shows that there is a nozzle with its particular dimensions for a given type of particles that produces maximum possible particle velocity at the moment of impact on a target surface.

One of the main problems in gas dynamic spray process is to provide the optimal velocity (kinetic energy) of the particles that form the coating [1]. Experimental data show that the efficiency of these dynamic parameters may be raised if we take care of some effects (boundary layer along the nozzle walls, a local high pressure region) which occur when the gas-powder mixture moves in the supersonic nozzle and when the jet impinges on the substrate. Thus, the consideration of the problems concerning the development of the Laval nozzles applied for the spraying is urgent. Gas dynamic principles that are at the basis of this paper are general for all conventional thermal spray techniques that use two-phase gas-particle mixture flows. The common problem for these techniques is the productivity increase and the product costs lowering, i. e. the possibility to apply rapidly the coatings over the larger surface area under the lower gas flow rate and energy consumption conditions. One of the ways to solve this problem is to use flat two-phase jets of the small thickness. It decreases the carrier gas consumption and allows the more even material deposition. This article is dedicated to the design and study of the nozzle shapes that produce these jets.

Figure 1 shows the shape and geometrical dimensions nomenclature of these nozzles. Expansion from the nozzle throat to the outlet cross-section is assumed to be proportional to the axial coordinate, i.e. the angle of the nozzle generator slope to the nozzle axis is constant. These nozzles are easily produced and make it possible to vary one of the dimensions of spray spot including to obtain one minimum possible spray spot size that is necessary in some cases of the practical application.
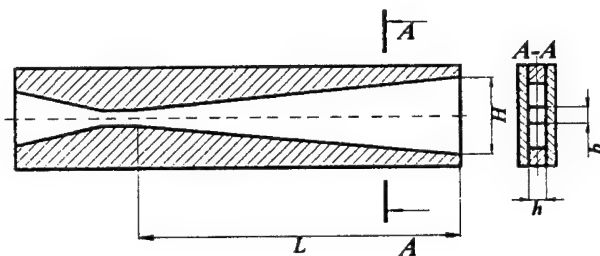

Fig. 1. Outward shape of investigated nozzles and applied
notation of parameters.

The particle velocity increase is known to result in the better coating quality. It is demonstrated by examples of developed high-velocity spray methods and devices (HVOF, JP5000, and CGS). Therefore, designed nozzles should provide the high particle velocities.

There are some phenomena that influence essentially on the gas dynamics and are important for the accelerating nozzle design. These are the presence of the boundary layer along the nozzle walls and the low-velocity subsonic high-pressure region that occurs in front of the target surface while the supersonic two-phase jet impinges on the substrate.

To accelerate particles in the nozzle up to the gas velocity it is necessary to increase the nozzle length L. However, as the nozzle length increases the boundary layer thickness increases too. It leads to the decrease of the effective nozzle cross-section area downstream in comparison to the geometrical cross-section area. As a result the gas velocity decreases at the nozzle exit in comparison to the ideal gas flow velocity.

The main governing statutes of the gas flow model suggested in [2] within the nozzle are the following ones. In subsonic part of the nozzle the calculation is performed according to the ideal gas model. From the nozzle throat the increase of boundary layers along the nozzle walls is numerically determined by Karman equation up to the point where boundary layer junction occurs. In this case the stagnation pressure near the nozzle axis is preserved. Then, starting from the point of the boundary layers junction the self- similar gas flow appears and calculation is performed by equations for the mean gas flow parameters. Axial parameter values are restored in accordance with the "1/7" velocity distribution law. In general other more accurate models can be used. However, this model is simple enough and permits to obtain quickly the estimates of the gas parameters near the nozzle axis at any axis point within the nozzle. To check the calculation correctness of the mentioned model the axial Mach number values at the nozzle exit were measured. Figure 2 shows ratio of the real Mach number M^* obtained by calculation and experimentally and the Mach number M_G that should be when the boundary layer along the nozzle walls was absent. This ratio is presented versus the ratio of the nozzle thickness and the nozzle length.

It should be noted that when h/L approaches infinity the ratio M^*/M_G tends to unity. It means physically that with the decrease of the nozzle length at constant thickness or with the increase of the thickness at constant length the influence of the boundary layer on the main gas flow vanishes and the gas flow acquires the features of the ideal gas flow.

1 - $M_G = 2.72$; $p_0 = 1.5$ MPa; $h = 3$ mm; $b/H = 0.3$; $h/L = 0.03$

2 - $M_G = 2.72$; $p_0 = 1.5$ MPa; $L = 0.1$ m; $b = 3$ mm; $H = 10$ mm

3 - $M_G = 2.72$; $p_0 = 1.5$ MPa; $h = 3$ mm; $b = 3$ mm; $H = 10$ mm

4 - $M_G = 2.18$; $p_0 = 0.6$ MPa; $h = 3$ mm; $b = 3$ mm; $H = 6$ mm

5 - $M_G = 3.45$; $p_0 = 1.5$ MPa; $h = 3$ mm; $b = 3$ mm; $H = 20$ mm

6 - $M_G = 3.45$; $p_0 = 4.0$ MPa; $h = 3$ mm; $b = 3$ mm; $H = 20$ mm

7 - $M_G = 3.45$; $p_0 = 4.0$ MPa; $h = 3$ mm; $b/H = 0.15$; $h/L = 0.03$
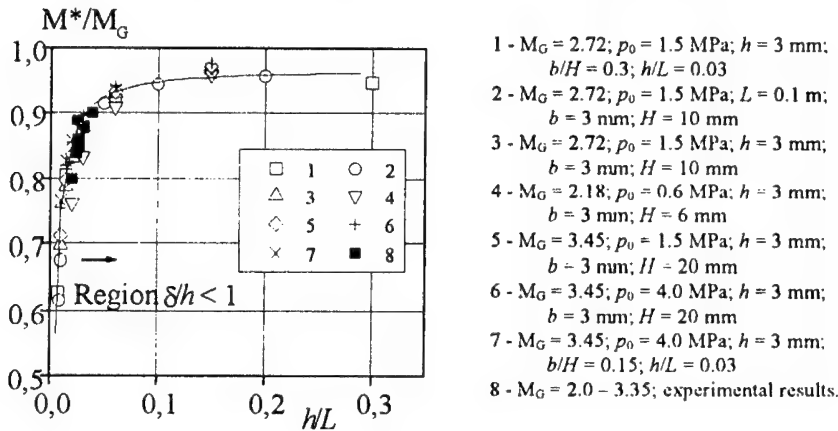
8 - $M_G = 2.0 - 3.35$; experimental results.

Fig. 2. Dependency of the relative Mach number at the nozzle axis on the relative extension of the nozzle.
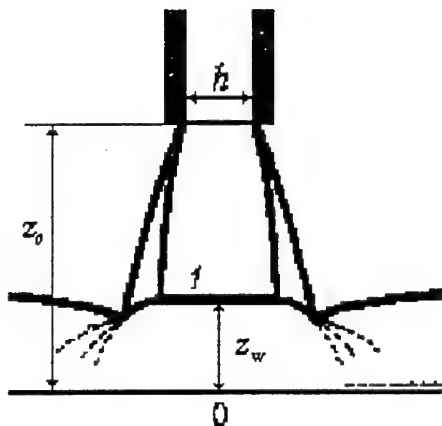
Fig. 3. The scheme of impingement of supersonic gas jet on flat unrestricted obstacle.
1 – detached shock; h – nozzle thickness, z_0 – distance from nozzle exit to an obstacle.

The results obtained prove that the nozzle lengthening for the best particle acceleration purposes at a given nozzle thickness is limited by an increase of the boundary layers along the nozzle walls. To diminish the boundary layer influence under an unchangeable nozzle length condition it is necessary to increase the nozzle thickness. However, it is shown later to be also limited.

Let's consider a supersonic jet impingement on the normally positioned obstacle (Fig. 3). A deceleration and turning of a gas flow occur in front of an obstacle surface. A transition from high velocity supersonic flow to low velocity subsonic one occurs by a shock that appears at some distance z_w from the obstacle surface. A high-pressure and high-density gas layer is created between the obstacle surface and a shock. Apparently small particles of the deposited material coming through this compressed layer will loose some quantity of their velocity. This quantity is the greater as the greater the compressed layer thickness.

To determine the compressed layer thickness several experiments with the nozzles of various thickness and axial Mach number values at nozzle exit were carried out [3].

Using the gas mass balance law written for the case of the rectangular cross-section jet impingement it is possible to obtain the next relationship.

$$z_w = k \frac{h/2}{1 + h/H} \tag{1}$$

The experimental results are satisfied choosing the value $k \approx 0,9$ that is unchangeable enough in a given range of parameters.

The variation of the axial Mach number value within a compressed layer can be approximated by polynomial of the third order satisfying the following boundary conditions.

After the shock $z = 0$: $M = M_s$ and $dM/dz = 0$,

on the surface $z = z_w$: $M = 0$ and $dM/dz = -0.5 M_s / z_w$,

where M_s is the Mach number just after a shock. Most of them are obvious. The last condition derives from the generalization of a great number of the experimental data [4, 5] and denotes that the velocity gradient at the point of a flow turn (point O in fig. 3) is uniform. The following dependency satisfies the boundary conditions mentioned above

$$M = M_s \left(1.5 \left(z/z_w \right)^3 - 2.5 \left(z/z_w \right)^2 + 1 \right).$$

Thus, compressed layer thickness depends on the main governing parameter that is the nozzle thickness. As it is seen from (1), the compressed layer thickness increases when the nozzle thickness h is set to the greater value and when the ratio h/H remains the same. As a consequence it leads to the increasing loss of the particle velocity of the deposited material. At impact on the substrate surface the particles will have smaller velocity than they have one at the nozzle outlet.

11

As it follows from the all above the nozzle optimization problem must be considered as the particle velocity maximization not at the point of nozzle outlet but at the point of contact with a target surface v_{pw}. Then, the thickness of the flat nozzles (or diameter of axisymmetric nozzles) as well as the nozzle length are both the most important parameters.

To obtain optimal values of the nozzle thickness and nozzle length we set the next limitations. The stagnation (total) temperature of gas is constant (the case of heat insulated nozzle walls). The throat areas and the values of stagnation pressure at the nozzle inlet p_0 are the same for the different nozzles.

These constraints make the gas flow rate in the different nozzles to be the same. It was supposed that the jet exhausts in a chamber where pressure is 10^5 Pa. To make pressure in the exhausted jet equal to ambient one (isobar exhaustion) a greater dimension of the nozzle cross-section at nozzle exit H was chosen. Simultaneously the nozzle thickness h remained the same and as a consequence the compressed layer thickness changed slightly. Thus, we have considered the optimization problem on the variety of wedge-shaped nozzles of equal gas flow rate producing the isobar jets.

To calculate the particle velocity v_p the model of the single particle motion is used. It allows one to pay no regard to the influence of particles on the gas flow parameters. The application of the single particle model is known to be justified by low powder loading the gas flow (volume concentration of particles less than $10^{-6} - 10^{-4}$) that is often used in practice. It is supposed that the particles move along the nozzle axis and along the jet axis. Particle velocity was calculated by equation

$$m_p v_p \frac{dv_p}{dz} = C_D \frac{\rho \left(v - v_p\right)^2}{2} S_{mid} ,$$

(2)

$$\mathrm{M}_p = \frac{v - v_p}{a} ; \quad \mathrm{Re}_p = \frac{\left(v - v_p\right)\rho d_p}{\mu}$$

where m_p, d_p, S_{mid} are the mass, diameter and cross-section area of the particle. The gas parameters are taken near the axis. Drag coefficient C_D is calculated by Henderson approximation [6].

To check the calculation correctness the particle velocity at the nozzle outlet was determined experimentally [7]. The calculation results compared with experimental ones. It is
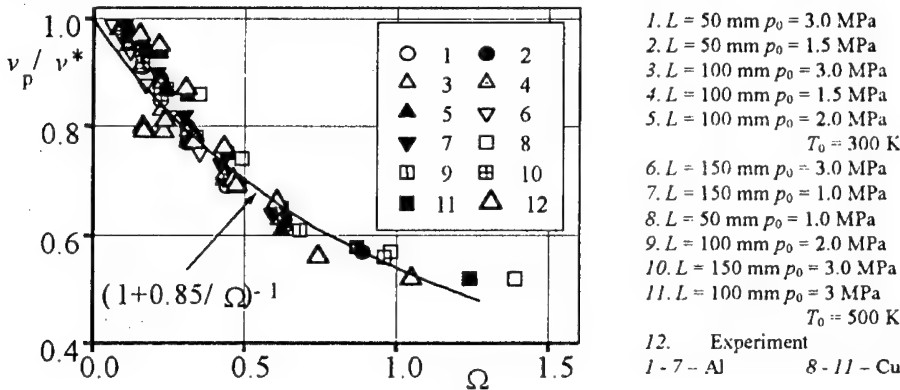

Fig. 4. Generalized dependency of relative velocity of particles at outlet of the flat supersonic nozzle,

$$\Omega = \left(d_p/L\right)^{0.5}\left(\rho_p v_*^2/p_0\right)^{0.5} .$$

presented in Fig. 4 as dependency of the ratio of particle velocity and gas velocity on the parameter that turns out to be the main one in the analysis of the particle motion equation (2) (ρ_p is density of particle material). It is seen that numerical and experimental data agree. It proves the reliability of the calculation data.

To determine the particle motion parameters in the jet the gas parameters were calculated by the formula from [8]. This formula was obtained by the experimental result approximation. The influence of the jet and compressed layer is shown in Fig. 5. Note the particles of the size less than 10 microns are well influenced by the jet length and compressed layer thickness. It is also seen from Fig. 5 that the impact velocity of small a particles increases when the jet length (standoff distance) increases. It occurs because of the weakening the shock. The particle velocity value at the shock decreases following the gas velocity in the jet. It lead to the weakening the shock and to the worse deceleration of the particles in the compressed layer. Thus the jet length is also very important parameter that controls the optimization circumstances. In Fig. 5 the optimal standoff distance is close to the 30 - 40 mm.

Including the jet length allows one to complete the particles motion model along the whole gas dynamic path and to start the searching for the optimal nozzle parameters.

This problem was solved by successive selection of the parameters h and L that are input parameters in calculation. By comparison of the obtained values of particles velocity at impact $v_{pw}(h, L)$ its maximum value and the values of optimal parameters respectively were found.
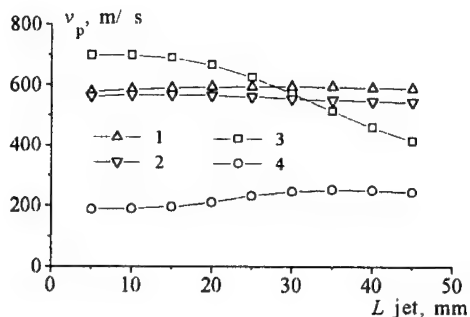

Fig. 5. Particle velocity dependence on the jet length (standoff distance).
1 – 10-mkm-particle velocity at the shock,
2 – 10-mkm-particle velocity at impact,
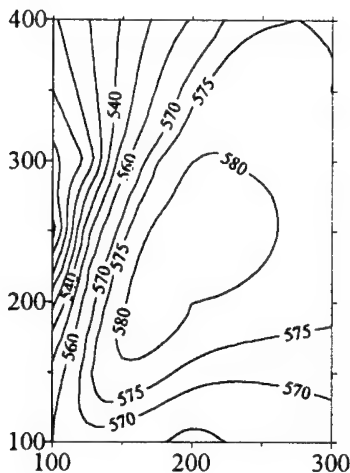3 – 1-mkm-particle velocity at the shock,
4 – 1-mkm-particle velocity at impact.

Fig. 6. Isolines of velocity of aluminum particles $d_p = 10$ μm at impact on the surface of an obstacle. $z_0 = 15$ mm, $T_0 = 470$ K, $p_0 = 1.5$ MPa. Abscissa is $100h$, mm, ordinate is L, mm. Numbers on the curves denote values of impact velocity, m/s.

13

Figure 6 presents a typical graph of isolines of the particles velocity at impact. It is seen that curves are concentrated round one region where particle velocity obtains maximum value (in Fig. 6 this region is bordered with isoline 580 m/s). It denotes that the maximum impact velocity can be produced only applying the nozzle of defined values of the length and thickness.

Figure 7 presents the dependence of the optimal parameters on the Al-particle size. Selecting these parameters one can produce the maximum impact velocity that is near the 600 m/s and doesn't vary for all watched particle sizes (Fig. 8).

Finally the comparison of the two different nozzles is presented in Fig. 9. First nozzle is one optimized for 5 – micron sized particle. Second nozzle is the non-optimized nozzle used often in practice (L = 100 mm, h =2 mm). It is seen from Fig. 9 that these nozzles are almost equal up to the particle size about 5 - 10 microns but quite differ below this value. In practice it may result in the less containing of the submicron particles in the coating and the greater coating porosity.

Unfortunately we had no possibility to test experimentally the particle velocity at impact with a surface. Thus, we rely upon results of calculation. These calculations, however, were tested at some stages experimentally which makes them reliable.
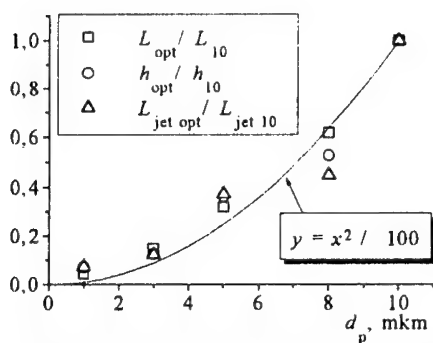

Fig. 7. Optimal parameter dependence on the particle size. L_{10} = 210 mm, h_{10} = 2.4 mm, L_{jet10} = 33 mm.

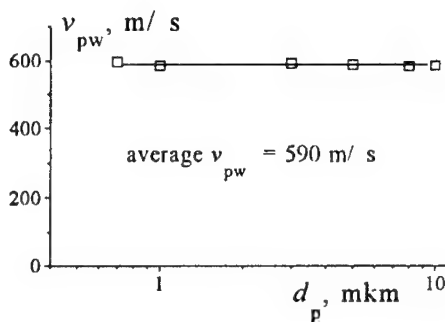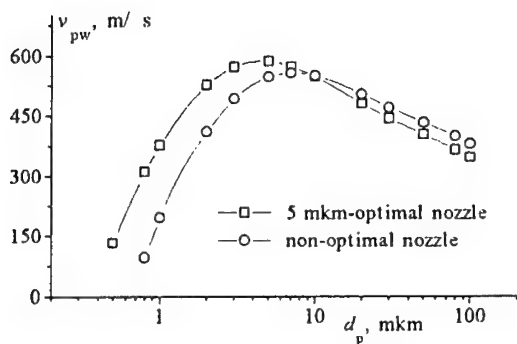Fig. 8. Maximum impact velocity dependence on the particle size

Fig. 9. Impact particle velocity dependence on the particle size fortwo different nozzles.

The approach presented here opens an opportunity for the spraying of the ultra-disperse powders ($d_p = 0.1 - 1$ μm) in contradistinction to the traditional estimates of the impact velocity by the velocity at the nozzle outlet. These estimates are not useful because the particles of such a small size form velocity balance two-phase flow of the small relaxation length. It means that the impact particle velocity is also very small. Otherwise, applying the approach described above it is possible to get the most favorable condition for the ultra-disperse powder spraying.

Thus, it has been shown that the effects of boundary and compressed layers make a sufficient influence on the final particle velocity, the smaller size of the particles is the greater influence is. This influence should be taken into account especially in the case of the cold spray nozzle design because the particle size of the commonly used powders is small and the impact particle velocity is very important.

The solution suggested here is thought to yield the optimal nozzle dimensions and impact particle velocity and going this way to forecast the behavior of the heterogeneous jet-obstacle interaction.

References

1. **Alkhimov A.P., Kosarev V.F., Papyrin A.N.** A method of cold gas-dynamic deposition // Dokl. Akad. Nauk SSSR. 1990. Vol. 315, No. 5. P. 1062-1065.

2. **Alkhimov A.P., Kosarev V.F., Klinkov S.V.** Flow in a rectangular supersonic nozzle of large aspect ratio // Thermophysics and Aeromechanics. 1999. Vol 6, No. 1. P. 49-55.

3. **Alkhimov A.P., Kosarev V.F., Klinkov S.V.** Impingement of the supersonic jet of the rectangular section on the flat obstacle // Thermophysics and Aeromechanics. 2000. Vol. 7, No. 2. P. 221-228.

4. **Belov I.A., Ginzburg I.P. Shoob L.I.** Supersonic underexpanded jet impingement upon flat plate // Int. T. Heat and Transfer. 1973. Vol 16. P. 2067-2076.

5. **Nakatogawa T., Hirata M., Kukita I.** Desintegration of a supersonic jet impinging normally on a flat plate // J. Spacecraft. 1971. Vol 8. No. 4. P. 410-411.

6. **Henderson C.B.** Drag coefficient of spheres in continuum and rarefied flows // AIAA J. 1976. Vol 14. P. 707-708.

7. **Alkhimov A.P., Klinkov S.V., Kosarev V.F., Papyrin A.N.** Gas-dynamic spraying. Study of a plane supersonic two-phase jet // J. of Applied Mechanics and Technical Physics. 1997. Vol. 38, No. 2. P. 324-330.

8. **Alkhimov A.P., Klinkov S.V., Kosarev V.F.** A study of supersonic air jets exhausted from a rectungular nozzle // Intern. Conf. Methods Aerophys. Research: Proc. Pt III. Novosibirsk, 1998. P. 41-46.

ELECTRON-BEAM DIAGNOSTIC OF HYPERSONIC WAKE

V.M. Aniskin

Institute of Theoretical and Applied Mechanics SB RAS, Novosibirsk, 630090, Russia

Introduction

The problem of flow stability in a hypersonic wake past various bodies is of great fundamental and practical interest. This interest was awakened by works on further improvement of mixing processes in combustion chambers of ramjets and scramjets. The full bibliography of relevant works can be found in [1]. The stability of the hypersonic wake under actual experimental conditions still remains poorly understood because of severe difficulties in using traditional experimental procedures in high-enthalpy wind tunnels. On the other hand, electron-beam-induced fluorescence has found widespread utility in measuring density and temperature in rarefied hypersonic flow [2]. Recently, this method has been successfully used to measure density fluctuations.

This work describes a technique which permitted us, by measuring the electron-beam-induced fluorescence, to determine characteristics of density fluctuations in the near wake past a cone and in the far wake past a hydrodynamic whistle at Mach number $M = 21$ and unit Reynolds number $Re_1 = 6 \cdot 10^5 \text{ m}^{-1}$.

Experimental setup and procedure

All measurements were carried out in the T-327 wind tunnel of the Institute of Theoretical and Applied Mechanics, SD RAS. In the experiment, a model of cone with a sharp nose and a hydrodynamic whistle were used. The length of the cone and the diameter of its base were 113 and 40 mm, respectively. The whistle was an 80 mm-long copper tube with inside and outside diameters 6 and 8 mm. The rim of the upstream end of the whistle was inclined at the angle $20°$ to the tube axis. Inside the whistle, a traveling piston equipped with a pressure gauge was installed, with a provision made for water cooling of the whistle housing. In the hypersonic flow around the whistle, 150-dB pressure fluctuations were generated. The frequency of the fluctuations was dependent on the piston position in the whistle. The pressure fluctuations in the whistle gave rise to fluctuations of flow characteristics in the wake. The experiments were carried out at fixed excitation frequencies 10.5, 8.3, and 5.6 kHz, as well as under flow conditions without fluctuations.

The schematic diagram of the measurement procedure is shown in Fig. 1. Electron beam (1) was generated by electron gun (2). The current, diameter of the electron beam in vacuum and the electron energy were 1 mA, 1 mm and 12-14 keV, respectively. Magnetic deflection system (3) was used to adjust the position of the electron beam along the normal to the model wake axis (4). The optical scheme intended for measuring fluorescence from nitrogen included fast lens (3), filter (6) with a transmission band width 360-500 nm, light-splitter (7) that restricted the field of vision of photomultiplier tubes (8) to an area of $1.7 \times 1.7 \text{ mm}^2$ in the directions across and along the beam. The beam current was determined by measuring the current across electron collector (9).

The wake field was scanned along X- and Y-axes by displacing the model across and along the flow. The optical scheme could scan the flow pattern along the electron beam (along the Z-axis).

To extract characteristics of density fluctuations, the fast Fourier transform of the temporal data arrays of the quantities of interest was used. Cross-spectra of signals of two photomultipliers, which measured the fluorescence intensity from the same point of observation were taken. In each cross-spectrum, only those parts of signals, related to density fluctuations, were retained which were common for both photomultiplier. For the whistle, cross-spectra of the whistle gauge and the signal of one of the photomultiplier were measured. This allowed us to extract density fluctuations at the excitation frequencies of pressure fluctuations in the whistle. The amplitude and phase spectra of the fluctuations were the output data of the Fourier transform.
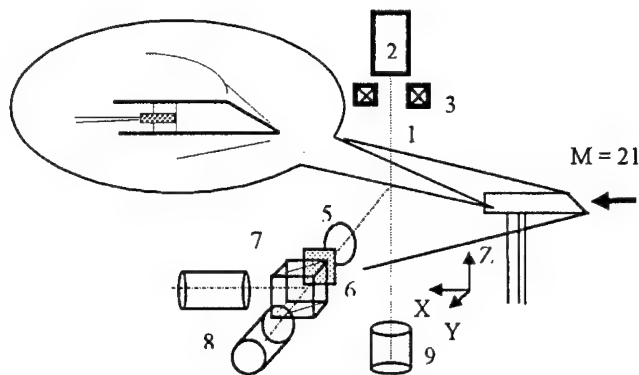

Fig. 1

The measuring system permitted two-point measurements in the flow. In measurements along the flow, the initial electron beam was split into two beams in the X-direction by feeding the magnetic system with electric pulses that were following at a repetition frequency of 20 kHz with the pulse period-to-pulse duration ratio equal to 2. By swinging the light-splitting cube, the observation points of each photomultiplier could be adjusted to trace the direction under examination. By turning the whole optical system through the right angle around the observation axis, we could drive the points of observation apart along the electron beam (i.e., along the Z-axis). In the above procedure, there was no need to split the initial beam into two components. The separation between the measurement points in both cases could be varied throughout the range from 0 to 0.04 m. The longitudinal phase velocity C_x and transverse phase velocity C_y were found from the phase difference between two measurement points. For the whistle, the longitudinal phase velocity was found from the incremental phase rise at the measurement point with respect to the phase of pressure fluctuations in the whistle. The density wave inclination angle was determined from the relation $\chi = \mathrm{atan}(C_x/C_z)$.

In mean density measurements, we made allowance for the signal attenuation caused by collisional molecule deactivation and electron scattering. Under conditions of our experiments, it was the first process that contributed significantly. The normalized density allowed for the deactivation was reconstructed using the formula $n/n_\infty = I/I_\infty/(1 - K_\tau\, I/I_\infty)$. Here n is the density in the wake (concentration); n_∞ is the approach stream density, I is the signal generated by the photomultiplier, I_∞ is the reference signal of the photomultiplier in the freestream, and K_τ is the constant of the excitation quenching [4]. The scattering in the gas was taken into account as a

the second-order factor. The correction factor for the scattering was calculated in an iterative process using the relation

$$\left(\frac{n}{n_\infty}(z)\right)_{N+1} = \frac{\left(\frac{n}{n_\infty}(z)\right)_0}{\exp\left(-\beta\int_a^z\left(\frac{n}{n_\infty}(l)\right)_N dl\right)}, \quad N=0, 1, 2, \ldots$$

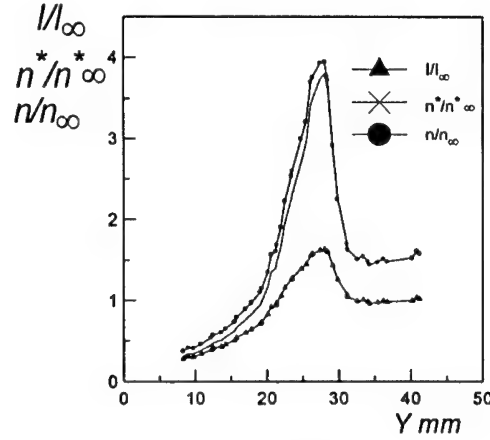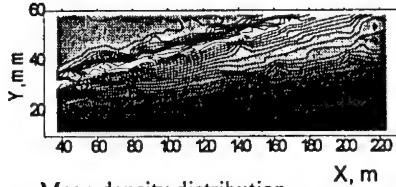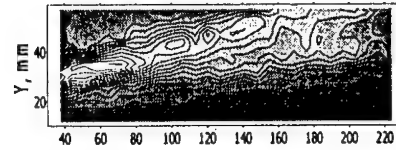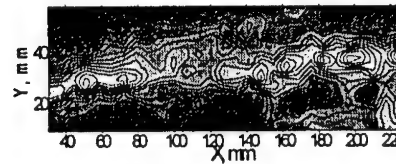Fig. 2

The subscript "0" here refers to the density calculated without allowance for the collisional molecule deactivation. The subscripts "N" and "N+1" denote the iteration step. The scattering coefficient β was determined from the signal decay rate in the outside flow prior to the shock wave. Its position along the Z-axis is given by the value of a. The procedure used in reconstruction of the mean density is illustrated by Fig. 2. Here curves ($\blacktriangle$), ($\times$), and ($\bullet$) show the distribution of the photomultiplier signal and the density profiles deduced from the experimental data with and without making allowance for the scattering.

The normalized pulsational density n'/n_∞ is related to the normalized amplitude of the pulsational component of the output signal I'/I_∞ in the measurement point by the formula $n'/n_\infty = I'/I_\infty \cdot (1+K_\tau \cdot n/n_\infty)$. The above relation allows for the effect of mean density on the amplitude of density fluctuations.

a. Mean density distribution

b. Distribution of the density pulsations

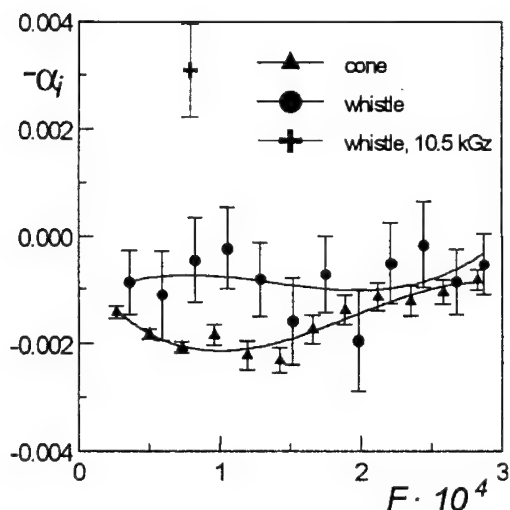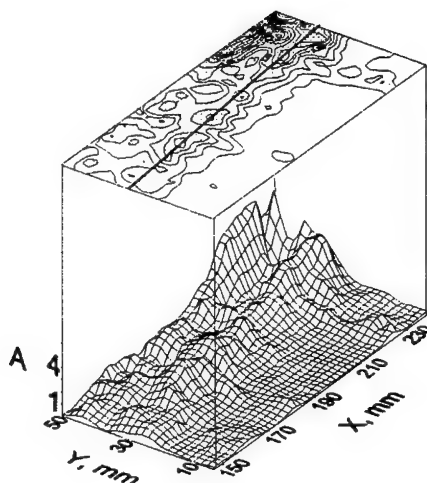c. Density pulsations to mean density ratio

Fig. 3

Fig. 4

Fig. 5

The increment value was determined using the generally accepted procedure. The absence of a clear line of maximum integral fluctuations in the wake past the cone and the closed whistle similar to the line observed in the flow around a plate [3] was the main difficulty in calculation of the pulsational density increment. To identify such a line, we used normalization of the total pulsational signal (Fig. 3 b) to the mean density one (Fig. 3 a). It is along this line of maximum density fluctuations (Fig. 3 c) that the increment of fluctuations was calculated. The growth rate spectrum of the pulsational density in the wake past the cone is shown in Fig. 4 (▲).

The increment of pulsational density in the wake past the closed whistle, Fig. 4 (●), was determined along the line of maximum fluctuations. The increment of pulsational density at the wake excitation was determined along the line of maximum fluctuations at the fundamental frequency and harmonics (the data for $f = 10.5$ kHz are shown in Fig. 5). The increment for the fundamental frequency 10.5 kHz is shown in Fig 4 (✛). The pulsational density in the wake is seen to increase markedly under the action of strong outside disturbances.

References

1. Ramaswamy M., Loth E. Tone excitation of a supersonic bounded shear layer // AIAA J. 1996. Vol.34, №10. P. 1997-2004.
2. Experimental methods in rarefied gas dynamics / Ed. S.S. Kutateladze. Novosibirsk: Institute of Thermophys., USSR Acad. Sci., Siberian Branch, 1974.
3. Maslov A.A., Mironov S. G., Shiplyuk A. N. Wave processes in the hypersonic shock layer on a flat plate // Fluid Dynamics. 1998. Vol. 33, № 5. P. 772-777.
4. Belikov A.E., Kusnetsov O.V., Sharafutdinov R.G. The rate of collisional quenching of N_2O^{*+}, N_2^{*+}, O_2^{*+}, O^{*+}, O^*, Ar^*, Ar^{*+} at the temperature < 200K // J. Chem. Phys. 1995. Vol. 102. P. 2792-2797.

CONTROL OF STREAKY STRUCTURES BY
LOCALIZED BLOWING AND SUCTION

A.A. Bakchinov [1,3], **M.M. Katasonov** [2], **P.H. Alfredsson** ,[1] and **V.V. Kozlov** [2]

[1] Dept. Mechanics, Royal Institute of Technology, S-100 44 Stockholm, Sweden
[2] Institute of Theoretical and Applied Mechanics SB RAS, 630090 Novosibirsk, Russia
[3] Present address, Thermo and Fluid Dynamics, Chalmers, S-412 96 Gothenburg, Sweden

1. Introduction

In many forms of by-pass transition [1, 2], the stages before an incipient spot is formed is characterized by the formation of streamwise streaky structures in the flow. These structures consist of regions of high and low streamwise velocity and they undergo a breakdown to turbulence, which is preceded by a secondary instability of wavy type. Several studies indicate that the wave instability is driven by the spanwise inflectional profile which is a result of the streaky structures. Transition to turbulence under high levels of free stream turbulence is common in engineering applications and has been shown to include all the different aspects mentioned above.

Transition control has previously been focussed on global methods such as pressure tailoring, suction at the wall, compliant surfaces, heating or cooling the wall, or local methods which has been aimed at cancellation of wave type disturbances (strip heating, moving 2D wall-membranes etc.). Although some of the global methods may have an effect also on by-pass transition they have mainly been used for decreasing the growth of Tollmien – Schlichting type wave disturbances. It is of course of large interest to also be able to control transition in flows where by-pass mechanisms are dominating. In the present study we investigate the effect of blowing/suction on the breakdown of streaky structures. Both the spanwise position relative to the structure as well as the duration and time-location of the control were investigated.

2. Experimental set-up

The present investigation was made in the MTL wind tunnel at KTH. The tunnel is equipped with a flat test plate (Fig. 1) and the disturbance is introduced through a slot in the plate. The disturbance is a pulse of air ejected from a 7.5 mm wide slot located at $x = 95$ mm ($x = 0$ is at the plate leading edge) giving rise to an elongated structure of approximately 20 ms duration [3, 4]. On top of this disturbance a high frequency signal of 200 Hz is introduced. Each disturbance is generated by a separate loudspeaker which are connected in parallel to the slot. With this arrangement a streaky structure with a central low velocity region and two high velocity regions is formed and on this structure a secondary instability is triggered by the high frequency disturbance. The wave-type disturbance grows in amplitude, whereafter it breaks down and a turbulent spot is formed, [4, 5]. Without the high frequency disturbance the streaky structure will eventually die out. The measurements were made at a free stream velocity $U_0 = 5.6$ m/s using hot-wire anemometry.
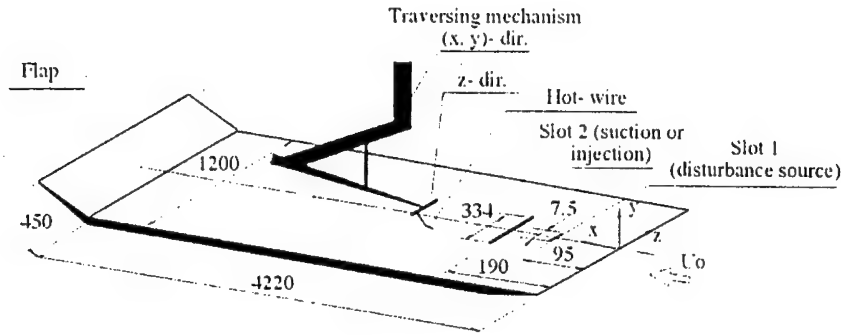
Figure 1. Experimental set-up

3. Results

The control is applied at $x = 190$ mm, where a spanwise slot is located. The slot is covered by a thin plastic tape and holes at the desired positions are made in the tape. The holes have a diameter of approximately 0.5 mm. Two different studies were made, the first aimed to determine the most effective spanwise position for control and the second to optimize the start and duration of suction. In the first study the most effective position for suction was studied by varying the spanwise positions of the holes. During this study suction was continuous. It was clearly shown that for transition delay suction should be applied in the central region below the low velocity region of the structure. If instead suction was applied below the high velocity region breakdown was actually promoted. The influence of suction can be illustrated in Fig. 2, a, where the mean velocity distribution in the spanwise direction is shown. If suction is applied at the centre, below a region with low streamwise velocity, the
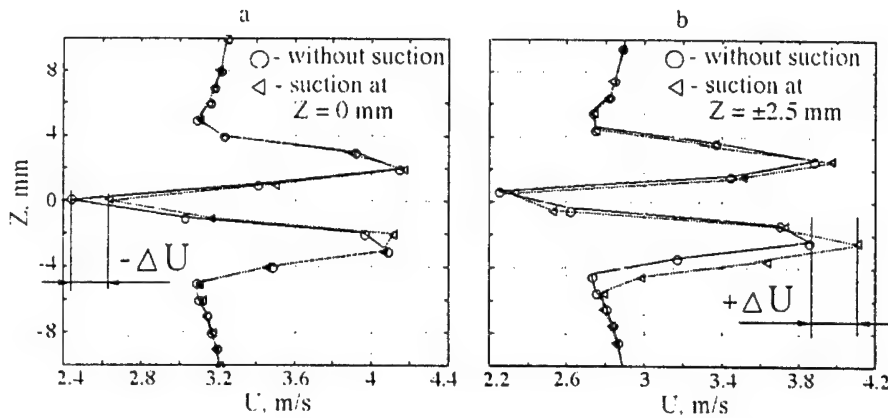
Fig. 2. Mean velocity distribution in spanwise direction when the longitudinal structure is present in the boundary layer; a) positive influence of suction, below a region with low streamwise velocity (turbulent spot appearance is delayed); b) negative influence of suction, below regions with high streamwise velocity (turbulent spot appearance is accelerated). The measurements are carried out at $x = 250$ mm and close to the wall-normal position with maximum disturbance amplitude ($y = y|_{u_{max}}$).

Fig. 3. Time traces of suction influence on longitudinal structure. $z = 0$ mm, $y = y|_{umax}$.
a: longitudinal structure at $x = 195$ mm; b: turbulent spot at $x = 700$ mm; c, f: suction region, 30 and
100 ms duration at $x = 195$ mm; d, g: interaction between longitudinal structure and suction region
at $x = 195$ mm; e, h: interaction result at $x = 700$ mm.

amplitude of the negative region becomes less ΔU and the dU/dz – gradient decreases. This
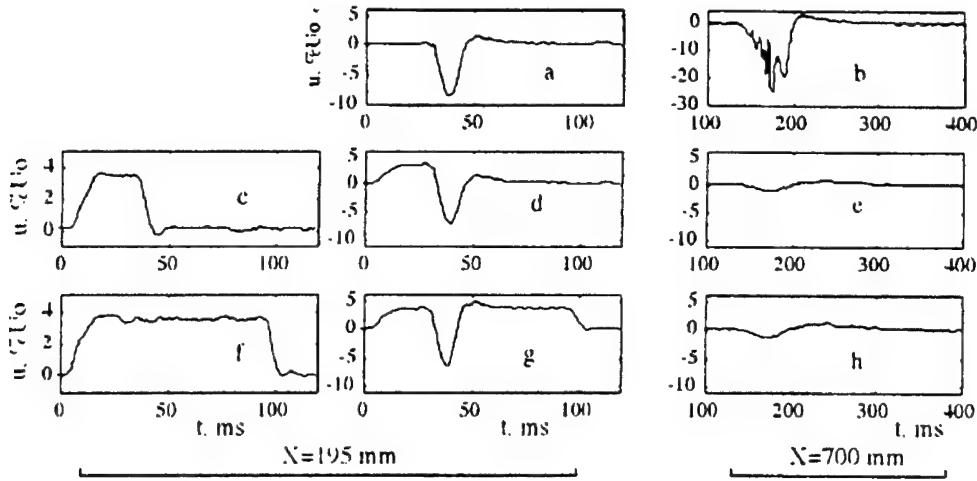means that conditions for the development of the secondary (200 Hz) disturbance are less
favourable, and breakdown to turbulence is delayed. If suction instead is applied below regions
with high streamwise velocity Fig. 2, b, the dU/dz – gradient is instead increased which leads
to faster growth of the secondary disturbances.

The second part of the study optimized the start and duration of suction. During this
study the slot was connected to a fast acting valve which made it possible to change both the
start of suction/blowing and its duration. By studying if the disturbances had developed into a
turbulent spot at $x = 700$ mm we could vary the control parameters over a wide range in order
to optimize the time-pattern of the control. The results are presented in Fig. 3 as time traces. It
is shown that a duration of suction of 30 ms is as effective as 100 ms duration to hinder the
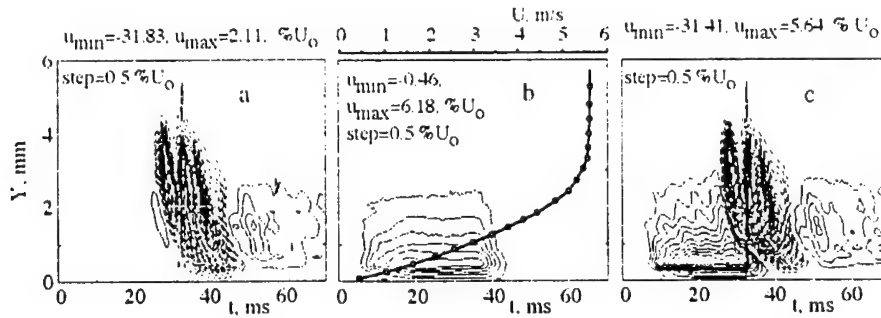development of a turbulent spot at $x = 700$ mm. Suction has to be applied slightly before the

Fig. 4. Contour lines of streamwise disturbance velocity, u, in (y, t)-plane at $z = 0$ mm, $x = 195$ mm.
a: longitudinal structure without suction, b: suction only and wall-normal profile of streamwise mean
velocity (for undisturbed flow), c: longitudinal structure with suction.

22

arrival of the longitudinal structure, because the propagation velocity of the longitudinal structure is higher than the velocity of the region of suction. In Fig. 4 it is clearly seen that suction only need to influence the front of the streak in order to be effective and that it is not necessary to apply the suction over the whole length of the structure.

Figure 5 summarizes our findings for the near optimal configuration for both suction and injection. For the suction case the suction position was located at $z = 0$ and for the injection case two control holes were located at $z = \pm2.5$ mm. Without suction a turbulent spot had developed at $x = 700$ mm whereas for both the controlled cases breakdown had not occurred.
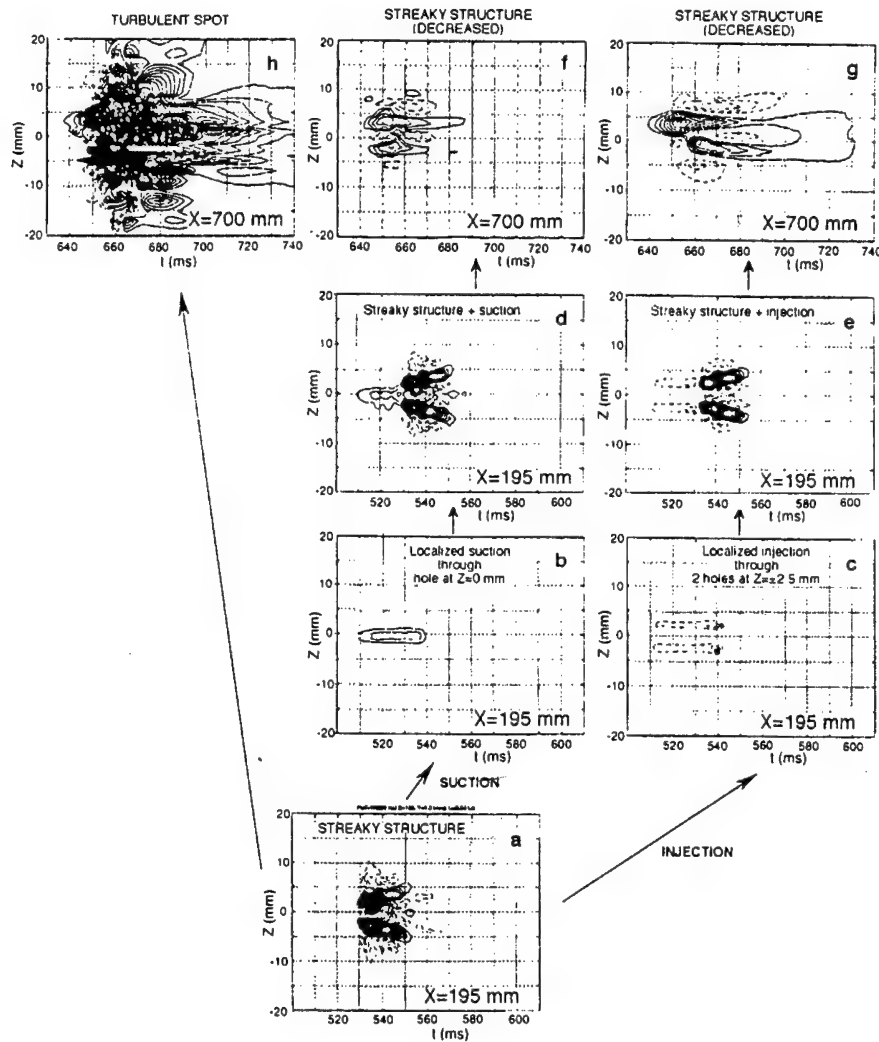

Fig. 5. Contour lines of streamwise velocity disturbance, u, in (z, t) — plane
at $y = y|_{umax}$, $x = 195$ mm

23

The results with control are seen in Fig. 5 *b*, *c*. The duration of the control is approximately 30 ms and it is located in the front part of the structure. The composite structure is seen in Fig. 5 *d*, *e* and shows that at this position it is almost only a superposition of the structures. However at $x = 700$ mm the structures are still deterministic and breakdown has not occurred (Fig. 5 *f*, *g*) as compared to the uncontrolled case (Fig. 5 *h*).

4. Conclusions

An initial study which has demonstrated that control of streaky structures to hinder or delay breakdown to turbulence is possible through local (in time and space) blowing/suction. The study has shown where the control should be applied (in space and time) in order to be effective. It is maybe somewhat surprising that the most effective control occurs when applied ahead of the structure. Suction has previously been shown to be effective, however the present study show that also blowing could be used for control. In a practical application fluid which is withdrawn through suction has to inserted into the flow somewhere, and it has been questionable whether this could be done without triggering other instabilities. However the present study shows that this fluid also can be used for control purposes. Future work will include studies where structures are randomly generated and the control will be complemented with sensors and also with fast acting multi-valve systems. In the future we foresee the possibility to use control devices based on the development of MEMS-technology which will enable control also at higher velocities.

References

1. Alfredsson P.H., Matsubara M. Streaky structures in transition // Transitional Boundary Layers in Aeronautics / Eds. R.A.W.M. Henkes and J.L. van Ingen. Elsiever Science Publishers, 1996. P. 374-386.
2. Boiko A.V., Grek G.R., Dovgal A.V., Kozlov V.V. Origin of turbulence in wall shear layers. Novosibirsk: Nauka. Sib. Predprijatie RAN, 1999. –328 p.
3. Westin K.J.A., Bakchinov A.A., Kozlov V.V., Alfredsson P.H. Experiments on localized disturbances in a flat plate boundary layer. Pt 1. The receptivity and evolution of a localized free stream disturbances // Eur. J. Mech./Fluids. 1998. Vol. 17. P. 823-846.
4. Bakchinov A.A., Westin K.J.A., Kozlov V.V., Alfredsson P.H. Experiments on localized disturbances in a flat plate boundary layer. Pt 2. Interaction between localized disturbances and TS-waves // Ibid. P. 847-873.
5. Bakchinov A.A., Grek G.R., Katasonov M.M., Kozlov V.V. Experimental study of the interaction between streaky structures and high-frequency disturbances // Proc. of the Third Intern. Conf. on Experimental Fluid Mechanics. Korolev, Moscow region, 1997. P. 28-33.

FORMATION OF A COLLECTIVE BOW SHOCK WAVE AHEAD OF A SYSTEM OF SPHERICAL BODIES

V.M. Boiko, K.V. Klinkov, and S.V. Poplavski
Institute of Theoretical and Applied Mechanics SB RAS, 630090, Novosibirsk

Introduction. It is known that the effect of formation of a collective bow shock wave ahead of a cloud of particles is observed under certain conditions in a two-phase flow behind the shock wave [1]. This phenomenon leads to uncertainty of the gas-phase parameters in the cloud, which is experimentally verified by the difference in dynamics of such a system and a single particle. It is also known that, apart from kinematic features of behavior of the system, the collective wave is accompanied by additional heating of the gas in regions of elevated concentration, which is evidenced, for example, by a dramatic decrease in ignition delays in reactive dust-laden flows [2].

Obviously, the nature of this phenomenon is based on aerodynamics of closely located bodies in a supersonic flow affecting both of them. The available publications on this topic [3] were confined to high Mach numbers of a steady flow around rigidly attached bodies. In the present study, we examined the flow around a combination of spherical bodies behind the shock wave both for fixed and freely accelerated bodies.

Experiment. Phenomena on the leading edge of the cloud were modeled using two spheres of diameter $d = 5$ mm located across the flow with different distances l between their centers. The dimensionless parameter $\lambda = l/d$ varied within the range of 1.5-6. The experiments were conducted in a UT-4M shock tube for flow Mach numbers from 1.2 to 1.7. The dynamics of formation of a collective wave was registered by high-speed shadowgraphy on the basis of a stroboscopic laser source of radiation.

Figure 1 shows typical shadow pictures illustrating the basic types of the wave structure for a system of spheres obtained in the present work. The regime of regular reflection (RR) of bow shock waves is illustrated in Fig. 1, *a*. In some cases, this regime is transformed to a structure shown in Fig. 1, *b* with Mach reflection (MR) or to a triple configuration (TC). Fig. 1, *c* shows the third type of shock-wave interaction: a developed collective wave (CW) formed in the case of small distances between the spheres or arbitrary distances at moderate supersonic velocities.
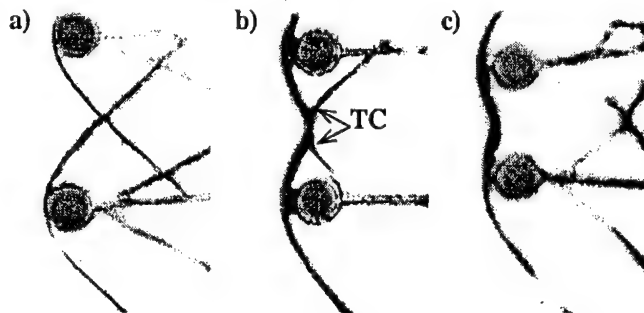

Fig. 1

Shadow pictures of the dynamics of formation of a collective wave showed that the first two types of interaction are necessary transient stages for the third type if the third configuration is formed. Thus, it is convenient to consider these three types of wave structures as stages of one process, though this process can be terminated at any stage.

Figure 2 shows schematically the types of shock-wave structures (SWS) as stages of formation of a collective bow shock wave. Transonic flow regions ahead of the spheres and a disturbed wake behind them are marked in the figure. The disturbed gas is understood to undergo a nonisothermal transition through the transonic region or the normal shock.

RR $\longrightarrow$ **MR** $\longrightarrow$ **Unification**
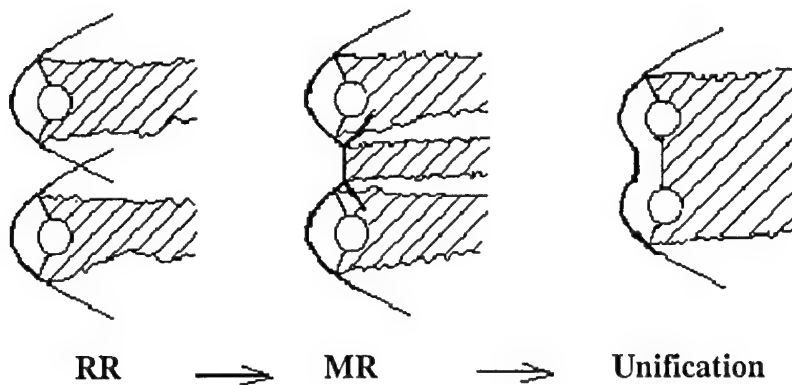
Fig. 2

Since the formation of a collective shock wave is studied here in application to clouds of particles, it is important that the degree of influence of the crossflow system of particles on the downstream parameters of the gas increases with transition from one type of the SWS to another. From this viewpoint, even the shock-wave structure with Mach reflection (Fig. 1, b and Fig. 2 (MR)), which is a necessary condition for unification of the bow shock waves, alters the qualitative pattern of the flow and the thermal parameters of the gas in the wake flow. The third stage is already an extreme case with dramatically increasing amount of the disturbed gas (interphase interaction) and drastically increasing probability of leeward particles entering the disturbed flow region (intraphase interaction of leeward and windward particles).

We consider the criteria of formation of a shock-wave structure with Mach reflection (MR). The local theory of interference of gas-dynamic discontinuities allows calculation of the flow parameters in a vicinity of the point of their intersection. It should be noted that the supersonic flow around two spheres is three-dimensional. Theoretical investigations of these flows are rather complicated. Therefore, we use theoretical conclusions for a two-dimensional case to obtain criterial estimates of experimental results: reflection of a shock wave from a solid wall or, due to symmetry, reflection of two identical shock waves from each other. We determine the regions of existence of regular and irregular (Mach) reflection.

The degree of interaction of shock waves is determined by their strength J at the intersection point. It is assumed [4,5] that the transition from regular reflection of the shock wave from the wall to Mach reflection (Fig. 2) occurs for the value of J equal to J_R [6], which limits the region of existence of the solution of equations of gas-dynamic matching on gas-dynamic discontinuities. This conclusion is supported by experiments

with unsteady shock waves. For steady shock waves, a more suitable criterion of transition is the value of J equal to J_0 [6] at which the so-called steady Mach configuration is formed. The strength J_0 is calculated from the triple configuration of shock waves in which the main shock is normal. At a certain flow Mach number $M = M_0$, the calculated values of J_R and J_0 coincide. Thus, the transition criterion from regular reflection of a steady shock wave from the wall to Mach reflection for $M > M_0$ can be considered to be J_0. For $M < M_0$, the transition begins at $J = J_R$.

The angle of inclination of the shock wave to the velocity vector of the gas and its strength are related by known equations [7]. Knowing the angle of the tangent at all points of the bow shock wave (BSW), we can determine the shock-wave strength at an arbitrary point of the BSW ahead of a sphere, i.e., we need an analytical form of the BSW shape as a function of the flow Mach number.

Approximation of the shape of the bow shock wave for a single sphere. It was shown theoretically and experimentally that the shape of the shock wave formed in a supersonic flow around a sphere has a "conic cross section" [8]. For simplicity, we represent the BSW cross section as a hyperbola whose asymptotes are Mach perturbation lines in a co-current flow (Fig. 3).

In the canonical hyperbolic equation

$$\frac{x^2}{a^2} - \frac{y^2}{b^2} = 1,$$

with account of the slope of the curve coinciding with Mach perturbation lines at infinity, we should assume

$$a = R \cdot (M^2 - 1), \ b = R\sqrt{M^2 - 1},$$

where R is the center of curvature at the apex of the hyperbola. The center of the sphere of unit radius is located at the point with the coordinates $(x, y) = (a + \varepsilon_0 + 1, 0)$. The parameters ε_0 (stand-off distance of the BSW from the sphere at the axis of symmetry) and R depend on the flow Mach number M. Figure 4 shows empirical dependencies of the curvature radius R (1) and the parameter $1 + \varepsilon_0$ (2) – BSW stand-off distance from the center of the sphere.
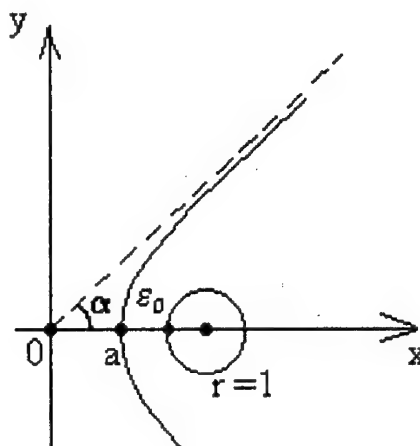
Fig. 3

These parameters have been previously studied in hypersonics and were assumed to be identical. It is seen from Fig. 4 that they are really close for $M > 5$, but for $M < 2$ the values of R and $1 + \varepsilon_0$ differ significantly.

When passing to the coordinate system $x' = x/a$ and $y' = y/b$, all experimental points of the BSW obtained in this work and also in papers [9,10,11] lie on one curve $x'^2 - y'^2 = 1$ (Fig. 5).
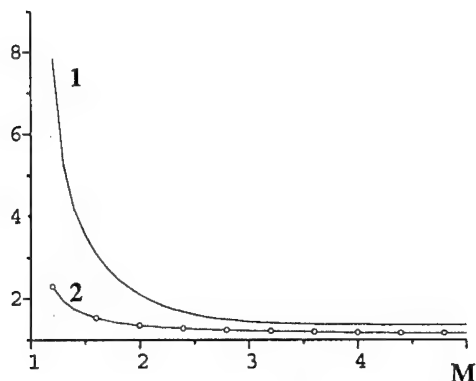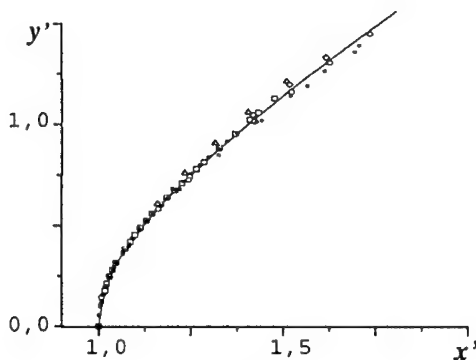
Fig. 4

Fig. 5

Thus, a possibility of hyperbolic approximation of the BSW shape ahead of a sphere is demonstrated for a wide range of Mach numbers from 1.15 to 5.

To find the distance y from the centerline to a point on the BSW at which the tangent line is inclined at an angle α to the centerline corresponding to the shock-wave strength J, we use the formula

$$y = \frac{R}{\sqrt{tg^2(\alpha) - \dfrac{1}{M^2 - 1}}} .$$

Figure 6 shows the distances between the centers of the spheres for which MR is assumed to arise for different flow Mach numbers for unsteady (1) and steady (2) flows.

Similarly, using the condition for the value of the shock-wave strength J_s at the sonic point on the BSW [7], we find the distance λ_S from the centerline to the sonic point on the BSW, in other words, the boundary of the subsonic region of the shock layer ahead of the sphere.
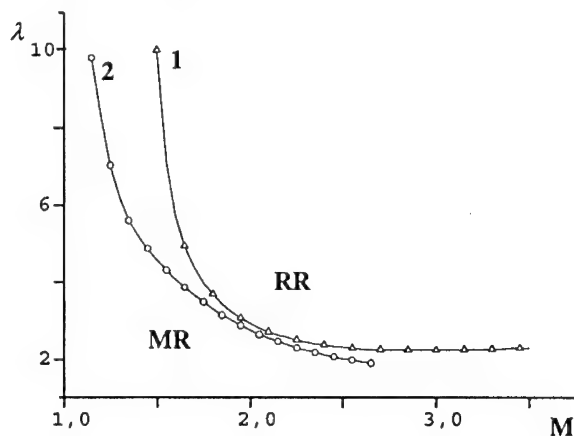
Fig. 6

Discussion of results. Based on the above reasoning, we consider the process of transition of regular interference of the bow shock waves to the Mach configuration with subsequent formation of a single wave front as the bodies in a supersonic flow come closer to each other.

At the point of intersection, the bow shock waves have a strength J, which increases as the bodies come closer. For $J = J_R$, which corresponds to the distance between the spheres λ_R, regular interference (Fig. 7, a) transforms into Mach interference with formation of a bridging shock wave that forms two symmetric triple configurations

28

(Fig. 7, b). A further decrease in the distance between the bodies and an increase in the Mach stem lead to an increase in the strength of the incident shock wave J at the triple points, and the bridging shock wave becomes curved (Fig. 7, c).

For some values of J, the reflected shock wave becomes normal, then changes its direction, and disappears at $J > J_S$. The interference of the bow shock waves leads to formation of a single curved shock wave (Fig. 7, d) with a completely subsonic flow behind it. The distance between the spheres λ_{MS} is greater than λ_S calculated for merging of sonic regions without account of the Mach stem height (bridging shock length).

Fig. 7

Thus, three typical ranges can be distinguished:

– The first range of distances between the spheres $\lambda > \lambda_R$ corresponds to regular reflection at the point of interference of bow shock waves. There are no noticeable changes in the flow pattern around a system of spheres.
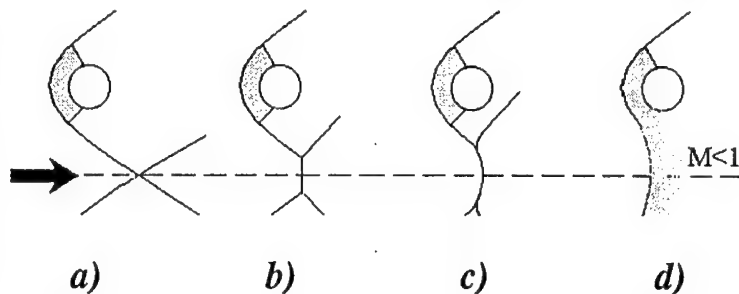– In the second range of distances $\lambda_R > \lambda > \lambda_{MS}$ Mach reflection of the BSW from the plane of symmetry is observed. In this case, the flow near the spheres seems to remain unchanged, i.e., the interaction remains supersonic. However, the subsonic region behind the normal Mach shock can significantly affect the downstream flow.
– Finally, for distances between the spheres $\lambda < \lambda_{MS}$ we can speak of a single bow shock wave (or wave front ahead of a cloud of particles) with a large subsonic flow region. A qualitatively new flow pattern around a system of spheres as a unified configuration is observed.

The flow pattern around a system of spheres was classified in the experiment as belonging to one of the three ranges described above. The results are presented in Fig. 8. The calculated curve (1) shows the distance between the spheres at which the transition from regular to Mach reflection occurs. The calculated curve (2) is a doubled radius of the subsonic region ahead of a single sphere. The experimental data are presented by points 3 (regular interference), 4 (Mach reflection), and 5 (collective wave front). The vertical bars (I) denote the length of the Mach shock bridging the subsonic flow regions near the spheres. For comparison, the results of similar experiments [3] (+A, +B) in a steady flow with the Mach number $M_2 = 2.5$ are given.

It is seen that the experimental data are in good agreement with the numerical results though a two-dimensional model of shock-wave interaction was used. Calculating the Mach stem height, which seems to depend on the degree of flow compression in the region between the spheres, we can predict the possibility of formation of a single wave front ahead of a system of bodies in a supersonic flow.
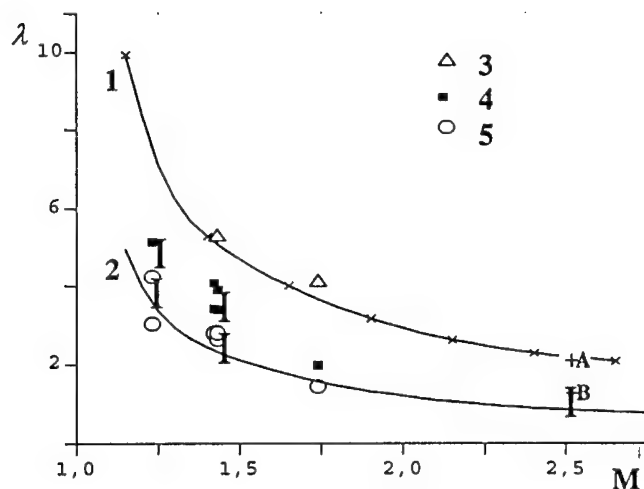
Fig. 8

Conclusion. The study of three known types of the shock-wave structure near a crossflow system of spheres (regular and Mach interaction, collective wave) by the method of shadow photography shows that these shock-wave structures are the stages of the formation process of a collective shock wave. Based on extensive experimental data, an analytical approximation of the shape of the bow shock wave was obtained to estimate the strength of the bow shock waves from two spheres at the point of their intersection. A criterion of the transition from regular to Mach interaction was found as a necessary condition of formation of a collective shock wave. The criterion was validated within the range of the flow Mach numbers behind the shock wave from 1.15 to 1.75 by experiments of the present work and by the data of [3] for $M = 2.5$ in a steady flow.

References

1. Boiko V.M., Fomin V.M., Kiselyov V.P., Kiselyov S.P., Papyrin A.N., Poplavski S.V. Shock wave interaction with a cloud of particles // Shock Waves. 1997. V.7, N5. P.275-285.
2. Boiko V.M., Papyrin A.N., Poplavski S.V. Mechanism of dust ignition in transient shock waves // Combustion, Explosion, and Shock Waves. 1993. V.29, N3. P.143-148.
3. Kuznetsov O.M., Stulov V.P. Supersonic flow around two spheres with a crossflow centerline // Aerodynamics of Bodies Entering Planetary Atmospheres / Ed. G.F. Telenin, Moscow: Izd-vo MGU, 1983.
4. Arutyunyan G.M., Karchevsky L.V. Reflected shock waves. Moscow: Mashinostroenie, 1973.
5. Reichenbach G. Shock waves in gases // Physics of Fast Processes (Collection of papers). V.3, Moscow: Mir, 1971. P. 56-102.
6. Adrianov A.L., Uskov V.N., Starykh A.L. Interference of steady gas-dynamic discontinuities. Novosibirsk: Nauka, 1995.
7. Kochin N.E., Kibel' I.A., Rose N.V. Theoretical hydromechanics. Moscow, 1963.
8. Maslennikov V.G. The shape of a detached shock wave formed upon supersonic motion of a hemisphere in various gases //Aerophysical Research of Supersonic Flows. (Ed. Yu.A.Dunaev). Moscow: Nauka, 1967. P.241-264.
9. Lyubimov A.N., Rusanov V.V. Gas flow around blunt bodies. Moscow: Nauka, 1970.
10. Belotserkovsky O.M. Supersonic flow around blunted bodies, theoretical and experimental studies. Moscow: Computing Center of URRS Acad. Sci., 1967.
11. An album of fluid motion / Assembled by M. van Dyke. Standford: Parabolic Press. 1982.

DETERMINATION OF THE GAS PARAMETERS IN NONRELAXING TWO-PHASE FLOW ON DYNAMICS OF ADMIXTURE PARTICLES

V. M. Boiko, V. V. Pickalov, S. V. Poplavski, and N. V. Chugunova
Institute of Theoretical and Applied Mechanics SB RAS, 630090, Novosibirsk

Introduction. The study of inter-phase and in-phase interaction in unsteady two-phase flows is a research field, which is very important for solving various fundamental problems of gas dynamics such as heterogeneous detonation or explosion of dust materials. However, the experimental modeling of cooperative phenomena behind a shock wave in a two-phase flow around an ensemble of particles have faced serious methodical difficulties. Among these difficulties are inapplicability to such flows of the majority of traditional methods intended for diagnosing gas flows, unsteadiness of the processes of interest, and non-equilibrium state of the mixture with respect to the velocities of the constituent phases.

Since an individual measurement of gas parameters in a two-phase flow is difficult, we propose here to access them from dynamic characteristics of dispersed-phase particles at an early stage of the phase relaxation process. This strategy constitutes a novel approach to the well-known Particle Track Velocimetry (PTV). This work presents an extension of this method to the case of unsteady flow of a two-phase mixture. From the practical viewpoint, this extension turned out to be possible due to solving the following two main methodical problems:

– high-speed shadow photographing of the two-phase flow under study performed with the help of a laser-based flash light source; this procedure ensures taking a series of 10 - 20 shadow photographs that reflect the kinetics of the ensemble of particles registered with a short time interval between photographing;

– adequate computer-aided deciphering of the particle displacement field with the help of specially designed software facilities [1]; these facilities permit processing of the series of shadow photographs recorded and accumulation of a great body of data on the motion of a great number of particles.

However, in order to obtain gas parameters by this method, special mathematical tools are required. In this work, an algorithm for data processing is proposed which employs smoothening regularizing splines adaptable to the amplitude of the noise component of the initial data arrays [2]. The algorithm is checked on experimental data obtained for the case of an isolated particle in a flow by comparing the results obtained with known parameters of the undisturbed flow behind a shock wave.

Experiment and analysis of measurement errors. The experiment was performed in an UT-4M shock tube. As a test particle, a hollow sphere with a smooth surface was used, whose diameter and mass were $d = 5.25 \pm 0.05$ mm and $m = 24 \pm 0.2$ mg, respectively. The particle size is chosen rather large to reduce the relative error in the determination of the particle size and mass before the experiment and ensure both reliable photographing of the particle and correct determination of its trajectory when processing shadow photographs. Owing to the hollowness of the sphere, its effective density was made low ($\rho_p = 334$ kg/m^3) to ensure its considerable displacement for the observation period and thus minimize the relative error in the determination of its trajectory.

Prior to the experiment, the sphere was suspended inside the channel on a thin caprone thread. The thread was disrupted by local burning-up just before the arrival of the shock wave. The disruption of the thread was initiated by a signal generated by the synchronizing system.

On the arrival of the shock wave at the region under study, the laser stroboscope was turned-on. The motion dynamics of the free sphere in the flow behind the shock wave was recorded by a high-speed camera, which provided 21 photographs taken at a time interval $\Delta t = 30$ µs. The time t_i of the occurrence of the sphere in each photograph with the number i was determined from its position with respect to the wave front in the first photograph and known wave-front velocity. The wave-front velocity was determined by two methods:

1) from the interval between the signals generated by pressure pickups immersed into the flow with a known separation between them;

2) from the displacement of the wave front in shadow photographs for a known time interval between taking successive photographs.

From the experimentally determined velocity of the shock-wave front, the Mach number of the shock wave ($M_s = 3.15$) and the flow parameters behind its front as a function of M_s (air density $\rho = 0.64$ kg/m^3, flow velocity $u = 820$ m/s, temperature $T = 820$ K, Mach number of the flow $M = 1.44$, Reynolds number (calculated from the sphere diameter) Re $= 7.3 \cdot 10^4$ were found with making allowance for variation of the adiabatic exponent [3].

The quantity to be measured on a shadow photograph was the position S_i of the sphere at a moment t_i. It was assumed that not only the displacement of the particle but also its velocity $V(t)$ and acceleration $a(t)$ could be used to determine the flow parameters behind the shock wave. Indeed, the acceleration of a free body with a known mass in a flow is determined in a unique manner by the aerodynamic forces acting upon the body. This acceleration can be expressed in terms of gas parameters using this or that approximation. For example, for a steady flow behind a shock wave, at an early stage of the velocity relaxation, when the coefficient of the aerodynamic resistance of the sphere $C_D \approx$ const, the equation of motion gives the following dependence for the acceleration:

$$\frac{dV}{dt} = \frac{1}{\delta}(u - V(t))^2, \quad \delta = \frac{4}{3}\frac{\rho_p}{\rho}\frac{d}{C_D}, \tag{1}$$

where V is the velocity of the particle, δ is the relaxation path length, u is the gas velocity and ρ is the gas density. The solution of (1) which satisfies the initial condition "$V = 0$ at $t = 0$" is

$$V = u(1 - 1/(1 + t/\tau)), \quad \tau = 4\rho_p d / 3\rho u C_D \tag{2}$$

Integration of this solution gives the expected trajectory

$$S(t) = u\left(t - \tau \ln\left(1 + \frac{t}{\tau}\right)\right), \tag{3}$$

where τ is the relaxation time. As is seen, expressions (2) and (3), written in the general form as $F(t) = F(t; u, \tau)$, can be employed for two-parametric approximation of the corresponding data arrays, for example, by the least square method. It is well known, however, that even in one-parametric problems with the number of points lesser than 30 the accuracy of this method abruptly diminishes, while for a two-parametric approximation requirements imposed on the inaccuracy of the initial data array become considerably more stringent. It is why in the present work, alongside with measures taken to improve the measurement accuracy, a method was employed which allows one, when processing the data, to pass over to a single-parametric problem. This method is based on the fact that each of the parameters to be found enters the corresponding fitting function as a multiplier. In this case this parameter can be eliminated from the consideration by passing from the data vector F_i to the matrix $F_{ij} = F_i/F_j$, $i > j$. Then, as follows from (2), the relaxation parameter τ can be independently found by statistical treatment of the set of values

$$\tau_{ij} = t_j \frac{1 - V_{ij}}{V_{ij} t_{ij} - 1}, \text{ where } V_{ij} = \frac{V_i}{V_j}, t_{ji} = \frac{t_j}{t_i} \tag{4}$$

Applying a similar elimination procedure to the parameter δ, one can determine the gas velocity by averaging the set of values

$$u_{ij} = V_j \frac{\sqrt{a_{ij}} - V_{ij}}{\sqrt{a_{ij}} - 1}. \tag{5}$$

Thus, the flow parameters can be found from the displacement array by solving a two-parametric approximation problem, while using derivatives permits independent determination of the parameters. As experiments showed, an increase in the noise component of the derivative data arrays V_i and a_i caused by numerical differentiation of the initial "signal" S_i with an admixed noise permits using procedures (4) and (5) only as preliminary estimation procedures. The fact that, in a first approximation, the estimate $\delta = u\tau$ of the relaxation parameter can be obtained for any data array S_i, while in a test experiment the quantity δ should be determined using (1) from preliminarily known values, is extremely important here. Then, as follows from (1), the gas velocity to be found is

$$u = V(t) + \sqrt{\delta \cdot a(t)}, \tag{6}$$

where $V(t)$ and $a(t)$ are the smoothened derivatives of the initial data array taken at one and the same moments of time.

We shall estimate now the error in the determination of flow parameters in a test experiment and the inaccuracy of the experimental data array on the displacement of the body. Since all gas parameters behind the shock are functions of the shock wave Mach number, to estimate their inaccuracy, we use here formulas of an ideal theory. The relative error in the determination of the function $G(M_S)$ is related to that in the determination of the quantity M_S by the formula

$$\frac{\Delta G}{G} = \frac{M_S}{G} \frac{dG}{dM_S} \frac{\Delta M_S}{M_S}.$$

For instance, for gas velocity we have

$$u = \frac{2c}{\gamma + 1}\left(M_S - \frac{1}{M_S}\right), \quad \frac{\Delta u}{u} = \left(\frac{M_S^2 + 1}{M_S^2 - 1}\right)\frac{\Delta M_S}{M_S} \le 1.2\frac{\Delta M_S}{M_S}.$$

Estimates of the inaccuracy of the density of the particle and those of the gas density and the quantity M_S to be measured give

$$\frac{\Delta\rho_p}{\rho_p} = \frac{\Delta m}{m} + 3\frac{\Delta d}{d} \approx 0.02, \quad \frac{\Delta\rho}{\rho} \le 0.5\frac{\Delta M_S}{M_S}, \quad \frac{\Delta M_S}{M_S} \le 0.01.$$

Finally, we have $u = 820 \pm 10$ m/s, $\rho = 0.64 \pm 0.003$ kg/m^3, $\rho_p = 334 \pm 7$ kg/m^3, and $\delta = 3.322 \pm 0.07$ m.

Our final remarks are concerning the error in the determination of the displacement of the body. The shadow photographs, which give successive positions of the body on each photograph, are to be scanned and converted into a graphic BMP-file. The actual magnification of the photographs and the resolution power of the scanner permit to obtain a pixel size of about

44 μm. Thus, the total error in the determination of the coordinate of the reference point and that of the sphere amounts to 90 μm.

Algorithm for Treating Particle Trajectories in a Shock Wave. The noise component of the data array S_i greatly hinders the calculation of both V and a by simple numerical differentiation. In this work, we propose an effective procedure intended for determining the flow velocity at a known relaxation parameter. The procedure employs smoothening regularizing splines that should be chosen with due regard for the noise level of the "signal" to suppress the noise component of the experimentally determined data arrays [2].

To determine the coefficients of a spline $S(t)$ that smoothens a mesh function S_i, we have to minimize the functional

$$\Phi(S^s) = \left\| S^s(t_j) - S_i \right\|^2 + \alpha \int \left(\frac{dS^s(t)}{dt} \right)^2 dt , \qquad (7)$$

where the norm $\left\| f \right\|$ is defined as $\left\| f(t) \right\|^2 = \sum W_i f_i^2$ and the weights W_i are to be chosen inversely proportional to the noise dispersion. The smoothening parameter a is to be chosen from a residual criterion. The obtained coefficients of a cubic polynomial permit calculation of the smoothed function S_i:

$$S^s(t) = \sum_{k=0}^{3} c_i^k (t_{i+1} - t)^k, t \in [t_i, t_{i+1}), \qquad (8)$$

as well as its smoothened first- and second-order derivatives that give the velocity and acceleration of the particle in the flow, respectively.

To carry out a numerical experiment, we set $u = 822$ m/s, $\tau = 4.1$ msec. and, using formula (3), find the values of $S(t)$ that can be considered as an initial data array resulting from tracing the particle motion in a flow. Since, normally, the experimental data contain a noise, it is required to "distort" the function $S(t)$ thus obtained with a noise component. In our numerical experiment, we considered the following types of the noise component: 1) at each nodal point, the noise amplitude amounted to $\sigma\%$ of the function value at this point; 2) at each nodal point, the noise amplitude is a constant equal to $\sigma\%$ of the maximum value of the function.

The standard deviation of measurement results is given by the formula

$$\Delta_s^2(\%) = \frac{\sum (S_\sigma - S)^2}{\sum S^2} \cdot 100\%, \qquad (9)$$

where S is the true value of the function and S_σ is that with an admixed noise.

Figure 1 exemplifies a function $S(t)$ and its first- and second-order derivatives $V(t)$ and $a(t)$ (*a* and *b*, respectively) calculated according to formulas (1-3) and the same functions obtained by fitting the above dependencies with splines without smoothening (the noise with $\sigma = 0.36\%$ is superimposed on the signal $S(t)$

As is seen, this type of noise only slightly distorts the true values of the function $S(t)$. The effect due to this type of noise can be clearly observed only at the initial section of the curve (the error $\Delta_S = 0.95\%$). In Fig. 1, *b*, the disturbing influence of this noise is clearly pronounced in the graph of the function $V(t)$, the error appearing to be increased $\Delta_V = 4.3\%$. The effect due to this low-amplitude noise was found to be especially pronounced in the case of the second-order derivative $a(t)$ (Fig. 1, *c*): $\Delta_a = 204.5\%$. Apparently, the values of $V(t)$ and $a(t)$ that are distorted to such an extent cannot be used for further calculations.
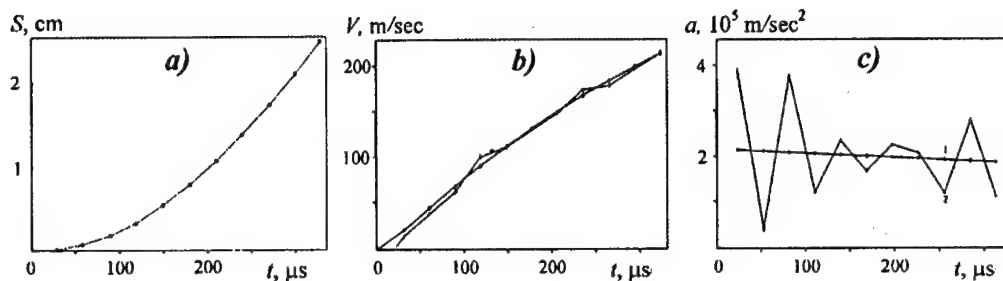
Fig. 1.

The results obtained with using the adaptive splines are shown in Fig. 2. Since the noise component in the measured data had rather low amplitude, the smoothening of the data, although have resulted in an improved accuracy ($\Delta_V = 0.58$ %), has led to changes poorly observable in the plot of Fig. 2, a.
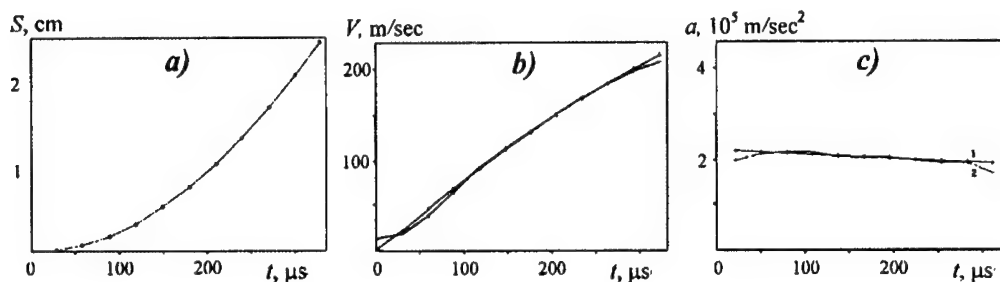

Fig. 2.

The effect due to adaptive splines is clearly observed on the first- and second-order derivatives: the error here turned out to be decreased by a factor of two ($\Delta_V = 2.3$%) and the curve $V(t)$ in Fig. 2, b is smoother than that in Fig. 1, b.

The effect due to splines appeared to be especially pronounced for the acceleration $a(t)$. The use of the splines allows one to obtain a smoothened function $a(t)$ (Fig. 2, c) that perfectly coincides with the function $a(t)$ calculated analytically. In this case, the error has decreased by a factor of 16 ($\Delta_V = 13.5$ %).

To gain a better insight into the potentialities of splines, we studied not only various types of the noise component superimposed on the signal but also varied random numbers used for noise admixing. The effect of a median filtration was also studied since, for some types and amplitudes of the noise component, the second-order derivative required an additional processing. The numerical modeling showed that in those cases where splines were used the boundary values appeared to be distorted, which turned out to be especially pronounced in the case of the second-order derivative (Fig. 2, c). If we take into account this peculiarity and choose a certain window in order to exclude the end points, we will be able to reproduce the flow velocity with formula (6) with a better accuracy.

Then, using formula (6), from the smoothened values $V_{sp}(t)$ and $a_{sp}(t)$ we obtain the data array for the flow velocity $u(t)$ and, for the chosen window, find the average value u_{sp}. The average flow velocity thus obtained was substituted into formula (3) and the resultant values of $S_{sp}(t)$ were compared with the initial dependence. In a similar manner, the standard deviation σ_s

of the mean value of was found u_{sp} using the values of $u(t)$ in the window. In the numerical experiment with the first type of the noise component, the following results were obtained: $u_{sp} = 817 \pm 5.3$ m/s, $\Delta_V = 1.1$ %. For the second noise component, it was found that $u_{sp} = 814 \pm 15.8$ m/s and $\Delta_V = 1.7$ %.

Treatment of data obtained in actual experimental conditions yielded the following estimate for the flow velocity: $u_{sp} = 817$ m/s, $\Delta_V = 4.8$ % (the second type of the noise component assumed).

Conclusion

A method for determining the flow velocity from the displacement data array for an admixture particle behind a shock-wave front is proposed. This method employs smoothening regularizing splines chosen with due regard for the noise level of the initial data arrays. The comparison with a test experiment is performed. The error of the method proposed is shown to fall within acceptable limits.

References

1. Boiko V.M., Giljov V.M., S. Ocheretny S.G., Poplavski S.V. Software complex for velocity field measurements on the basis of multiframe shadow pictures of two-phase flow // Intern. Conf. on the Methods of Aerophys. Research: Proc. Pt 3.- Novosibirsk, 1998. P.78-83.
2. Pickalov V.V., Melnikova T.S. Plasma tomography. Novosibirsk: Nauka, 1995.
3. Lapworth K.C. Normal shock wave tables for Air, Argon, Carbon Dioxide, Carbon Monoxide, Hydrogen, Nitrogen, Nitrous Oxide and Oxygen. London: Aeronautical Research Council, 1970. C. P. No. 1101.

GENERATION AND DEVELOPMENT OF COHERENT STRUCTURES IN BOUNDARY LAYER AT PULSE EXITATION

V.I. Borodulin, V.R. Gaponenko, Y.S. Kachanov
Institute of Theoretical and Applied Mechanics SB RAS, 630090, Novosibirsk, Russia

INTRODUCTION

The well-known Λ−structures were studied in a large number of experiments on laminar-turbulent transition. It was found that their formation and evolution depends on initial conditions and can be described by several physical mechanisms. It was also found in [1,2] that various initial conditions (as well as various physical mechanisms) lead to formation of similar coherent structures. These structures have the same spatial and temporal scales and seem to be very important at final stages of transition and flow randomisation. It was supposed that: (i) they are of a universal type characteristic of the transitional boundary layer; (ii) their temporal and spatial scales are 'eigen values' which not depend on the frequency and wavenumber spectra of initial disturbances; (iii) being localised in the external part of the boundary layer, they influence the near-wall region were the flow randomisation begins. Moreover, there is a lot of evidence that not only transitional but also turbulent boundary layer contains similar structures produced by similar mechanisms (see [3]).

All suppositions listed above were formulated on a basis of experiments performed at periodical initial disturbances and assumed to be true for non-periodic case. However, some authors believe that in case of non-periodic initial disturbances there is another way to turbulence [4-6]. (Although the results discussed in [4-6] may have various interpretations.) Additionally, a comparison of the transition scenarios initiated by wave packets [7-9] with those excited by periodical in time perturbations demonstrates also a similarity of the dominant physical mechanisms. Anyhow, one can see a contradiction of the viewpoints that should be cleared up experimentally.

In a bulk of previous experiments the periodical excitation of Λ−structures (and associated coherent structures) was observed after introduction into the flow of the unstable (or neutrally stable) Tollmien-Schlichting (TS) waves. In this case the streamwise wavelength of perturbations applies some restrictions on the data analysis. As the Λ−structure is stretched in the streamwise direction, it becomes longer than the wavelength of the primary wave and very soon its near-wall part turned out to be lying under the structures generated on every period of initial wave. To get a more clear data on some possible interactions between the near-wall and external parts of the perturbed boundary layer it is necessary to give a possibility to the flow to generate a single Λ−structure propagating in a non-disturbed background, i.e. to establish a streamwise period of excitation that would be equal physically to infinity.

The goal of the present paper was to develop some methods of excitation of a disturbance localised in time and space and to investigate its downstream evolution and its properties at late stages of the laminar-turbulent transition induced by this perturbation in a flat-plate boundary layer.

EXPERIMENTAL PROCEDURE

Experiments were conducted in the low-turbulence wind tunnel T-324 of the Institute of Theoretical and Applied Mechanics (Novosibirsk). The transitional boundary layer was formed on a flat plate (1000 mm wide, 1300 mm long) mounted in a test section at a zero attack angle.

In order to have possibility to compare the present experimental data with previous ones (obtained in [1, 2] for periodical excitation), the free-stream velocity was set at 9.18 m/s. Background perturbations were less than 0.02% (in a frequency range higher than 1 Hz).

Initial disturbances were introduced into the boundary layer by means of a modified classical method of vibrating ribbon, Fig. 1. Similar to [1], a spanwise positioning of the
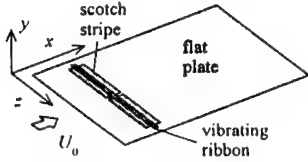

Figure 1. Sketch of experimental model and coordinate system.

Λ–structures was established with the help of a scotch stripe pasted onto the plate surface under the ribbon. The stripe had an opening at $z=0$ which produced a very weak spanwise modulation of initial disturbance and the mean flow. In contrast to [1], the ribbon was actuated by a special electronic device that produced several short pulses with a period of repetition of about 1 s. During this period all the investigated structures passed the whole model length and the boundary layer had relaxed to its undisturbed state.

Spatio-temporal distributions of the streamwise components of the mean-flow velocity vector $U(x,y,z)$ and the velocity fluctuation vector $u(x,y,z,t)$ were measured by hot-wire anemometer. Actuating signal triggered all the measurements providing conditions for ensemble-averaging the fluctuations. In every spatial point (x,y,z) number of time traces $u(t)$ have been registered. The sampling period was about 0.2 ms. Spatial steps between points of measurements were 10, 0.1-0.2 and 1 mm in x, y and z directions respectively.

To provide a short enough duration of the vibrating ribbon response in time, a special component was added to the signal feeding the ribbon. This component had a frequency close to the eigenfrequency of the ribbon oscillations and a specially adjusted phase leading to suppression the eigen oscillations of the ribbon after every pulse.

COMPARISON OF COHERENT STRUCTURES GENERATED AT PULSE AND PERIODICAL EXITATION

It turned out that coherent structured generated at pulse-like and periodical excitation [1, 2, 10] are generally coincide even quantitatively. All the data obtained in this work confirms the known scenario: formation of Λ–structure, its stretching and reconnection. Fig. 3 shows contours of constant amplitudes of velocity fluctuations in (y,t) plane (which, in a certain sense, corresponds to $(y,-x)$ plane) for the two cases. The data are documented at $x=500$ mm that corresponds approximately to a stage of transition called usually the '4-spike stage'. The spikes correspond to isolated regions of low-speed fluid attributed to ring-like vortices which appear due to a series of reconnections of the lambda-vortex legs near its tip (see [1, 2]). When the ring-like vortex passes by the hot-wire probe it produces a spike on the time-trace. Three spikes can be seen on Fig. 2, which shows a time trace $u(t)$ obtained at $y=4.5$ mm in the non-periodical

Figure 2. Example of time traces $u(t)/U_0$ used for building Fig. 3 — 5. $x=500$ mm, $y=4.5$ mm.

regime (see the bottom of Fig. 3). The fourth spike is positioned closer to the wall and not seen in Fig. 2. A high shear layer formed due to a rotation of fluid in the lambda-vortex legs is also very well seen in Fig. 3. One can perceive that the wall-normal and temporal scales of the ring-like vortices and the high shear layers almost coincide in the two regimes.
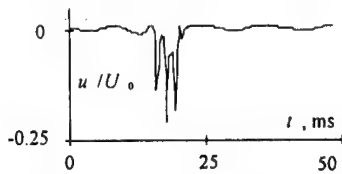
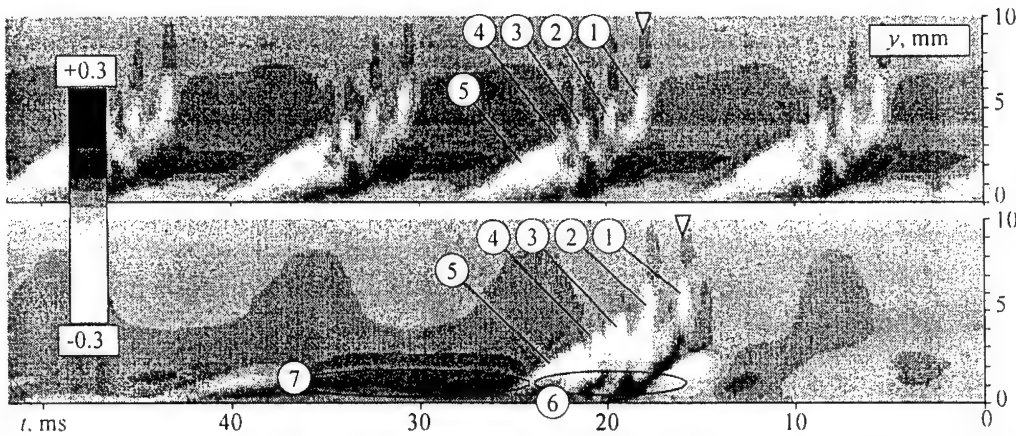The same is true for distributions of the u-component of velocity fluctuations in planes (z,y) and

Figure 3. Contours of $u(y,t)/U_0$ at $x=500$ mm, $z=0$. Top: periodical excitation, bottom: pulse excitation. 1...4 — spikes (ring-like vortices), 5 — high shear layer formed by Λ-structure, 6 — area of stochastic fluctuations, 7 — calm region. Triangles indicate time instants for Fig. 4.
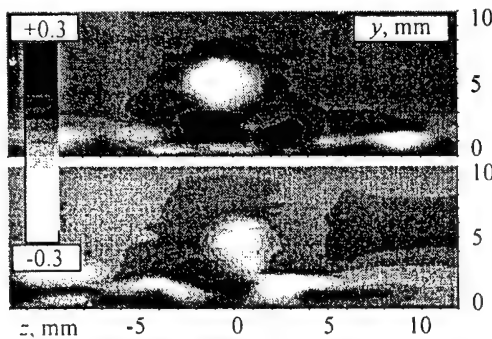

Figure 4. Contours of $u(y,z)/U_0$ at $x=500$ mm. Top: periodical, bottom: pulse excitation. Time instants are indicated on Fig. 3 by triangles
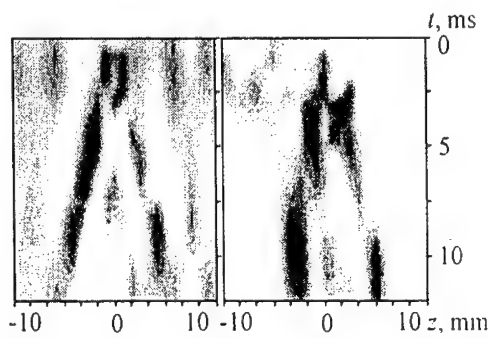
Figure 5. Contours of $u(z,t)/U_0$ at $x=500$ mm. $y=0.4$ mm normalised by local maxima. Left: periodical, right: pulse excitation.

(z,t) shown in Figs. 4 and 5. The time instants in Fig. 4 correspond to the first spike on $u(t)$ time-traces, i.e. to the first ring-like vortex. The vortices look like white spots (negative u-values) surrounded by grey rings (positive u-values). In both cases the areas occupied by the ring-like vortices have almost the same shape, size, and positioning with respect to the wall. As to the Λ-structures, they can be visualised in different ways but all the methods give their very similar shapes and scales. One of possible comparisons is presented in Fig. 5. Again, one can see a resemblance between the two regimes compared. A set of maps like those shown in Fig. 5 obtained for different downstream positions has demonstrated another property of the Λ-structures known from previous experiments: their stretching in the streamwise direction during their downstream propagation (not shown).

Comparison was performed in the range from $x=450$ (the 1-spike stage) to $x=600$ mm (a multi-spike stage and an almost turbulent flow near the wall). It has been found that in the whole studied range of temporal and spatial scales the structures generated at pulse-like and periodical excitation are very similar in the two regimes. The same is true for the values of du/dy (which coincide, in practice, with the spanwise vorticity ω_z).
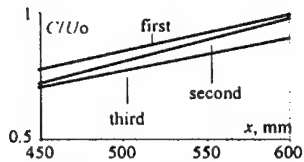
39

Figure 6. Downstream speeds of the first 3 ring-like vortices.

Shown in Fig. 6 is a speed of downstream propagation of the first three spikes (and the corresponding ring-like vortices) measured in the present experiment (the pulse excitation). After their formation in the middle part of the boundary layer, the ring-like vortices move away from the wall and accelerate downstream. Similar to the periodical case studied in [1], the first vortex reaches the external edge of the boundary layer at $x\approx600$ mm and have an almost free-stream velocity. The other two spikes accelerate downstream somewhat slower. Fig. 6 might be considered as an indirect evidence of a possible (very interesting) new kind of instability of the ring-like vortex train. Indeed, the 1st and 2nd spikes approach each other slowly, while the 2nd and 3rd ones move away from each other. Note, however, that Fig. 6 is based on an approximated experimental data, which had originally a quite significant scattering. That is why the vortex-train instability mentioned above has to be studied in the future experiments more accurately.

Some details of the disturbance development observed at very late stages of transition in the present study seem to differ from those found in [1], or, more exactly, some of phenomena occurred in the transitional boundary layer can be seen more clearly in the case of pulse-like excitation. In particular, the process of formation of a turbulent spot (from an ensemble of structures shown in Fig. 3, bottom) is very distinctly observed in the present experiment. At a certain stage of the transition development some random fluid motions appear in the near-wall region inside the 'incipient' turbulent spot. This region is marked in Fig. 3 as a 'stochastic spot'. Random velocity fluctuations are amplified rapidly in a streamwise domain positioned between the shear layer (induced by the Λ–structure) and the first ring-like vortex. However, the stochastic spot is positioned in the near-wall region *under* the ring-like vortices and the Λ–structure. Some other properties of the incipient turbulent spot and stochastic spot are discussed in the next section.

INTERACTION OF RING-LIKE VORTICES WITH NEAR-WALL REGION AND FLOW RANDOMIZATION

An analysis of not-averaged time-traces allows to conclude that the flow randomisation begins in the near wall region. As an example, one can compare two sets of the time-traces recorded in the outer part of the boundary layer and in the near wall region, Fig. 7. The two sets show a presence of an irregular (stochastic) component that is much stronger in the near wall region
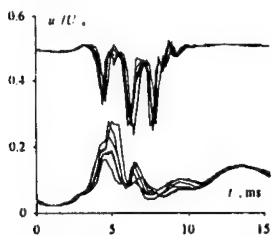

Figure 7. Not averaged time traces $u_i(t)/U_0$ (6 instants) at $x=500$ mm (3-spike stage). Top: $y=4.5$ mm, bottom: $y=0.2$ mm.

and has a form of 'variations' of the instantaneous disturbance magnitude in a random way from one realisation to another. A certain irregularity of the spatio-temporal position of the ring-like vortices (seen on the top traces in Fig. 7) is caused, most probably, by three reasons. First, a very low-frequency (less then 1Hz) random temporal modulation of free-stream speed existing in the wind tunnels. This modulation is rather intensive (about 0.3 to 0.5 %) and present even in the best low-turbulence wind tunnels, like T-324. Second, the process of formation of ring-like vortices during reconnection of the Λ–vortex legs seems to be very sensitive to background perturbations and, due to this, amplifies these perturbations. Third, the train of

the ring-like vortices seems to be also unstable (see also the end of previous section). This instability can lead to a modulation of speeds and, maybe, spatial (in the (y,z)-plane) position of the rings, i.e. the spikes. Of course, the first reason mentioned above influences the near wall region as well. However, a possible interaction of the outer and inner parts of the boundary layer occurred in the beginning of the randomisation process, found in [10] for the case of periodical excitation, has to be examined in more detail.

In order to investigate the process of flow randomisation a 'stochastic spot' was determined as follows. Ensembles of not averaged time traces $u_i(t)$ were taken. Then: ensemble averaging was performed: $u(t)=\langle u_i(t)\rangle$; stochastic component was extracted as $s_i(t)=u_i(t)-u(t)$; analytical signal corresponding to $s_i(t)$ was calculated, $c_i(t)=G\{s_i(t)\}$, where G — Gilbert transform.; envelopes of were calculated as $s_i(t)=[s_i(t)^2+c_i(t)^2]^{1/2}$; ensemble averaging was performed: $e(t)=\langle e_i(t)\rangle$.
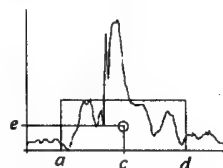

Figure 8. Definition of the form parameters of stochastic spot.

Due to absence of any theoretical models of the randomisation process it is naturally to consider the simplest form parameters of $e(t)$ (see Fig. 8). Let us find a 'centre of gravity' (c,e) of a figure formed by $e(t)$ and the time axis and build a rectangle with the same position of its centre and with the same 'mass'. Let us name the time instants a, b and c (marked in Fig. 8) as a leading edge, a trailing edge and a centre of the stochastic spot. The height of the rectangle equal to $2e$ (see Fig. 8) can be considered as a measure of a magnitude of the stochastic spot. Downstream evolution of all the form parameters are shown on Figs. 9 and 10.

Fig. 9 shows the location of the leading and trailing edges and the centre of the stochastic spot in (x,t)-plane together with the location of the first spike. Slope of lines in this figure corresponds to the streamwise velocity. Two grey lines corresponds to velocities 9.18 m/s ($U/U_0=1$) and 1.2 m/s ($U/U_0=0.13$). It is clearly seen that the first spike and the leading edge move downstream at the free-stream speed.
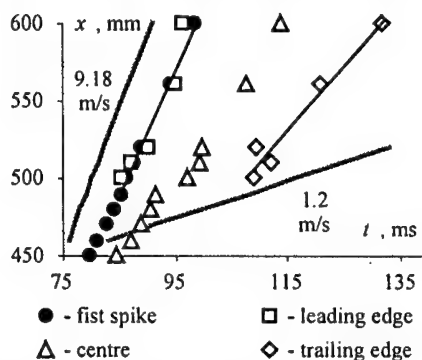

Figure 9. Localisation of the stochastic spot and the first spike. Slopes of grey lines correspond to the velocities of free stream and in the near wall region.

The 2^d, 3^d, ... spikes also have velocities close to U_0. Meanwhile the local speed at $y=0.2$ mm where all form parameters were determined is much less and equals to $U/U_0=0.13$.

The magnitude of irregular fluctuations within the stochastic spot increases downstream exponentially, see Fig. 10. The magnitude of spikes, on the contrary, decreases gradually from 0.3 U_0 to 0.1 U_0 (see [1]).

Thus, a conclusion can be drawn that the outer part of the boundary layer influences the process of the flow randomisation observed in the near-wall region. In a certain sense, the ring-like vortices 'roll' along the top of the boundary layer and acts as a kind of 'peristaltic pump' exciting the wall region and providing development of the incipient spot to the turbulent spot. It is found that at very late stages of
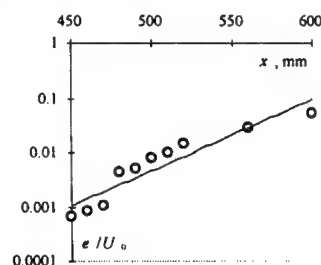

Figure 10. Magnitude of the stochastic spot.

the transition ($x \approx 600$ mm) the ensemble of vortical structures transforms into a quite developed turbulent spot which internal structure remains, however, rather similar to that observed at the stage of flow randomisation discussed above.

CONCLUSIONS

The results of the present study can be formulated shortly in the following way.
- It is found no any significant difference in the shape and main properties of the coherent structures generated by the flat-plate boundary layer at late stages of the laminar-turbulent transition initiated by periodic and pulse-like TS-wave.
- Similar to the periodic case, in the case of pulse-like excitation the ring-like vortices excite the near-wall region and play a significant role in the flow randomisation process observed at final stages of transition.
- The isolated lambda-structure produces a set of associated structures and lead to formation of an ensemble of structures (or an incipient spot) and, then, the turbulent spot. The leading part of this spot consists mainly of the ring-like vortices (and the corresponding spikes on time-traces). The centre is occupied with the tip of the continuously stretching lambda-vortex and with growing irregular near-wall perturbations induced by the vortex rings. In the tail of the spot a calm region is observed with low instantaneous flow velocity and elongated streamwise structures (associated with the continuously stretching legs of the lambda-vortex) and other nearly streamwise vortices induced by them near the wall.
- The structure of the turbulent spot found in the present experiment is very similar to that well known from previous experiments. However, in the present case we have got, in addition, a very important information about the mechanisms of formation of this structure.

REFERENCES

1. Borodulin V.I., Kachanov Y.S. Formation and development of coherent structures in transitional boundary layer // Applied Mechanics and Technical Physics. – 1995. – Vol. 36, No. 4. – P. 60-97.
2. Bake S., Kachanov Y.S., Fernholz H.H. Resemblance of K- and N-regimes of boundary-layer transition at late stages // Eur. J. Mech., B/Fluids. – 2000. – Vol. 19, No. 1. – P. 1-22.
3. Kachanov, Y.S. On a universal nonlinear mechanism of turbulence production in wall shear flows // Intern. Conf. on the Methods of Aerophysical Research: Proc. Pt 2. Novosibirsk, 2000. P. 84-91.
4. Gaster M. The nonlinear phase of wave growth leading to chaos and breakdown to turbulence in a boundary layer as an example of an open system // Proc. Roy. Soc. London. Ser. A. – 1990. – Vol. 430. – P. 3-24.
5. Gaster M. The origins of turbulence // New Approaches and Concepts in Turbulence, Monte Verita. – Basel: Birkhauser Verlag, 1991.– P. 235-250.
6. Shaikh F.N., Gaster M. The non-linear evolution of modulated waves in a boundary layer // J. Eng. Mathematics. – 1994. –Vol. 28. – P. 55-71.
7. Cohen J., Breuer K.S., Haritonidis J.H. On the evolution of a wave-packet in a laminar boundary layer // J. Fluid Mech. – 1991. – Vol. 225. – P. 575-606.
8. Cohen J. The evolution of a wave packet in a laminar boundary layer // Phys. Fluids. – 1994. – Vol. 6(3). – P. 1133-1143.
9. Breuer K.S., Cohen J., Haritonidis J.H. The late stages of transition of a wave packet in a laminar boundary layer // J. Fluid Mech. – (Accepted for publication.)
10. Meyer D.G.W., Rist U., Borodulin V.I., Gaponenko V.R., Kachanov Y.S., Lian Q.X., Lee C.B. Late-stage transitional boundary layer structures. Direct numerical simulation and experiment // Laminar-Turbulent Transition: Proc. IUTAM Symposium / Eds. H. Fasel and W.S. Saric. Sedona, AZ/USA, 1999. – Berlin: Springer-Verlag, 2000.

HEAT EXCAHNGE RESEARCH IN A DIAMETER DISK FRICTIONAL PUMP

V.P. Fomichev, S.V. Khaidarov, and S.S. Pravdin
Institute of Theoretical and Applied Mechanics SB RAS

The conducted researches of diameter disk fans (DDF) have shown practical advisability and certain advantages of their use in comparison with other types of such devices. One of DDF characteristic properties is a developed disk surface which makes promising their application as flow reactors and heat exchangers, for example. Therefore, the study of the heat exchange process in such an apparatus is of great interest. The presence of two areas in the inter-disk gap, differing in the heat exchange intensity – internal and peripheral, has been found in the works [1, 2], where visualization of temperature fields was carried out with the help of the method of Liquid Crystal Thermography. An intense heat exchange takes place mainly in the peripheral area, being insignificant in the internal range. Such a difference is likely to be explained through transition from a laminar flow regime in the shaft region to a turbulent flow with generation of strong vortices at the disk periphery. The aim of this research is to obtain the quantitative characteristics of heat exchange in a diameter disk fan.

Experimental setup

A sketch of the experimental setup is shown in Fig.1 and has been detailed in [1, 2]. The experimental installation consisted of body 1, disk rotor 2 housed horizontally in side the body, and inlet-outlet channels 3 and 4, situated contiguously aside the rotor and divided from each other by a baffler 5. The rotor represented a package of aluminum disks 6, which were placed along the shaft with equal gaps b between them using separating rings 7. As the shaft is running, the gas arrives at the pumping region from the suction one due to viscous friction in the boundary layers on the disk surfaces. The installation design allowed changing the angular velocity of shaft rotation ω. Disk heating was realized with the help of ohmic heater 8 located inside the hollow shaft. A configuration was studied with the following parameters: external radius R_1 of 180 mm, internal radius R_0 of 60 mm, distance b between adjacent disks of 8 mm, outlet channel height h of 120 mm.

The temperature of the disk surface was measured by five thermistors, each of them being made as follows. Two radial lines of orifices were drilled in the disk ring. The distance
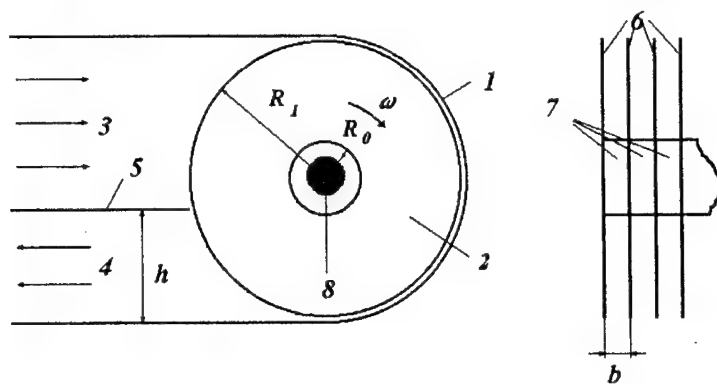

Fig. 1. 1 – body; 2 – rotor; 3 – input channel; 4 – output channel; 5 – separating partition; 6 – aluminium disks; 7 – separating rings; 8 – ohmic heater.

between the lines was 20 mm. Each line contained 40 orifices of a 0.5-mm diameter with a 0.5-mm pitch between them. In order to avoid the overlapping of orifices, they were positioned in two lines in the quincunx order with an inter-line interval of 1 mm. A copper wire of 0.02-mm diameter was coiled around a disk through the orifices with its ends soldered to connectors at the internal diameter of the aluminium ring. The sensor contacts were brought out to the collector rake through the assembly of the disk and then to an analog-digital converter. The electric resistance of thermistors varied from 40 to 80 Ohm. The calibration of thermistors was carried out in a thermostat using the mercurial thermometer with a 0.1°C scale resolution. In spite of the noticeable difference in resistance of individual sensors, the dispersion of temperature resistance coefficients which were obtained after calibration did not exceed 0.5 percent (Fig.2). The voltage was supplied to thermistors from a power supply with stabilised current. The signal obtained from the sensor was registered with a personal computer with the help of the analog-digital converter. The sensor inquiries were realised in series. During each inquiry 1000 readings with interval of 5 milliseconds were performed. A digital milliammeter was also included in the metering circuit. The sensor resistance was defined after obtained measurements of the electric current strength and voltage in the circuit.

The experiment was performed as follows. The shaft was driven up to a given angular velocity, voltage readings in the sensor circuits were recorded by the analog-digital converter and the electric current strengths were read by the milliammeter. The resistances of circuits with various sensors were calculated. The values of resistances of the corresponding sensors at a given room temperature, which were obtained after calibration, were subtracted from the obtained values. Thus, for the circuit of each sensor, the value of its partial resistance with an excluded thermistor was obtained. This value was considered as unchanged during the
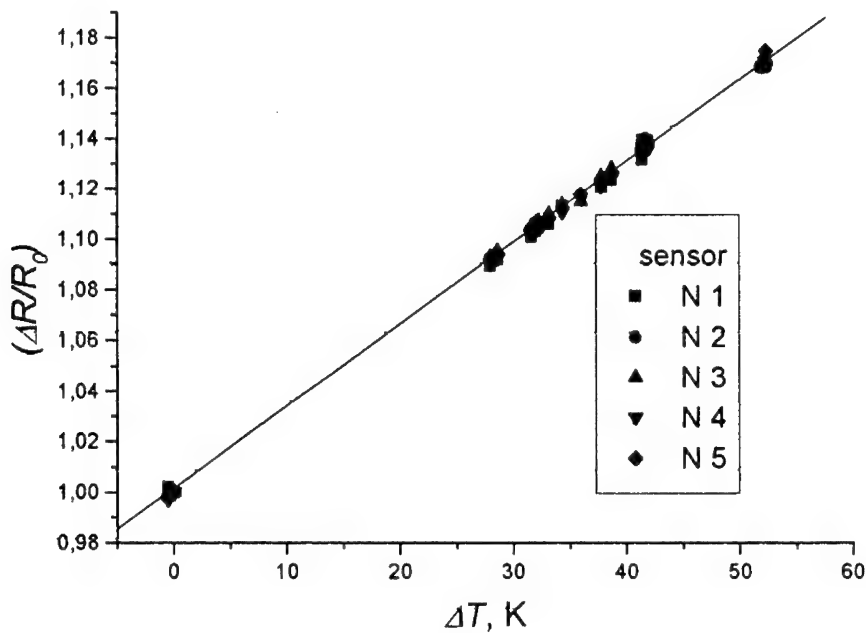

Fig. 2. Calibration of thermistors.

44

experiment because the external part of the metering circuit was not heated up, and thus, its resistance did not change; while the change in resistance of cables connecting the collector and thermistor connectors was ignored due to the extremely low value of these resistances in comparison with the resistance of the sensors. Further, the heating was switched on and the system stayed for $1.5 \div 2$ hours to reach at the stationary regime. In the course of the experiment, $25 \div 30$ above described inquiries of each sensor were made. The values of voltages obtained at one inquiry were averaged; the values of resistances of the sensors and the temperatures were calculated after them.

The basis for processing of the temperature distributions obtained was the method described in [3]. The method of determination of local and average heat exchange coefficients reduces to the solution of an one-dimensional inverse temperature problem. The equation of heat transfer in a thin disk of constant width looks like

$$\frac{d}{dr}\left(r\frac{dT}{dr}\right) - m^2 rT = 0, \ m^2 = \frac{2\alpha}{\lambda\delta}. \tag{1}$$

Integrating equation (1) twice in the limits from R_0 to r_i, we have

$$\alpha_i = \frac{\lambda\delta}{2} \frac{r_i T_i - R_0 T(R_0) - \int\limits_{R_0}^{r_i} T dr - R_0 \frac{dT(R_0)}{dr}(r_i - R_0)}{\int\limits_{R_0}^{r_i} dr \int\limits_{R_0}^{r} T r dr}. \tag{2}$$

The local values of the heat-transfer coefficient α_m were calculated through the values of average $\alpha(r)$ calculated by (2). By definition,

$$\alpha(r) = \frac{\int\limits_{R_0}^{r} \alpha_m(r) T r dr}{\int\limits_{R_0}^{r} T r dr}. \tag{3}$$

Differentiating (3) we obtain:

$$\alpha_m(r) = \alpha(r) + \frac{1}{Tr}\frac{d\alpha(r)}{dr}\int\limits_{R_0}^{r} T r dr. \tag{4}$$

The heat-transfer coefficients α_{av} averaged over the disk were also determined by another method. The accurate solution of heat-transfer problem (1) for a circular rib of constant width with a constant heat-transfer coefficient α is known in Bessel functions [3]. The heat-transfer coefficient was varied to minimise the dispersion between the experimentally determined and the calculated temperature values (Fig.3). The α_{av} was taken as the coefficient value thus obtained.

Results

In Fig. 4, the results of calculation of the average heat-transfer coefficients are presented according to experimental data in the axes lgNu(lgRe) where:

45

$$Nu = \frac{\alpha_{av} R_1}{\lambda}, \quad Re = \frac{\omega R_1^2}{\nu}.$$

From the presented plot, it is seen that firstly Nu increases with Re. But further, beginning with a certain value, this increase stops and stabilisation of the Nu value is observed. It may be related to the fact that at first, as the rotation velocity rises, the convective heat exchange
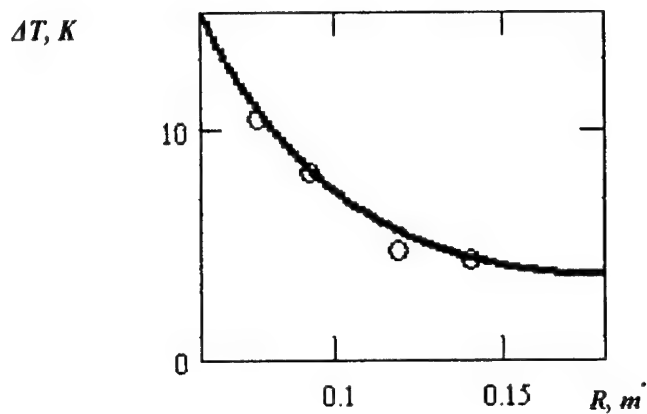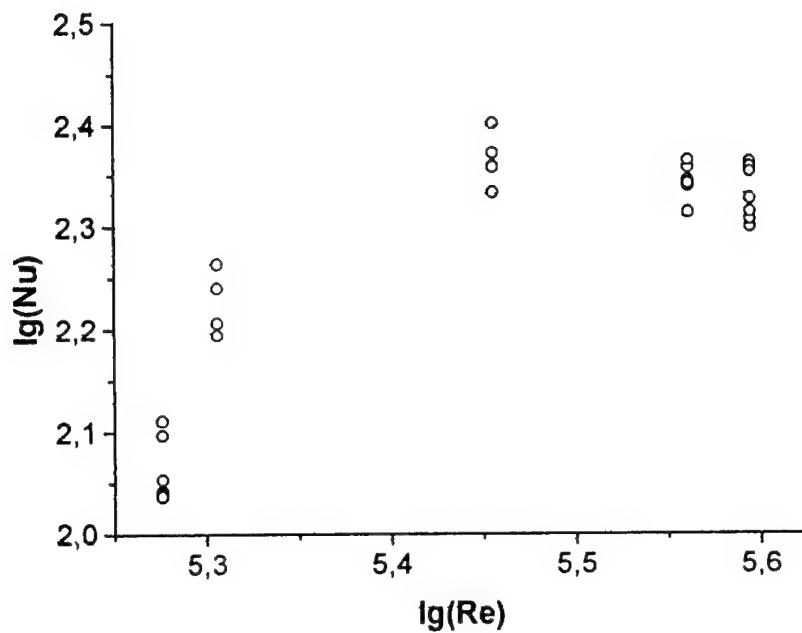

Fig. 3.

Fig. 4. Calculation of average heat-transfer coefficients.

strengthens on the disk surface; yet as flow velocity rises, the period of gas residence in the inter-disk gap decreases and a further increase in the rotation velocity does not result in heat-transfer coefficient increase.

The results of calculation of local heat-transfer coefficients are presented in Fig. 5. Here:

$$\mathrm{Nu}_m = \frac{\alpha_m r}{\lambda}, \quad \mathrm{Re}_m = \frac{\omega r^2}{\nu}$$

The experimental dependences of local heat-transfer coefficients, which correspond to the laminar and turbulent flow regimes, are also presented in the figure, which have been obtained in [3] for a single freely rotating nonuniformly heated disk, and in turn are in satisfactory agreement with theoretical results of L.A. Dorfman [5]. It is evident that the results of our research, as correlated with the results of V.M. Kapinos and L.A. Dorfman, correspond to the area of transition from laminar to turbulent flow regimes. In this case, the points corresponding to small radii lie on the branch of laminar flow. Thus, the supposition is confirmed that the previously found difference in intensity of heat exchange in internal and external areas of the inter-disk gap is associated with the change in the flow regime.

Conclusions

1. Experimental data of average and local heat-transfer coefficients in the inter-disk gap of a diameter disk fan are obtained.
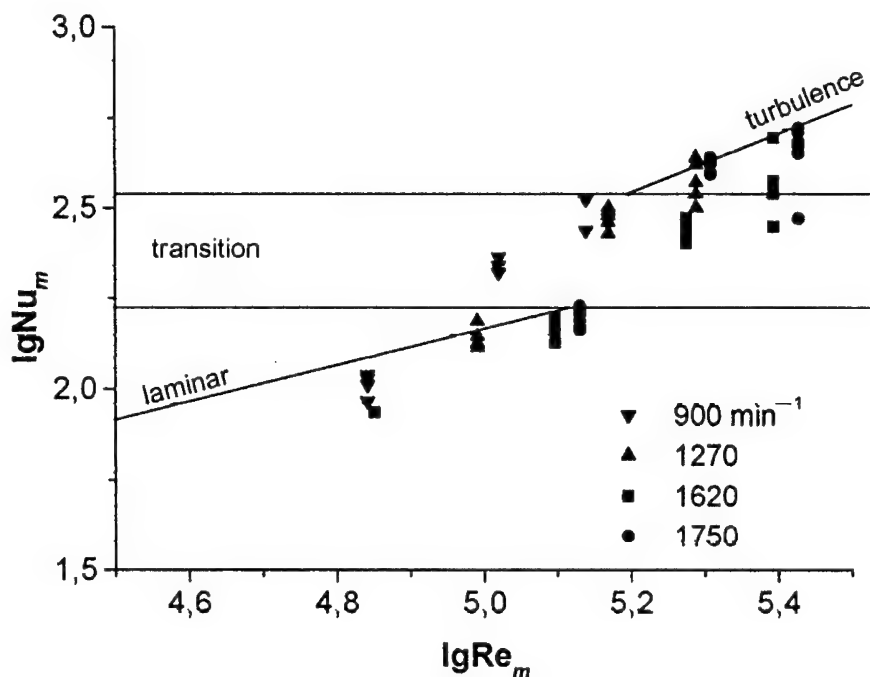

Fig. 5. Calculation of local heat-transfer coefficients.

2. The existence of a limit value of Re_{av} is found, the excess of which does not result in α_m increase.

3. The obtained values of local heat-transfer coefficients α_m are in satisfactory agreement with the known theoretical and experimental results for heat exchange of an individual disk and hence may be used for calculation of α_m, at least for quite wide inter-disk channels (in the studied case, $R_1/b = 22.5$).

References

1. V.P. Fomichev, S.V. Khaidarov, V.N. Kovrizhina, S.S. Pravdin, G.M. Zharkova. The study of special gasdynamic features of the flow in a diameter disk pump by means of liquid crystal thermography. (Int. Conf. on Methods of Aerophysical Research: Proc., Part II. Novosibirsk, 1998, P. 42-47).
2. Zharkova G.M., Kovrizhina V.N., Pravdin S.S., Fomichev V.P., Khaidarov S.V. Peculiar Features of Heat Exchange in Diameter Disk Pumps. // Thermophysics and Aeromechanics. 1998. Vol. 5, No. 4. P. 453-458.
3. Kapinos V.M. Heat Transfer of a non-uniformly heated rotating disk. // J. of Phys. Engineering. 1963. Vol. 6, No. 3. P. 12-20 (in Russian).
4. Isachenko V.P., Osipova V.A., Sukomel A.S. Heat Transfer. Mocow: «Energia», 1965. 424 p. (in Russian).
5. Dorfman L.A. Heat Transfer of a Rotating Disk. // J. of Phys. Engineering. 1958. Vol. 1, No. 6. P. 3-11 (in Russian).

NUMERICAL SIMULATION OF SUPERSONIC JET PENETRATION IN COUNTER SUPERSONIC FLOW

V.M. Fomin[*], A.A. Maslov[*], N. Malmuth[†], A.P. Shashkin[*], T.A. Korotaeva[*]

[*]Institute of Theoretical and Applied Mechanics SB RAS,
630090 Novosibirsk, Russia

[†]Rockwell Science Center, USA

At the present time significant attention is devoted to the study of supersonic flow around the bodies with nonuniform gas stream. The nonuniformity of the free stream may influence severely the flow structure in front of the body and thereby the distribution and summary aerodynamic characteristics of the vehicle (see, for example, [1 - 10]).

One probable method of nonuniformity creating in the stream is a jet, which is ejected from the body's face into the free stream. A number of experimental works [3 - 7] are devoted to the problem of the influence of counter-flow jets on the stream structure. These works illustrate the significant effect of the counter-flow jets on the aerodynamic characteristics of bodies. Possible regimes of supersonic cold jet penetration into the free stream are studied in [5]. In papers [3, 6] plasma counter-flow sonic jets were considered. The flow structure around a cone-cylinder model was researched in [5, 6]. The blunt cone had a flat end with a nozzle outlet orifice. It was shown experimentally that for cold and hot jets there are regimes of short (SPM) and long (LPM) jet penetration into the counter-flow free stream. Then a redistribution of pressure occurs on the side of the cone surface, and as a consequence, the body drag changes.

Isolated experimental results should be correlated with the help of numerical models. In [8] there is an example of numerical calculation of the short penetration regime (SPM). In the present work, the numerical research of various regimes of forming jet outflow and study of the influence of these regimes on the aerodynamic characteristics of bodies in supersonic flow was conducted. The research was realized within the frame of the inviscid gas model by the method of finite volumes. The central-difference numerical scheme was applied; it was explicit in time and implicit in area and had the second order of approximation [9]. A nonstationary problem was solved by the time-explicit method. The solution without the jet was used as initial data. The conditions in the free stream were the boundary lines in the external zone; the second derivative from stream parameters in velocity direction taken on outlet boundary line was equal to zero. The slip conditions were used on the body. In the jet outlet, the parameters were determined from the solution of the one-dimensional isoentropic problem of a gas flowing out from a nozzle with known parameters (such as the Mach number at the outlet, stagnation temperature and stagnation pressure).

The calculations were carried out for a circular cone with a half angle $\theta_c = 10°$. The cone had a bluntness and a flat end of diameter d. A nozzle outlet hole of diameter d_j was at this flat end. The free-stream Mach number was $M_\infty = 2.04$, the angle of attack was $\alpha = 0°$, $d = d/d_j = 3.08$. The Mach number on the boundary of the nozzle was $M_a = 3.8$. The relative thrust of the jet was in the range of $3 \leq (P = P_{0j} / P'_{0f}) < 90$. Here P_{0j} is the stagnation pressure in the jet, P'_{0f} is the stagnation pressure in the free stream after the normal shock wave. The

stagnation temperature in the jet was taken equal to the stagnation temperature in the free stream.

The numerical solution of the problem of counter-flow jet penetration into the supersonic stream captures two basic regimes of flow - SPM and LPM. Regimes of transition exist also, i.e. areas with possible fluctuating, nonstable penetration regimes.

Fig. 1 shows the dependence of the counter-flow jet length L/d (jet length relative to the end diameter) on P . Calculation results (solid curve a) agree successfully with the data of experiment (points) [4]. In Fig.1, area (1) corresponds to the SPM regime, (2) correlates with the transition regime SPM→LPM, (3) complies with the LPM regime, (4) is in accord with the transition regime LPM→SPM, and (5) confirms the SPM regime.

The solid line b in Fig. 1 also shows the calculated dependence of the relative drag of a blunt cone (C_d/ C_{dc}) on P, here C_d is the drag of the blunt cone with a jet, C_{dc} is the drag of the blunt cone without a jet. This dependence includes the reactive jet component. It is seen that the counter-flow jet presence reduces the drag of the cone. In the transition regime SPM-LPM (area 2), reduction of drag (with respect to the cone without a jet) reaches the value of 30%. Here the cone and liquid contour form a surface, which is close to the model surface of minimum drag. In other areas the drag of the body is greater. The cone- drag decrease in area (5) is explained by the fact that this model has a short cone part. In this case, the zone of reattachment flow is in the end of the cone.
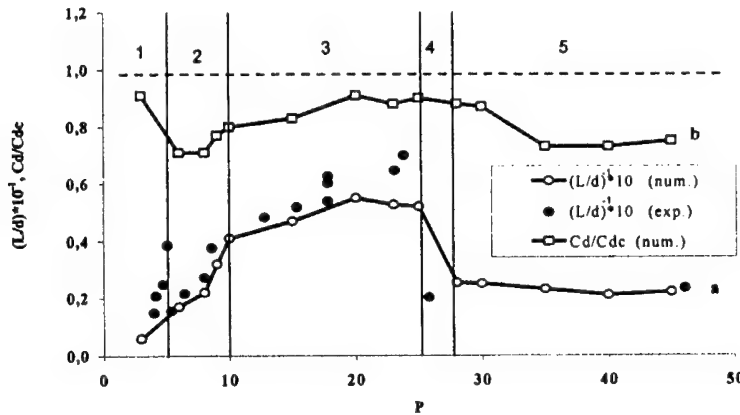

Fig. 1. Dependence of the length of jet penetration on pressure ratio (a), Dependence of the drag on pressure ratio (b).

Many parameters determine the length of jet penetration into the free flow, such as the Mach number on the nozzle bluntness, pressure ratio P, temperature and physical-chemical jet features, nozzle angle and the relation between the diameter of outlet nozzle orifice and the bluntness diameter $\overline{d} = d/d_j$.

In the present work, the influence of P on the jet- penetration length was studied. This parameter may characterize the ratio of the specific impulse of the jet to the free stream impulse. If the value of P in the jet is small, a shock is generated; it decreases the initial specific jet impulse. The SPM regime is formed. In this regime, the jet is not able to overcome the distance between the body and the bow shock wave. The jet forms a zone of vortex gas flow, and the

flowing around the blunt body part is formed as the flow around some liquid contour. The calculated structure agrees with the scheme in paper [10], where it is described quite comprehensively.

With an increase in P, the SPM regime is transformed into the LPM regime. Such conditions are formed when cross sectional area of the jet decreases and the specific impulse increases because

$$P_{0j}^1 \approx P_{0j} F_a / F .$$

Here F_a, F are is jet areas at the nozzle outlet and in the flowing cross section respectively. The increased specific impulse allows the jet to "go through" the bow shock wave. After the jet comes into the free stream, a multi-barrel periodical structure organizes; it is supported by toroidal vortices. Figure 2 is an example of the LPM regime from the numerical simulation. Here the isobars field is given for one of the calculated variants. The scheme of LPM flow produced through multiple calculation is presented in Fig. 3.
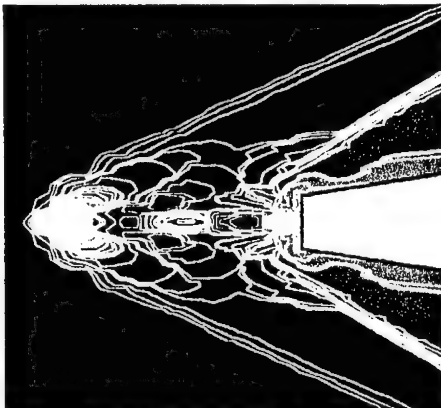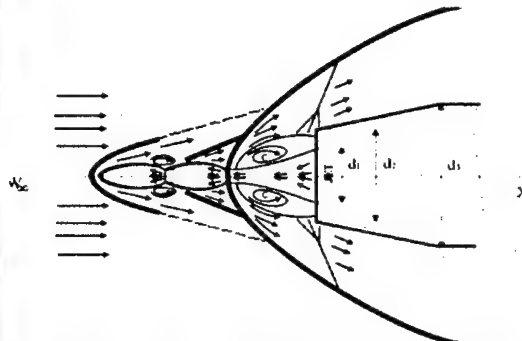

Fig. 2. LPM ($P=15$). Isobars injected jet: – LPM

Fig. 3. Scheme of flow around the body with an upstream

For initiation of the LPM mode it is necessary to require:

a) the stagnation pressure of a jet should exceed the stagnation pressure of the flow behind the normal shock;

b) the jet should be overexpanded integrally

When the penetration is relatively short, the decrease in pressure, which is observed on the side surfaces of the body, is significant. A rather long penetration at small thickness of the jet does not lead to a significant decrease in pressure on the side surfaces of the body. There is an optimal range of parameters, which gives the most effective decreasing of the drag. A further increase in P forms an underexpanded jet flow in front of the body. In this case, the jet area rises and the value of P_{0j}^1 becomes equal to the free- stream stagnation pressure P_{0f}'. The SPM regime is observed again. The calculation results have shown that LPM generation is determined mainly by the value of the jet pressure ratio $\tilde{n} = \tilde{p}_j / \tilde{p}$. Here $\tilde{p}$ and $\tilde{p}_j$ are the average pressure values along the jet boundary and inside it. For the LPM mode to exist, the $\tilde{n}$ value must lies in the range $0.3 \leq \tilde{n} \leq 1$, i.e. the condition for an overexpanded jet should be satisfied. In areas (4), (5) the other parameters can influence essentially.
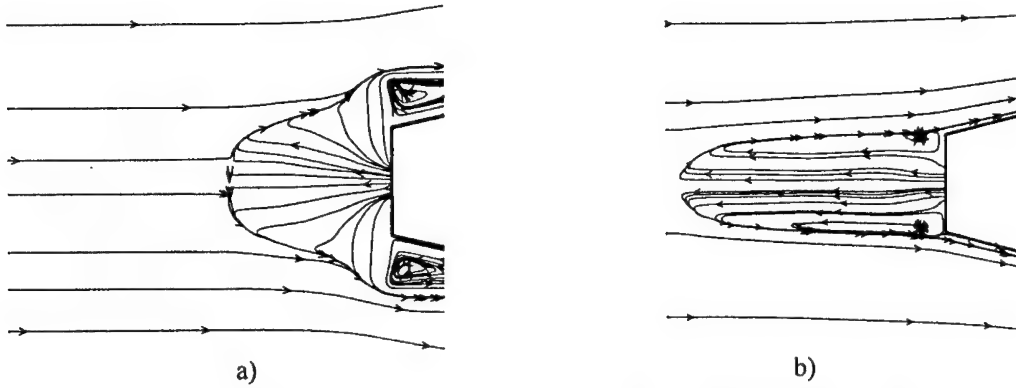
a)

b)

Fig. 4. Effect of nozzle expansion angle on the length of jet penetration a) SPM mode, $P = 45$, $\theta_a = 20°$; b) LPM mode, $P = 45$, $\theta_a = 0°$
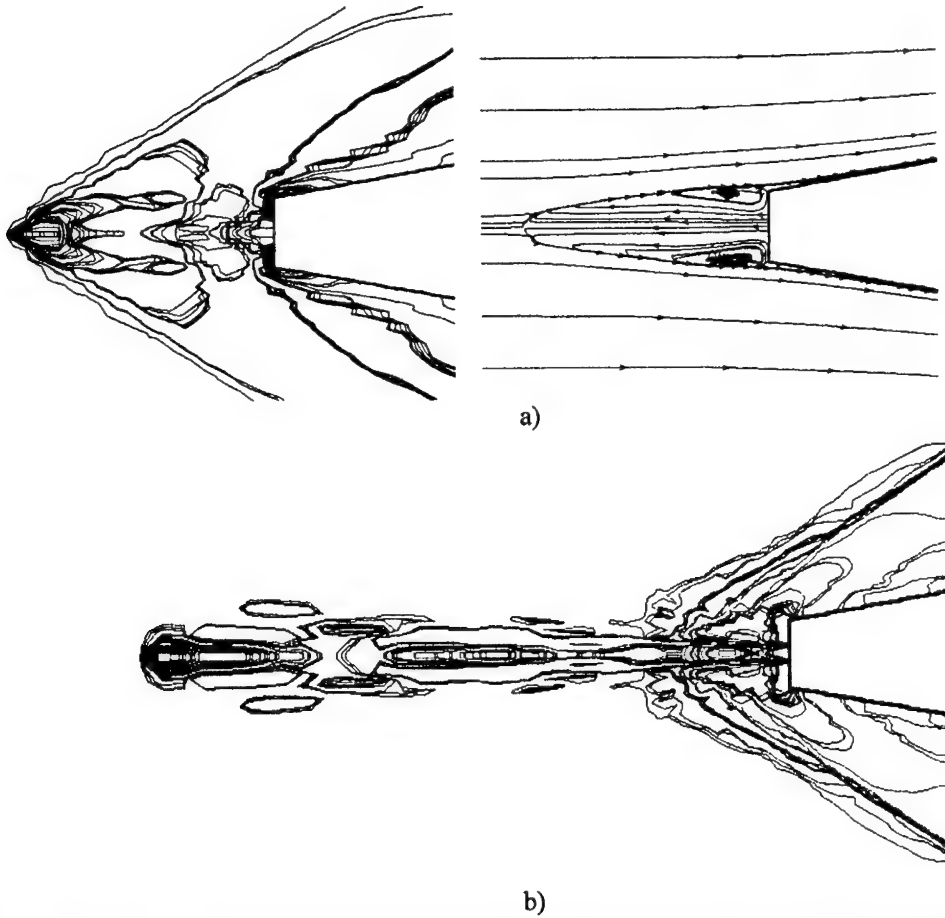

a)

b)

Fig. 5. The temperature effect on the length of jet penetration into the counter flow $M_\infty = 2.04$, $Ma = 3.8$, $P=26.6$; a) Ta=300K field of isobars and streamlines, b) Ta = 5000K, field of isobars

In Fig. 4, the streamlines for two calculated variants are shown. They differ only by the angle of nozzle expansion. In numerical calculations, the nozzle angle is simulated by changing the slope of velocity vectors.

The calculation was carried out when the jet had a temperature $T = 5000K$ at the nozzle exit. In Fig. 5, the isobar field is shown for this calculation. Here one can see that the length of jet penetration into the free flow was considerably increased in comparison with a cold jet. Three barrels of the jet are well visible.

Thus, the numerical simulation of penetration a supersonic counter-flow jet shows the basic regimes that were observed experimentally; and the mechanism of long penetration of the jet into the free stream (LPM). From the point of view of decreasing the wave drag, the most profitable are the areas of transition regimes SPM→LPM and LPM regimes with relatively small lengths of jet penetration. The research showed that, if the length of jet can be changed, the flow structure around the body can be influenced and thereby its total aerodynamic characteristics are changed considerably.

REFERENCES

1. Tretyakov P.K., Fomin V.M., Yakovlev V.I. New Principes of Control of Aerophysical Processes Research Development //Intern. Conf. On the Methods Aerophys. Research : Proc. Rt 2. Novosibirsk, 1996. P. 210-220.
2. Chernyi G.G. The impact of electromagnetic energy addition to air near the flying body on its aerodynamic characteristics // II Workshop on Weakly Ionized Gases: Proc. Norfolk, 1998. P. 1-20.
3. Leonov S. Experiments on Influence of Plasma Jet Lift and Drag of Wing // Workshop on Weakly Ionized Gases: Proc. Vol 1, Colorado, 1997. P. J1-J24.
4. Klimov A. Anomalous Superconic Flow and Shock Wave Structure in Weakly Ionized Plasmas // Workshop on Weakly Ionized Gases: Proc. Vol 1. 1997, P. G1-G20.
5. Yudintsev Yu. N. and Chirkashenko V.F. Modes of interference of a counter jet with a free supersonic flow // Gasodinamika i acustica struinyh techenii, ITPM, Novosibirsk, 1979, P.75-106. (in Russian).
6. Fomin V.M., Malmuth N.D., Maslov A.A., Fomichev V.P., Shiplyuk A.N., Pozdnyakov G.A., Postnikov V.V., Pozdnyakov B.A. The influence of plasma jet on summary and disributing aerodynamics characteristic of blunt body // DAN. 1999. Vol 368, No 2, P. 197-200 (in Russian).
7. Shang J.S, Ganguly B., Umstattd R., Hayes J., Arman M. and Bletzinger P. // XXXVIII Aerospace Sciences Meeting: Proc. Reno, 2000, AIAA 2000-0447. P.10.
8. Nomura H., Aso S., Nishida M. Numerical simulation of opposing sonic jets // The II Japan-Soviet Union Joint Symp. on Computation Fluid Dynamics: Prepr. Tsucuba, 1990. P.281-284.
9. Korotaeva T.A., Fomin V.M. and Shashkin A.P. Spatial supersonic flow around of the sharp-nose body at input of energy before it // Prikladnaya mekhanika i tekhnicheskaya fizika, 1998. No 5. P. 116-121.
10. Finley P.J. The flow of a jet from a body opposing a supersonicfree strem // J. Fluid. Mech. 1966. Vol 26. No 2. P. 337-368.

MEASUREMENT TECHNIQUES FOR DETECTION OF FLOW DISTURBANCES AND TRANSITION LOCALIZATION IN A SHORT DURATION WIND TUNNEL

U. Gaisbauer, H. Knauss, S. Wagner, J. Weiss

Institut für Aero- und Gasdynamik Universität Stuttgart, Germany

1. Introduction and Problem

The location of boundary layer transition in the flow around slender generic configurations of hypersonic vehicles is of great importance in their design. But the simulation of reliable transition Reynolds numbers (Re_t) in super- and hypersonic wind tunnel experiments, directly relatable to free-flight conditions must be put in question (Stetson [1]). Beckwith [2] has shown that Re_t -values of free-flight cone experiments are up to one order of magnitude higher compared with corresponding transition experiments in conventional supersonic wind tunnels. The reason for this discrepancy is the receptivity of the model boundary layer to disturbance fields which are superimposed to the test section flow. These can be "sound waves" radiated from the turbulent boundary layer of the tunnel/nozzle walls as well as "entropy spottiness" or "vorticity", embedded in the core flow and convected from further upstream to the test section (Lebiga et al. [3]). Only in two blow down facilities, the Mach 3.5 quiet tunnel of NASA Langley [2] and the Mach 2 quiet tunnel T-325 of ITAM, Novosibirsk [3], [4], as well as in the short duration Mach 5 Ludwieg tube (RWG) at DLR Göttingen [5], Re_t -values on a 5° half angle cone have been found, which are unambiguously within the scatter of the free-flight data and show furthermore no "unit Reynolds number effect" over a wide range of unit Reynolds numbers (R/m). This last result points out that a modification of intensity and spectral distribution of the different kind of disturbances, which could be accompanied by a change of the unit Reynolds number have no essential influence to the transition process with a particular Mach number, even when the noise level is not within the so-called quiet range. So Stetson [1] argued, that most of the free stream noise is not important for instability and transition studies; the only significant part is at frequencies similar to those of the dominant instabilities on the model boundary layer. (A fact also confirmed in the investigation of Wendt et al. [6] in the DLR Ludwieg tube). These facts demonstrate the complexity of the receptivity in the boundary layer and point out the absolutely necessary knowledge of the character of the different kind of disturbances and their spectra. They are an important part of the "boundary conditions" if the results should be validated or used as a benchmark experiment of DNS computations.

At IAG at Stuttgart University, a large short-duration supersonic facility, the so called "shock wind tunnel" (SWK) designed by A. Weise [7] with a working principle alike the DLR Ludwieg tube has been reactivated for transition measurements. Because of the size of the test section, Reynolds numbers based on relevant reference lengths can be simulated partly in the available Mach range of 1.75÷4.5. The SWK has some peculiarities due to its design and size which are promoting for a reduction of the noise level in the test section. This has been confirmed partially in pilot pitot pressure measurements [8] ($P_{t,\,rms}/P_t = 0.1÷0.3$ %). Because of the short measuring time of about only 120 ms per run, very harsh flow conditions due to a diaphragm closure downstream of the test section and all existing consequences of such an arrangement, make the necessary qualifying measurements more difficult than in a conventional blow down facility or even the RWG Ludwieg tube at DLR Göttingen. The detection of free-stream disturbances and corresponding transition measurements on a cone, as a kind of validation of the test section flow quality, cannot be performed completely by the well established measurement techniques without an adaptation to the existing measuring conditions. Modifications have been carried out partly by taking restricting or enlarging measures in these

methods. Moreover a pilot experiment for transition detection by means of a new sensor has been carried out. It is the intention of this paper to give a short survey about the used methods and the very first results.

2. Wind tunnel facilities

a)

tube arrangement on high/low pressure side
for submitted experimental results

Details of Test Section (schematic)

Test sections equipped with 2-dimensional rapid expansion nozzle blocks :

SWK scale 1:1

HMMS scale 1:4
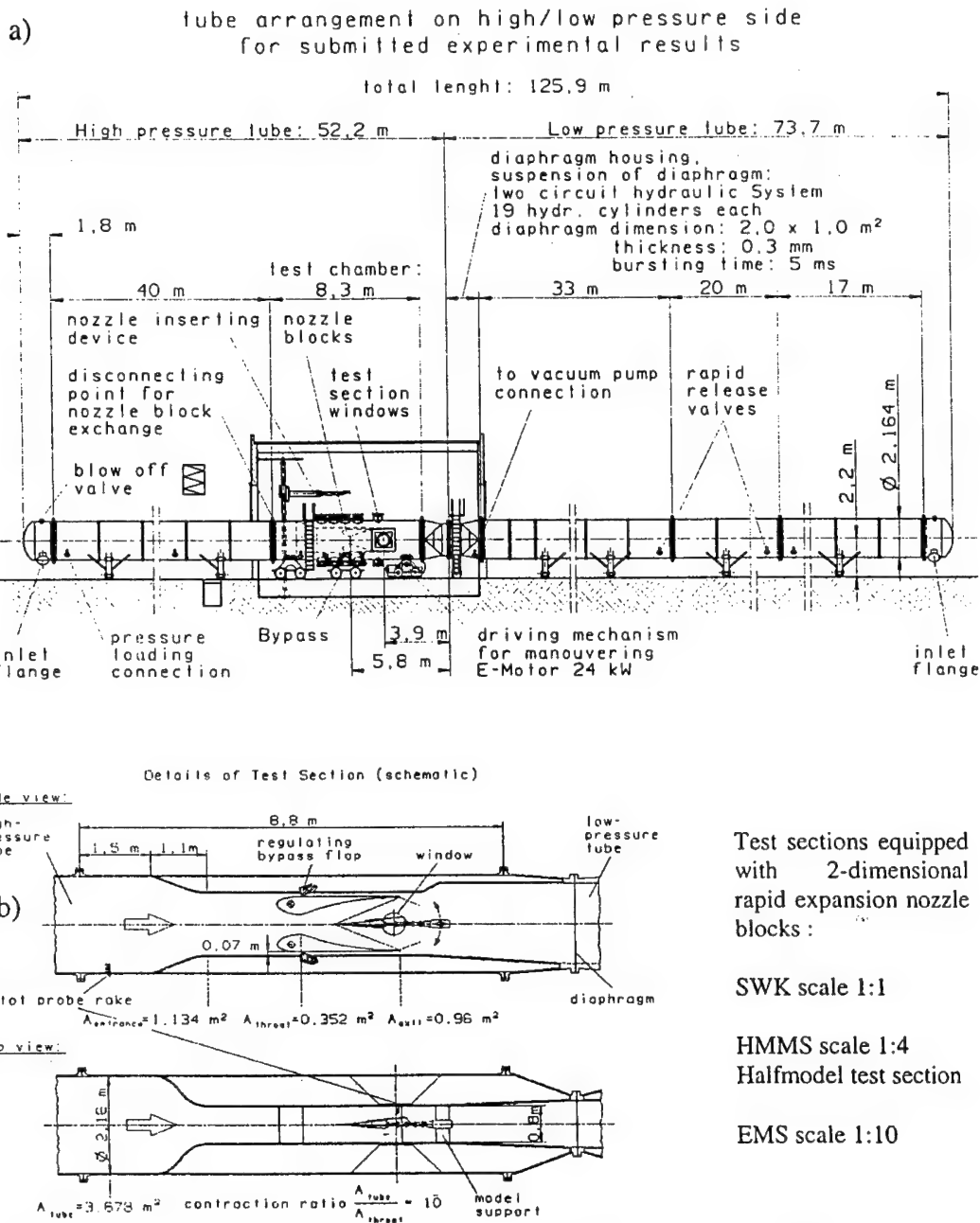Halfmodel test section

EMS scale 1:10

Fig. 2.1 a) The "shock wind tunnel" (SWK), total view; b) Principal construction and main dimensions of test section and corresponding scaled versions (schematic) used for calibration and comparative measurements

MEASUREMENT TECHNIQUES FOR DETECTION OF FLOW DISTURBANCES

3. Free-stream disturbance level measurements

The preceding "noise level" detection in the SWK test section flow [8], by means of *Pitot pressure* as well as mass-flux-fluctuation measurements are up to now strictly speaking of only limited meaning, because of general confining reasons inherent in the methods with the quantities determined as well as the special existing test conditions.

First, the scaling between Pitot pressure-, mass-flux- and static-pressure-fluctuations (the latter as the actual quantity for the definition of sound intensity) remains unsolved. Only if some further information about the character of the flow is given or assumed, the classic interpretation of the fluctuating Pitot pressure signal by Stainback et al. [9] can be used, but the inherent uncertainty of this method is still a factor of 2. According to Chen et al. [10], when the peak energy of the fluctuations is below 30 to 40 kHz, this factor, which is also depending on Mach number and disturbance source velocity, can reach unity.

Second, the dynamic response of the used miniaturized pressure transducer is mostly not known and depends on its design. The natural frequency of the diaphragm has only an essential meaning for the frequency range of the transducer, when it is flush mounted at the front of the housing. Otherwise with the cavity in front of the diaphragm even with a very high natural frequency the available frequency range of transducers (housing diameters in the order of 1.5 – 2.0 mm) will be reduced to about 40 kHz, i.e. about 50 % of the cavity resonance frequency according to Gossweiler [11]. To conclude, 4 redundant Pitot pressure fluctuation distributions measured in the test section in streamwise direction, with four different transducers, have shown an average standard deviation over 60 single measurements of about 20 %.

With a performance of the preceeding disturbance measurements using the more informative *hot-wire technique* a first difficulty arises because of the fragility of the hot-wire probe. Already with a very low boost pressure (1.1 bar, $R/m = 11 \cdot 10^6$) a 5μm tungsten wire fails, <u>not</u> during the stationary flow but at the end in the high unsteady break down phase. Because of the large tubing size of the tunnel (2.1 m) no fast shut-off valve upstream but a diaphragm closure downstream of the test section must be used, and in consequence very harsh flow conditions with multiple shock wave passages and a high turbulence exist in the unavoidable pressure balancing flow between high and low pressure tube.

A remedy was found in using a DANTEC 55R31 wedge shaped hot-film probe. Partial criticism in the literature for using such a probe for free stream disturbance measurements (in detail outlined in [8]) could be dispelled. Redundant comparative mass flux fluctuation measurements in the test section flow of some different and smaller supersonic wind tunnels (at IAG in the EMS, HMMS and the SWK for $R/m = 10 \cdot 10^6$ as well as at ITAM in the T-325 for $10 \cdot 10^6 \leq R/m \leq 32 \cdot 10^6$) have been performed ([8], [12]) by a simple "dynamic calibration" with one high overheat ratio (τ), as well as by means of a "full calibration" method (i.e. determining mass flux- and temperature-sensitivity coefficients versus overheat ratio $0.2 \leq \tau \leq 1$). For the hot-film, in reference to a corresponding respective calibrated hot-wire probe and by using the Kovasznay method, attenuation factors 0.5÷0.75 were found in the measured mass flux fluctuation of the hot-film in reference to the hot-wire, dependent on the specific sensor resistance. All probes have been operated by a DANTEC 55M10 CTA as well as an AN1003 CTA anemometer device at IAG and ITAM respectively in these measurements.

The application of the Kovasznay disturbance mode diagram technique in the SWK test section flow was a first step, not only to determine a pure numerical value of the mass flow fluctuation (equivalent 0.1÷0.5 % to a hot wire measurement) with higher accuracy, eliminating a possible influence of temperature fluctuations, but also to reveal the character of a disturbance

field. It was found that the free-stream fluctuations in the SWK are likely to be dominated by aerodynamic sound in the sense of Lighthill and by shivering Mach waves emanating at imperfections in the nozzle contour.

But in the application of this modal analysis the used independent variable, the so called modal analysis parameter (i.e. the sensitivity ratio $r = -F(\tau)/G(\tau)$, for specific τ with corresponding hot-film signal) had been assigned to a sequence of successive runs with a constant specific R/m-value. This procedure implied absolute constant stagnation condition for each run, which must be put in question up to a certain degree. In particular the SWK, like all short duration facilities, (Ludwieg tube, shock tunnels etc.) has neither a special settling chamber with screens of decreasing meshes nor a high contraction ratio (here only 1:10 for M = 2.5), the existing initial conditions of the "state of quiescence" in the driver tube will be transmitted and transformed almost uninfluenced downstream in the test section flow. In the "state of quiescence" residual vorticity produced during the charging period of the driver tube and starting free convection current can be present and are of a stochastic nature. The latter will be greater with a large driver tube diameter and is evident when the Grashof-number based on the tube diameter is taken as a criterion for free convection. Schneider [13] has also addressed this issue but was not going into this special problem. Therefore it is of great importance to determine the order of magnitude of such unavoidable vorticity and total temperature fluctuation, as well as the reproducibility of the flow conditions including the disturbance field. For an unambiguous estimation of the size of these uncertainties it becomes inevitable to adjust a sufficient number of τ-values simultaneously within one run. A rapid scanning device for a stepwise change of τ within the available 120 ms is necessary (similar to Walker et al. [14]).

In a cooperation between IAG, A.D. Kosinov at ITAM and a German company (COSYTEC electronics [27]), a fast CTA scanning system was developed. Although the use of a CCA technique for free flow disturbance measurements is advantageous compared to CTA, especially concerning the detection of temperature fluctuations in a higher frequency range (Owen et al. [15]) when operating at very low overheating with a "cold wire", the CTA has been chosen. Reasons have been the omission of adjustments for compensation of the thermal lag as well as short-running times even for the necessary pre-adjustment of the frequency response in the available smaller wind tunnels before transferring the system to the SWK for measurements. Moreover Bestion et al. [16] show that spectral measurements of fluctuations in free flow are in good agreement for CCA and CTA at least when turbulence is reduced essentially to acoustic waves of a lower frequency range, compared to rotational turbulence in boundary layer.

With the use of such a fast scanning procedure, no adjustment for an optimum frequency response of each overheat is possible, and it is known that the roll-off frequency f_R of a CTA system is dependent on this parameter. Smits et al. [17] have shown, that in this case the roll-off frequency behaves like $f_R \propto \tau$. Therefore the largest possible f_R-value must be aspired in the initial adjustment at highest overheat ratio.

The bridge: The CTA bridge circuit by A.D. Kosinov and V.V. Repkov (Institute of Nuclear Physics, Novosibirsk) is specially designed for a high frequency response. The initial adjustment is made by a 4 parameter optimization and by means of a square wave test. On the passive arm of the bridge (ratio 1:10) an adjustment can be made by a trim inductivity as well as a trim resistance. The offset current can be changed by a potentiometer. A fourth adjustment possibility is the gain of the low noise amplifier (Burr Brown OPA 37) in the feedback loop. For $\tau = 0.8$ a cut-off frequency $f_R = 900$ kHz was measured with a square wave test in a M = 2.54 free stream and 700 kHz were found using a sine wave test at ITAM in a 30 m/s free stream flow (Kosinov [18]).
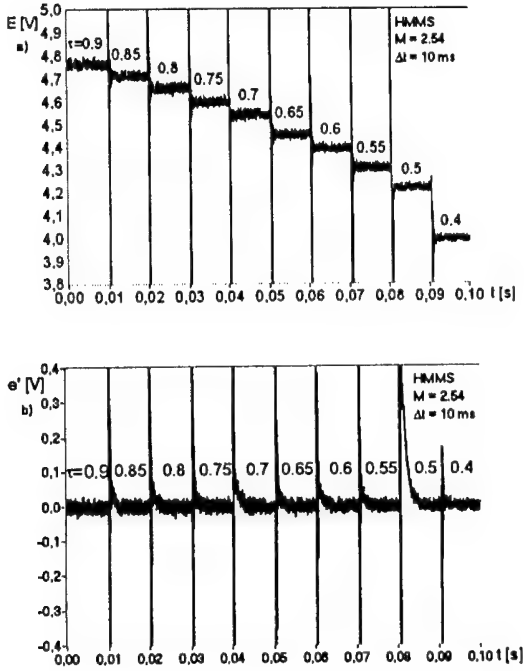
Fig 3.1. Typical signal conditioned output with stepped overheat ratio : a) DC: mean value E(t), b) AC: fluctuation e'(t).

The scanning system: The logic of the system allows the setting of max. 10 overheat ratios in one test sequence. The adjustable maximum overall time of a sequence is 2.5 s. Temporal resolution of the system is 1 ms. But the system can also be operated quite conventionally without time limit and at arbitrarily overheat settings. The total cascade resistance in the passive arm of the bridge is 512Ω, to allow the operation of higher ohmic hot-film probes ($R_0 = 17\Omega$) at high overheatings. For a typical 4Ω wire, the fine grading in the cascade resistance ($\Delta R = 0.05\Omega$) gives an overheat resolution of 0.005. By means of an integrated signal conditioning unit the bridge output is separated into a DC- and AC-signal, representing mean and fluctuating values. The resolution in A/D-conversion (sampling rate 800 kHz/s) of the fluctuation signal can be optimized by using the complete voltage range of a 14 bit A/D converter (3 in Fig. 4.3). The AC coupling is performed by a RC-high pass filter of 1 kHz cutoff frequency.

Experiments: First measurements and comparative tests of the COSYTEC CTA scanning device and a DANTEC 55M10 CTA have been performed in free stream disturbance measurements in the HMMS suck-down wind tunnel test section flow for M = 2.54. A modified and full calibrated DANTEC 55P11 probe (as aforementioned) with a slackened 5 μm tungsten wire was used for the fluctuation detections. Fig. 3.1a shows a typical DC output signal E (t, τ_i) of a scanning sequence with a total time of 100 ms (SWK flow duration 120 ms). The overheat ratio is varied from 0.9 to 0.4 in 10 stages of 10 ms. Fig. 3.1b represents the corresponding AC output signal e'(t, τ_i). A data processing according to the Kovasznay analysis out of 5 sequences with 6 overheat ratios (0.4 ÷ 0.9) in 20 ms
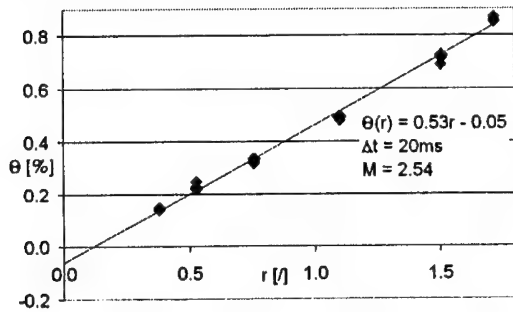

Fig. 3.2. Mode diagram of HMMS free stream disturbances by scanning system.

steps each, results in a mode diagram shown in Fig. 3.2. Normalized effective fluctuation values $\Theta_{rms}(\tau_i) = e'_{rms}(\tau_i)/E(\tau_i) \, G(\tau_i)$, plotted versus corresponding modal parameter $r(\tau_i) = -F(\tau_i)/G(\tau_i)$ show approximately the linear dependence $\Theta_{rms}(\tau_i) r(\tau_i)(m'_{rms}/m) + (T_{0,'rms}/T_0)$, typical for a dominating acoustic disturbance field.

An averaged normalized mass flux fluctuation $m'_{rms}/m = 0.53 \%$ has been found for this specific flow test in the HMMS with a scattering of 5 % rms, in a total sequence time of 120 ms. Additional corresponding tests with increasing times of
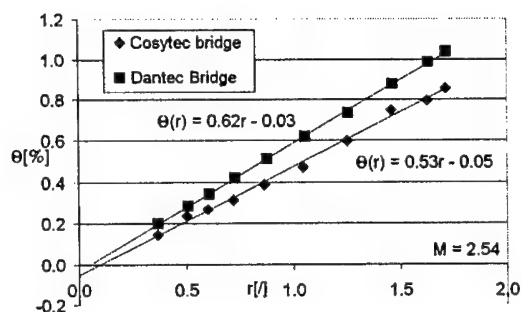
58

Fig. 3.3. Mode diagram of HMMS free stream disturbances, DANTEC and COSYTEC bridge in comparison.

interval from $\Delta t = 10 \div 70$ ms have shown that the scattering in this time limited signal analysis is logically decreasing with increasing the sampling time Δt. It is obvious that a critical sampling time exists always for a time limited signal analysis and will be dependent on the main character (intensity and dominant frequency range) of the disturbance field. That means at least a temporal mean value (reference value m) independent on sampling time Δt must be definable within the sample of a specific overheating stage. Such mean values have been proved by simulating corresponding SWK sampling times ($\Delta t = 10 \div 20$ ms) in the aforementioned HMMS free flow measurements. The definition of a normalized stagnation temperature fluctuation $T_{0,}'_{rms}/T_0$ by means of an extrapolation of the linear regression in Fig. 3.2 would be too speculative. For a meaningful modal analysis concerning the determination of temperature fluctuations, measurements have to be performed in an overheating range of $0 < \tau_i < 0.5$. But the hot-wire calibration available, covered only an overheating range of $0.3 < \tau_i < 1$ and therefore another uncertainty would be introduced by extrapolated values of the calibration functions. A more detailed investigation in this CCA domain has been therefore first of all deferred. But otherwise only a negative interception in linear regressions of all measurements with overheat ratios larger 0.4 allows the assumption and the conclusion that there is not a complete correlation between temperature and mass flux fluctuation in this test section flow, but a minor superposition of another disturbance mode, presumably vorticity.

Comparative measurements with a conventional DANTEC 55M10 CTA (measurement time of $\Delta t = 160$ ms) for overheat ratios in the range of $0.1 < \tau_i < 1$ and the COSYTEC scanning device with corresponding overheatings out of some successive sequences with a sampling time of 20 ms each have been performed and are shown in the mode diagram of Fig. 3.3. There is a clearly larger mass flux fluctuation value of about 20 % determined by the DANTEC system. Also taking into account an uncertainty of 5 % because of the shorter sampling time, a significant difference of about 15 % remains. The reason of the discrepancy is not known yet. However it seems that the high frequency behavior of the two bridges could be the reason. Fig. 3.4 shows two power spectra with an overheat ratio of 0.9 for both CTA systems. It is seen
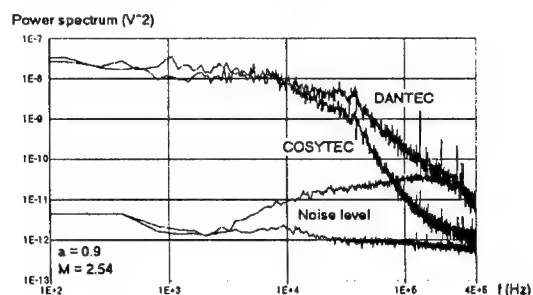

Fig. 3.4: Power spectra of disturbances in the HMMS free stream. DANTEC and COSYTEC bridge in comparison.

that there is a significant decrease at approximately 20 kHz in the spectra of the COSYTEC CTA system. But the spectra also shows that the noise level of the scanning system in the higher frequency range is much lower.

A further analysis of the DANTEC mode diagram reveals that there is a stepwise decreasing of the slopes with decreasing overheat ratios and a transition to positive interceptions with the ordinate. This confirms the assumption of a slight curvature of the mode diagram i. e. a minor

uncorrelation between mass flow and temperature fluctuations (vorticity) in the flow. The COSYTEC system shows a similar trend but with a bigger scattering.

Further investigations are planned to explain the different frequency response as well as the behavior of the bridge with lower overheat ratio.

MEASUREMENTS TECHNIQUES FOR TRANSITION LOCALIZATION
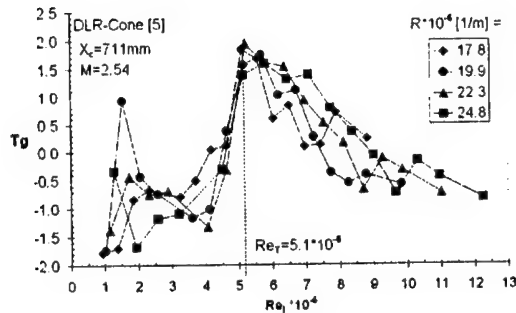
4. Different methods for transition detection

Fig. 4.1. Transition detection by *the thin wall technique* for different Re/m values.

A criterion to qualify the test section flow is the transition Reynolds number (Re_t) on a 5° cone and its behavior when changing unit Reynolds number (R/m). One of the most established and suitable method for transition detection in short duration wind tunnels is the *thin wall technique*, where thermocouples are completely integrated into the thin cone wall (0.15 – 0.2 mm thickness) without producing artificial roughness on the surface. Owing to the friendly cooperation of Krogmann (DLR Göttingen) an instrumented cone, optimized for transition tests in the DLR Ludwieg tube [5] has been available for first tests in the SWK. Because of the diaphragm closure to the low pressure tube downstream of the test section in the SWK, in contrast to the RWG, the model is exposed to the initial high boost pressure. With the release of the run and because of the sudden static pressure drop during flow establishment, a high differential pressure is acting on the thin wall because of a delayed ventilation in the cavities adjacent to the cone wall of the supporting cone body. A rough strength analysis resulted in an allowable differential pressure of 0.8 bar. Experiments with a PVC dummy cone showed that the stagnation pressure must not exceed 2.5 bar, corresponding to about R/m = $25 \cdot 10^6$, not to cause permanent distortion in the cone skin. Electric disturbances (but only during flow) in the thermocouple signals, a low uncontrollable stagnation temperature T_0, i. e. according ambient condition and therefore a low heat flux in the wall too, resulted in a low signal to noise ratio. Only by a preceding digital low pass (30 Hz) filtering of the N = 19 thermocouple time histories and by a statistical evaluation process, a significant local change of a normalized temperature time gradient T_g in the cone wall which is indicating transition, could be detected. The course of these dimensionless gradients defined by the relation $T_{g,i} = ((dT/dt)_i - (dT/dt)_{mean})/(dT/dt)_{rms}$, with the dimensional local gradient $(dT/dt)_i$ of the thermocouple "i", the average $(dT/dt)_{mean} = (\Sigma(dT/dt)_i)/N$ and the rms value $(dT/dt)_{rms} = ((\Sigma(dT/dt)_i - (dT/dt)_{mean})^2)/N)^{0.5}$ is shown in Fig. 4.1 between $17.8 \cdot 10^6 \leq R/m \leq 24.8 \cdot 10^6$.

Fig. 4.2: Insert and used hot films, dimensions in mm.

The peaks of the four plots belonging to different R/m numbers coincide at $Re_t \approx 5.1 \cdot 10^6$ and demonstrates independence of R/m number. The upper Re/m limit of these measurements was defined by the reason mentioned
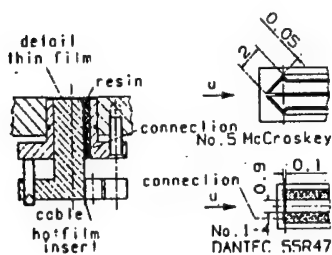
60

Thin film probes:
flat plate, IAG-cone

- McCroskey: ET-TG-GAG-0050
  operational temperature:
  111°C (I=82mA),
  181°C(I=100mA)

- DANTEC Glue-on-probe 55R47
  operational temperature:
  135°C (I=45mA)

signal

CCA-bridge:
Cosytec constant current circuit
I=45; 82; 100mA

signal

Amplifier:
Cosytec BRVST2
dc: amlpification: 20/40dB
bandwidth: 1Hz÷1kHz
ac: amlpification: 60dB
bandwidth: 0.1kHz÷1MHz
alternativ:1kHz÷1MHz

Power
supply:
battery:
U=±12V

ac   dc

A/D-converters and data-saving:

1 Tektronix TDS 420 digital os-
  cilloscope, 10bit, 120ms,
  500kS/s

2 Eckelmann A/D-converter SCP
  3200, 12bit, 128ms, 500kS/s,
  anti-aliasing filter installed:
  $f = 100; 250kHz$.

3 IMTEC A/D-converter, 14bit,
  128ms, 800kS/s

IEEE-488 interface / Ethernet

Data-processing:
Sun-workstation
used software: LabVIEW

Fig. 4.3: Schematic diagram of instrumentation
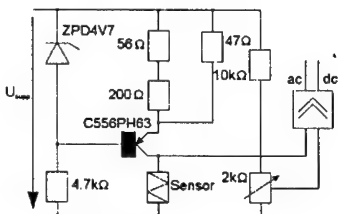
Fig.4.4: CCA circuit with signal conditioning unit.

above. To enlarge this range to an aspired upper bounds of R/m ~ $60 \cdot 10^6$ for M = 2.54 an alternative method must be used.

The *thin hot-film technique* is also in supersonic boundary layer studies the most meaningful method concerning information on the surface when transition occurs, but also the most expensive one (Hall et al. [19]), especially when micro-thin film sensors are deposited directly onto the model surface (Johnson et al. [20]) to get a "high fidelity" surface finish. In the present case such a depositing high technology technique is not available and also multi sensor elements on a large foil have not been taken into consideration. The leads leaving laterally of the sensor array on the surface could produce a regular roughness which is promoting the transition process. To avoid such a troublesome side effect, commercially available single glue-on probes have been preferred. The commercially available single sensors are applied on special standardized two-part PVC-inserts (Fig. 4.2) which are adapted to the local curvature simultaneously while the shape of the model is manufactured and surface finishing work is carried out.

The protruding caused by substrate thickness and adhesive coat could be minimized by a precise adjustment of the inner part of the insert after application, and in combination with a special sealing procedure, which also allows a slurring of the substrate and insert edges to a remaining maximum roughness height of about 2 μm. In the present case, where mirror quality could be realized at the cone surface, these sensor regions can be regarded more as single roughness, one order of magnitude above the rms-value of about 0.2 ÷ 0.3 μm of the cone surface. To minimize this roughness influence and the total heat flux into the laminar boundary layer from all sensors, positioned along one surface line, which both can have a destabilizing effect to the boundary layer, as well as to reduce heat flux interference to adjacent downstream sensors (Nitsche et al. [21]), a sensor spacing of approximately 30 mm was chosen for first transition measurements in a two-dimensional boundary layer of a flat plate in the EMS test section. Fig. 4.3 shows in a schematic block diagram the arrangement of the components (with main specifications) in the measuring chain from sensor to data processing.

The transition region can be detected by calibrated or uncalibrated sensors. In the latter case which has been used here the fluctuating part of the hot-film signal must be analyzed by statistical methods. The position of the peak in the rms fluctuation values (indicating transition) matches with an intermittency factor of $\Gamma = 0.5$. But in using this method,
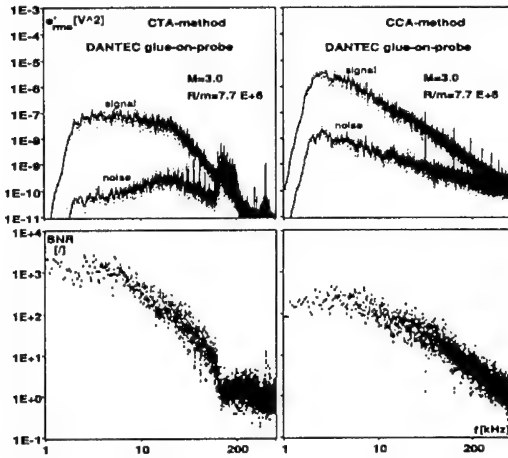
Fig.4.5. Comparison of frequency response in the turbulent BL of the EMS test section side wall and signal to noise ratio (SNR)
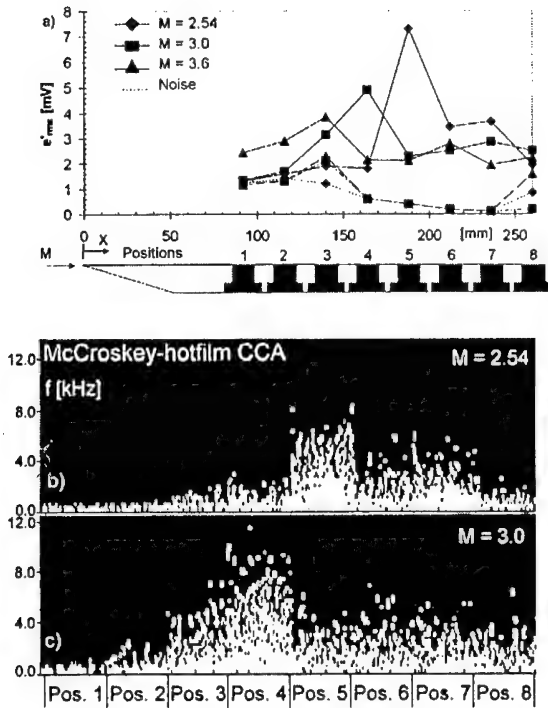

Fig. 4.6. a) rms values of hot film fluctuation signals in flat plate BL (EMS)

b, c) Spectrogram of position 1÷8, sampling time Δt = 40 ms, for different Mach numbers.

the frequency response i. e. cut-off frequency and signal to noise ratio (SNR) are important factors. In a further simplification to [19], the sensors are not operated in a CTA- but in a CCA-mode (Fig. 4.4) (something more costly like in Kornberger [22]), but also without any frequency compensation. In spite of a poor frequency response of this CCA-mode compared with the CTA-mode (Fig. 4.5), determined in a turbulent boundary layer at $\tau = 0.3$ for a DANTEC 55R47 glue-on probe, as well as a McCroskey sensor, significant peaks can be defined in the rms fluctuation plots, for all three Mach numbers measured (Fig. 4.6a).

Transition moves upstream and the raise of the peaks is decreasing with increasing Mach number, as in [19]. The latter is caused by the decreasing density when Mach number is increased with constant stagnation pressure. Besides the rms-values and the closed look at the different time histories and spectra, a far reaching analysis of the time signals is given by the application of the Joint Time Frequency Analysis (JTFA; Qian et al. [23]) for the transition detection. By means of Short Time Fourier Transform (STFT) it is possible to determine time- and frequency dependent power spectra, which form both the spectrogram versus the time-frequency-plane. The 3-dim. spectrogram is usually reduced to a 2-dim. graph by projection into the time-frequency-plane and the unit of measuring to describe the intensity distribution is generally performed by a grey graduation or even by a shade of the corresponding colors. In the present case the intensity is more or less roughly divided in a low (black) and high (white) level range. In Fig. 4.6b,c) such kind of spectrograms of all eight measuring positions are stringed together for the two Mach numbers 2.5 and 3.0. Here, the "defined" transition points 5 and 4 of Fig. 4.6a) are characterized by a corresponding sudden increase of the intensity with higher frequencies and
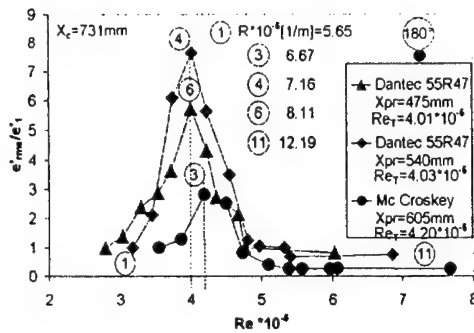
62

Fig. 4.7: Normalized rms-values of hot film signals in cone BL (SWK), M=2.54.

represent a peak region too in the overall distribution of all eight spectrograms. Downstream of this peak in the turbulent state the energy distribution is slightly broader in the frequency bandwidth compared with that upstream of the peak in the more laminar region.

In the performance of this analysis the sample within the total time of 120 ms, with a sampling rate SR = 500 kS/s was truncated to a third (Δt = 40 ms) for the particular 8 different time signals because of storage limitation.

First transition experiments in the SWK using the thin-film technique have been performed on a 5° cone, positioned 20 mm downstream of that of the DLR cone. On this model 5 thin hot-films have been installed along a surface line, relatively far downstream, beginning at 475 mm from apex with equal spacing. Because this IAG cone has been primarily designed for the detection of stationary disturbances and also for the alignment of the modified prolonged model support into the flow direction, by pressure distribution measurements around and along the cone surface [8], no positioning of sensors more upstream was possible in the cone of a total length of 1 m. Unfortunately two of the hot-films failed and the spacing became twice the one that was originally planned. Because of a PSI module limited to 20 psi installed inside the cone and the used hot-film instrumentation, a transition measurement was only possible by changing R/m in the range of $5.65 \cdot 10^6 \leq R/m \leq 13 \cdot 10^6$. Fig. 4.7 shows the measured rms fluctuation values normalized by the e_{rms}-value corresponding to the lowest R/m-value of the particular hot-film. The rms peaks 4 and 6 of the two adjacent hot-films and of the same type coincide fairly well with $Re_t = 4.0 \cdot 10^6$, while the most downstream situated hot-film of the second type shows a peak value 3 with a $Re_t = 4.2 \cdot 10^6$, about 5 % higher. The explanation of this discrepancy could have different reasons. On one hand the different type of hot-film and on the other hand a R/m-dependency, which is more probable. Only the information from an enlarged instrumentation and further measurements with both sensor types will give a sufficient reliable answer.

The *Preston tube* with a wall Pitot pressure measurement is a further possibility for a transition detection. But because only a single poi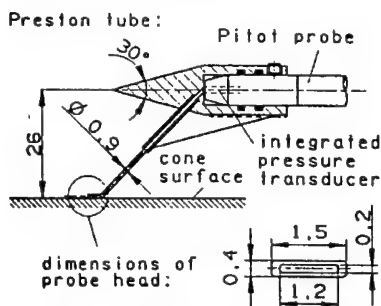nt measurement is possible and no traversing within the short time along a surface line of the cone, transition detection must be performed by changing R/m-values with a fixed probe position. Investigation of the R/m-influence onto the Re_t -values must be carried out by a sequence of such R/m-variations with fixed probe but for different distances from the apex along the surface line. The course of measured wall Pitot pressure normalized with stagnation pressure and plotted versus the local Re-number, based on the particular probe position, must coincide when there is no R/m-dependency. But both Re_t -numbers which can be defined in a qualitative wall Pitot pressure course, one in the beginning and a second in the
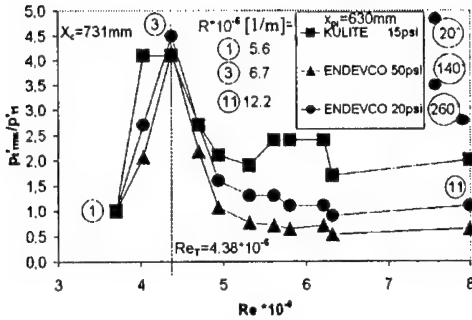

Fig. 4.8: Preston tube / pitot probe combination, dimensions in mm.

63

Fig. 4.9: Normalized rms values of pitot pressure fluctuations in cone BL (SWK), $M = 2.54$.

peak value at the end of the rise are not comparable with corresponding Re_t -values of the film technique. The measured physical quantity is different and has another behavior in the transition process. Only the qualitative course of the fluctuations in the wall Pitot pressure could be a comparable criterion and was realized by a special Preston tube design shown in Fig. 4.8.

The actual probe with a flattened front opening is supported by a cone-cylinder shaped head piece and is put on a Pitot probe with a flush mounted miniature high frequency response, piezo electric transducer. Such an installation minimizes the volume of displacement between the front opening and the diaphragm of the pressure transducer and therefore results in a small time constant for the pneumatic system as well as concerning low damping. Although pressure signals from the transducer are of course distorted in amplitude and phase by the tubing, the fluctuation distributions measured when changing the R/m number, are fairly well in accordance with the hot-film fluctuation distributions: Fig. 4.9 shows the effective wall Pitot pressure fluctuation, normalized with the respective first measured value for three different Preston tubes, installed 630 mm downstream of the cone apex, on three positions around the cone circumference.

For the angular positions 140° and 260° the peaks of the distributions are matching at $Re_t = 4.38 \cdot 10^6$ while for the 20° position, by a local extrapolation, a peak value can be defined at $Re_t = 4.15 \cdot 10^6$. This is a deviation of 3.5 % in reference to a total averaged value of $Re_t = 4.3 \cdot 10^6$ which could be caused by uncontrollable differences in the probe models including the individual, integrated transducer. On the one hand the averaged Re_t -value of the Preston tubes is unambiguously above the corresponding one with $Re_t = 4.07 \cdot 10^6$ of the hot-film technique, but on the other hand such an averaging is only sensible when there is no R/m effect. Considering that the results of Fig. 4.7 and 4.9 of both techniques have been found simultaneously in the test section (with identical stagnation i.e. free-flow conditions (R/m)), and taking into account additionally a finite R/m dependency, it is obvious that the length between the cone apex and respective probe is a decisive magnitude. This is seen clearly when $Re_t = 4.2 \cdot 10^6$ of hot-film position $X_{Pr} = 630$ mm is compared with the averaged $Re_t = 4.3 \cdot 10^6$ of the Preston tubes, positioned at $X_{Pr} = 605$ mm. In this case therefore the discrepancy in the two methods is only about 2.5 % in the peak position detection.
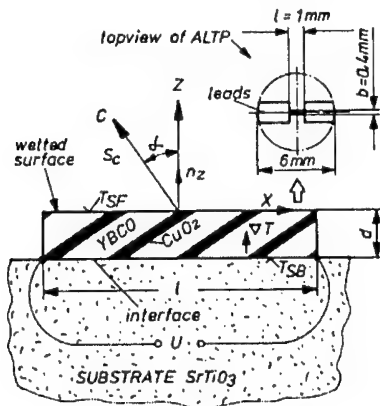
5. Atomic Layer Thermopile

For measuring fast time response of temperature fluctuations at the wall surface which are the base phenomena here for transition detection, a new ultra fast heat flux sensor was tested. The sensor also known as *atomic layer thermopile* (ALTP) [24] is already widely used for measuring the power of laser. Any heat flux (due to laser radiation or direct contact with a hot medium)
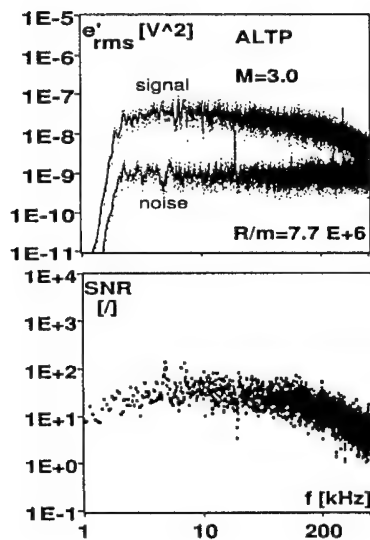

Fig.5.1: Structure and working principle of ALTP

64

Fig.5.2: Frequency response and SNR
with EMS test section conditions like
in Fig. 4.5.

which is related to a temperature gradient gives rise to a voltage signal with response time in the ns-range. The fast thermopile is based on transversal thermo-electric Seebeck voltage in highly unisotropic tilted thin-films. For this unisotropic material, consisting of layered structure of HTSC (high temperature super conductor) is grown epitaxially on single crystalline substrate with a tilt angle α of the material with respect to the surface normal n_z (Fig. 5.1)

Any heating of the surface will produce a thermal gradient ∇T in the thin-film. The Seebeck coefficient S_C of the used material in c-direction is about 15 μV/K whereas the corresponding normal component to it is near zero. ∇T causes an electrical field $E = \nabla T \cdot S_C$ in c-direction. By making electrical constants at the sides of the thin-film, we look at the projection of the electrical field in the x-axis. A temperature gradient in the thin-film, caused by a changing boundary condition on the surface and related with a heat flux, will produce a voltage $U = \Delta T \cdot l \cdot S_C \cdot \sin \alpha$, where $\Delta T = (T_{SF} - T_{SB})/d$ is the temperature gradient, l the length of the active film size (normal to the layers) and d the thickness of the film. Since the thickness of the film is in the range of μm and l in the range of mm, we get a large amplification of the relative weak Seebeck effect S_C. Additionally the small thickness also results in a small time constant of the response in the range of nanoseconds. Therefore, such a sensor will respond to a steady heat flux as well as a fast sequence of heating and cooling on the wetted surface and will thus provide a genuine image of the fluctuation frequencies in the turbulent boundary layer close to the wall. Besides this, it is an active element with no disturbing heat production like in a heated thin-film sensor.

Analogue experiments to the hot-film glue-on probes have been performed with an ALTP applied to one of the standardized PVC-inserts. The thermopile (YBCO-CuO$_2$, heat capacity C = 2.5 J/m^{3}K, heat conductivity k = 1.5 W/mK, density ρ = 6.3 g/cm^3, length l = 1 mm, width b = 0.4 mm) was produced by FORTECH [25]. For a not too long exposure (few seconds) one can assume the used substrate (SrTiO$_3$, C = 2.75 J/m^{3}K, k = 10 W/mK, density ρ = 3.5 g/cm^3, diameter $\varnothing$ = 6 mm and 1 mm thickness) as a heat sink to provide a stable reference temperature T_{SB} at the interface (Fig. 5.1). A high spatial resolution requires of course a small active sensor area while on the other hand the sensor size enhances sensitivity. Here we have in principle a similar confinement alike in a hot-film as shown in [26]. Moreover, the width b of the ALTP is still four and t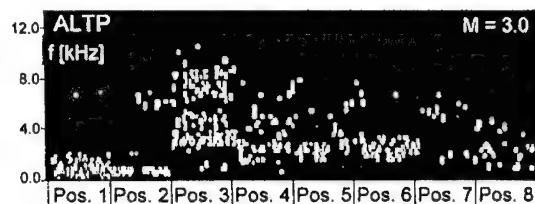en times larger compared to the DANTEC and McCroskey glue-on probes respectively. But micro structuring of a ALTP is a standard technique, where established lithographic processes can be used and manufacturing of smaller sensor would not be the problem. Because of the low ohmic resistance (15-30Ω) the necessary amplification of the output signal in the present "cold supersonic flow" could be easy realized by a corresponding low

Fig. 5.3: Spectrogram of ALTP signal in flat plate BL
position 1÷8, Δt = 40 ms

noise amplifier BRVST2 as specified in Fig. 4.3. Fig. 5.2 shows that SNR of such a sensor is low in comparison with thin-films operated in CCA or CTA modes. But frequency response is higher even related to the latter case. Corresponding flat plate transition measurements in the EMS test section demonstrate the applicability of such uncalibrated ALTP to a transition detection.

The 8 spectrograms stringed together in Fig. 5.3 convey the same facts as in Fig. 4.6b, c achieved by heated thin-film sensors. Further investigations concerning sensitivity in relation to sensor size will be performed.

Due to a low thermal conductivity, large thermal gradients can be maintained in such an ALTP and therefore a use in higher enthalpy flows is possible. Finally, the sensor has a high dynamic range and a linear dependence from very low heat flow, a few mW/cm^2 up to 20 kW/cm^2 which is the damage threshold for 1 ms duration of heat flow, measured using pulses of a CO_2 laser. The sensor can be used for stationary temperature in the range of 100 K up to 400 K.

Conclusion

A CTA-anemometer combined with a scanning system for a fast stepwise change of overheat ratios is presented as an enlargement of the hot wire anemometry technique. It is shown that this device will allow to measure mass flow fluctuations in a short duration wind tunnel. By using the mode diagram technique from Kovasznay [34], not only a mass flow fluctuation value will be determined but also further information will be received at least about the dominant disturbance mode which characterizes the flow in the SWK. To enlarge the operational range of the CTA-system to lower overheat ratios, i.e. to the CCA-domaine, furthermore comparative measurements, also using a CCA-anemometer, will be necessary. For anemometer probes operated in the CTA-mode, the transfer function of the total system is depending on overheat ratio in contrast to CCA. Therefore these functions must be determined by using sine-wave tests. Only with those available, a reliable interpretation of the hot-wire signal for different overheat ratio will be possible.

For transition detection by means of the hot-thin-film technique a CCA-circuit has been developed and used in combination with commercially available glue-on probes mounted on special standardized inserts.

Besides, a Preston tube with a small time constant allowed to measure wall Pitot pressure fluctuation and gives therefore a better possibility for a comparison with the temperature fluctuations of the hot-film sensors, when a Re_t-number is defined.

In addition, a pilot experiment with an atomic layer thermopile shows that such a kind of sensor can also be used as a transition detector and is in principle easier to handle compared to a hot-film and will have some advantages.

Moreover, it is shown that the use of the JTFA for the analysis of time series also allows the detection of transition.

Acknowledgement

References

1. Stetson, K.F.: Hypersonic Transition Testing in Wind Tunnels. In Instability and Transition. H.Y. Hussaini u. R.G. Voigts Eds. Band I, Springer Verlag, New York, 1990. P. 91-100.
2. Beckwith, I.E.: Development of a High Reynolds Number Quiet Tunnel for Transition Research. AIAA Journal, 1975.13 (3). P. 300-306.
3. Lebiga, V.A., Zinoview, V.N.: Fluctuation Characteristics of Flows in Test Sections of High-Speed Wind Tunnels, published in Aerodynamics of Wind Tunnel Circuits and their Components, AGARD CP 585, 1997.

4. Kosinov, A.D., Semionov, N.V., Yermoslaev, Yu.G.: Disturbance in Test Section of T-325 Supersonic Wind Tunnel: Preprint No. 6-99, Institute of Theoretical and Applied Mechanics SB RAS, 1999.

5. Krogmann, P.: An Experimental Study of Boundary Layer Transition on a Slender Cone at Ma = 5, AGARD CP No. 224, Symposium on Laminar Turbulent Transition, 1977. P.22.1-26.12

6. Wendt, V., Kreplin, H.P., Höhler, G., Grosche, F.R., Krogmann, P. and Simen, M.: Planar and Conical Boundary Layer Stability Experiments at Mach 5, AIAA 93-5112, AIAA/DGLR 5th International Aerospace Planes and Hypersonic Conference München.

7. Weise, A. and Schwarz, G.: The Shock Wind Tunnel of IAG at University Stuttgart. ZfW 21. 1973, Heft 4, P. 121-131 (in German)

8. Knauss, H., Riedel, R., Wagner, S.: The Shock Wind Tunnel of Stuttgart University, a Facility for Testing Hypersonic Vehicles, AIAA Paper 99-4959, AIAA Conference Norfolk, Nov. 1-4, 1999.

9. Stainback, P.C., Wagner, R.D.: A Comparison of Disturbance Levels measured in Hypersonic Tunnels using a Hot-Wire Anemometer and a Pitot Pressure Probe, AIAA Paper No. 72-1003, 7th Aerodynamic Testing Conference, Palo Alto, CA, September 1972.

10. Chen, F.J., Beckwith, I.E., Creel, T.R. jr.: Correlation of Supersonic Boundary Layer Transition on Cones Including Effects of Large Axial Variations in Wind Tunnel Noise, NASA TP 2229, 1984.

11. Gossweiler, C.H.: Sonden und Meßsystem für schnelle aerodynamische Strömungsmessung mit piezo-resistiven Druckgebern, Diss. ETH Zürich Nr. 10252, Zürich, 1993 [15].

12. Kosinov, A., Gaisbauer, U., Knauss, H., Wagner, S.: Comparison of Hot Wire- and Hot Film Measurements in Supersonic Flow, Using Constant Temperature Anemometer. In preparation

13. Schneider, S.P., Munro, S.E.: Effect of Heating on Quiet Flow in a Mach 4 Ludwieg Tube, AIAA Journal, Technical Note. 1998, Vol. 36, No. 5.

14. Walker, D.A., Ng, W.F. and Walker, M.D.: Experimental Comparison of Two Hot Wire Techniques in Supersonic Flows, AIAA Journal, 1989. Vol. 27, No. 8, August.

15. Owen, F.K., Horstman, C.C. and Kussoy, M.I.: Mean and fluctuating Flow Measurements of a fully developed, non adiabatic hypersonic boundary layer J.F.M. 1975, 70, P. 393-413

16. Bestion, D., Gaviglio, J. and Bonnet, J.P.: Comparison between constant current and constant temperature hot-wire anemometers in high-speed flows, Rev. Sci. Instrum. 1983, 54 (11) November.

17. Smits, A.J., Hayakawa, K., Muck, K.C.: Constant Temperature Anemometer Practice in Supersonic Flow, Part I: The Normal Wire; Experiments in Fluids I, 1983, P 83-92.

18. Kosinov, A.D.: Private Communication, Febr. 2000.

19. Hall, R.M., Obara, C.J., Azzay, M.: Comparison of Boundary Layer Transition Measurement Techniques at Supersonic Mach Numbers, AIAA Journal, 1991, Vol. 29, N° 8, P. 685-691

20. Johnson, C.B., Carraway, D.L.: A transition detection study at Mach 1.5, 2.0 and 2.5 using a micro-thin hot-film system. ICIASF '89 Record, Proc. Int. Congr. on Instrumentation in Aerospace Simulation Facilities, P. 82-94.

21. Nitsche, W., Suttan, J., Haselbach, F. and Sturzebecher, D.: Surface Forces Measurements with High Spatial and Temporal Resolution by Means of Liquid Crystal Foils, Piezofoils and Surface Hot-Film Arrays, preprint of RTO/AGARD FDP-Meeting, Sept. 22-25, Seattle, USA, 1997.

22. Kornberger, M.: Multisensorheißfilmtechnik zur Transitionserkennung im Windkanal- und im Flugversuch, D82 (Dissertation RWTH Aachen) Verlag Shaker Aachen, 1992.

23. Qian, S., Chen, D.: Joint Time Frequency Analysis, Prentice Hall PTR, Upper Saddle River, N.J. 07458, ISBN 0-13-254384-2.

24. Renk, K.F., Betz, J., Zeuner, S., Lengfellner, H. and Prettl, W.: Thermopile effect due to laser radiation heating in films of high-Tc materials, Institut für Angewandte Physik, Universität Regensburg (Germany); Physica C235-240 (1994), P. 33-40 (North Holland).

25. Fortech HTS GmbH: Sensortechnologie und Hochtemperatur-Supraleiter, Zum Alten Schloß 1, D-93170 Bernhardswald, Germany

26. Moen, M.J. and Schneider, S.P.: The Effect of Sensor Size on the Performance of Flush Mounted Hot-Film Sensors, Journal of Fluids Engineering, June 1994, Vol. 116.

27. COSYTEC: cosytec Ingenieurbüro Elektronikentwicklung, Am Ahornrain 9, 73447 Oberkochen, Germany

THE FLOW IN A WAKE OF A LONGITUDINAL ELECTRIC DISCHARGE

A.F. Garanin, P.K. Tretyakov, A.V. Tupikin

Institute of Theoretical and Applied Mechanics SB RAS
630090, Novosibirsk, Russia

Nowadays a great interest is arisen to the study of gasdynamics of flow with local inhomogeneities created by various means of energy transformation from the outer sources to find the effective control of flying vehicles aerogasdynamic characteristics [1, 2].

One of the ways to effect using the outer energy supply is to create weak ionization. The important investigations of this problem were performed by the researchers of Ioffe Physical-technical institute, St.-Petersburg (G.I. Mishin, A.P. Bedin, A.I. Klimov et al). The analysis of the experimental results showed a complexity of the separation of heat supply and ionization effects. The interpretation of the anomalies observed in the experiment is interpreted by the scientists of this school in a different way [3, 4].

In the presented paper an attempt was made to avoid the effect of the flow heat at electric discharge formation.

The experiments were performed in the wind tunnel TS of ITAM SB RAS (Fig. 1). The outer flow velocity M = 4, static pressure P_{ST} = 9.4 kPa, stagnation temperature T = 300 K, test section dimensions 200 × 200 mm^2 (*3*).
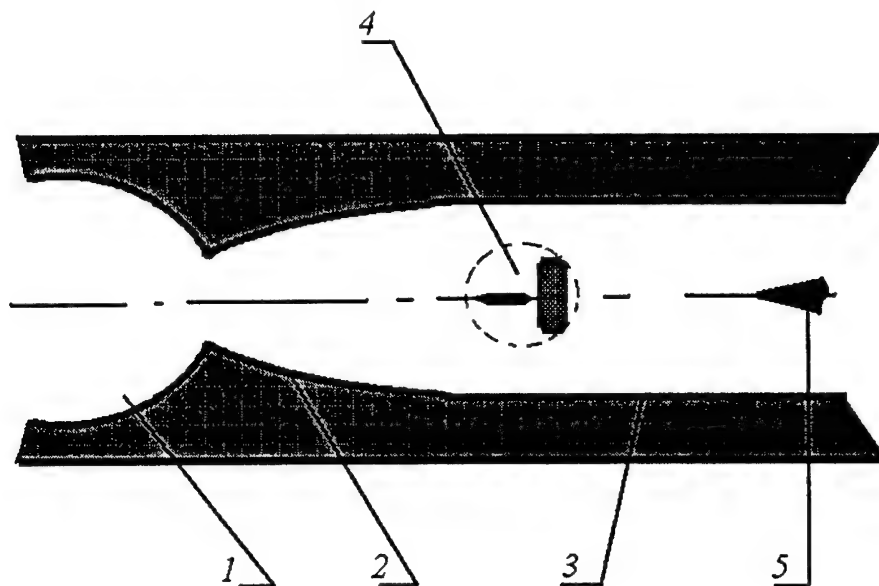

Fig. 1. Experimental setup.
1 – plenum chamber; *2* – nozzle; *3* – test section; *4* – electric scheme; *5* – model.

The following elements of the electric scheme were mounted in the wind tunnel test section (*4*): anode in the form of a spike d_A = 5 mm, l_A = 5 sm; cathode in the form of a ring (the

inner one with the diameter d_k = 14 mm, the outer $D_k = D$ = 16 mm, the distance between them is l = 8 mm).

Downstream the flow at a distance $L \approx$ 20 sm the body was located (5 cone-cylinder d_B = 6 mm, round angle α = 35°).

A steady combustion regime was reached at intensity U = 6 kW and current I = 300 mA in which a long lighting trace (wake) was observed (Fig. 2, a). The attempt was made to extend the domain of the steady combustion regime parameters by introducing argon in the discharge zone. It led to the intensity growth range but the wake length decreased till 25 mm (Fig. 2, b). The flow stagnation temperature was measured in the wake behind discharge. The temperature appeared to be leveled off at a distance about 25 mm till its value in the outer flow and further it is constant in the flow cross-sections.
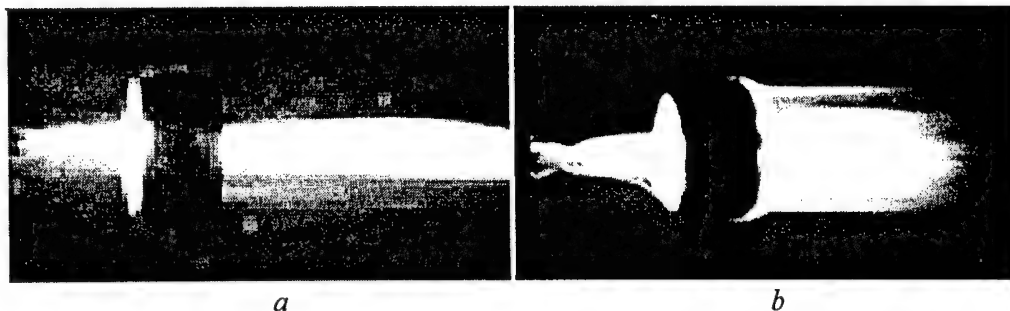

a b

Fig. 2. Electric discharge in a supersonic flow.
a – in air; b – in air with argon.

Gas after passing through a discharge zone (i.e. the wake) flew around the model. The change of the angle of the reattached shock wave on the cone was observed on the obtained Schlieren pictures (Fig. 3, a – without discharge, 3, b – with discharge). The calculation shows that the velocities M = 3.5 and M = 2.7 correspond to these angles at gas flowing around the cone.

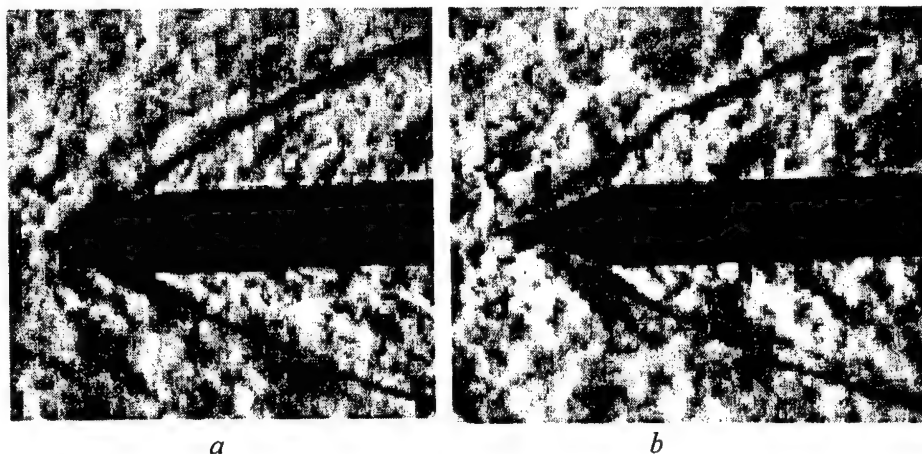a b

Fig. 3. Supersonic flow around cone-cylinder (α = 35°).
a – without discharge; b – with electric discharge.

69

The measurements of the total pressure field in the cross-section corresponding to the model location in the flow is shown in Fig. 4, *a* and Fig. 4, *b* shows the Mach number in the same cross-section (the dashed line and dots correspond to the flow with a discharge, the solid
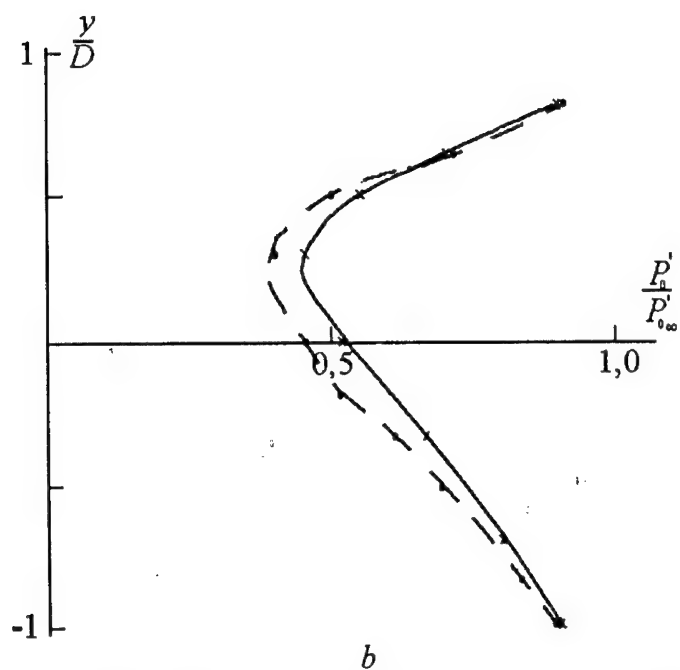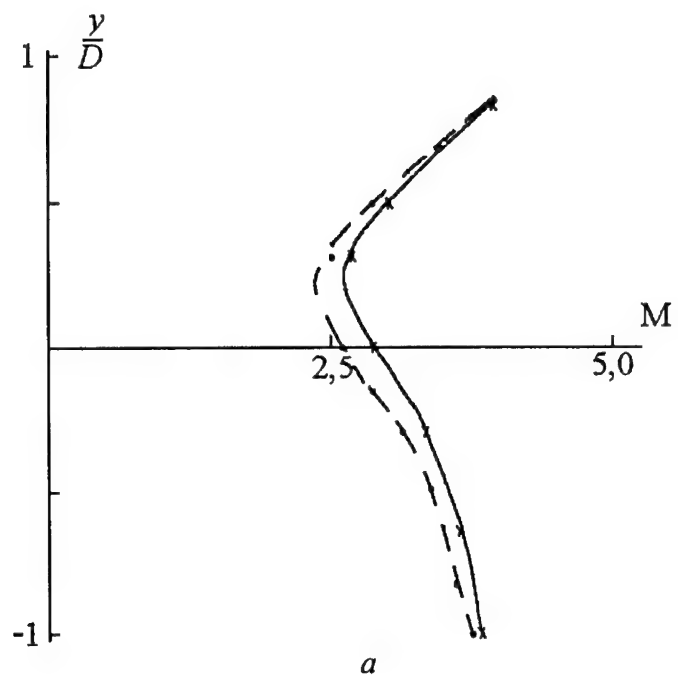

Fig. 4. Total pressure distribution (*a*) and the Mach numbers (*b*) at cross-section $x = 20$ sm

line and crosses to the flow without discharge). One can see in the diagram that the Mach number variation maximum is in the region of the body diameter order of magnitude. Therefore, the angles registered on the photographs correspond to some mean values and do not give information about the Mach number variation near the model tip. As follows from the information presented the difference of the model flow around with a discharge is caused by the total pressure profile change in the wake. The contribution of ionization to the change of the flow around structure is not noticeable at the background of the effect mentioned above.

In the end it should be noted that to make an objective conclusion about the weak ionization effect on the flow around it is necessary to perform a condition of a dynamic similarity (the Euler criterion constancy in the place of the model location: pressure fields should be equal at the constant flow initial parameters.

REFERENCES

1. 2-nd Weak Ionized Gases Workshop: Proc. April 27-30, 1998, Norfolk, Virginia, USA. – Reston: AIAA, 1998. – 268 p.
2. Perspectives of MHD and Plasma Technologies in Aerospace Applications: Proc. March 24-25, 1999, Moscow, Russia. – Moscow: IVTAN, 1999. – 168 p.
3. Mishin G.I. Equation of weak-ionized gas-discharged plasma // Pis'ma v ZhTF. – 1997. – Vol. 23, Iss. 14. – P. 81 – 88 (in Russian) .
4. Bedin A.P. On the features of the low temperature gas-discharged plasma // Ibid. – Iss. 16. – P. 88 – 93 (in Russian) .

CORPORATIVE INFORMATION SYSTEM *
OF SCIENTIFIC RESEARCH

V. M. Gilyov, V. V. Bublik, V. F. Kurmell, O. N. Mosseichuk, and S. G. Ocheretny

Institute of Theoretical and Applied Mechanics SD RAS,
630090, Novosibirsk, Russia

In aerophysical studies, much attention is being given to computerized technologies. For example, in the automated system for scientific research developed at the Institute of Theoretical and Applied Mechanics in early 80ths [1,2], computer facilities were widely used in both experimental and computational studies.

Recently, due to the all–round change–over to personal computers and further development of local computer networks and the Internet concept, both the architecture of information systems and their potentialities have been grossly changed.

This report describes the information system for scientific research of ITAM SD RAS intended for further improvement of the effectiveness of experimental and computational studies in the field of aerophysics. The system under consideration leans upon the following hardware/software components:

- the Institute's computer network;
- a computer class;
- a high–performance shared computer server;
- parallel calculations;
- local complexes for computer–aided experimental studies;
- a shared–access database.

The computers of individual users can operate on different operating platforms: UNIX, WINDOWS, or DOS. They are provided with an access to the computer network in accordance with their prescribed authority.

Network technologies

Much attention in the information system of research studies of the Institute is given to modern network facilities. The computer network of the Institute is a developed network architecture designed in close analogy to Ethernet. All computers hooked up to the network are united in an integrated information space with free access to Internet. Up to date, more than a hundred computers allocated immediately at the working places of users are included into the computer network.

To the computer network, abonents are connected, which are located in three main blocks of the Institute. In addition, a number of departments have their local networks that are connected to the integrated computer network of ITAM. As the protocols, TCP/IP, IPX/SPX

ones and some others are used, which allows simultaneous work of several users that employ a great variety of software products without interfering with each other.
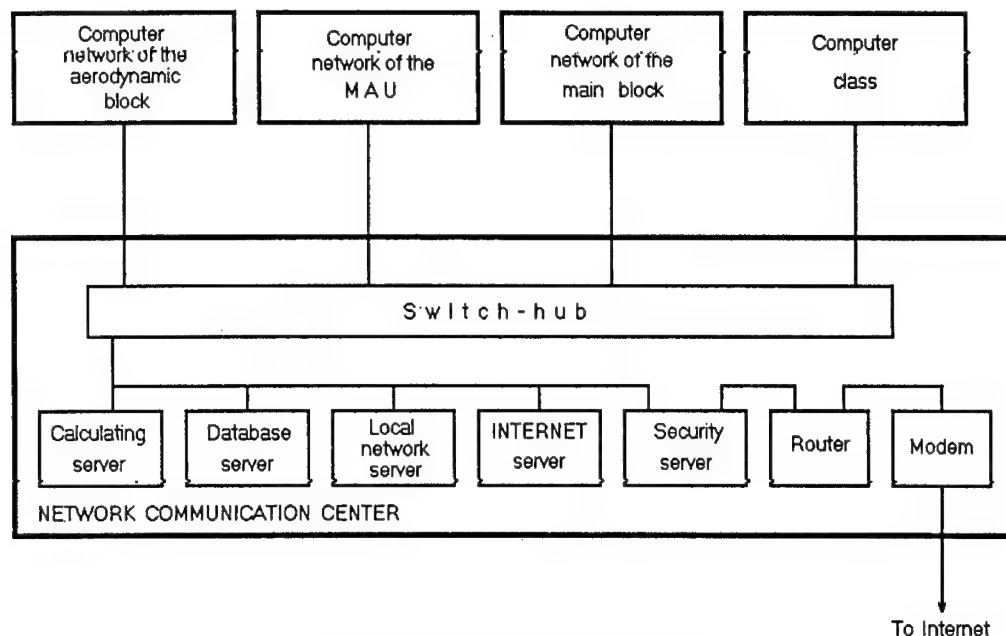

Fig. 1. Topology of the computer network.

For segmentation of the network, the hooking up of net abonents situated in different blocks is organized through a switch-hub system. In the same manner, also a number of local departmental networks are connected to the main one, as well as rather large groups of users sharing a common territory. The use of the above hardware facilities permits dividing the Institute's network into eight independent segments, which prevents penetration of network packages intended for a given segments into other parts of the system. This structure substantially improves the performance and raises reliability of the network.

The network communication center is the central component of the system, by means of which telecommunications and network control are organized. In the center, specialized network servers are located, each performing its definite functions:

– an Internet server providing an access to the Internet network; it functions also as mail, FTP- and WWW-servers; with the help of this server, a search for desired information in the Internet and an access to remote high-performance computers located in various scientific centers of Russia and other countries are possible; on the remote computers, numerical studies and searching for various information of interest in databases are being performed;

– a local-network server intended for exerting control over the Institute's local network; this server is also used as a file–server of the network;

– a database server, in which both experimental and computational results are stored; here, these results can be compared with one another; also, comparison between results of different authors is possible; the database is based on the client–server technology, it consists of

73

the database as it is and various facilities that provide an access to the database, an SQL–server being the core of the system;

— a calculating server based on a high–performance RISC–processor ALPHA operating at a 533 MHz frequency; the server is available for all users and intended for solving computation–intensive problems;

— a security server intended for the protection of the computer network against unauthorized access from Internet;

— a router providing an access for an individual user of the Institute's computer network to Internet, the data communication being ensured by a modem connected immediately to a prescribed Internet channel.

The use of network technologies, while performing aerophysical studies, offers a great variety of opportunities for all abonents of the Institute's computer network.

An individual user of the local network is provided with the following scope of opportunities:

— storage of user's data on the local–network server, as well as of various software products being used, in particular, for installing user programs on individual computers;

— storage of numerical data gained in the course of aerophysical and modeling studies on the database server;

— performing computation–intensive numerical studies in the field of mechanics on the calculating server.

The following opportunities are available when working in Internet:

— receipt/sending of e–mail correspondence;

— searching for information of interest on various WWW– and FTP–servers available through Internet;

— data exchange with foreign partners;

— computations on high–performance remote computers located both in Russia and abroad;

— work with remote databases.

Computer class

The computer class is a constituting component of the ITAM's network infrastructure. Staff–members of the Institute, as well as students and post–graduate students of higher educational institutions taking their training or doing their research work at the Institute, are the users of the class.

The class is equipped with present–day computer facilities. At the present time, as the computer terminals, six personal computers of the Pentium type are used. In the nearest future, their number is expected to be increased. Figure 2 shows the structural scheme of the computer class.

The computers are connected together by means of Ethernet, and they share a common disk operating system, the loading being executable also through the network. In the class, a multi–platform support of all computers is provided, which ensures the possibility to run each computer under Linux or Windows. The latter can be made possible by proper adjusting of the hardware/software facilities of the server and individual computers. On a computer being used as the server, the operating system Linux is installed. A Samba server permits authorization of works and communication between the server and satellite stations working under Windows.
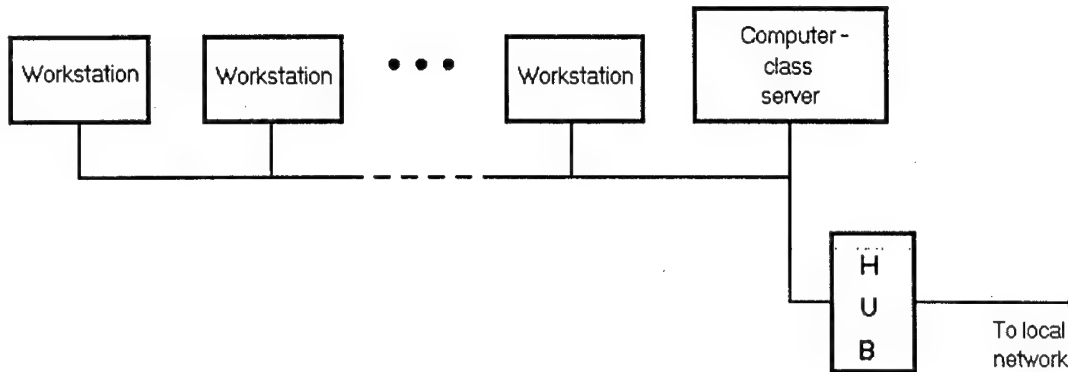
Fig. 2. Structural scheme of the computer class.

Parallel technologies

In the Institute, much attention is given to further development of modern methods of numerical research. The successive accomplishment of computational studies requires considerable computational power. In many cases, the time required for solving a problem of interest run into tens or hundreds hours of the machine time. It is a wide–spread opinion that further progress in numerical modelling can be achieved by introducing various parallel algorithms, i. e., by developing parallel technologies [4].

At present, the following approach is widely employed in the Institute: as computing elements of a parallel machine, standard computers are used, in particular those of the terminal class. With special software installed, these computers, being integrated in a computing cluster by a rapid–operating network, in fact constitute a parallel multi–processor computer with a distributed memory. The MPI communication medium widely accepted in modern parallel supercomputers is a means chosen for designing parallel algorithms. This computer complex allows developing computational methods and technologies of top quality.

Implementation of computers in the experiment

The experimental information provided by modern experimental facilities, often complex and expensive, cannot be processed in an outdated fashion because of its great amount and high rapidity of processes under study. This is why almost all the experimental setups of the Institute are equipped with computers. The all–round automation of the experiment cuts the time required for performing studies as well as labour consumption.

The CAMAC standard has gained widest utility in the Institute for inputting experimental data into a computer [2]. The CAMAC modules can be connected immediately to a personal computer located in the immediate vicinity of the experimental setup equipped with transducers. Figure 3 shows the structural scheme of a typical measuring system. The signals generated by transducers income to a normalizer's channels, each having its own gain factor.

This module normalizes all input signals to a certain standard level. The output signal of the normalizer, through a commutator, is transferred to a digitizer, where it is measured and the resultant digital code is further passed to a computer.
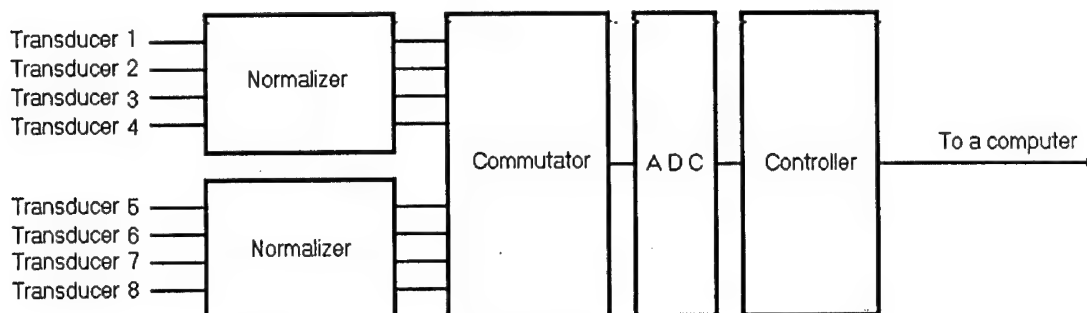

Fig. 3. Structural scheme of a typical measuring system

Another example of the successive use of computer technologies is a number of automated data acquisition/processing systems designed at the Institute and intended for panoramic visualisation of flow patterns and temperature fields with the help of liquid–crystal coatings. Such systems, for example, permit the researcher to obtain data on fields of displacements and velocities of individual particles in two–phase supersonic flows [5]. Without computers, such experiments would be impossible.

Databases for experimental and numerical results

To ensure a long–term storage of experimental and numerical data, as well as their easy comparison, works are under way at the Institute aimed at development of various databases. In the Institute, a great body of information obtained in aerophysical and computational studies is accumulated. The effective use of these data is possible only by employment of present–day data storage facilities and those facilities that ensure data exchange both all over the Institute and with foreign partners.

The database of ITAM is built according to the client–server technology. It consists of the database as it is and various means permitting a remote access to it [6]. An SQL–server is the core of the system. The users work with the database via the computer network using special software facilities. These facilities provide to the user a convenient graphic interface and highly developed visualisation means. The users can input information into the database, modify it, scroll/list its segments search for those of them which satisfy specified conditions, etc. The software products function on different operating platforms (UNIX or Windows). The database can be replenished with the results of new experimental and computational studies aimed at solving various problems related to designing new super– and hypersonic flying vehicles.

Conclusions

In conclusion, the use of modern software/hardware facilities permits drastic improvement in the research methodology, both in the field of experimental and computational studies. This allow the researchers to raise their activity onto a higher level.

REFERENCES

1. Vyshenkov Yu. I., Dulov V. G., Ivanov M. S., Kharitonov A. M. Current tendencies in aerodynamic studies and their realization at ITAM // Methods of Aerophysical Research: Proc. of the IV All–Union School on the Methods of Aerophysical Research. – Novosibirsk: ITAM, SD of the USSR Acad. Sci., 1987. – P. 3–24.
2. Vyshenkov Yu. I., Gilyov V. M., Tikhomirova T. P. Software for accumulation and storage of experimental data. – Novosibirsk, 1990. –24 p. –(Preprint/Acad. Sci. of the USSR, Siberian Division, ITAM; No. 3–90).
3. Gilyov V.M., Kurmell V.F., Mosseichuk O.N., Ocheretny S.G. The use of network technologies in aerophysical research at ITAM SB RAS // Proc. of 9 International Conference on the Methods of Aerophysical Research, Novosibirsk, 29 June – 3 July, 1998. – Novosibirsk, 1998. – Pt. III. P. 125–129.
4. Ivanov M., Markelov G., Taylor S., Watts J. Parallel DSMC strategies for 3D computations. Proc. Parallel CFD'96 / Eds P.Schiano et al. – Amsterdam: North Holland, 1997. P. 485–492.
5. Boiko V.M., Gilyov V.M., Ocheretny S.G., Poplavsky S.V. Software complex for velocity field measurement on the basis of multiframe shadow pictures of two–phase flow // Proc. of 9 International Conference on the Methods of Aerophysical Research, Novosibirsk, 29 June – 3 July, 1998. – Novosibirsk, 1998. – Pt. III. P. 78–83.
6. Mosseichuk O.N. The development of a database of aerodynamic experiments and computations performed at ITAM // Proc. of 9 International Conference on the Methods of Aerophysical Research, Novosibirsk, 29 June – 3 July, 1998. –Novosibirsk, 1998. – Pt. III. P. 193–199.

INFLUENCE OF FAVORABLE PRESSURE GRADIENT ON 3D VIBRATIONAL RECEPTIVITY OF BOUNDARY LAYER

A.V. Ivanov[1], Y.S. Kachanov[1], S. Bake[2], K. Neemann[2]
1) Institute of Theoretical and Applied Mechanics SB RAS, Novosibirsk, Russia
2) Hermann-Föttinger Institut, Berlin Technical University, Berlin, Germany

1. Introduction

This work is devoted to generation of the Tollmien-Schlichting (TS) waves by means of unsteady surface non-uniformities. The problem of excitation of the 3D TS-waves in 2D boundary layers by surface vibrations has not been studied experimentally until [1]. There are also a very restricted number of theoretical studies of this problem (see e.g. [2-5]). A comparison of the experimental and the theoretical results on the receptivity was performed in [6]. A very good *qualitative* agreement was found, including the growth of the receptivity with the frequency of surface vibrations and a higher receptivity of the Blasius boundary layer to 3D perturbations as compared to 2D ones. A *quantitative* comparison has shown that the experiment yields somewhat different estimations of the receptivity amplitudes, which are about 30% lower than the theoretical ones.

The present combined experimental and theoretical study was performed in order to extend a knowledge on the vibrational receptivity of boundary layers. The goal of the first part of the present paper is to obtain a quantitative information on the linear receptivity characteristics of a 2D non-gradient boundary layer at excitation of 3D TS waves with different spanwise wavenumbers and frequencies by means of localized wall vibrations. The 2D Blasius boundary layer develops on a cylinder wall with a rather weak spanwise curvature. It is assumed that the weak wall curvature does not influence the receptivity process. This assumption supposed to be checked by a direct comparison of the experimental and theoretical results.

The second part of the study is devoted to the same receptivity mechanism, but in a flow with a streamwise favorable pressure gradient (FPG). The influence of a pressure gradient on the receptivity coefficients is very poorly investigated at present. There is the only the experimental work [7] where a significant reduction of the vibration receptivity amplitudes was found in an adverse pressure gradient case. Qualitatively this result is in agreement with calculations performed for 2D modes in [4] and for 3D modes in [5]. The aim of the second part of the present investigation is to obtain an experimental information about the vibrational receptivity coefficients in presence of a favorable pressure gradient and to perform a quantitative comparison of the experimental results with receptivity calculations.

2. Experimental Setup

The experiments were conducted in the Laminar Wind Tunnel of the Hermann-Föttinger-Institute of Berlin Technical University. It is a closed-circuit tunnel with an axisymmetric test section with an inner diameter of 441 mm. This wind tunnel has a nozzle contraction-ratio 18:1 over a length of 2 m and the boundary layer of the nozzle is blown out. The wind tunnel has a main radial fan and an additional blower to supply inside the pressure for blowing boundary layer out the nozzle. The free-stream turbulence level was below $Tu = 0.05\%$ in the frequency range between 0.1 and 1000 Hz at the flow conditions of the present experiment.

The boundary layer under investigation starts at the elliptic leading edge of the test section and develops downstream on its inner wall (Fig.1). Sources of disturbances mounted on the two revolving metal rings. The axisymmetric shape of the test section provides spanwise uniformity of the flow under investigation.
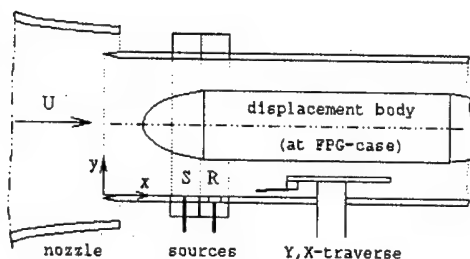
Fig.1. Experimental setup.

In the present experiments two kinds of disturbance sources were used. The main source (R-source) was a surface vibrator [8] with a circular rubber membrane (of 6 mm in diameter) mounted flush with the wall at a spanwise position $z = 0$ mm and a streamwise position $x = x_r = 644$ mm. The shape of the membrane oscillations was measured by means of a laser vibrometer.

The wavenumber spectrum of the vibrations was obtained with the help of 2D spatial Fourier transform. The amplitude of vibrations in the membrane center kept fixed in each regime of measurements. The corresponding values are presented below in Tables 1 and 2.

The second disturbance source (S-source) was a point source positioned at streamwise coordinate $x = x_s = 547$ mm. It was used for determining the downstream disturbance behaviour including the vicinity of the R-source (see [8] for more detail). By means of plastic pipes the two sources were connected to loudspeakers fed by harmonic signals produced by a computer, D/A-converters, and power amplifiers.

3. Mean Flow Characteristics and Regimes of Measurements

3.1. Blasius flow case. Because of a constant diameter of the wind-tunnel test-section the downstream growth of the boundary layer thickness provides a very weak flow acceleration. Nevertheless, the mean flow in this case was very close to the theoretical Blasius flow. Indeed, the shape factor H_{12}, determined from the measured profiles, was equal 2.58 that is very close to Blasius value ($H_{12} = 2.59$). Hence the boundary layer under investigation can be considered as the Blasius one. The Reynolds number and other experimental parameters are shown in Table 1. The displacement thickness, the flow velocity, and the Reynolds number are determined at the position of the vibrator. The studied dimensional frequencies of vibrations and the corresponding frequency parameters are also shown in Table 1. Dimensional amplitudes of vibration h_r were measured in the center of the R-source.

Table 1

U_{0r}, m/s	δ_{1r}, mm	Re	f, Hz	$F \cdot 10^6$	h_r, mm
7.5	1.91	946	37.75	64.2	0.057
7.5	.1.91	946	55.75	94.9	0.072
7.5	1.91	946	75.00	127.6	0.091

3.2. FPG flow case. In order to provide a moderate favorable pressure gradient that corresponds to Hartree parameter $\beta_H = 0.1$ an axisymmetric displacement body was mounted on the test-section axis. The mean-velocity profiles were shown to be in a good qualitative agreement with the corresponding theoretical Falkner-Skan profile. Due to a growth of the background disturbance level observed in the wind-tunnel at higher free-stream speeds, it was difficult to provide in the FPG-experiments the same value of the Reynolds number as that used in the Blasius case. Therefore, in the FPG-case the Reynolds number was somewhat lower (see Table 2). The boundary layer and frequency parameters for the experiments at pressure gradient are also shown in Table 2. The dimensional frequencies of disturbances were changed to provide the same frequency parameters $F = 2\pi f v / U_o^2$ for the both types of the flow.

Table 2

U_{0r} , m/s	δ_{1r} , mm	Re	f , Hz	$F \cdot 10^6$	h_r , mm
12.4	0.87	698	103.1	65.1	0.056
12.4	0.87	698	152.5	97.8	0.041
12.4	0.87	698	205.0	130.7	0.033

4. Method of Calculations

The boundary value problem for the disturbance produced by the vibrating membrane is solved in the framework of the classical hydrodynamic stability theory. The incompressible Navier-Stokes equations are linearized around a basic flow described by a solution of the Falkner-Skan equation of boundary layer theory. The slow streamwise variation of the basic flow and the small velocity component normal to the wall are neglected in the spirit of the parallel flow assumption.

The disturbance input is represented by an inhomogeneous boundary condition at the wall, which reads after linearization at the position $y = 0$:

$$u = -DU(0)h(x,z)\exp(-i\omega t) , \qquad v = -i\omega h(x,z)\exp(-i\omega t) , \qquad w = 0,$$

with $h(x,z)$ describing the shape of the vibrating membrane and $DU(0) = dU/dy|_{y=0}$.

The time dependence of the disturbance motion is assumed to be imposed by the vibrating membrane, i.e. in pure harmonical form exp(-$i\omega t$). After applying a Fourier transform with respect to the streamwise and spanwise coordinates x and z respectively, the problem is reduced to a three-dimensional Orr-Sommerfeld equation with inhomogeneous boundary conditions at the wall.

When performing the inverse Fourier transform, the travelling wave or Tollmien-Schlichting part of the solution can be extracted by means of the residue theorem, yielding for a single mode of spanwise wave number β:

$$u_{TS}(x,y,z,t) = \underbrace{\tilde{h}(\alpha_{TS},\beta)}_{(a)}\underbrace{\frac{\omega - i\Delta(0)DU(0)}{\left.\dfrac{\partial \tilde{v}_e(\alpha,y=0,\beta,\omega)}{\partial \alpha}\right|_{\alpha=\alpha_{TS}}}\tilde{u}_e(\alpha_{TS},y,\beta,\omega)}_{(b)}\underbrace{\exp\left(i(\alpha_{TS}(x-x_s)+\beta z - \omega t)\right)}_{(c)} .$$

Similar expressions can be obtained for v_{TS} , w_{TS} and p_{TS} ,. α_{TS} is the Tollmien-Schlichting eigenvalue for given frequency ω and spanwise wavenumber β; $\tilde{u}_e$ and $\tilde{v}_e$ are the corresponding eigenfunctions. The denominator $\partial \tilde{v}_e(\alpha,y=0,\beta,\omega)/\partial\alpha|_{\alpha=\alpha_{TS}}$ in the second term (b) is a consequence of the residue theorem, and the numerator $\omega - i\Delta(0)DU(0)$ results from the inhomogeneous boundary conditions at the wall. For more details see [2-5] and the references cited therein. The second term (b) in the equation couples the Fourier spectrum of the membrane (a) with the wave term (c) and is defined as the receptivity coefficient

$$G(\beta,\omega,y) = \frac{\omega - i\Delta(0)DU(0)}{\left.\dfrac{\partial \tilde{v}_e(\alpha,y=0,\beta,\omega)}{\partial \alpha}\right|_{\alpha=\alpha_{TS}}}\tilde{u}_e(\alpha_{TS},y,\beta,\omega).$$

The receptivity coefficient G is independent of the amplitude and the shape of the vibrating membrane. It can be interpreted as complex initial amplitude, normalized by the input spectrum

$\tilde{h}(\alpha_{TS},\beta)$, of the T-S wave at the source position $x = x_r$, or as a transfer function between the external disturbances and the wave motion downstream of the source. G still depends on the wall distance y, but is conveniently evaluated at a position near the maximum of $|\tilde{u}_e|$.

5. Measurement Technique and Results of Measurements

All measurements in the flow were conducted with a constant-temperature hot-wire anemometer. Spanwise scans of the amplitude and the phase of the excited frequency were measured in boundary layer at six x-positions downstream the operating R-source. The probe distance to the wall for these measurements was carefully chosen in order to correspond to maximum amplitudes of fluctuations in the boundary layer. The closest x-position to the R-source at the receptivity measurements was $x - x_r = 50$ mm for Blasius-case and $x - x_r = 36$ mm for the FPG-case to ensure that the near field (consisting of continuos-spectrum modes and bounded fluctuations) has decayed. After these measurements, according to the procedure described in [8], the R-source was switched of and the upstream S-source turned on. The measurements with S-source were performed at the same flow conditions and in the same downstream positions but they included an additional spanwise scan at the position of the R-source (x=644 mm). The results of these measurements contained information about the boundary layer stability in an extended spatial region and were used for evaluation of initial amplitudes and phases of the instability modes generated by the surface vibrations.

In order to obtain information about the normal instability modes, the wave trains generated in the flow were subjected to spanwise Fourier decomposition. An example of the spanwise wavenumber spectra is presented in Fig. 2 for the FPG-case, R-source, and one of frequencies studied ($f = 152,5$Hz). The corresponding spectra for the S-source are shown in Fig. 3. (only amplitude parts are shown). For the R-source the spectral amplitudes are normalised by the membrane vibration amplitude h_r. The downstream behaviour of the normal mode amplitudes, that was obtained from spectra like those presented in Figs. 2 and 3 for every fixed value of the non-dimensional spanwise wavenumber, is illustrated in Fig. 4. The open symbols represent the spectral amplitudes of a single instability mode ($\beta\delta_{1r} = 0,138$, as an example) generated by the R-source. The closed symbols represent the amplification curve for the same mode but obtained from the S-source measurements and multiplied by a certain factor in order to match the two amplification
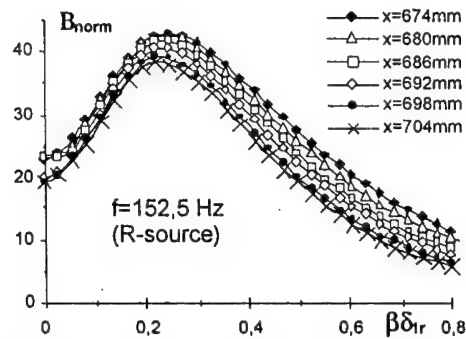

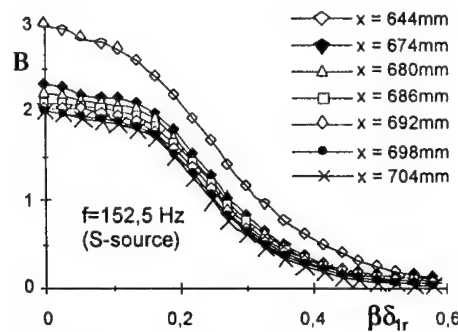Fig. 2. Wavenumber spectrum of disturbances generated by the R-source.

Fig. 3. Wavenumber spectrum of disturbances generated by the S-source.

81

curves. The closed symbol at x-x_r = 0 gives the initial amplitude of the given normal mode. Similar procedure performed for the phase parts of the spectra gave us information about the initial phases of the instability modes generated by vibrations. (For more detail see [8].)
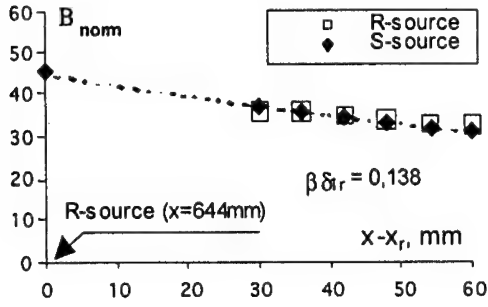

Fig. 4. Method of initial amplitudes determination.

In the Blasius case a similar technique was used for evaluation of the initial wave amplitudes with the only difference that the theoretical amplification curves were used instead of the experimental ones obtained in the FPG case with the help of the S-source.

After determination of the initial spectra of the generated waves, the receptivity coefficients were determined according to the procedure used in previous studies, namely, as a ratio of the initial spectrum of the TS-waves and the 'resonant' spectrum of the surface vibrations (determined for wavenumbers of the instability modes). For more detail see [6].

6. Receptivity Functions

The main results of the present study are presented in Figs. 5 and 6, where the complex receptivity coefficients for surface vibrations are shown for the Blasius boundary layer and the FPG boundary layer as functions of the spanwise wavenumber and frequency of vibrations. Figures (a) show the amplitude parts of the receptivity functions, while figures (b) – the phase parts. The general behaviour of the receptivity functions is in agreement with the previous theoretical and experimental investigations [1, 5]. However, in contrast to [6], a very good quantitative agreement
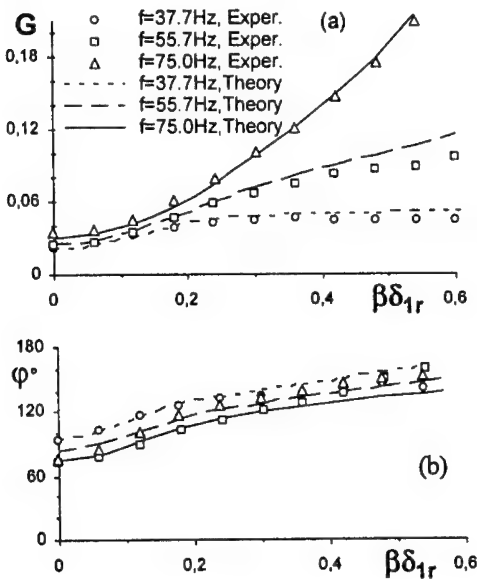

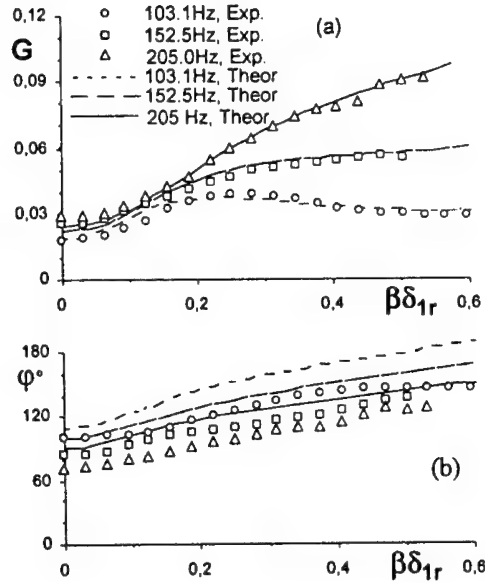Fig.5. Receptivity coefficients of the Blasius boundary layer.

Fig.6. Receptivity coefficients of the FPG boundary layer.

of theoretical and experimental results is observed. (The only significant difference, is about 25-degree shift in the receptivity phase for the FPG-case.) The good agreement observed between the experimental receptivity coefficients, obtained for a curved (cylindrical) wall, and the theoretical ones, calculated for the case of a flat plate, testifies that the present spanwise curvature of the wall does not influence the receptivity characteristics.

Calculations performed for the Blasius flow and the same value of the Reynolds number as that studied (both experimentally and theoretically) in the FPG-case have showed that the FPG leads to an increasing of the vibrational receptivity coefficients compared to the non-gradient case. Somewhat lower values of the receptivity coefficients obtained in the present experiments for the FPG-case compared to the Blasius case are explained by a lower value of the Reynolds number in the FPG-case.

References

1. Ivanov A.V., Kachanov Y.S., Obolentseva T.G. Experimental investigation of flat-plate boundary-layer receptivity to 3-D surface vibrations // EUROMECH colloquium 359. Collection of abstracts. Stuttgart, 1997, Abstract 5.
2. Michalke, A. Receptivity of axisymmetric boundary layers due to excitation by a Dirac point source at the wall // Eur. J. Mech. B/Fluids 14, 1995, p. 373–393.
3. Michalke, A., Neemann, K. . Excitation of instability waves in wall boundary layers with adverse pressure gradients by various types of Dirac sources // Acta Mech. 122, 1997, p. 33–48.
4. Michalke, A., Neemann, K. Excitation of 3D-disturbances in wall-bounded shear flow with adverse pressure gradient// Acta Mech. 124, – 1997, P. 219–224.
5. Neemann, K. Theoretische Untersuchungen zur Anregbarkeit instabiler Wellen in kompressiblen Wandgrenzschichten // PhD thesis, Technical University Berlin, Germany, 1999.
6. Ivanov A.V., Kachanov Y.S., Obolentseva T.G., Michalke A. Receptivity of the Blasius boundary layer to surface vibrations. Comparison of theory and experiment // International Conference on Methods of Aerophysical Research. Proceedings. Part I. Novosibirsk: Inst. Theor. & Appl. Mech., 1998, p. 93–98.
7. Kachanov Y.S., Koptsev D.B., Smorodsky B.V. 3D stability and receptivity of two-dimensional self-similar boundary layer with adverse pressure gradient // Laminar-Turbulent Transition. IUTAM Symposium, Sedona, AZ/USA; 1999./ H.Fasel & Saric, eds. Berlin Heidelberg: Springer, 2000. (accepted for publication.)
8. Bake S., Ivanov A.V., Kachanov Y.S., Fernholz H.H. A method of experimental study of vibrational receptivity of a boundary layer on a curved wall // International Conference on Methods of Aerophysical Research. Proceedings. Part I. Novosibirsk: Inst. Theor. & Appl. Mech., 1998, p. 17–22.

ON A UNIVERSAL NONLINEAR MECHANISM
OF TURBULENCE PRODUCTION IN WALL SHEAR FLOWS

Y.S. Kachanov

Institute of Theoretical and Applied Mechanics, 630090, Novosibirsk, Russia

The paper is devoted to the problem of nonlinear laminar-flow breakdown in wall bounded shear flows during their transition to the turbulent state. A brief review of some previously obtained results in this field is presented. The main attention is concentrated on a comparative analysis of the nonlinear phenomena and mechanisms observed in boundary layers, channels, and pipe flows.

1. Introduction

From the experimental viewpoint the transition in boundary-layer flows is investigated much better, at present, rather than the transition in other wall shear flows. At the same time, there is much evidence that some important nonlinear phenomena, associated with the laminar flow breakdown, are rather similar in different wall-bounded flows. In order to analyze this circumstance in more detail, first of all a description of some significant physical phenomena of the nonlinear flow breakdown is presented for the boundary-layer case in section 2. A conclusion is drawn that several nonlinear mechanisms are very universal in transitional boundary layers. These mechanisms are shown to be very weakly dependent on both the initial spectra of instability modes and the mean-flow characteristics.

At the next step of the analysis a comparison of the boundary layer case with the flat channel flow and circular pipe flow is performed in sections 3 and 4. From the linear-stability viewpoint these three flows are quite different. In particular, the pipe flow is absolutely stable in contrast to two other cases. However, some very important nonlinear phenomena can appear in a bypass way, i.e. without stages of linear development of the instability modes. This can be equally observed in both the boundary layers and Poiseuille flows. That is why, some nonlinear phenomena can be similar in all these (at least) flows. An evidence of this similarity is presented. One of these nonlinear mechanisms leads to formation of hairpin- (or Λ-, or horseshoe-) vortices, another one is responsible for generation of trains of Ω- (or ring-like) vortices and spikes. The physical nature of these phenomena is discussed. These mechanisms correspond, most probably, to strongly nonlinear stages of transition. A weakly nonlinear mechanism of the resonant interaction of instability modes seems to be also very universal. This mechanism can amplify a wide continuous spectrum of low-frequency quasi-subharmonic perturbations in boundary layers and flat channel flows (at least) and, in particular, lead to formation of hairpin- (or Λ-, or horseshoe-) vortices.

Finally, a close connection of the nonlinear transition phenomena with the structure of the developed wall turbulence is discussed in section 5. There are three important points in this discussion. First, the wall turbulence has very universal properties in different wall-bounded shear flows. Second, the structures of these developed turbulent flows is quite similar to the structure of the corresponding transitional flows at their late stages. Third, a notion that the developed wall turbulence is just a continuous laminar-turbulent transition seems to be very close to reality. If all three statements are true than all transition scenarios in all discussed flows must coincide with each other and lead to a certain universal scenario of the wall turbulence production that is inherent in the developed wall turbulent flows.

2. Structures in boundary-layer transition

2.1. General characteristic of nonlinear stages of transition. As was mentioned above, at present the late stages of transition are studied best of all in the case of the boundary layer flow. Excluding the bypass transition scenarios attributed to so-called streaky structures and the transient (non-modal) growth, there are two main scenarios of nonlinear stages of laminar-turbulent transition observed in 2D (flat-plate) boundary layers (see for review [1, 2] and also [3, 4]): the K-regime of transition and the N-regime (or the subharmonic one) of transition. These two types of transition are studied much better than others, especially experimentally. Weakly nonlinear mechanisms of wave interactions leading to initial stages of these two regimes are more or less clear at present (see [1, 2, 5, 6]), especially for the N-regime. These mechanisms are quite different and correspond to several kinds of resonant interactions of instability waves. They can be described alternatively in terms of either weakly-nonlinear theory [5] or Floquet theory [1]. However, these mechanisms explain only very initial stages of the two regimes of transition. Late stages are characterized by formation of coherent structures, their development, and interaction with each other and with the basic flow (see c.f. [4]). These stages display strong nonlinearity of the disturbed flow field and can be studied, at present, mainly in experiment or in DNS. There are also several very important results in this field obtained within the framework of asymptotic theories (analytical or semi-analytical ones) valid for asymptotically large Reynolds numbers (see c.f. [7]).

Despite a very significant difference of non-linear mechanisms at initial stages of the K- and N-regime, it was shown recently in [3] that the late stages of transition in these two scenarios are rather similar to each other. It was found, in particular, that in the two case the flow forms very similar coherent structures such as: Λ-structures, 3D Λ-shaped high-shear layer, and spikes associated with ring-like vortices. Successive stages of evolution of these and other structures leading to flow breakdown are briefly described below in sections 2.2 and 2.3.
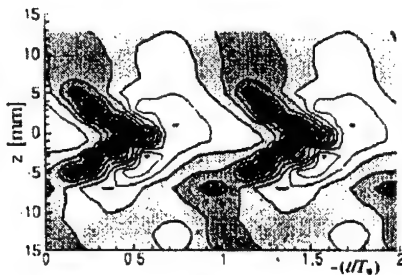

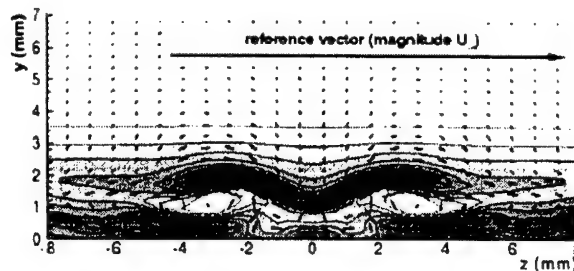*Fig. 1.* Λ-structures at 1-spike stage. Contours of ω_z. Experiment [4].

Fig. 2. Cross-section of Λ-vortex and HS-layer. DNS [4].

2.2. One-spike stage. This stage of transition development is very well studied in numerous experimental and DNS investigations. This stage is characterized by appearance of a developed Λ-structure shown in Fig. 1 (from experiment [4]) in a projection onto (z,t)-plane (where z is the spanwise coordinate) as contours of the instantaneous spanwise vorticity disturbance integrated in wall-normal direction. A cross-section of this structure is shown in Fig. 2 (taken from DNS results in [4]) together with the instantaneous velocity field visualizing the fluid rotation in the Λ-vortex legs positioned between two high-shear (HS) layers. One HS-layer is above the vortex, another one — below it. The Λ-structure is a very important element of the process of turbulence production.
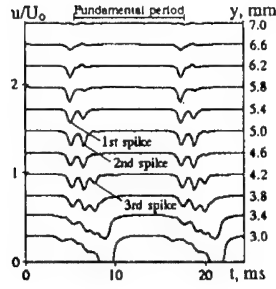
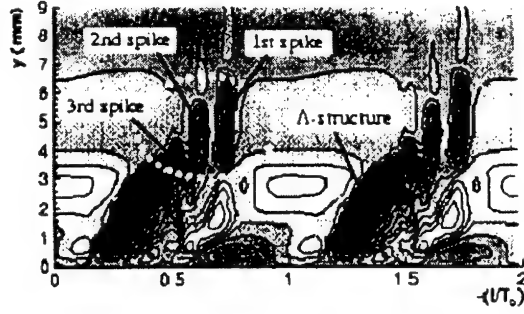Fig. 3. Time-traces at 3-spike stage. Contours of negative u-velocity disturbance.

Fig. 4. Spikes in instantaneous streamwise velocity field. Experiment [4], z=0.

At the 1-spike stage the first spike in the streamwise velocity time-traces appear near the Λ-structure tip under a kink in the 3D HS-layer near the plane of symmetry of the Λ-structure. The spikes represent a intensive low-velocity fluctuation localized both in time and space with a typical spatial scale close to the boundary layer displacement thickness. Its temporal scale is usually less than the period of the primary instability wave by an order of magnitude.

Note again, that all these phenomena are observed both in the K- and N-regime of the boundary layer transition in both experiment and DNS.
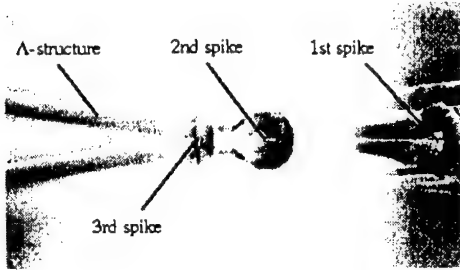

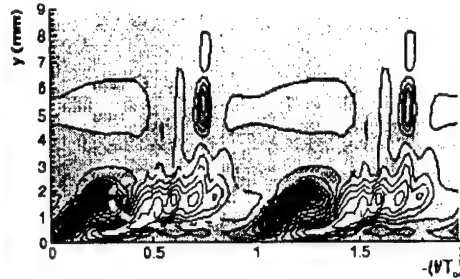Fig. 5. Λ-vortex and ring-like vortices at 3-spike. stage. λ-two criterion, DNS [9].

Fig. 6. Near-wall perturbations induced by ring-like vortices. Experiment [4], z=2 mm.

2.3. Three-spike stage and beginning of flow randomization. As it has been shown in classical experiments [8] as early as in 1962, further downstream the transitional flow generate the second, third, fourth, etc. spikes. The spikes observed at the '3-spike stage' are seen in time-traces shown in Fig. 3 from [4]. The spikes appear in the middle part of the boundary layer and move quickly away from the wall towards the external boundary-layer edge. In the picture of instantaneous streamwise velocity disturbance, observed at the peak position $z = 0$ (Fig. 4), the 1st and 2nd spikes look at this stage like isolated regions of low-speed fluid. The 3rd spike is still forming and positioning near the Λ-structure tip. The Λ-structure itself is visualized in Fig. 4 as a large region of low-speed fluid positioned rather close to the wall under the HS-layer.

The instantaneous vorticity field at 3-spike stage is illustrated in Fig. 5 in physical space (top view) by means of so-called λ-two criterion visualizing vortices. Every spike is observed inside a ring-like vortex snatching away from the Λ-vortex. The 3rd ring-like vortex is not very well formed yet and looks like an 'Ω-vortex' (the term introduced by Hama in [10], as well as the term 'ring vortex').

A simple numerical analysis of the process of formation of the vortex rings made in [10] has shown that the rings can be formed just due to an inviscid self-induction of two vortex filaments associated with the Λ-vortex legs. This kind of instability has been later called 'the Crow instability' (see [11] and figure 116 in [12]). Very similar mechanism was studied later in [13] with the aim to explain deformation of the 'horseshoe-vortex' in the developed turbulent flow and formation of 'typical eddies' observed in external part of the turbulent boundary layer (see [14]). At present, it is almost clear that this is the mechanism that is responsible for production of the ring-like vortices (and spikes) by the Λ-structure during its downstream evolution.

As was shown in [4] the ring-like vortices play an important role in the beginning of subsequent flow randomization and final breakdown to turbulence in the boundary-layer transition process. They induce in the near-wall region some very intensive perturbations (see Fig. 6) which look like positive velocity fluctuations ('positive spikes') propagating downstream with the same very high speed as the speed of the spikes (and the ring-like vortices). First irregular motions observed in the same near-wall region are associated with variation of positions of the positive spikes in time and space from one structure to another. These low-frequency motions seem to play a dominant role in subsequent flow randomization. Their origins are, most probably, connected with a sensitivity of the Crow-instability mechanism to background perturbations and a possible instability of vortex-ring trains. Subsequent amplification of random motions can be connected with the mechanism of subharmonic-like resonance studied in [16].

It is important to note that the late-stage transition scenario briefly described above is observed in 2D boundary layers in a wide rage of variation of the initial disturbance conditions. The results presented above were obtained in the K-regime of transition induced by a periodic 2D instability wave. However, the same scenario is found in [3] at late stages of the N-regime of transition and in [15] in a case of transition induced by a 2D wave packet of instability waves.
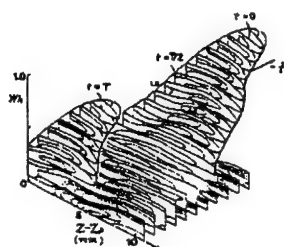

Fig. 7. Λ-shaped HS-layer in channel flow. Experiment [17].

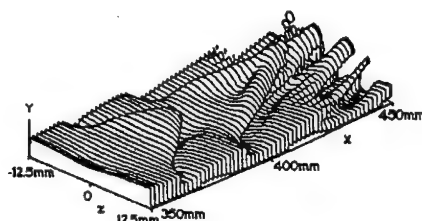Fig. 8. Λ-shaped HS-layer in boundary layer. DNS [18].
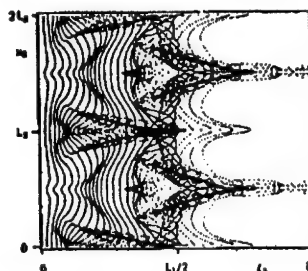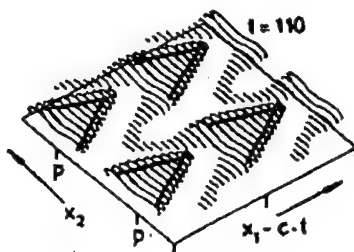

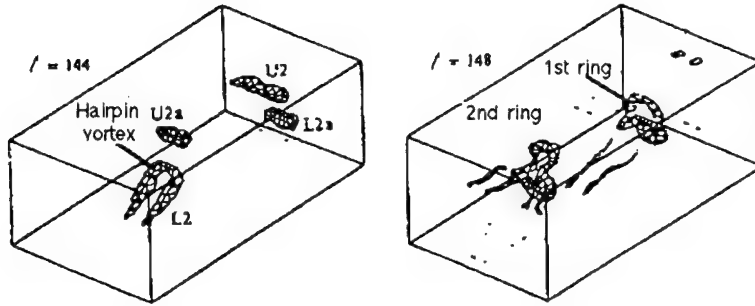Fig. 9. Staggered and aligned in rows Λ-structures in channel flow. DNS [20, 21].

87

Fig. 10. Hairpin- and ring-like vortices observed in channel flow. DNS [22].

3. Structures in channel-flow transition

The HS-layers detected in experiment [17] at 1-spike stage of the transitioning channel flow are illustrated in Fig. 7. Their comparison with the HS-layers observed in the boundary layer transition (DNS [18]) shows a very similar shape of the structures (Fig. 8). It has been also shown in experiments [19] that similar to the boundary layer transition the two regimes of transition (the K- and N-regime) are observed in the channel flow transition. This fact is illustrated in Fig. 9 taken from DNS results obtained in [20, 21]. The structures aligned rows (Fig. 9 left) correspond to the K-regime, while in the staggered order of the structures (Fig. 9 right) correspond to the N-regime of transition.

At later stages of the channel-flow transition the formation of hairpin- and ring-like vortices is also observed (Figs. 10 left and 10 right respectively). These and other results show that all main features of the late-transition structures are very similar in plane channel flows and boundary layers.

4. Structures in pipe-flow transition

Very recent experimental [23] and DNS [24] investigations of the nonlinear stages of transition in the pipe-flow have also shown that many features of this process resemble very much the corresponding stages of the boundary-layer transition. In particular, the generation of spikes was found in both experiment (Fig. 11) and simulation. DNS has shown also formation
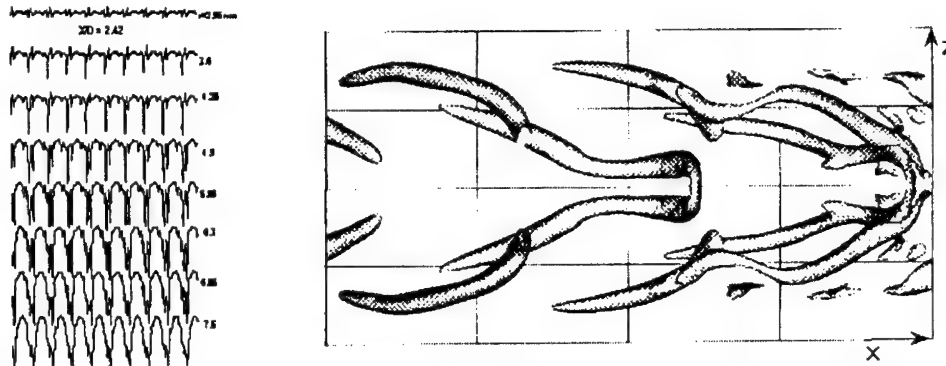

Fig. 11. Spikes in pipe-flow transition. *Fig. 12.* Formation of Ω- and ring-like vortices in pipe-flow
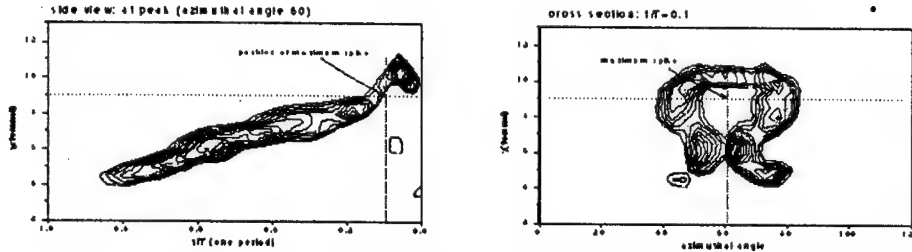Experiment [23].   transition. DNS [24].

Fig. 13. W-vortex at 1-spike stage in pipe flow. Experiment [23].

of Ω- and ring-like vortices attributed to spikes (Fig. 12). The Ω-vortices have been found experimentally at the 1-spike stage (Fig. 13). A great number of other peculiarities detected in [23] and [24] indicated to a very deep physical analogy of the turbulence production processes in the two basic flows.

5. Structures in developed turbulent wall-bounded flows

An idea about existence of a deep physical analogy between the nonlinear phenomena observed at late stages of transition with those found in the developed wall turbulent flows is discussed for many ears (see [2] for review). Recent rapid development of the DNS studies of turbulent flows provides an additional very important information in this field. An instantaneous vortex structures of the turbulent channel flow calculated in [25] serves as a bright example of this analogy (Fig. 14). Qualitatively, the vortex structures presented in Fig. 14 have completely the same shape and position with respect to the wall as the structures discussed above for the transitional flows (see e.g. in Fig. 5).
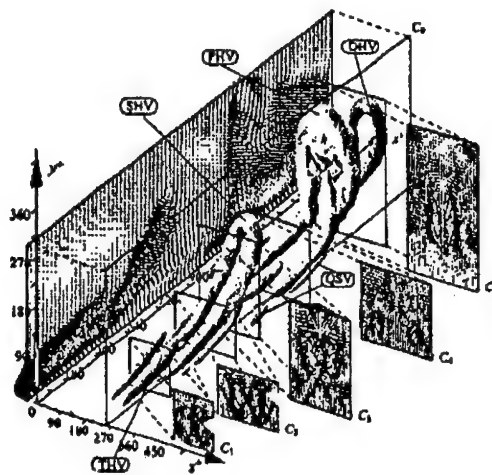

Fig. 14. Vortex structures in turbulent channel flow. DNS [25].

6. Conclusions

The results presented and discussed in the this paper give a possibility to draw the following main conclusions.
1. A universal physical mechanism of turbulence production seems to exist in a number of wall bounded shear flows, in particular in boundary layers, channel flows, and pipe flows.
2. This mechanism is common for transitional and turbulent flows.
3. Conclusions 1 and 2 does not mean, however, that the discussed mechanism is a unique one for all wall-bounded shear flows and all environmental conditions.

The most significant aspects of the universal mechanism are the following: (i) appearance of a vortex loop, (ii) formation of the Λ- (hairpin-) vortex, Λ- (hairpin-) shaped high-shear layer, and first spike, (iii) continuous stretching the Λ- (hairpin-) vortex and rapid growth of vorticity in their legs, (iv) self-induction of the Λ- (hairpin-) vortex legs (Crow instability), (v) multiple reconnection of the vortex loop and formation of a train of Ω- and ring-like vortices (or typical eddies), and associated spikes, moving toward the external boundary-layer edge, (vi) interaction of the ring-like vortices (or typical eddies) with each other, attributed to a train instability, leading to growth of low-frequency irregular motions, (vii) appearance of near-wall perturbations induced by ring-like vortices that have a significant irregular component, and (viii) an amplification of quasi-random near-wall motions by a mechanism of their resonant interaction with organized large-scale motions (the structures discussed above).

7. Acknowledgements.

References

1. Herbert T. Secondary instability of boundary layers // Ann. Rev. Fluid Mech. - 1988. - V. 20. - P. 487-526.
2. Kachanov Y.S. Physical mechanisms of laminar-boundary-layer transition // Ann. Rev. Fluid Mech. - 1994. - V. 26. - P. 411-482.
3. Bake S., Fernholz H.H., Kachanov Y.S. Resemblance of K- and N-regimes of boundary-layer transition at late stages // Eur. J. Mech., B/Fluids. - 2000. - V. 19, N 1. - P. 1-22.
4. Borodulin V.I., Gaponenko V.R., Kachanov Y.S., Mayer D.G.W., Rist U., Lian Q.X., Lee C.B. Late-stage transitional boundary-layer structures. Direct numerical simulation and experiment // J. Fluid Mech. - 2000. (Accepted for publication).
5. Zelman M.B., Maslennikova I.I. Tollmien-Schlichting-wave resonant mechanism for subharmonic-type transition // J. Fluid Mech. - 1993. - V. 252. - P. 449-478.
6. Rist U. & Kachanov Y.S. Numerical and experimental investigation of the K-regime of boundary-layer transition // Laminar-Turbulent Transition / ed. R. Kobayashi. - Berlin: Springer, 1995, pp. 405-412.
7. Kachanov Y.S., Ryzhov O.S., Smith F.T. Formation of solitons in transitional boundary layers: theory and experiments // J. Fluid Mech. - 1993. - V. 251, - P. 273-297.
8. Klebanoff P.S., Tidstrom K.D., Sargent L.M. The three-dimensional nature of boundary-layer instability // J. Fluid Mech. - 1962. - V. 12. - P. 1-34.
9. Rist U., M_ller K., Wagner S. Visualization of late-stage transitional structures in numerical data using vortex identification and feature extraction // Proc. 8th Int. Symp. Flow Visualization., Sorrento, Italy, 1998, paper No. 103.

10. Hama F.R. & Nutant J. Detailed flow-field observations in the transition process in a thick boundary layer // Proc. 1963 Heat Transfer & Fluid Mech. Inst. - Palo Alto, Calif.: Stanford Univ. Press, 1963, pp. 77-93.

11. Crow S.C. Stability theory for a pair of trailing vortices // AIAA J. - 1970. - V. 8. - P. 2172-2179.

12. Van Dyke M. An album of fluid motion. - Stanford, California: Parabolic Press, 1982.

13. Moin P., Leonard A. & Kim J. Evolution of curved vortex filament into a vortex ring // Phys. Fluids. - 1986. V. 29, No 4. - P. 955-963.

14. Falco R.E. Coherent motions in the outer region of turbulent boundary layer // Phys. Fluids Suppl. - 1977. - V. 20, No 10. - P. S124-132.

15. Borodulin V.I., Gaponenko V.R., Kachanov Y.S. Generation and development of coherent structures in boundary layer at pulse excitation // 10th Int. Conference on Methods of Aerophysical Research. Proceedings. - Novosibirsk: Inst. Theor. & Appl. Mech. 2000 (Paper in this volume.)

16. Dryganets, S.V., Kachanov, Y.S., Levchenko, V.Y. & Ramazanov, M.P. Resonant flow randomization in K-regime of boundary layer transition // Zurn. Priklad. Mekh. i Tekhn. Fiziki. – 1990. – V. 2. – P. 83-94 (in Russian). (Transl. J Appl. Mech. & Tech. Phys. – 1990. – V. 31, N. 2. – P. 239-249.)

17. Nishioka M., Asai M. Evolution of Tollmien-Schlichting waves into wall turbulence // Turbulence and Chaotic Phenomena in Fluids / ed. T. Tatsumi. - Elsevier Science Publishers (North-Holland), 1984, p 87-92.

18. Rist U. Numerische Untersuchung der räumlichen, dreidimensionalen Störungsentwicklung beim Grenzschichtumschlag. Ph.D. thesis Inst. A Mech. Univ. Stuttgart, 1990.

19. Kozlov V.V., Ramazanov M.P. Resonance interaction of disturbances in Poiseuille flow // Dokl. Akad. Nauk SSSR. – V. 275, N 6. – P. 1346-1349 (in Russian).

20. Kleiser L., Laurien E. Three-dimensional numerical simulation of laminar-turbulent transition and its control by periodic disturbances. // Laminar-Turbulent Transition / ed. V.V. Kozlov. - Berlin: Springer-Verlag, 1984, p. 27-37.

21. H_rtel C., Kleiser L. Subharmonic transition to turbulence in channel flow // Applied Scientific Research. - 1993. – V. 51. – P. 43-47.

22. Sandham N.D., Kleiser, L. The late stages of transition to turbulence in channel flow // J. Fluid Mech. – 1992. - V. 245. – P. 319-348.

23. Han G., Tumin A., Wygnanski I. Laminar-turbulent transition in Poiseuille pipe flow subjected to periodic perturbation emanation from the wall. Part II. Late stage of transition // J. Fluid Mech. – 2000. (Accepted for publication.)

24. Reutner J., Rempfer D. A hybrid spectral/finite-difference scheme for the simulation of pipe-flow transition // Laminar-Turbulent Transition / ed. H. Fasel & W.S. Saric. – Berlin: Springer-Verlag. (Accepted for publication.)

25. Zhou J., Adrian R.J., Balachandar S., Kendal T.M. Mechanisms for generating coherent packets of hairpin vortices in channel flow // J. Fluid Mech. - 1999. - V. 387. - P. 353-396.

MIXING PROCESSES OF SUPERSONIC FLOWS IN A SCETCHY MODEL OF A ROCKET SCRAMJET ENGINE

A.M.Kharitonov, A.V.Lokotko, and A.V.Tchernyshyev

Institute of Theoretical and Applied Mechanics SB RAS, Novosibirsk, Russia

V.I.Kopchenov, K.E.Lomkov, and A.S.Rudakov

CIAM, Moscow, Russia

Introduction

One of the important problems arising in the development of scramjets for aerospace plane with horizontal take-off and landing is the study of the mixing processes of supersonic flows for the purpose of obtaining the maximum increase in mixing intensity in order to organize combustion within a limited length with the minimum momentum loss.

The studies of various methods for mixing intensification are discussed in [1-4]. In particular, the use of elliptical nozzles in combination with various vortex generators is considered. An azimuthal variation of curvature is responsible for nonuniform self-induced flows and complex three-dimensional vortices. They are related to the property of splitting of an exhausted jet; hence, a significant improvement of mixing can be expected. However, the manifestation of this property depends on a number of factors: ellipse axes ratio, nozzle pressure ratio, degree of flow parallelism, etc.

The mixing of supersonic turbulent jets in the duct under the conditions of strong nonuniformity of the fields of gasdynamic parameters behind the inlet is a very complicated problem for numerical simulation. The difficulties are also aggravated by the desire to obtain the maximum splitting of the injected substance. The development of these numerical techniques is also limited by the absence of reliable experimental data that satisfy the requirements of verification of numerical models.

A brief description of the results obtained for the fuel pylon designed previously by CIAM and ITAM and experimentally investigated by ITAM was presented in [5, 7]. The afterbody of the fuel pylon was shaped to provide intense secondary air flows.

Results of an experimental and numerical study of the mixing process in supersonic jets and a cocurrent flow are presented in this paper. The jets with different degrees of dispersion and configurations are injected into a rectangular duct modeling one of the versions of real propulsion.

Experimental conditions, model

The experiments were carried out in the supersonic wind tunnel T-313 with a closed 0.6×0.6 m test section based at ITAM SB RAS. The free-stream conditions were as follows: Mach number M=4.03, Reynolds number Re=$55 \cdot 10^6$ m^{-1} and stagnation temperature 286 K.

A sketch of the model with geometric characteristics of its basic elements is shown in Fig. 1. The model inlet has a flat lower compression surface 1 with a 6° wedge, the upper cowl 2, side walls 3, and pylon 4 with a 40° sweep angle of the leading edge and 10° plan apex angle, which is mounted at the longitudinal axis of symmetry. The wedge surfaces of the pylon are also compression surfaces; thus, the construction as a whole is a three-dimensional inlet. In the base part of the pylon, there is a packet of supersonic nozzles, the high-pressure gas being injected from them. Three types of pylons were used.

Pylon 1 has a symmetric nozzle disposition and shallow turbulizing grooves between the nozzles at the side surface. Pylon 2 differs from it by an asymmetric nozzle arrangement. The

profile of the nozzle exit section of pylon 3 is close to elliptical. The major axis of the elliptic cross section of all the nozzles was parallel to the upper and lower walls of the model. The noz-
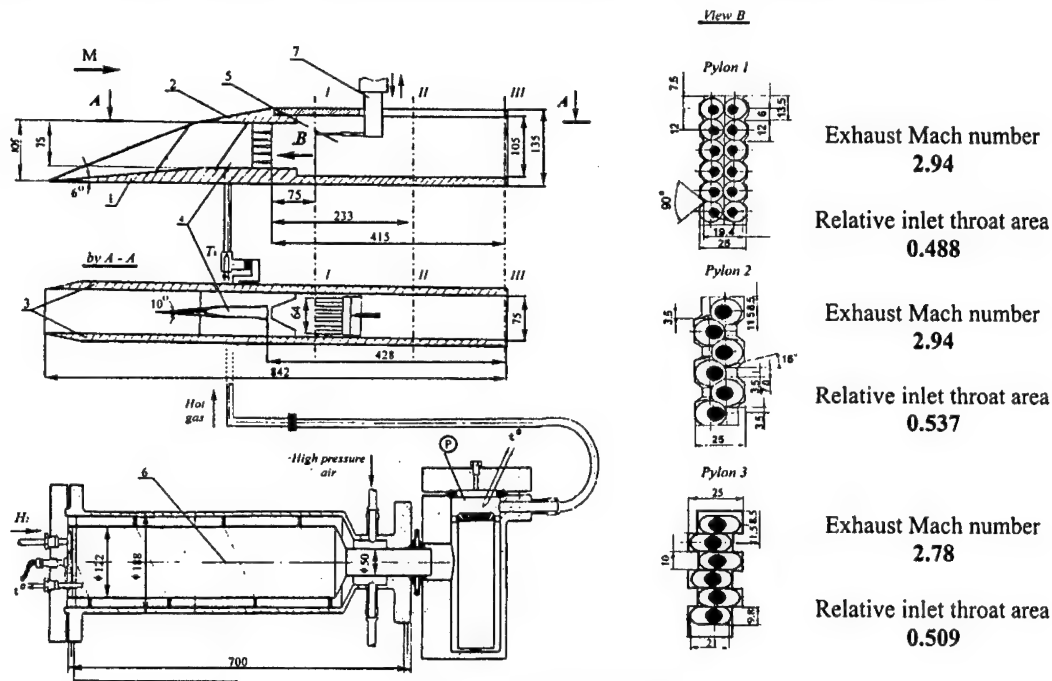

Fig. 1. Sketch of the model.

zles have the incidence angles equal to 7.5° realized in such a manner that neighboring nozzles provide the fuel jet scattering in opposite sides in lateral directions. Moreover, special recesses turned on the lateral sides of the pylon are made. These recesses provide the air flow in the regions between the neighboring fuel jets at the same angle.

The mixing chamber (MC) 5 is a channel with a 75×105 mm cross section and 420 mm length. At the top and bottom of the MC entrance, there is a system of 3D oblique steps with a sweep angle of 70° connected with each other by straight steps.

For jet identification, a hot gas (473-483 K), the products of hydrogen combustion in the air, is supplied to the pylon nozzles. The source of gas is the gas generator 6 (Fig. 1) [11]. The pressure ratio at the nozzle exit (determined for conical nozzles) was varied approximately from 0.4 to 2.25 for upper and lower nozzles, respectively, which, in turn, was determined by the pressure variation over the duct height in the inlet throat cross section coinciding with the nozzle exit cross section.

In the course of experiments, the fields of Pitot pressures p_0', p, and T_0 in three measurement cross sections (I-III) along the duct were measured. The cross-section coordinates are shown in Fig. 1. The temperature of hot gases in the pipeline, called conventionally the "temperature at the control point" T_c (Fig. 1), was taken as the initial in the temperature, the current temperature distribution flow being compared with it.

Probes was combined to corresponding rakes – 10 probes for p_0' and T_0 rakes and 6 probes for p rakes. All three rakes were fixed in one traverse gear 7 that ensured the motion accuracy of 0.1 mm along the OY axis at a distance of 105 mm.

The integral parameters in three cross sections were calculated using the results measured at 160 points from the conditions of mass flow, total energy and momentum conservation in the mean and initial non-uniform flows.

Mathematical model and numerical method

The calculations were performed using the designed code for numerical solution of parabolized Navier-Stokes equations for supersonic multispecies nonequilibrium reacting flow. The one-equation differential turbulence model [8, 9] is used. A detailed scheme of chemical kinetics [10] is implemented to describe the combustion processes in a hydrogen-air mixture. The space-marching numerical scheme is a modified version of the stationary analogy [11] of the Godunov scheme for supersonic flows. The modification provides a high-order accuracy. An adaptive grid can be used along with a regular one.

The first series of computations was performed to investigate the mixing of heated hydrogen injected through the nozzles with the main air stream. The influence of different factors – jet injection at an angle to the main air stream, the air flow turning due to recesses on the lateral sides – on the mixing efficiency was estimated. This computational series included the following cases:

1. The basic case when the jets are injected in the direction of the main stream, which is supposed to be uniform.

2. The jets are injected at an angle of 7.5° to the direction of the main air stream, which is uniform. The neighboring jets have lateral velocity components of the opposite sign.

3. The jet injection is realized identically to that in case 2. However, the air stream in the cross section of jet injection is nonuniform. It is obtained as the result of the main air flow calculation with account of the real geometry of the pylon afterbody. The air flow in the cross section ahead of the afterbody is assumed to be uniform. Therefore, the nonuniformity of the main air stream is generated by recesses on the lateral sides of the pylon.

4. The computation begins from the inlet entry; thus, the flow nonuniformity is taken into account at the cross section from which the pylon is specially designed.

The conditions in the heated jets injected through the nozzles and in the main air stream in the cross section ahead of the pylon afterbody are presented in Table 1. These data were used in the calculations of cases 1-3. In case 4, the calculations begin from the inlet entry. The entry boundary conditions were formulated in accordance with experimental conditions.

The computational geometry was simplified at this stage of investigation. This first simplification is concerned with the fact that the pylon leading edge has the

Table 1

Parameters	Heated air jets	Main stream
M	2.94	3.11
p, bar	0.185	0.185
T_0K	179	91.9
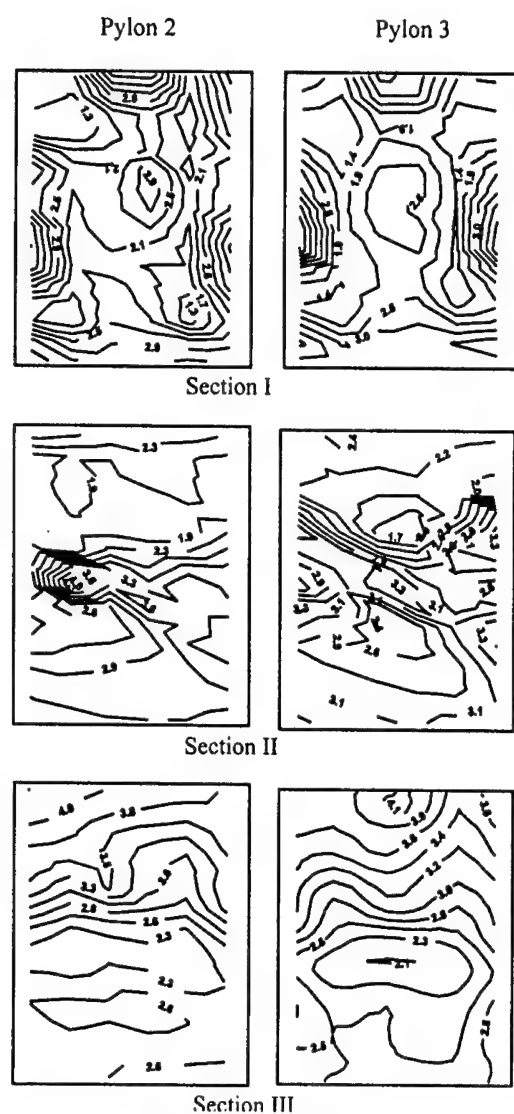
backward sweep and the computational configuration was without sweep. The pylon also has small base faces in the section of jet injection around each jet. These base regions were not accounted for the estimations of the mixing efficiency. Special recesses were also made on the lower wall of the combustor of experimental configuration. The computational configuration has only an expansion angle to model the duct expansion due to these recesses.

Pylon 2   Pylon 3

Section I

Section II

Section III

Fig. 2. p/p_∞ isolines.

Results and discussion

The fields of relative static pressures p/p_∞ measured in three cross sections along the MC are shown in Fig. 2 for pylons 2 and 3.

An analysis of the pressure fields demonstrates that they are almost identical qualitatively. In cross section I, the general level of pressure increase is almost identical and varies within $1.3 \div 4$. More detailed previous studies show that a complex interaction of shock waves with the formation of contact discontinuities and generation of vortex structures occurs in the entry section of the inlet. The vortex structures are destroyed at the entrance to the mixing chamber when they pass the closing shock wave. Zones of intense spreading of the soot-oil mixture (Fig. 3), which characterize an increase in pressure, are formed on the vertical walls.

In cross section II, a comparatively constant static pressure over the duct height with a small increase to $p/p_\infty = \cdot 3.3 \div 4$ in the middle and lower sections is typical of both pylons. The local pressure peaks observed in the middle part of the cross sections are related to the upstream presence of the shock waves from flow reattachment e_1-e_2-e_3 (Fig. 3) after the stabilizing steps. The pressure profile for pylon 2 differs by a somewhat more expressed asymmetry of the flow, which is manifested in the existence of a separate pressure peak, where $p/p_\infty \approx 4$. This is related to the presence of deeper turbulizing asymmetric recesses, which generate flow swirling.

In cross section III, the pressure profiles become more uniform over the duct width. A significant pressure increase is observed in the upper part of the duct in both pylons, as compared with the lower part, which is determined by the wave structure of the duct flow.
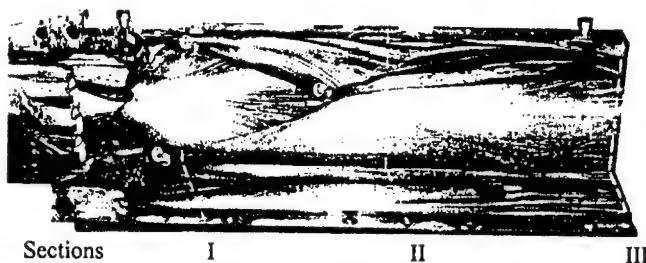

Sections   I   II   III

Fig. 3. Limited streamwise lines in the MC of the model.

In this section a more uniform pressure profile is clearly observed for a pylon with elliptical nozzles. This can be an indication of better mixing for pylon 3.

Distribution of relative excess temperature It is known [12] that the propagation of heat and additive concentration obey the same laws. This gives grounds to consider the process of heat
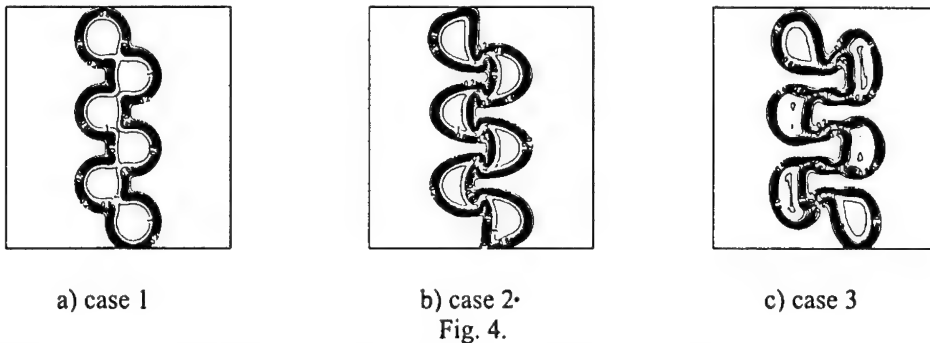

| a) case 1 | b) case 2· | c) case 3 |

Fig. 4.

propagation in the heated jets as a characteristic of the degree of mixing.

The fields of relative excess total temperature θ for computational cases 1-4 at the cross section $X = 75$ mm are shown in Fig. 4, 5. It is necessary to note that in the first case the jets propagate in the direction of the main stream and gradually mix with it (Fig. 4a). Developed secondary flows are not observed. In the second case, the nozzle inclination angle provides a deflection of the jets in the lateral direction alternatively to the right or to the left of the plane of symmetry of the mixing chamber. The contact surface between each jet and the external air

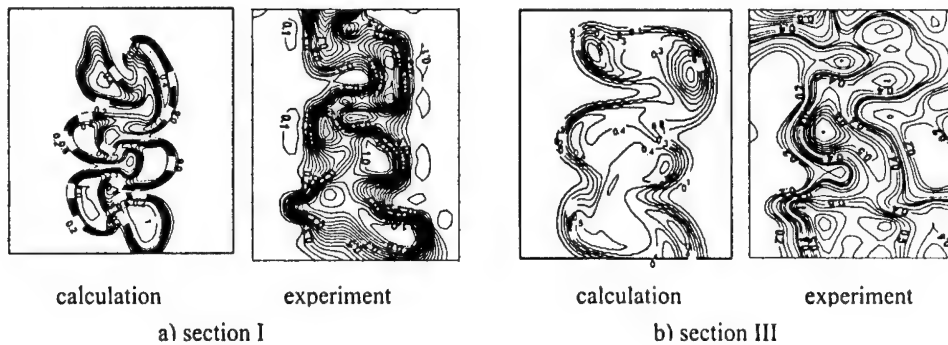| calculation | experiment | calculation | experiment |
| a) section I | | b) section III | |

Fig. 5.

stream increases, and this factor is favorable to the mixing enhancement (Fig. 4b). However, the most intense (among the cases considered) external air flow into the region between the jets is provided by the recesses on the lateral sides of the pylon afterbody. This effect is followed by a considerable increase in the contact surface between the jet and the external air stream. Moreover, this contact surface acquires a whimsical flexed shape (Fig. 4c). This provides an additional mixing enhancement in comparison with previous cases. Case 4 corresponds most closely to the experimental investigation. It is necessary to note that in this case the flow at the inlet ahead of the pylon afterbody is significantly nonuniform. The relative total temperature θ for case 4 is plotted in Fig. 5a. Despite the above-mentioned simplifications of the pylon and
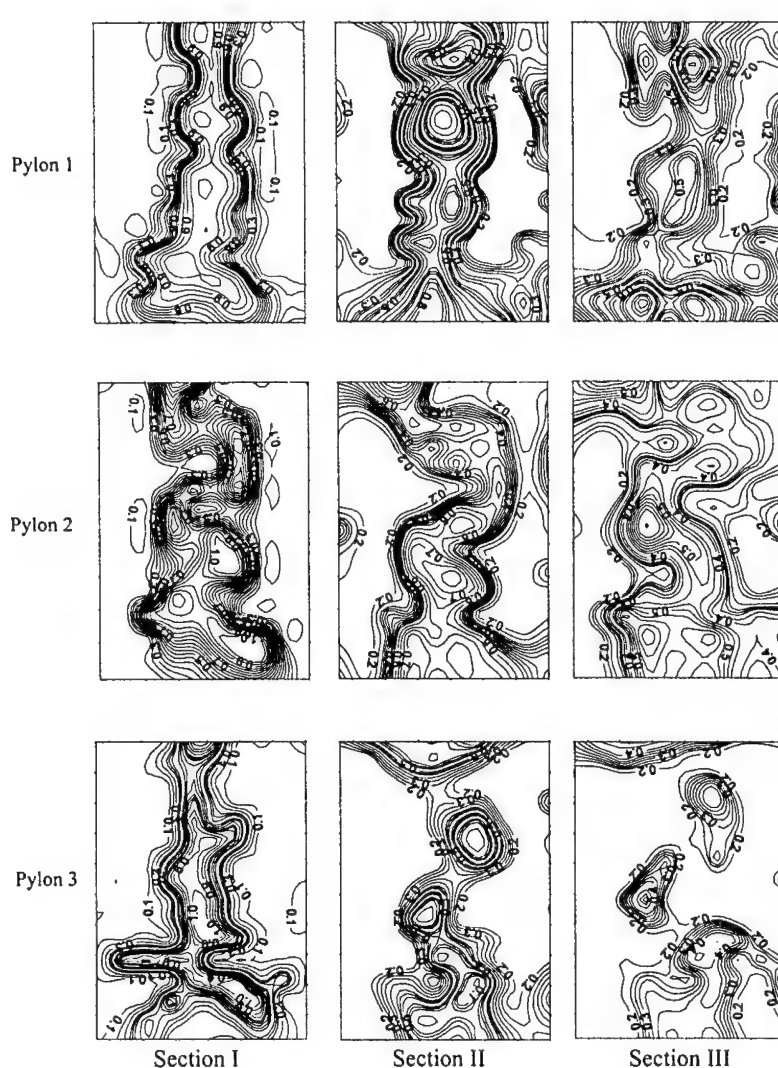
Fig. 6. Isolines of relative excess temperature. Experimental data.

duct geometry, a significant nonuniformity of the velocity field at the entrance to the mixing chamber makes a considerable contribution to the formation of the field of excess temperatures.

Fig. 6 shows the measured isotherms of the relative excess temperatures for three pylons. The general feature for all pylons is an expansion of the heating zone in the lower part of the first cross section. This can be explained by the change in the nozzle pressure ratio over the duct height, which is determined by the special features of the inlet flow. Complete merging of the jets occurs in this cross section for pylon 1, which is characterized by the presence of a continuous vertical region where $\theta = 1$ [7]. The greatest degree of splitting of the hot flow is typical for pylon 2, and an intermediate pattern is observed for pylon 3. We can assume that a comparatively weak dispersion of the hot flow in the latter case is related to flow separation in elliptical nozzles in the plane of the major axis of the ellipse where the maximum degree of nozzle expansion is observed.

In cross section II, the best quality of mixing is observed for pylon 3, where the general level of θ is lower and the maximum value $\theta = 0.7$ is observed only in limited regions; the worst quality of mixing is observed for pylon 1: there are zones of mixing of jets in which the mixing has not yet begun ($\theta = 1$).

In cross section III, the pylon with elliptical nozzles has clear advantages: the heating extends over the entire flowfield, the maximum value $\theta = 0.5$ is registered only in a very limited region, practically, in a point. Pylon 1 is again the worst one, since we have $\theta_{max} = 0.8$ for this pylon and there are regions with a complete absence of heating ($\theta = 0$).

Figure 5 shows a comparison of the computational field with the experimental one. A comparison of Fig. 5a for the cross-section I demonstrates the qualitative agreement in the main flow features concerned with the mixing process. The same is observed for the exit cross-section (Fig. 5b). Hence, we can assume that the further computations for a more detailed geometry of the leading edge of the pylon and with account of stabilizing steps will provide not only qualitative, but also quantitative agreement with experimental data.

Various numerical criteria can serve as a quantitative measure of the degree of mixing. In particular, the mixing factor in [8, 12] is the ratio of the energy that can be produced in a particular cross section of the flow depending on the concentration composition of the fuel-air mixture determined by the mixing intensity to the total energy of the fuel being oxidized by air. Such a criterion can be calculated numerically. In processing of experimental data, the most reasonable and representative criterion is the relative root-mean-square deviation of the temperature from the mass-mean value in each cross section: $\eta = 1 - \sigma_j / \sigma_e$; σ_j and σ_e belong the inspected and entrance cross section accordingly. The corresponding numerical and measurement values are shown in the Fig. 7. The quantitative disagreement observed in this figure is a consequence of significant simplification of the pylon geometry, stabilizing steps and other assumptions, accepted in the calculation method.

Hydraulic losses in the mixing zone

Hydraulic losses in ducted combustors are usually characterized by the total pressure recovery, which can be conveniently expressed in fractions of dynamic pressure:

$$\nu = 1 - (\xi \kappa \pi(\lambda) M_I^2) / 2.$$

The loss for mixing can be also estimated from the change in specific momentum I in three measurement cross sections along the duct. It is determined as the momentum calculated on the basis of the measurement results in each cross section $I = [(\kappa - 1) <a_*>Z(\lambda)] / 2\kappa$,

Fig. 7.

where a_* is the the critical speed of sound calculated from the mass-mean temperature.

Table 2 shows the calculated coefficient of pressure recovery and the change of the specific momentum between the I and III cross sections for three pylons.

It is seen that the highest coefficient of total pressure recovery is obtained with the use of elliptical nozzles. In this case, the gain ν in is about 16% as compared with pylon 1 and about 9% as compared with pylon 2.

Table 2

Type of pylon	1	2	3
δ_{I-III} (%)	6.83	3.85	3.57
ν	0.563	0.609	0.667

The greatest total loss is observed for pylon 1. The lowest total loss is registered for pylon 3 with elliptical nozzles.

Concluding remarks
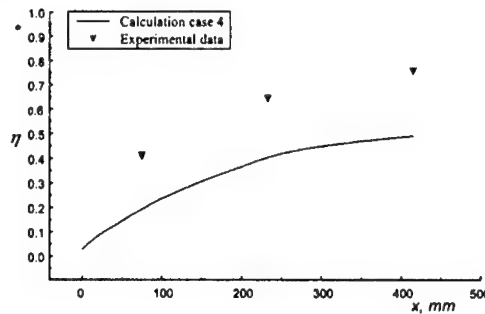
A series of experimental investigations of the process of mixing of supersonic jets in the model of a hypersonic rocket scramjet engine with pylons of different geometry and different number of nozzles has been performed. It has been shown experimentally that a pylon with six elliptical nozzles ensures a more intense mixing and the lowest loss of total pressure and specific impulse under the conditions examined.

A comparison of the calculation results of the excess temperature fields for the pylon with circular nozzles with experimental data demonstrate good qualitative agreement.

Nomenclature

X	Axial coordinate	a_*	Critical speed of sound
Y	Vertical coordinate	η	Mixing efficiency
Z	Transverse coordinate	ν	Total pressure recovery
M	Mach number	ξ	Drag coefficient
Re	Reynolds number	κ	Ratio of specific heats
p	Pressure	$\pi(\lambda)$	Gasdynamic function for pressure
T	Temperature	$z(\lambda)$	Gasdynamic function for momentum
G	Mass flow	h	Throat height
I	Specific impulse		Subscripts
$n = p_n/p_\infty$	Nozzle pressure ratio	∞	Free-stream conditions
$\theta = (T_i - T_0)/(T_c - T_0)$	Relative excess temperature	0	Stagnation quantities
		max	Maximum
σ	Root-mean-square deviation	i	The i-th measurement point
		c	The temperature at the control point

References

1. Haimovitch Ya., Gartenberg E., Roberts A.S. Jr. Effects of internal nozzle geometry on compression-ramp mixing in supersonic flows. AIAA J. 1997. Vol. 35. No. 4. P. 663-670.

2. Alexandrov V., Mnatsakanyan Yu., Prokhorov A., Shutov A., Panin A. Experimental investigation of supersonic jet mixing by using optical methods in appliance to scramjet combustor // Intern. Conf. on the Methods of Aerophysical Research: Proc. Pt 3. Novosibirsk, 1996. P. 5-10.

3. Husain H.S. Measurements in an elliptic whistler jet // Proc. Seventh Asian Congress of Fluid Mechanics. Chennai, India, 1997. P. 203-206.

4. Kopchenov V.I., Lomkov K.E. Numerical simulation of the supersonic combustion enhancement and 3-D scramjet combustor design with account of nonequilibrium chemical reactions // High Speed Aerodynamics. 1997. Vol.1, No.1. P.43-53.

5. Gogish L.V., Zheltovodov A.A., Kurmashov R.Kh., Lokotko A.V., Kharitonov A.M. Effect of the rectangular channel entrance conditions on the internal supersonic flow structure: Preprint No. 13. Novosibirsk: ITAM, 1990. 39 p.

6. Lokotko A.V., Kharitonov A.M., Tchernyshyev A.V. An investigation of flow formation and mixing processes in a rectangular channel // Intern. Conf. on the Methods of Aerophysical Research: Proc. Pt 3. Novosibirsk, 1996. P.195-200.

7. Lokotko A.V., Kharitonov A.M., Tchernyshyev A.V. A study of mixing processes of a supersonic flow in a rectangular channel // Proc. Third European Symp. on Aerodynamics for Space Vehicles. ESTEC, Noordwijk, 1998. P. 469-478.

8. Bezgin L., Ganzhelo A., Gouskov O., Kopchenov V., Laskin I., Lomkov K. Numerical simulation of supersonic flows applied to scramjet duct // ISABE 95-7082, 1995. P.895-905.

9. Gulyaev A.N., Kozlov V.E., Sekundov A.N. A universal one-equation model for turbulent viscosity // Fluid Dynamics. 1993. Vol. 28, No.4. P.485-494.

10. Dimitrow V.I. The maximum kinetic mechanism and rate constants in the H_2-O_2 system // React. Kinetic Catal. Lett. 1977. Vol. 7, No.1.

11. Godunov S.K., Zabrodin A.V., Ivanov M.Ja., Kraiko A.N., Prokopov G.P. Numerical solution of multidimensional gas dynamics problems. Moscow: Nauka, 1976.

12. Abramovich G.N., Girshovich T.A., Krasheninnikov S.Yu., Sekundov A.N., Smirnova I.P. Theory of turbulent jets. Moscow: Nauka, 1984. 715p.

13. Kharitonov A.M., Lokotko A.V., Tchernyshyev A.V., Kopchenov V.I., Lomkov K.E., Rudakov A.S. Mixing processes of supersonic flows in a model duct of a rocket scramjet engine. AIAA Pap. No. 2000-0559, 2000. 10 p.

THE PECULIARITIES OF NUMERICAL SIMULATION OF SUPERSONIC FLOW AROUND COMPOUND BODIES BY THE METHOD OF FINITE VOLUMES

T.A.Korotaeva, A.P.Shashkin

Institute of Theoretical and Applied Mechanics SB RAS,
630090, Novosibirsk, Russia

At the present time the great experience in the area of solution of individual problems of real aerodynamic processes simulation has been already gained. The spectrum of models for description of aerodynamics problems includes various approximations beginning from algebraic relations to Navier — Stockes complete equations. Navier — Stockes equations considering dynamical processes and medium viscosity are differential ones in second-order partial derivatives. Their application in solution of a spatial task of real aircraft flow is problematic at the modern stage of computer techniques and numerical method development. An other approach demanding much less consumptions but with many advantages is in use of simpler Euler equations where the components showing the influence of gas viscosity are absent. These equations allow one to follow accurately (Rankine – Hugoniot) conditions on shock waves. They reproduce convective vortex transfer, and due to this fact the calculation of vortex-type flows has been made possible with no previous vortex eduction. But the question about vortex sources still remains unsolved (curvilinear shock wave, approximation errors, etc.).

In the paper, one of varieties of the finite volume methods is offered for numerical solution of 3-D Euler equations. Recently this method has received wide acceptance. It is based on representation of the considered equations in the integrated form for volume of a cell of the investigated area. The partition into elementary volumes permits to account for a complicated configuration of solution region without entering a curvilinear system of coordinates. The method of finite volumes offers the property of conservatism. Writing down the equation in a conservative form and using discrete transformations which preserve mass, etc., it is possible to obtain a solution which satisfies the a weak form of initial equations. As Lax and Wendroff [1] have shown, the solutions of equations written in weak form satisfy automatically the Rankine - Hugoniot conditions on any shock wave which may appear in the flow. The shock waves are the most abundant type of such discontinuities. Thus, the solution of discrete equations registers automatically the behavior of shock waves, both their intensity and velocity distribution in non-stationary flows. It allows one to use the method of shock-capturing at the solution (i.e. without previous eduction of singularities). The major difficulty of application of the shock-capturing method is the generation of abrupt parameter change profiles at transition through the shock wave. The interest in schemes which ensure a description of shock waves and other discontinuities of gas-dynamical parameters (when oscillations of the solution are absent) has caused wide distribution of total variation diminishing schemes of– TVD [2]. Some of them may be considered as difference schemes with specially matched artificial dissipative terms. In this paper, the use of a smoothing operator of the relaxation type is offered [3]. On the one hand, its application allows one to decrease the width of the zone of the shock wave; on the other, it allows one to avoid matching of dissipative components.

The governing equations are three-dimensional Euler equations in an integral form:

Continuity equation
$$\int_V \frac{\partial \rho}{\partial t} dV + \int_S \rho \overline{w} \cdot \overline{n} dS = 0 .$$

Momentum equation
$$\int_V \frac{\partial \rho \overline{w}}{\partial t} dV + \int_S [\rho(\overline{w} \cdot \overline{n})\overline{w} + p\overline{n}] dS = 0 . \qquad (1)$$

Energy equation
$$\int_V \frac{\partial E}{\partial t} dV + \int_S \rho \left[e + \frac{w^2}{2} + \frac{p}{\rho} \right] (\overline{w} \cdot \overline{n}) dS = \int_V \dot{Q} dV ,$$

where $\dot{Q}$ is the heat - transfer velocity to a unit volume, E and e are the total and specific internal energy, respectively. A perfect gas is considered with the following equation of state:
$$p = \rho R T .$$
A Cartesian coordinate system is used. The equations and the boundary conditions are nondimensionalized:

$$x^* = x/L, \quad y^* = y/L, \quad z^* = z/L, \quad T^* = T/T_\infty, \quad p^* = p/\rho_\infty W_\infty^2, \quad \rho^* = \rho/\rho_\infty,$$
$$t^* = W_\infty t/L, \quad u^* = u/W_\infty, \quad v^* = v/W_\infty, \quad w^* = w/W_\infty.$$

Equations (1) describe a three-dimensional unsteady motion of an inviscid compressible gas. If there is no energy input, the right-hand side in the energy equation should be equal to zero. The last term in the energy equation is taken into account at calculations with local energy sources in the flow.

The gas flow is considered as unsteady with a prescribed initial flow field. To obtain a steady-state solution, the pseudotransient method is used. The shock-capturing technique is employed. The slip condition on the wall is taken as the absence of mass flux and normal to wall momentum.

A certain three-dimensional domain G is considered. Generally speaking, its boundary has some inflections. The domain G is split into cells and their shape is represented as an arbitrary hexahedron. To calculate the gas-dynamic parameters in each cell by the finite-volume method, we introduce the operator G_m in the following form:

$$G_m(\cdot) = \frac{\int_s (\cdot) d\overline{s}}{V} , \qquad (2)$$

where V and $d\overline{s}$ are the cell volume and the vector of an element of the volume surface, respectively. In terms of finite volumes, equations (1) can be written as

$$\frac{\partial \rho}{\partial t} + G_m(\rho \overline{w}) = 0 ,$$

$$\frac{\partial \overline{w}}{\partial t} + (\overline{w} G_m)\overline{w} + \frac{1}{\rho} G_m(p) = 0 , \qquad (3)$$

$$\frac{\partial f_s}{\partial t} + G_m(f_s)\overline{w} = \frac{\gamma - 1}{p} \rho \dot{Q} .$$

The solution is sought on a set of grid functions corresponding to node points. For definition of parameters on the sides and inside the volume of a cell, the linear interpolation of parameters in node points is used. Then generalized derivative (2) can be written

$$G_m^h(g) = \sum_{k=1}^{6} \left(\frac{\mu^{(2)} g \overline{S}_k}{V} \right)_i,$$

(4)

where k is the number of sides of the cell i, $\overline{S}_k$ is the vector of the area, V is the volume of the cell, $\mu^{(2)}$ is the operator of averaging over the area.

It is supposed that the problem solution is smooth everywhere in G excluding a finite number of surfaces. Considering the integral form of the equations, the problem solution in a point should be understood generally in a class of functions with limited variations. This solution belong to a class of BV-functions. To analyze the existence, uniqueness and convergence of the solution of gas-dynamics equations, there is a developed mathematical apparatus [4] in the function-BV class which is expedient to be applied at production and vindication of numerical calculating schemes of solution of gas-dynamics tasks. In the BV class, non-divergent writing of hydrodynamics equations is possible for discontinuous functions. This writing is completely similar to the known writing of equations for smooth functions; the difference is that physical values should be taken either as volume-average or as mass-average ones depending on the equation writing form.

On mesh function multitude in BV class the task (3) is formulated as follows: the solution of equation system is sought

$$\delta_t g + \overline{A} \cdot G_m^h(g) = 0$$

(5)

with conditions on the boundary $\Phi^h(g) = 0$ and initial data $g^h = f(x_1, x_2, x_3)$,

where x_1, x_2, x_3 are coordinates of points in G area.

$$\delta_t^{n+1/2} g = (\mu^{(3)} g^{n+1} - \mu^{(3)} g^n)/\Delta t$$

Δt is the time step, $\mu^{(3)}$ is the operator of volume-averaging. Here $\overline{A} \equiv \overline{A}(\mu^{(3)} g)$ is the vector-matrix which is shown for a perfect gas in an orthogonal system of coordinates:

$$\overline{A} = \begin{pmatrix} \overline{w} & \rho \overline{i} & \rho \overline{j} & \rho \overline{k} & 0 \\ \dfrac{\gamma p}{\rho^2} \overline{i} & \overline{w} & 0 & 0 & \dfrac{p}{\rho^2} \overline{i} \\ \dfrac{\gamma p}{\rho^2} \overline{j} & 0 & \overline{w} & 0 & \dfrac{p}{\rho^2} \overline{j} \\ \dfrac{\gamma p}{\rho^2} \overline{k} & 0 & 0 & \overline{w} & \dfrac{p}{\rho^2} \overline{k} \\ 0 & f_s \overline{i} & f_s \overline{j} & f_s \overline{k} & \overline{w} \end{pmatrix}.$$

The solution of system (5) for an m-dimension spatial task is carried out by a time explicit scheme, in two stages.

$$g_i^{n+\alpha} = \mu^{(3)} g_i^n - \alpha \cdot \Delta t \cdot \overline{A} \cdot Gm^h(g).$$

(6)

A scheme of first-order approximation is used on the first step. The values of the vector-function calculated on the step are used on the final step

$$g_{i+1}^{n+1} = \beta g_{i+1}^n + (1 - \beta) g_i^{n+\alpha} - \beta \cdot \Delta t \cdot \overline{A} \cdot Gm^h(g^{n+\alpha}).$$

(7)

Here i is the a number of cell (in the three-dimension case the index i corresponds to the triplex index i, j, k, and the index $i+1$ corresponds to the index $i+1, j+1, k+1$). The parameters α and β $0 \le \alpha \le 1$, $0 \le \beta \le 1$) characterize scheme variants.

102

Introducing the designation $\Lambda = \overline{A} \cdot G_m^h$, one may obtain

$$g^{n+1} = \{\beta J + [(1-\beta)J - \beta \cdot \Delta t \cdot \Lambda](J - \alpha \cdot \Delta t \cdot \Lambda)\}g^n , \tag{8}$$

where J is a unit matrix.

It is easy to verify that on smooth solutions the scheme (8) has the second-order approximation when $\alpha = 0.5 + O(h)$, $\beta = 1$, where $h = \max(h_1, h_2, h_3, \Delta t)$.

The system of equations (3) for each cell characterizes the change in impulse mass and entropy due to flows in the cell. For correct description of the gas flow, the balance of internal, kinetic and total energy is important not to be broken. On smooth solutions, such a disbalance is not considerable, but on the solutions which change drastically with space and time it may achieve a noticeable value which is compared to the total energy of the system. The numerical scheme should be "completely" conservative in terms of [5]. The solutions from the BV class satisfy these requirements. Volume derivative approximation by formula (4) allows one, through algebraic operations, to obtain from equations (1) the approximation of equations of another type.

Gas dynamics equations are invariant relative to some group of point transformations in the space of independent and dependent variables. This invariance is a consequence of invariance of conservation laws. The scheme considered in the present paper have the properties of BV class. It is not only completely conservative but also invariant.

In the solution of gas-dynamics complicated tasks, when it is impossible to stipulate for situation of discontinuity surfaces, the numerical schemes of shock-capturing are appropriate to be applied. In most cases, one may observe oscillations of the solution near the discontinuity. The paper [6] shows the conditions under which a concrete scheme of second-order approximation offers a monotonic solution. In a manner similar to [6], let us consider scheme (8), (9) at $\beta = 1$, $\alpha = 0.5 + \varepsilon$, where $\varepsilon = O(h)$, for a space dimension $m = 3$. The existing randomness in α permits to change dissipative properties of the scheme to the value comparable to its dispersion value.

Considering the properties of positive matrices together with the fact that the matrix $\overline{A}$ allows nonsingular similarity transformation which makes diagonal matrix $\overline{A}$, we obtain

$$\tilde{r}(2\alpha\tilde{r} - 1) > 0, \tag{9}$$

$$1 - 2^{2-m}\alpha\tilde{r}^2 > 0, \tag{10}$$

where $\tilde{r}$ is the maximum proper number of the transition matrix. From (10), the ordinary condition of stability [6] follows:

$$K \leq 1 / m\sqrt{2^{2-m}\alpha} , \tag{11}$$

where $K = \max|r_1|$.

Partly, when $\alpha = 0.5$, scheme (7), (8) proposes a stable solution if $K \leq 2/3$ at $m = 3$. The necessary monotony condition follows from (9)

$$K \geq 1/2m\alpha . \tag{12}$$

Thus, (11), (12) determine the necessary conditions for K when the solution according to considered scheme may be not only stable but also monotonic. So, at $\alpha = \Theta/2$, where

$\Theta = 1 + \varepsilon$, $0 \leq \varepsilon \leq o(h)$ $1/3\Theta \leq K \leq 2/3\sqrt{\Theta}$ at $m = 3$.

Conditions (11), (12) are not sufficient conditions but their meeting allows one to hope for a small ratio of solution non-monotony [6]. Application of smoothing for strengthening scheme

103

monotony was carried out and discussed in many papers, for instance in [7]. In the present paper, for the oscillation phenomenon to decrease, a smoothing operator of the relaxing type is used. It smoothes only short-wave disturbances. The implementation of this procedure decreases the approximation order only in the region of oscillating values of parameters and allows one to decrease dispersion errors without an approximation order decrease on smooth solutions.

The boundary conditions for continuum demand the flow to be parallel to a wall, i.e. the normal velocity here was nil. According to the chosen calculation scheme, the approximation of slipping condition on the solid wall realizes through generation of a fictitious calculation layer. In the present algorithm, the establishing of boundary conditions of the second kind [7] is used. In this case, while considering symmetry relative to the tangential plane to a calculated point, a change in the pressure gradient on the curved surface due to centrifugal forces is counted. Thus, applying these method we obtain flow parameters on the wall with second-order approximation. In the symmetry plane, the conditions of flow symmetry are established. At infinity, the flow parameters are taken as equal to the parameters of the incident flow. On the "output" boundary, linear extrapolation is used [7].

To demonstrate the abilities of the given algorithm, an example of calculation of a complicated surface exposed to a hypersonic flow is presented. The flow around a blunted cone of length L = 1, with thick wings and fin at a Mach number M = 21 and an angle of attack α = 7° is considered. The scheme of the vehicle is shown in Fig. 1. The vehicle of that kind needs a study of streamline topology to estimate aerodynamic heating and efficiency of steering surfaces.
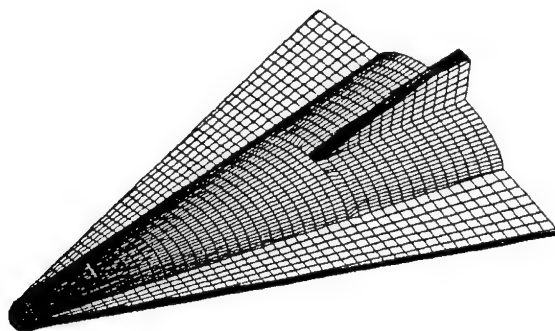
Fig. 1. A mathematical model of vehicle form

It follows from the results obtained that on vehicle crest before the fin one may observe rarefaction. It is a consequence of screening with the wings of flows from a more convex underbody of the vehicle. In section x = const on the vehicle underbody, the pressure changes by the law which is close to the law of flow around an elliptic - cone windward part. Above the vehicle crest (excluding the wings and fin), the pressure changes slightly at all "x".

In Figure 2 there are streamline fields in a conic system of coordinates for the vehicle crest (above the wing) in various cross sections. From the analysis of streamline topology in a conic system of coordinates one may see that, in the vehicle crest (above the wing) at an angle of attack α = 7°, evident pictures of flow are formed, with peculiarity of A.Golubinsky [8] (Fig.2a, b) before the fin and Ferry points (in fin presence). As "x" rises, the Golubinsky peculiarity passes from the vehicle surface to the symmetry plane, draining Ferry point emerges and evident vortex structure is formed on vehicle surface in the regions between the fin and the

wing. The pressure in all region of the structure is practically constant and the fin operation efficiency in such conditions is insignificant.
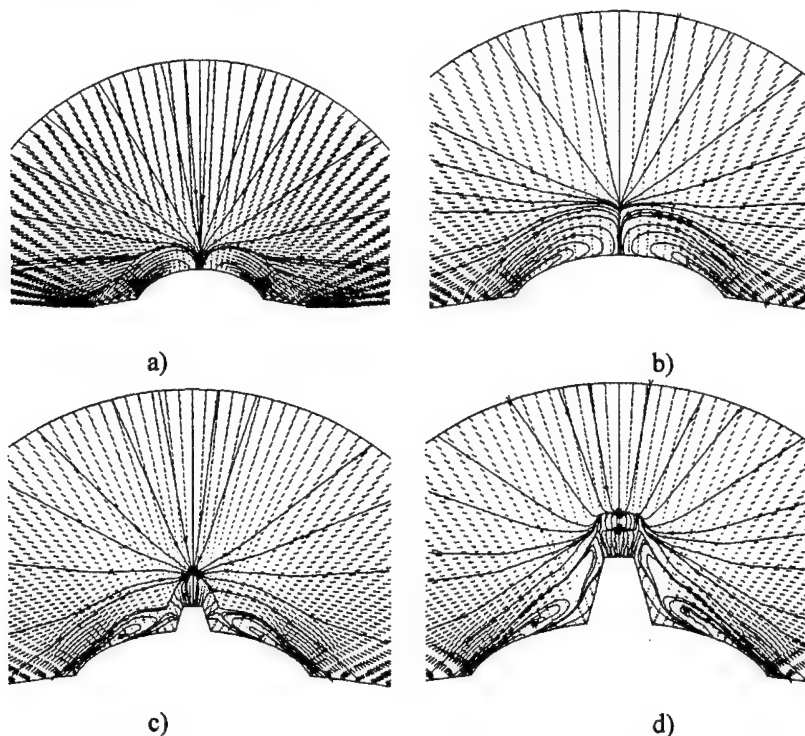

Fig. 2. Streamlines and field of velocities. Angle of attack $\alpha = 7°$. a) x = 0.500, b) x = 0.675, c) x = 0.792, d) x=1.000

Thus, the given algorithm allows one to describe the generation of vortex structures which are formed because of entropy gradients in the flow.

References

1. Lax P.D., Wendroff B. Systems of conservation laws // Com. Pure and Appl. Math., 1960. Vol 13. P.271-237.
2. Yi G.S., Harten. A. The implicit scheme TVD for hyperbolic systems of the equations, written down in the conservative form in curvilinear coordinates //Aerokosmicheska tehnika. 1987. No 11. P.11-21.
3. Korotaeva T.A., Fomin V.M., Shashkin A.P. Numerical research of effect of local energy input on spatial supersonic flow around of the sharp-nose bodies: Preprint No 1-96, - Novosibirsk, ITAM. 1996 (in Russian).
4. Volpert A.I., Khudyaev S.I. The analysis in a class of the bounded functions and equation of mathematical physics. – M: Nauka, 1975. (in Russian).
5. Popov Yu.P., Samarsky A.A. Completely conservative difference scheme for the equations of fluid dynamics in Euler's variables //Jurnal Vychislitelnoy Matematiki i Matematicheskoy fiziki. 1969. No 4. P. 953-958. (in Russian).
6. Shashkin A.P. About construction of the monotonic second-order accurate scheme // Chislenny analiz. – Novosibirsk, 1978. P. 111-118. (in Russian).
7. Roache P. Computational fluid dynamics. Albuquerque, Hermosa, 1976.
8. Golubinsky A.I. Especial surfaces of streamlines in conic flows of gas // Prikladnaya mekhanika i tekhnicheskaya fizika. 1970. Vol 34. No 6. P. 1058-1066. (in Russian).

INFLUENCE OF PLASMA AND HOT-TEMPERATURE GAS JETS ON AERODYNAMIC DRAG

A.V. Krasilnikov, A.V. Panasenko

Central Research Institute of Machine Building (TSNIIMash),
Korolev, Moscow Region, Russia

Reduction of drag of flying devices is a very real and important problem. Fuel is now half of the aircraft's base weight and even more than that for rockets. A 1 % decrease in drag leads approximately to a 10 % increase in aircraft passengers payload or increased range. The result of the progress in aerodynamics for the last decades is that the traditional method of drag reduction by finding an optimum configuration of flying devices has practically exhausted itself. As a result, it was necessary to seek new drag-reduction technologies.

One of the methods is the use of superstructures such as a spike and injection of a gas jet at the tip of the flying devices into the oncoming flow [1, 2]. Regulation of spike position or injected gas pressure permits both a considerable surface-pressure redistribution and a reduction of the drag coefficient. The effect is attained as a result of formation of flow separation zones ahead of the body, wherein the pressure is lower than behind separated shocks ahead of similar bodies without spike or gas injection.

The drag can be reduced as a result of formation of a narrow rarefied channel ahead of the body [3]. Such a channel of a rarefied gas induces separation zones and flow reconstruction near the body.

A significant drag reduction (up to ~50 – 60 % for a sphere) was found in numerical calculations of blunted [4] and pointed [5] bodies in the presence of external energy addition. The effect of an electric discharge in front of an axisymmetric body on the supersonic flow was studied in [6 – 9].

The papers [10, 11] are devoted to experimental researches of the possibility of aerodynamic drag reduction as a result of plasma injection from the body surface into the oncoming flow. Wind-tunnel tests were carried out at Mach numbers 0.59, 0.89, 0.96, 1.18, 4 and Reynolds numbers within the range $(0.82 – 2.8) \cdot 10^6$.

For these tests, a cone-cylinder model with a built-in plasma generator (plasmatron) and strain gauges was designed and manufactured. Plasma was generated as a result of an arc discharge during ~0.05 s initiated by short-circuiting the plasmatron electrodes with a thin copper wire when voltage was fed to the electrodes. The plasma from the plasmatron chamber was injected through a Laval nozzle with a Mach number $M_j = 3.65$ opposite the external flow.

During the tests, we measured the pressure in the plasmatron chamber, the axial aerodynamic force, the parameters of the wind-tunnel flow, and a series of shadowgraph pictures were obtained to study the flow field structure using a shadowgraph and a high-speed digital color video camera. The shadowgraph pictures show that injection of a plasma jet considerably changes the flow pattern near the model for all free-stream Mach numbers. Thus, the aerodynamic drag reduction up to 2 – 4 times is observed.

In [12], the results of numerical calculations at Mach number 4 with air injection from the model surface toward the external flow are presented. The geometrical model parameters, the parameters of the external flow, the jet stagnation pressure were same as in the experiment, but the jet stagnation temperature varied within the range $T_{0j} = 600 – 6000$ K. The unsteady Euler

equations of the ideal perfect gas in an integral conservative form were considered for the mathematical model, and the well-known McCormac difference scheme was used. As a result of calculations, the fields of gas parameters were obtained. At T_{0j} = 6000 K, the form of the shock waves and the drag coefficient C_x were close to the experimental ones. The table lists the values of the drag coefficient C_x for different jet stagnation temperatures and without the jet.

T_{0j} K	C_x
without jet	0.56
600	0.52
2000	0.45
6000	0.32

It is seen from the table that, with an increase in the jet stagnation temperature, the value of C_x decreases. The reason is that the specific kinetic energy increases with increasing stagnation temperature for a constant jet stagnation pressure (identical impulse), which results in an increase in the jet penetration range and a more pointed form of "an effective liquid body".

In [13], the experimental results of the influence of a hot jet of combustion products of a solid fuel injected from the model toward the external flow on its aerodynamic drag are presented. During these tests, the same model and strain gauges was used as in tests with plasmatron, instead of which a solid fuel gas generator was used. The temperature of the hot gas was about 3000 K and time of exhaustion was 4 – 8 s.

The tests were carried out in a wind tunnel at a Mach number 3. The measurements of the axial force show reduction of aerodynamic drag up to ~2 times, and the shadowgraph pictures demonstrate a significant change in the flow structure near the body. It was noticed that the form of the detached bow shock wave differed from that in the case of plasma injection. It was more pointed.

The experimental and theoretical researches performed allow us to conclude that the significant reduction of aerodynamic drag of the model as a result of injection of hot jets and plasma from the model surface toward the external flow is the result of interaction of high-energy low-density flows with the free stream.

The jets with a low density but a high specific kinetic energy can be produced using light gases He, H_2, etc. with a significantly lower stagnation temperature. Calculations of He exhaustion from the same model with a Mach number M_j = 3.65 toward the external flow (M_∞ = 4) for jet stagnation temperatures T_{0j} = 300 and 600 K are given in [14]. The mathematical model used in [12] was supplemented here by the equations of state and continuity for a two-component mixture. The calculations show that the field of relative gas parameters (pressure, density, and Mach number, except for the temperature distribution) are rather similar, and the values of the drag coefficient C_x at T_{0j} = 300 and 600 K are equal to 0.320 and 0.298, respectively.

Thus, using the injection of plasma, hot gases (air, products of combustion) at T_{0j} = 300 – 6000 K and light gases at low temperatures T_{0j} = 300 – 600 K toward the external flow from the model surface, it is possible to reduce considerably its aerodynamic drag (up to 2 – 4 times).

References

1. Krasnov N.F., Koshevoi V.N., and Kalugin V.T. Separated flow aerodynamics. Moscow: Vysshaya Skola, 1988. 350 p.(in Russian).
2. Finley P.J. The flow of a jet from a body opposing a supersonic free stream // J. of Fluid Mechanics, Vol. 26, Pt. 2, P. 337-368.
3. Artem'ev V.I., Bergelson V.I., Nemchinov I.V., Orlova T.I., Smirnov V.I., Khazins V.M. Variation in the mode of supersonic flow past an obstacle due to the formation of a narrow rarefied channel ahead of it // Izv. AN SSSR, Mekh. Zhidk. Gasa. 1989. No. 5. 146 –151.
4. Georgievskii P. Yu., Levin V.A. Supersonic flow past bodies in the presence of external heat release sources // Pis'ma Zhurn. Tekhn. Fiz. 1988. Vol. 14, iss. 8, 684 –687.
5. Levin V.A., Terentieva L.V. Supersonic flow over cone in the presence of heat supply in the vicinity of its top // Izv. RAN. Mekh. Zhidk. Gasa.1993. No.2. P. 110-114 (in Russian).
6. Gridin A.Yu., Efimov B.G., Klimov A.I., Kuzin K.A., Zabrodin A.V. Calculation-experimental study of supersonic flow past a blunt body with a spike in the presence of an electrical discharge near the nose: Preprint No. 19. Moscow: M.V. Keldysh Institute of Applied Mathematics, Russian Academy of Sciences, 1995 (in Russian).
7. Pankova M.B., Leonov S.B., Shipilin A.V. Simulation of the specific feature of the interaction of ball lighting with the physical phenomena accompanying the flight of bodies through the atmosphere // Ball Lighting in the Laboratory. Khimiya. Moscow, 1994. P. 95 –112 (in Russian).
8. Beaulieu W., Klimov., Leonov S., Kolesnikov Y., Brovkin V. Development of cold plasma technology joint BNA and Russian program // 2nd Weakly Ionized Gases Workshop Proc. Supplement. Norfolk, VA.,1998.
9. Beaulieu W., Bytyurin V., Klimov., Leonov S., Pashina A., Timofeev B. Plasma aerodynamic WT tests with 1/6 scale model of nose part of F-15. AIAA Paper 99-4825, 3rd Weakly Ionized Gases Workshop. Norfolk, VA. 1999.
10. Ganiev Yu.,Gh., Gordeev V.P., Krasilnikov A.V., Lagutin V.I., Otmennikov V.N. Experimental study of the possibility of reducing supersonic drag by employing plasma technology // Dynamics Fluid. March – April, 1996. Vol. 31, No. 2. N.Y.: Consultants Bureau (translated from Izvestia Rossiiskoi Akademii Nauk, Mekhanika Zhidkosti i Gasa. 1996. No. 2. P.177-182).
11. Ganiev Y., Gordeev V., Krasilnikov A., Lagutin V., Otmennikov V. Experimental study of the possibility of reducing aerodynamic drag by employing plasma injection // Proc. of the Third Intern. Conf. on Experimental Fluid Mechanics. Korolev, Moscow region, 1997.
12. Ganiev Y., Gordeev V., Krasilnikov A., Lagutin V., Otmennikov V., Panasenko A. Experimental and theoretical study of the possibility of reducing aerodynamic drag by employing plasma injection // Proc. of the 2nd Workshop of Weakly Ionized Gases. Norfolk, VA, April 1998.
13. Ganiev Y., Gordeev V., Krasilnikov A., Lagutin V., Otmennikov V., Panasenko A. Theoretical and experimental study of the possibility of reducing aerodynamic drag by employing plasma injection. AIAA P. 99-0603, Jan. 1999.
14. Babichev Ju., Krasilnikov A., Panasenko A., Sipachev G. Effect of plasma jet characteristics on supersonic cone-cylinder drag. AIAA P. 99-4881, Nov. 1999.

SHOCK INDUCED VORTEX BREAKDOWN

Egon Krause
Aerodynamisches Institut, RWTH Aachen
D-52062 Aachen, Germany

1. Introduction

Recent industrial investigations of compressible swirling flows in cascades seem to indicate, that longitudinal vortices being formed in channels may encounter breakdown if they are exposed to a sufficiently large axial pressure rise or to the interaction with a normal shock in a locally supersonic flow. It is then also possible that choking may occur, since the burst part of the vortex can occupy a large segment of the cross-section of the channel such that the axial flow cannot pass through the region where the stagnation point is being formed. As pointed out in [1] compressor stall observed at high loads may therefore be caused by shock induced vortex breakdown. Although a proof of this conjecture could not be given until now, since no detailed investigations of this problem are yet available, it seems plausible that vortex breakdown could at least initiate the stall mechanism or even be the prime reason for it.

In contrast to incompressible flows vortex breakdown in supersonic swirling flow so far has received only limited attention. In a way this is surprising, as it is, for example, of vital importance to avoid bursting of the primary vortices on delta wings for reasons of flight safety. As was shown by Kandil et al. in numerical studies, see e. g. [2], unsteady vortex breakdown on a delta wing may cause severe tail buffeting. A detailed study of the problem of a normal and an oblique shock interacting with a longitudinal vortex was initiated only recently at the Aerodynamisches Institut in a combined numerical and experimental investigation [3]. First results of numerical simulations were obtained for inviscid and viscous supersonic flow. The results for the normal shock immediately lead to breakdown, since in passing through the shock the axial flow was abruptly decelerated to subsonic speeds and eventually a stagnation point was formed. The computations for the case of the interaction of a straight oblique shock with a longitudinal vortex yielded breakdown only after the shock was deformed into an S-shaped structure in the vicinity of the core, yielding subsonic flow downstream from the shock with further deceleration to locally stagnant flow.

Since breakdown could not be enforced for all conditions chosen, an attempt is made here to sort out those flow parameters for which the flow can be forced to generate a stagnation point on the axis. The considerations are restricted to isentropic deceleration of the axial flow and to transition through a normal shock. As pointed out before, straight oblique shocks have to change their shape into a locally normal shock near the axis of the vortex, if breakdown is to occur, and therefore they are not considered here..

It will be shown that the governing parameters are the circulation of the vortex and the Mach number of the axial flow at large distances from the axis of the vortex. Since only the overall and not the detailed relations are of interest for the present considerations, the Rakine vortex is chosen to represent the azimuthal velocity distribution in a compressible flow field. The axial flow is assumed to be independent of the radial distance. The radial pressure distribution is first obtained by integrating the simplified radial momentum equation. Then, following [4] the axial pressure field is related to the maximum radial pressure difference, yielding a unique relation for the circulation in terms of the axial free-stream Mach number.

2. The radial pressure distribution

In order to introduce a model as simple as possible, a Rankine vortex as sketched in Fig. 1 is considered: The azimuthal, radial and the axial velocity components $w(r)$, $v(r)$, and $u(r)$ are described by

$$r < R: \quad w(r) = \Omega r, \qquad v(r) = 0, \qquad u(r) = u_\infty$$

$$r > R: \quad w(r) = \Gamma/(2\pi r), \qquad v(r) = 0, \qquad u(r) = u_\infty. \tag{1}$$

In equ. (1) r is the radial coordinate, R the core radius, Ω the constant angular velocity of the flow in the core, and Γ the circulation of the vortex. The quantity u_∞ is the uniform axial velocity far upstream. The angular velocity Ω of the flow in the core is related to the circulation Γ, i. e. $\Omega = \Gamma/(2\pi R^2)$. The flow is assumed to be compressible but inviscid.
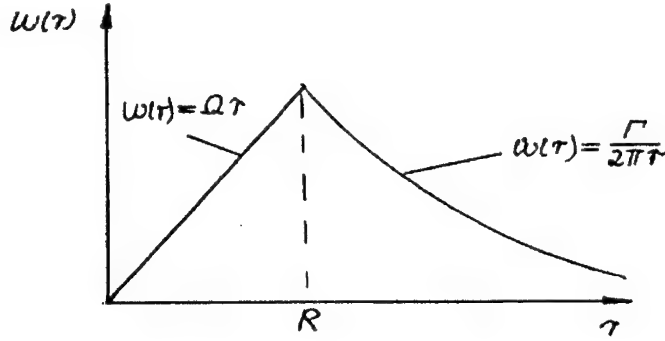
Fig. 1: Radial distribution of the assumed azimuthal velocity component: A Rankine vortex with $w(r) = \Omega r$ in the vortex core, i. e. for $r < R$, and a potential vortex with $w(r) = \Gamma/(2\pi r)$ is supposed to describe the axially symmetric flow. The axial velocity component is assumed to be uniform in r.

In addition to the radial velocity distribution just described the flow is supposed to have a constant stagnation temperature T_0, which is justified for external and also for internal flows. Since the azimuthal velocity component vanishes for $r \to 0$ and for $r \to \infty$, and as it is also assumed that the axial velocity component does not vary in the radial direction, the temperature distribution is given by

$$T(r) = T_\infty - w^2(r)/(2c_p) \quad \text{with} \quad T_\infty = T_0 - u^2_\infty/(2c_p). \tag{2}$$

Equ. (2) also implies, that the temperature on the axis is equal to the free-stream temperature, as $w(r = 0)$ vanishes there. From equ. (1) it follows that

$$r < R: \qquad T(r) = T_\infty - (\Gamma r)^2/(8\pi^2 c_p R^4),$$

$$r > R: \qquad T(r) = T_\infty - \Gamma^2/(8\pi^2 c_p r^2). \tag{3}$$

The radial pressure distribution is obtained by integrating the simplified radial momentum equation. It is assumed here, that the vortices considered are slender, i. e. the radial veloc-

ity component is small compared to the axial and the azimuthal component. As viscous forces are neglected, the radial pressure gradients are balanced by the centrifugal forces:

$$\partial (\ln p)/\partial r = [w^2(r)]/(R_G\, T) \tag{4}$$

In equ. (4) the density ρ was substituted by pressure and temperature through the thermal equation of state. Note that in equ. (4) R_G is the gas constant. After inserting equs. (1) and (3) into equ. (4), the integration is carried out within the limits $r = 0$ and $r = R$, and for the potential vortex from $r = R$ to $r \to \infty$. Both integrals are matched at $r = R$. After some rearrangement there is obtained with $p = p_\infty$ for $r \to \infty$:

$$r < R: \quad p(r)/p_\infty = [1 - (\Gamma^2/4\pi^2 R^2)/(2c_p\, R_G\, T_\infty)]^{2\kappa/(\kappa-1)}\, x$$

$$x[1 - (r^2\Gamma^2/4\pi^2 R^4)/(2c_p\, R_G\, T_\infty)]^{-\kappa/(\kappa-1)}$$

$$r > R: \quad p(r)/p_\infty = [1 - (\Gamma^2/4\pi^2 r^2)/(2c_p\, R_G\, T_\infty)]^{\kappa/(\kappa-1)} \tag{5}$$

Equ. (5) suggests the definition of an azimuthal Mach number $Ma_{c\infty}$ in terms of the maximum azimuthal velocity at the edge of the core, i. e. where $r = R$, and the speed of sound at free-stream conditions:

$$Ma_{c\infty} = w_c/(\kappa\, R_G\, T_\infty)^{1/2} \tag{6}$$

Then equ. (1) can be written as

$$r < R: \qquad T(r)/T_\infty = 1 - (\kappa-1)Ma^2_{c\infty}r^2/(2R^2). $$

$$r > R: \qquad T(r)/T_\infty = 1 - (\kappa-1)Ma^2_{c\infty}R^2/(2r^2) \tag{7}$$

It is immediately clear from equ. (7), that at the edge of the core, i. e. where $r = R$, the azimuthal Mach number $Ma_{c\infty}$ as defined above, cannot be increased arbitrarily. A certain limiting value, namely $Ma_{c\infty} < [2/(\kappa-1)]^{1/2}$ cannot be exceeded. Vice versa, equ. (7) also indicates that the temperature in the vortex reaches its lowest value for $r = R$, and for $r \to 0$, according to the model chosen, the temperature increases again, as pointed out before, and reaches its free-stream value T_∞

$$r = R: \quad T_c/T_\infty = 1 - (\kappa-1)Ma^2_{c\infty}/2. \tag{8}$$

In contrast to $Ma_{c\infty}$ the local Mach number $Ma(r)$ depends on the radial distance. It is related to $Ma_{c\infty}$ by the following expressions:

$$r < R: \qquad Ma(r) = Ma_{c\infty}(r/R)/ [1 - (\kappa-1)Ma^2_{c\infty}r^2/(2R^2)]^{1/2}$$

$$r > R: \qquad Ma(r) = Ma_{c\infty}(R/r)/[1 - (\kappa-1)Ma^2_{c\infty}R^2/(2r^2)]^{1/2} \tag{9}$$

Also the pressure distribution can be written in terms of the azimuthal Mach number as defined through equ. (6). If equ. (5) is substituted into equ. (5), it can be cast into the following form:

$$r < R: \quad p(r)/p_\infty = [1 - (\kappa - 1)Ma^2_{c\infty}]^{2\kappa/(\kappa-1)} x$$

$$x[1 - (\kappa - 1)Ma^2_{c\infty}r^2/(2R^2)]^{-\kappa/(\kappa-1)}$$

$$r > R: \quad p(r)/p_\infty = [1 - (\kappa - 1)Ma^2_{c\infty}R^2/(2r^2)]^{\kappa/(\kappa-1)} \tag{10}$$

The pressure on the axis becomes

$$r = R: \quad p(r=0)/p_\infty = [1 - (\kappa - 1)Ma^2_{c\infty}/2]^{2\kappa/(\kappa-1)} \tag{11}$$

Equ. (11) shows, that the ratio of the pressures on the axis and at far distances away from the axis decays rapidly with increasing azimuthal Mach number $Ma_{c\infty}$. The exponent $2\kappa/(/(\kappa-1))$ equals the value of 7 for $\kappa = 1.4$, and the pressure ratio $p(r=0)/p_\infty$ drops from unity for vanishing azimuthal Mach number, $Ma_{c\infty} = 0$, to zero for the limiting value of $Ma_{c\infty}$ given by equ. (6). If the axial flow is to be decelerated such that a free stagnation point can be formed, the pressure along the axis of the vortex must rise by the same amount on the axis as given by equ. (11). The deceleration of the axial flow will be considered next.

3. The deceleration of the axial flow

There are two possibilities to decelerate the flow to zero velocity. For internal flows, the cross-section of the duct can be contoured in such a way, that the flow remains isentropic. Then the pressure ratio between static and stagnation pressure is given by

$$P_0/p_{stat.} = [1 + (\kappa-1)Ma_\infty/2]^{\kappa/(\kappa-1)}. \tag{12}$$

If it is now assumed as suggested in reference [4] that the static pressure p_{stat} equals the pressure on the axis, $p(r=0)$ and if further the stagnation pressure P_0 is requested to assume the highest possible value of the pressure in the vortex, i. e. $P_0 = p_\infty$, then the reciprocate value of the pressure ratio given by equ. (11), namely $p_\infty/p(r=0)$ can be set equal to the ratio P_0/p_{stat}, given by equ. (12), There results then an expression that relates the maximum azimuthal Mach number $Ma_{c\infty}$ to the axial Mach number Ma_∞ in the form, given by the following transcendental equation:

$$[1 - (\kappa - 1)Ma^2_{c\infty}/2]^{2\kappa/(\kappa-1)} = [1 + (\kappa-1)Ma_\infty/2]^{\kappa/(\kappa-1)} \tag{13}$$

Equ. (13) can be solved for $Ma^2_{c\infty}$ to yield:

$$Ma^2_{c\infty} = 2\{1 - [1 + (\kappa-1)Ma^2_\infty/2]^{1/2}\}/(\kappa-1) \tag{14}$$

Equ (14) states, that for any axial Mach number $0 \leq Ma_\infty \leq \infty$ there exists an azimuthal Mach number $Ma_{c\infty}$, ranging from zero to its limiting value given above. The azimuthal Mach num-

ber can also be expressed through the circulation Γ. If a_∞ is the speed of sound at free-stream conditions, then

$$\Gamma^2 = 8\, a^2_\infty \, \pi^2 \, R^2 \{1 - [1 + (\kappa-1)\,Ma^2_\infty\,/2]^{1/2}\}/(\kappa-1). \tag{15}$$

In the analysis of reference [4] the breakdown criterion derived for an incompressible Rankine vortex resulted from equating the axial pressure change computed with to the Bernoulli equation with the maximum pressure difference in the radial direction. In the nomenclature of the present study the corresponding condition reads

$$w_c\,/u_\infty = (1/2)^{1/2}. \tag{16}$$

This result, which is in good agreement with experimental data for low speed flows can be recaptured from equ. (14) or (15). If the right-hand side is expanded for small values of Ma_∞, the value given by equ. (16) is readily recovered.

The other possibility to decelerate the axial flow is given by an oblique or a normal shock. As was already pointed out before, in the problem of an oblique shock interacting with a longitudinal vortex, the oblique shock is deformed locally into a normal shock near the vicinity of the axis of the vortex. It is only the strong shock, which can lead to vortex breakdown, since the weak shock does not decelerate the flow to subsonic speeds and also not to locally stagnant flow. For this reason only the normal shock is considered. With relation for the ratio of the total pressures across the normal shock given by

$$p_{02}/P_{01} = [1 + 2\kappa(Ma^2_\infty - 1)]^{1/(\kappa-1)} [(\kappa+1)Ma^2_\infty]^{\kappa/(\kappa-1)}[(\kappa-1)\,Ma^2_\infty + 2]^{-\kappa/(\kappa-1)}, \tag{17}$$

there results for $Ma^2_{c\infty}$ with equs. (11) and (12)

$$Ma^2_{c\infty} = 2\{1 - [1 + 2\kappa\,(Ma^2_\infty - 1)/(\kappa+1)]^{1/2\kappa} [(\kappa+1)Ma^2_\infty/2]^{1/2}\}/(\kappa-1). \tag{18}$$

As shown before, the azimuthal Mach number can again uniquely be expressed by the axial Mach number Ma_∞, and as before the azimuthal Mach number $Ma_{c\infty}$ can be replaced by the circulation Γ. Equ. (18) also shows, that for breakdown to occur, both Mach numbers cannot be chosen independent from each other. The above relations may therefore also be of use for establishing compatible inflow conditions for numerical calculations.

Another question that cannot be answered here is how to determine the position of the shock. For the present study it was assumed, that the shock position is in the immediate vicinity downstream from the station, where the azimuthal velocity profile is specified. The main emphasis is therefore placed on the qualitative validity of the above relation. As in incompressible flow, also in supersonic flow vortex breakdown will occur only, if the criteria given are met. The above considerations do not include the influence of shape of the radial profile of the azimuthal velocity component on the pressure variation in the axial direction, as for example explored in [5].

4. Concluding remarks

It is well known that breakdown of vortices in incompressible flow is always associated with the formation of a free stagnation point on the axis. P. Huerre and his coworkers cast this observation into a simple criterion, which by now is confirmed with experimental data.

113

In the present study, this criterion is extended to compressible flow for a Rankine vortex and an axial flow, that was assumed to be independent of the radial coordinate. First the radial pressure distribution was derived, yielding the maximum ratio for the pressures far away from and along the axis. Then the axial deceleration of the flow was considered for the case of insentropic flow and for the case of a normal shock. It could be shown that the maximum azimuthal Mach number, referenced to the speed of sound at free-stream conditions and the axial Mach number referenced to the same conditions must satisfy conditions, derived in the present study for breakdown to occur. The relations given may serve to determine compatible inflow conditions for numerical simulations.

References

1. Schlechtriem, M., Loetzerich, R.: Breakdown of tip leakage vortices in compressors at flow conditions close to stall, IGTI-ASME Conference, Orlanda, Florida, June 1997.
2. Kandil, O. A., Sheta, E. F., Liu, C. H.: Effects of coupled and uncoupled bending-torsion modes on twin-tail buffet response, in: *IUTAM Symposium on Dynamics of Slender Vortices, E. Krause and K. Gersten (eds.)*, 401-414, *Kluwer Academic Publishers*, 1998.
3. Thomer, O., Schröder, W., Meinke, M.: Numerical Simulation of Normal- and Oblique Shock-Vortex Interaction, GAMM Annual Meeting in Metz (France), 12-16 April 1999, ZAMM Band 80, Sub. 1, pp. 181-184, 2000.
4. Billant, P., Chomaz, J. M., Delbende, I., Huerre, P., Loiseleux, T., Olendraru, C., Rossi, M., Sellier, A.: Instabilities and Vortex Breakdown in Swirling Jets and Wakes, in: *IUTAM Symposium on Dynamics of Slender Vortices, E. Krause and K. Gersten (eds.), 267-*286, *Kluwer Academic Publishers*, 1998.
5. Krause, E.: Der Einfluß der Kompressibilität auf schlanke Wirbel, Abh. Aus d. Inst. der RWTH Aachen, Heft 27, 19-23, 1985.

POTENTIALITY OF HYPERVELOCITY WIND TUNNELS BASED ON PRESSURE BOOSTER PROSPECTS FOR DEVELOPING INDUSTRIAL-TEST INSTALLATIONS

A.P. Kurshin, V.P. Rukavets, N.S. Zubarev
TsAGI, Zhukovsky, Russia

TsAGI specialists have carried out comprehensive numerical and experimental studies for designing and developing hypersonic wind tunnels of the new type based on pressure boosters. In these devices the flow is provided by a piston that pushes the high-density hot gas from a low-diameter cylinder of the pressure booster into the convergent/divergent nozzle. Unlike hot-shot, shock and gun tunnels the booster-type installation generates stationary flow free of mechanical impurities and ensures a much longer work run duration. These facilities feature their low operation costs.

The efforts covered the following major areas:
- analytical research for improving the gas state equations and deriving the data necessary for evaluating the high-density gas flows; development of methods for designing the gas-dynamic facility components;
- studies for generating the high-density gas flows during experiments in aerospace industries;
- studies for preparing the superpressure technologies and other devices for the tunnel; and
- improvement of test procedures.

Several concepts of the wind tunnels with various methods for generating the working gas with the high stagnation-point parameters have been developed. A series of aerodynamic test installations and wind tunnel models are designed.

To exemplify the concept, the wind tunnel concepts depicted in Fig. 1 may be considered. These ensure the maximum stagnation temperature in the facility category in question.

In Fig. 1a version the working gas from a compressor 1 is run into the low-diameter cylinder 4 of the 1st pressure booster, isochorically heated in the heater 3 (integral with the cylinder 4), additionally compressed in 4, moved into the cylinder 12 of the main booster, finally heated (due to adiabatic compression) to the stagnation values prescribed, and pushed through the nozzle 16 into the test section, while having gas parameters constant in time.

In Fig. 1b version the working gas from the source 1 is fed into the pressure booster cylinder 4, compressed isentropically, run into the cylinder 12 of the main booster, heated in the heater 3 and throttle 10 and then additionally heated during adiabatic compression in the main pressure booster.

The versions depicted in Figs 1a and 1b do raise temperature in three stages: in the heater, owing to the positive Joule – Tomson effect in the throttle, and owing to compression in the main pressure booster.

In Fig. 1c version the working gas from the source 1 is heated in the heater 3, adiabatically compressed in the cylinder 4 of the 1st stage, fed into the cylinder 12 of the main pressure booster and adiabatically compressed here, thereafter is pushed by the piston into the nozzle 16. Temperature is raised in four stages: in the heater, due to compression in the first-stage pressure booster, due to throttling, and owing to compression in the main pressure booster.
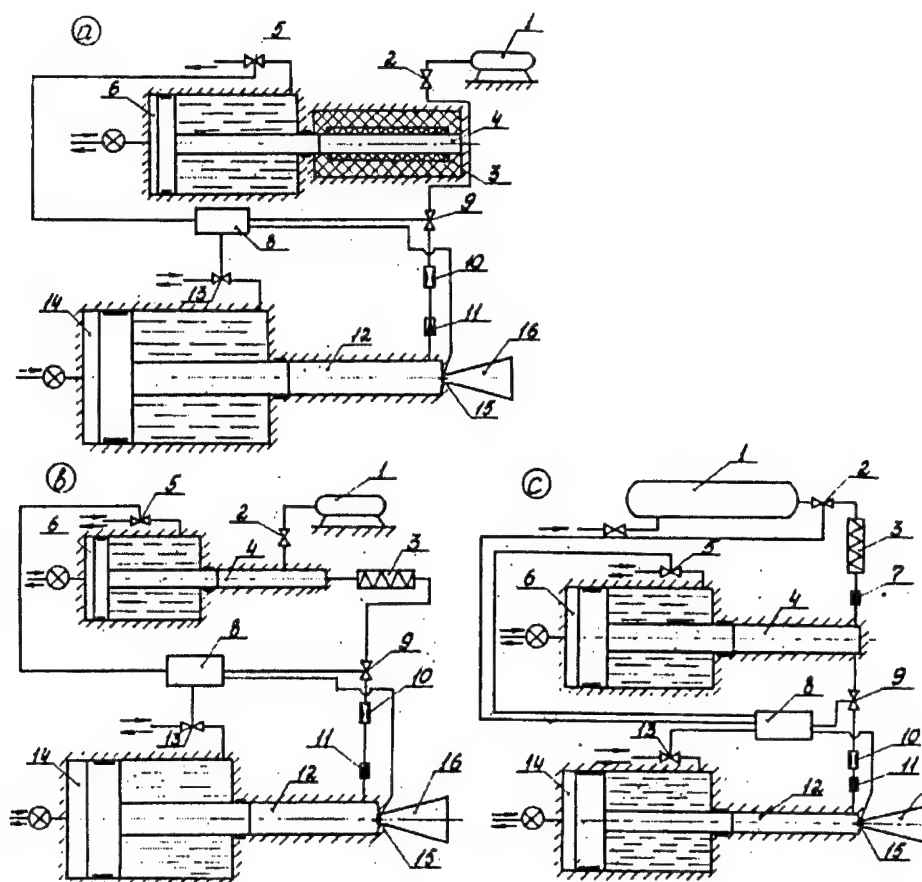
Fig. 1.
1, compressor (or gas-holder); 2, 5, 9, 13, 15, valve; 3, heater; 4, 12, low-diameter
cylinder; 6, 14, big cylinder; 7, 11, non-return valve; 8, synchronization system;
16, converging/diverging nozzle

In evaluating potentialities of Fig. 1 concepts, let us assume that the heater 3 raises temperature of the working gas (such as the air or nitrogen) to T_{ini} < 1000 K, whereas the gas source provides initial pressure P_{ini} in the low-diameter cylinders 4 as high as 100 MPa (for Fig. 1c) or 200 MPa (for Figs 1a and 1b). In this case the flow downstream of the stage 1 throttle may have parameters within the domains limited from above by curves 1 – 4 in Fig. 2. The plots are for devices where the first-stage booster can ensure the low-diameter cylinder pressure P_m < 500 or 1000 MPa at the adiabatic compression ratio of no greater than 10 for Fig. 1c. At P_0 < 300 MPa the stagnation-point parameter domains {P_0, T_0} which can be attained at no more than 10-fold compression (in the cylinder 12 of the main pressure booster) from curves 1–3, are limited with lines 5 – 7. The curve corresponding to gas compression from curve 4 is in the area {T_0 > 6000 K} and not shown in Fig. 2. Note that the upper boundaries of attainable stagnation temperature T_0 in the wind tunnels are shifted to higher values if the initial temperature T_{ini} (provided by heaters) is raised. In this case, T_0 grows by approximately the same value as T_{ini} is increased. Stagnation temperature below 3000 K may be obtained in simpler wind tunnel concepts with pressure boosters.

116
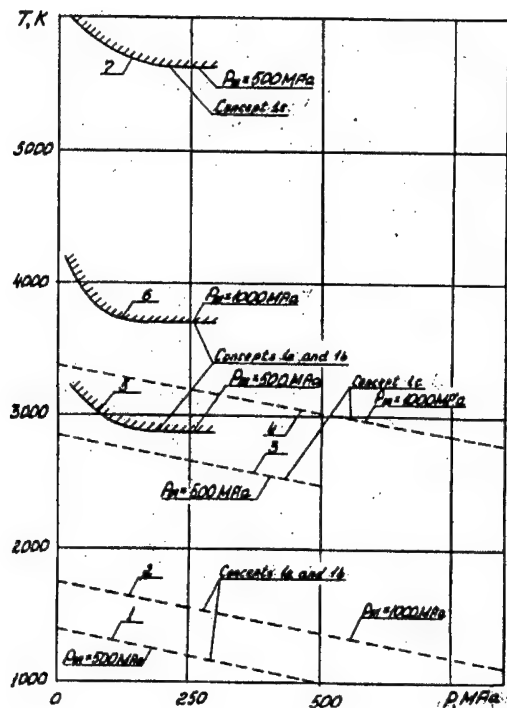
Fig. 2.

Various tunnel concepts are working from various initial gas conditions in low-diameter cylinders; thus, prior to a test run they accumulate various masses of the working gas in low-diameter cylinders of identical volumes; this immediately influences the run duration.

Figure 3 demonstrates the ratio m_i/m_1 as a function of entropy S. Here, m_1 is the mass accumulated in the low-diameter cylinder of the pressure booster with initial parameters $\{P_0 < 20$ MPa, $T_0 < 1000$ K$\}$; and m_i is the mass which can be accumulated in the same cylinder at other initial parameters specified in Fig. 3. The latter provides a reference – the values of P_0 and T_0 at which the S values take place. Figure 3 represents a general picture of the effect of initial parameters on the gas mass enclosed in a low-diameter cylinder with a certain volume.

Fig. 3.

117
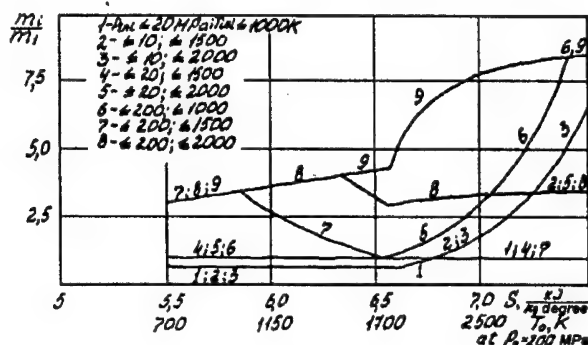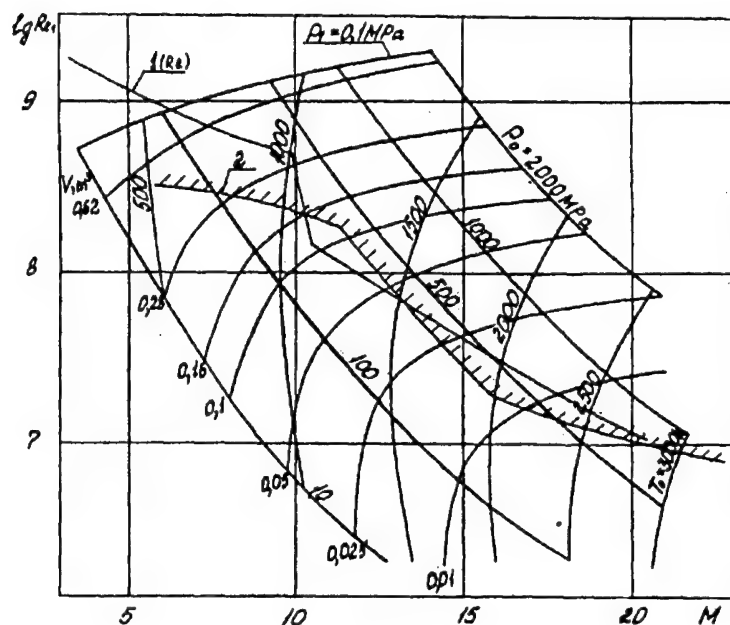
Fig. 4.

Figure 4 demonstrates a family of functions $Re_i = f(M)$ which can be at the exit of the nozzle with the diameter $D_1 = 1$ m in the case of nitrogen expansion to saturation. The lines are for various combinations of stagnation parameters: the series for $\{P_0 = const, T_0\}$ and the series for $\{P_0, T_0 = const\}$. In the diagrams M is Mach number and Re_1 is Reynolds number referred to a length of 1 m. Also, a reference is provided – the line corresponding to the nozzle exit static pressure $P_1 = 0.1$ MPa. For certain stagnation parameters the volume V of gas issuing for 0.1 seconds through the nozzle with the exit diameter of 1 m during expansion to saturation may be assessed by using Fig. 4 diagrams for particular constant V values.

Curve I in Fig. 4 is an envelope of the maximum in-flight Re numbers which are typical of the foreseen hypersonic vehicles. Curve 2 represents the upper boundary of the Re_1 number zone which may at M from 5 to 25 (in experiments with the air at the run duration over 0.1 seconds) be attained in the wind tunnels that utilize

– pressure boosters with the low-diameter cylinder volume $V = 0.1$ cu.m and pressure $P_m < 500$ MPa,

– gas sources with pressure of up to 200 MPa,

– heaters for 1000 K,

ensure stagnation parameters $\{P_0 < 300$ MPa, $T_0 < 2000$ K$\}$, and relies on the allowable overexpansion at $T_0 = 2000$ K. One can see that the curve I are rather close to the curve 2.

The above data and other characteristics of the usual hot-shot, shock and gun tunnels make it possible to conclude that the booster-type installation is notably better than the different wind tunnels throughout the hypersonic velocity range.

Versions of the booster-based tunnel may be composed of unified typical elements: pressure boosters, heaters, throttles, nozzle throats, control/synchronization systems, high-pressure compressors and pipe-lines, channels for moving hot dense gases, etc.

118

Comprehensive multidisciplinary studies were conducted to prepare various new methods and concepts. The approaches are the basis for creating new devices that outperform the components necessary for reaching the curve *2* in Fig. 4.

In general, Russian specialists possess know-how and industrial potential for developing large hypersonic booster-based wind tunnels with the test section flow diameter of 1 m and the run duration as long as 0.05 to 0.2 seconds. The facilities could offer experimental research of advanced hypersonic aircraft, while closely simulating real-flight conditions (in respect of M, Re, temperature, flow pressure and composition) and opening ways to dealing with various applied problems in gas-dynamics such as hypervelocity flow around a flight vehicle, aerodynamic heating, performance of ramjets and scramjets, etc.

RESEARCH OF HYDRODYNAMIC PARAMETERS OF STREAMS WITH APPLICATION OF FRACTAL MODELS

K. Kusaiynov, S.E. Sakipova

The Buketov Karaganda State University, Kazakhstan

By actual problem of modern physics continues to remain a problem of modelling impulse, fast variable, nonlinear hydrodynamic and heat-transport processes in fluid flows and gas. In present work was considered fluid with gas bubbles rather small gas concentration. It is known that the presence of a gas phase considerably complicates a character of current of gas-liquid mixtures on cylindrical pipes, it already at small flow velocities.

At modelling of dynamics gas-liquid mixtures with the methods of a mechanics of a continuous medium suppose superposition of some assumptions, in particular, the bubble sizes exceed much molecular- kinetic, i.e. contain rather large number of molecules. But thus sizes of gas bubble are significant less characteristic spans, lengths of waves. This supposition allow to describe macroscopic processes of distribution of waves in bubble fluids as populations mutually penetrating and interacting continuums, average reflecting interaction inside phases and between them.

It is supposed, that the macroscopic rotational structures formed at explosion, tend to self-organizing. In single-phase fluid the self-organizing is exhibited as whirlwind and their clusters, in multiphase fluid alongside with a whirlwinds the accumulations of drops of fluid or bubbles of gas as "shell" are possible, or clusters of rigid particles, i.e. the self-organizing of dispersiblis components is probable. The structures formed in multiphase mediums, have properties of self-similarity, that is confirmed in experiments with pipes of various diameters [1].

Therefore has allowed to create fractal models of a turbulence of two-phase fluid explaining known experimental outcomes [2]. The developed fractal models circumscribing bubble and projectile conditions of current of a gas-liquid medium, allow to calculate hydrodynamic parameters of a two-phase stream compatible with experimental assotiations in a broad band of velocities. The connection of fractal dimension D with factor volumetric gas concentration through an index scaling index γ (index scaled – invariant strains) is defined.

Creation of the fractal models of two-phase streams have found successful application in calculations of hydrodynamic parameters of a stream at impulse actions. As an example of the force nonlinear fast flowing process can consider electrohydraulic effect. Research of nonlinear processes accompanying an electrical discharge in a gas-liquid medium, as pure radiant of impulse pressure of large amplitude to is connected by importance it of applications in a power engineering, cryogenic engineering etc., as most economic and ecological methods.

In practice in an electrohydraulic process engineering of clearing of interior surfaces of pipes from rigid adjourment as a working medium the engineering water containing various impurities as of gas bubbles or rigid dispersiblis particles is usually used. A working medium is multiphase or, in particular, the two-phase medium representing mixture of fluid with of gas bubbles as a example of a relaxative medium supposing existence of shock waves with an oscillation structure. And at repeated impulse perturbation the water additionally is sated with gas, therefore, the conditions of shaping of the channel of a discharge, it hydrodynamic performances vary.

In installations, used in practice, the pressure reaches values $\sim 10^8 \div 10^9$ H/m^2, temperature $\sim 10^4$ K. On the other hand high-voltage electrical discharge has very small duration on time $\sim 10^{-4} \div 10^{-6}$ c, during which the medium can not exchange an energy with an environment. The

process is close to adiabatic. Nevertheless, is established, that in processes accompanying electrohydraulic effect, the entropy varies at the expense of structural reorganization of a working medium connected to a fractal nature of the most nonlinear medium and as the equation of a condition is necessary to use the equation of the polytropic PV^{κ} process = const, where κ – polytropic exponent depending on a structure of a medium. The polytropic exponent is possible to define with the help of relations

$$\kappa = (i + 2)/i . \tag{1}$$

Thus it is necessary to take into account, that the magnitude i in difference from a degree of freedom of molecular particles, characterizes a degree of freedom of turbulent motions of the macroscopic, structural elements formed in a nonlinear non-equilibrium medium at impulse addition of an energy. The degree of freedom of macroscopic motions accepts practically all continuous values in an interval ($1 \leq i \leq \infty$), while for a molecular level of motions of a value i are limited and are digital (for example, for monoatomic molecules i = 3, for diatomic – i = 5). Example of structural driving is the hydrodynamic turbulence [3], where i was determined by number of separate curls of fluid. In a developed turbulence the number of macroscopic degree of freedoms is determined [3]

$$i \sim (r_m/r_0)^3 \sim (Re/Re_k)^{9/4} , \tag{2}$$

where r_m, r_0 - space scales of driving. In the considered task to use the formula (2) it is inconvenient, as there is an arbitrariness in the definition Re_k. It is necessary to select a more universal mode of the definition i.

Most typical by a property structurality of a medium, irrespective of its concrete nature, the fractal performances are it. The fractals name plants having a structural and self-similar structure [4]. It is possible to connect fractal dimensionality through an scaling index γ, describing spatially – invariant strains, with factor gas concentration j in two-phase fluid.

Let r_m, r_0 – scales of bubble structures in two-phase fluid. Then appropriate fractal S (γ) and smooth S the surfaces are determined by a relation

$$S(\gamma)/S = (r_m/r_0)^{\gamma} . \tag{3}$$

In [5, 6] the examples of an evaluation γ for the concrete laws fractalysation of a medium are reduced, where the limiting magnitudes $\gamma_* = 0,7925$ и $\gamma_{\perp} = 0,465$, appropriate to isotropic and anisotropic cases are defined. Is shown, that all possible aspects of perturbations and strains are made between them. Taking into account (3) for fractal of a spherical symmetry we have:

$$S(\gamma) = 4\pi a_{ef}^2, \qquad a_{ef} = a(r_m/r_0)^{\gamma/2}, \qquad V(\gamma) = 4\pi a_{ef}^3/3, \qquad i = V(\gamma)/V = (r_m/r_0)^{3\gamma/2}. \tag{4}$$

where a_{ef} – effective scale, a – characteristic scale of a fractal structure.

Let's connect an scaling index γ with gas volumetric φ. Relative volume of a liquid phase is determined

$$V_l/(V_l + V_g) = 1 - \varphi, \tag{5}$$

where V_l, V_g – volumes of liquid and gas phases. Using (3) we have accordingly in cylindrical and spherical cases:

$$<r_m>/r_0 = (1 - \varphi)^{-1/\gamma} \qquad \text{and} \qquad <r_m>/r_0 = (1 - \varphi)^{-2/3\gamma}. \tag{6}$$

The formulas (6) determine $<r_m>/r_0$ of a gas phase through average value φ.

At rather large gas volumetric (a shell condition of current), the liquid phase is as though cut up, volume of fractal structures is determined by an integration from a center of drops of liquid with a fractal surface.

From relations (1), (4) and (6) we shall receive connection of a polytropic exponent k with fractal performances of a dispersiblis stream, in particular, scaling index γ, which value depends on the concrete fractalysation laws of a medium as follows:

$$\kappa = [2+(1-\varphi)^{-2/\gamma}](1-\varphi)^{2/\gamma} \quad \text{and} \quad \kappa = [2+(1-\varphi)^{-3/\gamma}](1-\varphi)^{3/\gamma}, \tag{7}$$

accordingly for cylindrical and spherical volumes.

The calculated interval of a modification of a polytropic exponent $1 < k < 3$ corresponds to an experimental range. In Fig. 1. the κ dependences from φ are reduced.
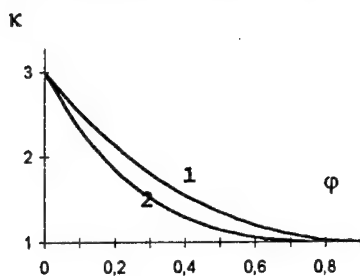
Fig.1. The dependences of a poly-tropic exponent from φ for: 1 – cylindrical, 2 – sphericses of a discharge sheet.

Therefore, the equation of a condition of a mass unit of a two-phase medium, is

$$P = P_1(\rho/\rho_1)^{\kappa}, \tag{8}$$

where P_1, ρ_1 – specific values of pressure and denseness. It should be decided together with the equations of driving, continuity and energy in view of a compressibility of a medium owing to formation of shock waves at electroexplosion.

The boundary conditions are set as lawes of conservation of mass, impulse and energy (relation the Hugoniot) at the front shock waves driven with the velocity u*. For the definition of dynamic characteristics, in particular, velocity of a shock wave u*, the law of the extension of a discharge sheet a(t) at electroexplosion is used the equation of an energy balance

$$N(t) = \frac{1}{\kappa-1} \frac{d(P(a,t)V(a,t)}{dt} + P(a,t)\frac{dV(a,t)}{dt}. \tag{9}$$

The researches have shown, that the outcome of modelling depends on a choice of an aspect of function of a potency of a selected energy N(t). The experimental dependence of a potency from time represents an oscillating and fast damping curve [7].

The advantage of volt-amper performance of an electrical circuit with a nonlinear resistance, assumes, that the oscillatory appearances should not be described by even degrees of argument, as they at an average reduce in emerging constant (not oscillatory) displacements of function from it of an equilibrium value. Then a unknown quantity the expression for a potency N (t) has an aspect:

$$N(t) = I \cdot U = \alpha_1 \sqrt{LC} \cdot \left[I^2(t) + \beta \cdot \frac{I^4(t)}{3} \right] \tag{10}$$

where I, U – force of a current and nonlinear voltage, L and C – inductance and capacity accordingly, α_1 and β – parameters of a circuit.

In Fig. 2 the dependences of a potency modification from time for various values α_1 ($\beta = \alpha_1^3$) are reduced which show, that the expression (10) correctly describes an

122
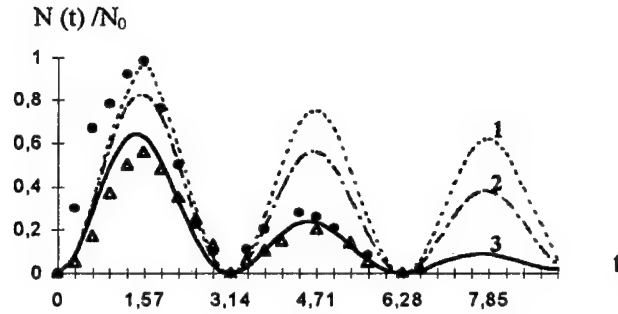
Fig. 2. Dependence of a selected potency of an energy of a discharge from time at α_1: $1 - 0,1$; $2 - 0,2$; $3 - 0,3$; experimental assotiations: $\bullet$ – at $U_0 = 60$ kV, $C = 120$ μF, $L = 1,5$ μG, $l = 0,28$ m; $\triangle$ – $U_0 = 25$ kV, $C = 0,4$ μF, $L = 0,9$ μG, $l = 0,28$ m.

experimental assotiation of a potency from time representing oscillating curve with damping. The damping happens the faster, than more parameter α_1.

Using the found regularity of selection of an energy of an electrodischarge, it is possible to trace evolution of digit space and pressure in him, thus is researched influence of byphase and connected with it fractality of a medium on dynamics of an appearance.

From the equation of an energy balance, by substituting a maximum value pressure achieved at the front of a shock wave, we shall define a temporal assotiation of the boundary of the extension of a discharge sheet a(t), which is gone with a velocity of a shock wave u*

$$a(t) = B_j \left(\frac{\kappa^2 - 1}{\kappa} \right)^{1/(3+j)} \left\{ \int_0^\tau \left[N(t) \right]^{1/3} dt \right\}^{3/(3+j)} \tag{11}$$

where

$$B_j = \left(\frac{j+3}{3} \right)^{3/(3+j)} \left[\frac{1}{2 \rho(1+j)C_j} \right]^{1/(3+j)},$$

Index $j = 1, 2$ for cylindrical and spherics of a discharge sheet, in particular

$$B_1 = (L \cdot C)^{3/8}(16/27 \cdot C_1 \cdot \rho_0)^{1/4}, \quad B_2 = (L \cdot C)^{3/10}(125/1627 \cdot C_2 \cdot \rho_0)^{1/5}.$$

The assotiation of pressure in time in an extending of a discharge sheet can be traced again from the equation of an energy balance, considering now by variable $P = P(t)$ and using the found expression for a (t). The equation (9) at a replacement of volume through a(t) gains an aspect

$$\frac{dP(t)}{dt} + f(t) \cdot P(t) = g(t) \tag{12}$$

$$f(t) = \frac{\kappa(j+1)}{a(t)^{1-j}} \frac{da(t)}{dt} \tag{13}$$

$$g(t) = (\kappa - 1) \cdot \sqrt{LC} \cdot N(t) \cdot C_j \cdot a^{j+1} \tag{14}$$

The solution of the equations (12-14) has an aspect

123
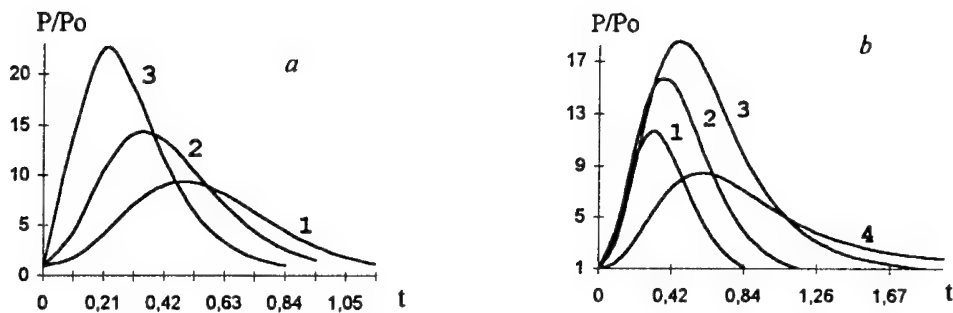
Fig. 3. Dependence of pressure in the channel of a discharge from time for case of cylindrical symmetries: a) $\kappa = 2,5$, α_1: $1 - 0,1$; $2 - 0,4$; $3 - 0,9$; b) $\alpha_1 = 0,4$,: κ: $1 - 3$; $2 - 2,27$; $3 - 1,63$; $4 - 1,11$.

$$P(t) = \exp(-\int f(t)dt) \cdot \left\{1 + \int \left[g(t) \cdot \exp(-\int f(t)dt\right]dt\right\}. \tag{15}$$

The values of pressure calculated on the formula (15) and reduced in Fig. 3, confirm a nonmonotone behaviour $P(t)$, observed in experiment [7]. The given fact is connected to that, the value $P(t)$ is not unequivocally determined by inverse proportionality to square of a discharge sheet ($\sim a^{-2}(t)$), as it the evolution depends on a derivative $a(t)$.

References

1. Isataev S.I., Kusaiynov K. Outcomes of experimental researches of current of a stream in channels // Thermophysics and Physical Hydrodynamics: The collection of the proceedings. – Novosibirsk, 1979. – P.17 - 22.
2. Kusaiynov K., Sakipova S.E. A fractal model of dynamics of two-phase fluid in a pipe // Thermophysics and Aeromechanics. – 1998. – Vol .5, No. 4. – P. 472 - 484.
3. Klimontovich Yu.L. Statistical Physics. – Moscow: Nauka, 1982. – 608 p.
4. Feder J. Fractals. – Moscow: Mir, 1991. – 254 p.
5. Shtern V.N. An elementary structural model of turbulent intermixing // Structural Turbulence / Ed. Goldshtik. – Novosibirsk: Inst. Thermophysics Sib. Branch, USSR Acad. Sci., 1982. – P.136 - 161.
6. Zhanabaev Z.Zh. A structural model of turbulent jets // Informations of USSR Acad. Sci., Series of engineering science. – 1988. – Vol. 5, № 18. – P. 83 - 88.
7. Krivitcky E.V. Dynamics of electroexplosion in fluid. Kiev: Nauk.dumka,1986. – 205 p.

VELOCITY MEASUREMENTS IN HYPERSONIC FLOWS

S. Larigaldie, M. Lefebvre, A. Mohamed, I. Ribet and J.P. Taran
ONERA, Fort de Palaiseau
91120, Palaiseau, France

INTRODUCTION

This paper procures an update on work recently accomplished at ONERA on several classes of optical techniques developed for velocity measurement in hypersonic facilities. Diode Laser Absorption Spectroscopy (DLAS) is one of the oldest measurement methods and has allowed much progress to be made in the field of combustion. It is a line of sight technique, so it does not give full spatial resolution, but it procures great accuracy in acquiring stream translational temperature and velocity, and is now used routinely in ONERA's high-enthalpy hot-shot wind tunnel F4 and in a shock-driven tunnel. It is presented first.

The technique of Coherent anti-Stokes Raman Scattering (CARS), also widely used for temperature measurements in combustion, has recently demonstrated its great potential in the analysis of high-enthalpy, nonequilibrium streams. Encouraging velocity measurement results were performed in a low enthalpy blow-down wind tunnel.

Electron-Beam-induced Fluorescence (EBF) is difficult to implement in high enthalpy streams because of the stray light, but use of the pseudo-spark switching device, which produces a strong electron beam, overcomes the problem. The velocity field could be recorded across a boundary layer into the flow core by using time-delayed imaging.

DIODE LASER ABSORPTION

Absorption, like emission spectroscopy, does not indicate the position of the absorbing species along the line of sight. Gas parameters can be measured only if the absorbing medium is homogeneous or presents some spatial symmetry, so it is applicable to determination of free stream parameters. A review of DLAS results in hypersonic european facilities was recently given.[1] The measurements at F4 have been performed with tunable semiconductor diode lasers in the infra-red. They offer the resolution needed in the absorption domain of molecules like NO or H_2O which are often naturally present. The wavelength is tuned to less than 10^{-3} cm^{-1} by adjusting the temperature and the current through the diode. The lines are scanned at up to 10 kHz The velocity of the flow is deduced from the Doppler shift of the lines, when the beam is not perpendicular to the flow axis; the measurement can be very accurate.

Figure 1 shows the experimental arrangement in the F4 wind tunnel. The emitting and receiving optics remain outside the vacuum chamber. The diode is kept in a cryostat cooled at 10 K by a helium compressor. Stabilized generators are used to monitor the diode temperature and current for laser emission. Wavelength and intensity calibration are accomplished with a Perot-Fabry and a low pressure cell filled with a known quantity of NO. The beam enters the vacuum chamber through CaF_2 windows and crosses the flow at an angle of 60° relative to the axis. HgCdTe photodetectors with 10 MHz bandwidth are used to measure the beam intensity. The electric signals are digitized at up to 10 MHz to get adequately resolved spectra. Two hundred pairs of spectra are taken at 1 to 10 kHz for each wind tunnel run. The corrected absorption spectrum is then matched to simulated spectra through an iterative non linear least-squares fitting procedure: one then derives the velocity of the flow, the temperature and concentrations of the species.
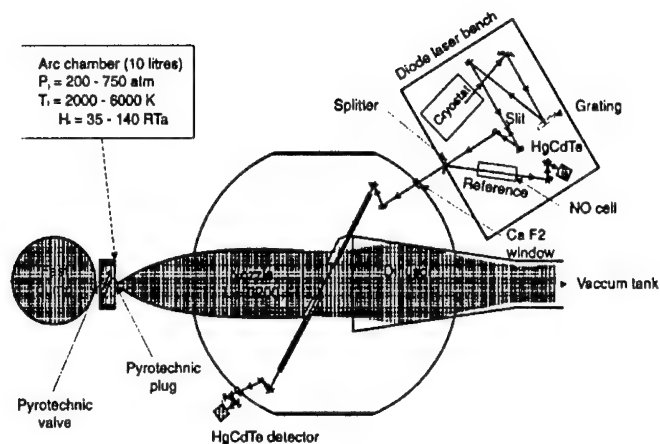
Fig. 1. Schematic of the DLAS spectrometer at F4.

Figure 2 shows a typical evolution of absorption spectra separated by 50 ms during a run. As the flow establishes, the Doppler-shifted line appears alone; subsequently, the line with zero Doppler shift grows as the test tank gradually fills with the spent gases. The derived velocity is displayed in figure 3 versus time for that particular run and for three others, showing the repeatability. Static temperature and NO density were also obtained.
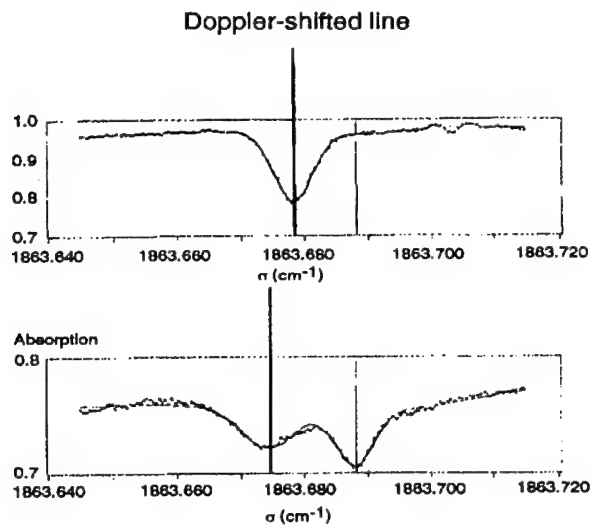
Fig. 2. NO spectra recorded during one of the F4 runs at reduced enthalpy 100.
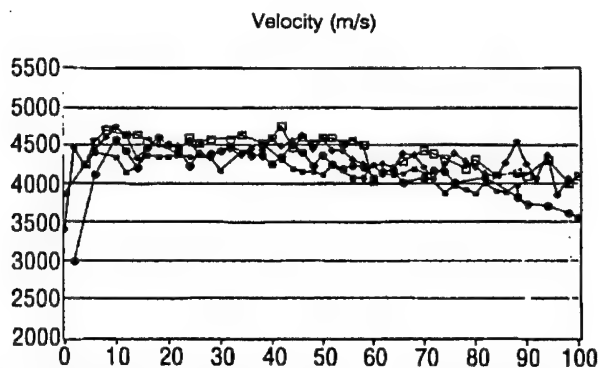
Fig. 3. Velocity from four wind tunnel runs.Horizontal scale is in ms.

CARS

CARS is a nonlinear optical method that affords the species selectivity of Raman scattering combined with excellent signal generation efficiency and stray light rejection.[2] It requires two pulsed lasers. One has fixed frequency (angular frequency ω_1) and the other is tunable (frequency ω_2, with $\omega_2 < \omega_1$). The beams from the two lasers are colinearly focused at the point of interest. If their frequency difference matches the vibration frequency of a molecular species present at the focus, the vibrations of the molecules are driven coherently, generating a coherent phase grating in the gas that scatters the incoming "pump" laser beams into a new colinear and coherent signal beam at frequencies $\omega_1 + (\omega_1 - \omega_2)$, called the anti-Stokes sideband. Spatial resolution is typically 1–10 mm long, with a beam diameter of 50 µm. Normally, CARS is employed for temperature and species concentration. Lately, it has been shown to also provide velocity from single shot, spatially-resolved recordings of transient signals. Several experimental strategies are possible. The first one consists in heterodyning the CARS signal from the flow, which is subject to Doppler shift, against, e. g., a static cell signal (Fig. 4). The ω_1 beam is typically a long (20–30 ns) pulse while the ω_2 beam is a short pulse applied at the beginning of the ω_1 pulse. The vibrational coherence is thus created early and keeps ringing like a tuning fork while it is probed by the tail of the ω_1 pulse, thus giving monochromatic signals. The two signals beat on the square law detector, and the beat frequency is proportional to the velocity. The approach operates down to 5 Pa. It has been demonstrated[3] in the free stream at the Mach 10 R5Ch (Fig. 5).
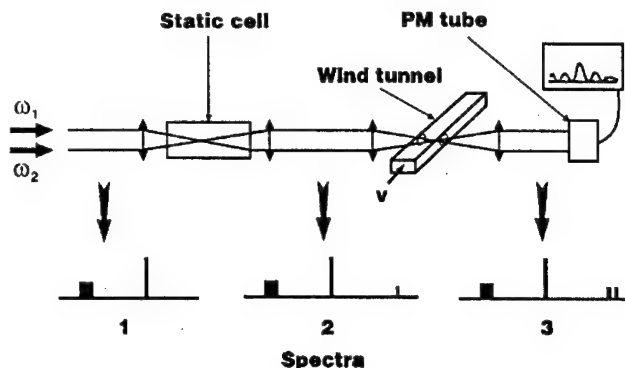
Fig. 4. Schematic diagram for CARS velocity measurement in a hypersonic flow.
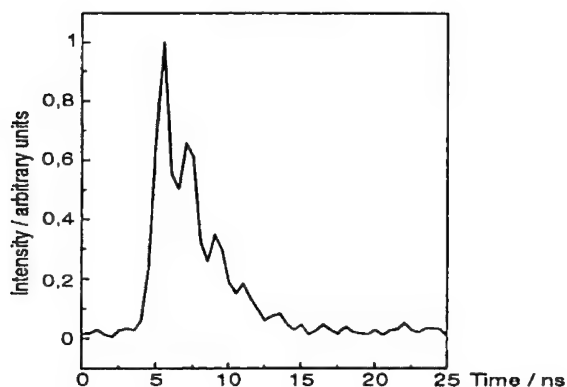
Measured velocity = 1500 m/s
Spatial resolution
Φ 50 μm x 2 cm

Fig. 5. Typical transient CARS self heterodyning trace at R5.

It works best on vibrational transitions. However, it is impaired by dephasing collisions, which destroy the molecular coherence and accelerate signal decay, so it should not be used at densities above a few 10^{-2} normal. The coherence is also destroyed by molecular random motion. At low pressure, this property gives an approach to static temperature measurement, through a measurement of the signal decay time. The temperature dependence also places a lower limit on the velocity that can be measured since at Mach 1 the beat period becomes comparable to the decay time and becomes difficult to determine. Finally, data reduction requires computer simulation to account for all obscuring effects like pulse shape, coherence decay, strong field effects, etc.

•excitation

Pump grating ✚ Stokes ⟹ Coherence grating

• readout

Probe grating (stationary) ✚ Coherence gr. (moving) ⟹ modulated signal
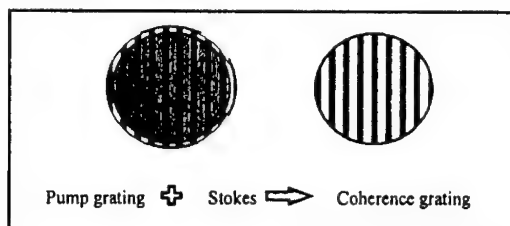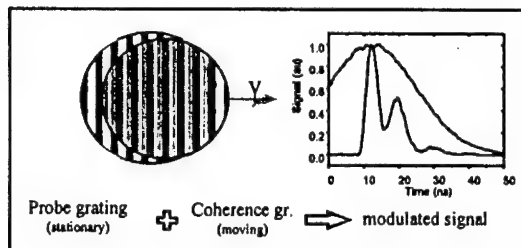
Fig. 6. Alternative CARS scheme for velocity measurements in rarefied flows based on a spatially modulated coherence grating and a BOXCARS beam arrangement.

128

A second attractive strategy is to create a spatially modulated grating of molecular coherence in the gas using the interference fringe pattern of intersecting laser beams (Fig. 6). For this purpose, the long pulse ω_1 pump beam is divided into two parallel beams that are focused to a common point and the short pulse ω_2 beam (also called Stokes by spectroscopists) is overlapped onto the ω_1 fringe pattern to produce the spatially modulated coherence pattern.[4] It is of interest in the velocity measurement to have long lasting coherences, so that as many periods of oscillation as possible can be recorded. While one could in principle still use vibrational resonances as a support of molecular nonlinearity, rotation proves superior here because of its longer coherence life in the face of collisions. In other words, it tolerates higher pressures. In addition, molecular nonlinearity is higher, procuring better signal strength, i. e. better detectivity. This technique has also been implemented in the R5Ch wind tunnel. The trace at the bottom of figure 6 is typical of the signal obtained as a consequence of the beating between the two gratings.

EBF VELOCITY IMAGING

EBF is obtained using electron guns like those used in electron microscopy. More powerful sources like pseudo-sparks are sometimes utilised. The high energy electrons induce broadband excitations onto the molecules under probe and ionise them. For N_2 at 10^{-4} normal density, the main process is:

$$N_2 + e_p^- \rightarrow N_2^{+*} + e_p^- + e_s^-,$$
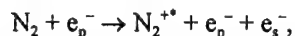
where e_p^- is a primary electron (from the electron beam) and e_s^- a secondary electron of a few eV energy emitted during the formation of the N_2^+ ion; this ion which is excited by the collision into one of its vibronic states, denoted by the * symbol, promptly loses its electronic energy via emission of a photon:

$$N_2^{+*} \rightarrow N_2^+ + h\nu$$
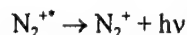
in the near UV. The luminescence is interesting because its intensity is proportional to the N_2 number density and its spectral content reveals the original population distribution on the quantum states of the N_2, allowing rotational and vibrational temperature measurements to be performed. This is achieved by dispersing the spectrum of the emitted fluorescence.

The secondary electrons remain confined in the immediate vicinity of the ions by the space charge, and keep having low energy collisions with them; these collisions re-excite the ions and maintain a luminescence by the processes:

$$N_2^+ + e_s^- \rightarrow N_2^{+*} + e_s^-$$
$$N_2^{+*} \rightarrow N_2^+ + h\nu.$$
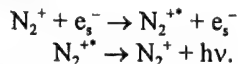
This may cause the luminescence to persist several μs or tens of μs after the electron beam has been turned off if the medium remains exposed to a bias voltage.

EBF has so far been used primarily in low or medium enthalpy facilities for imaging. Illumination is achieved by rastering the cw beam emitted by the electron gun, giving a trapezoidal field. Work at high enthalpy facilities is impaired by the weakness of the scattering. Higher current electron beams are then required. The pseudo-spark source is an ideal electron gun for such work and it has been used for velocity measurements. If a pulsed beam of small diameter is employed, the plasma it creates in a thin column of excited gas can be photographed after some delay, showing its displacement. One can then visualise the velocity field along one line, over a length of about 20 cm. This approach was tested recently[5] at F4. Figure 7 shows the experimental arrangement (nozzle not to scale) and Figure 8 the plasma column convected by the flow after 5 μs (top). The top of the column, which lies in the boundary layer, is bent, showing

the velocity gradient. The lower quarter is in the jet core. The experimental results are presented in the figure 9.

Note that the data are more dispersed near the collector rod, as a consequence of both aerodynamic disturbance and diffuse behaviour of the discharge near the linear, perpendicular electrode. In the flow core one measures velocities of the order of 4000–4500 m/s, within 5–10 % of
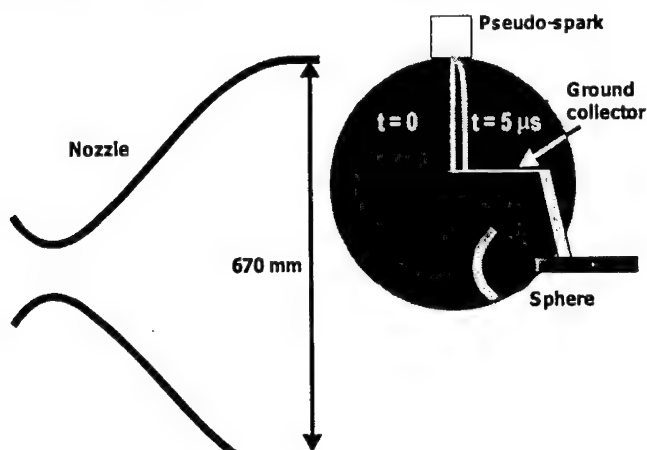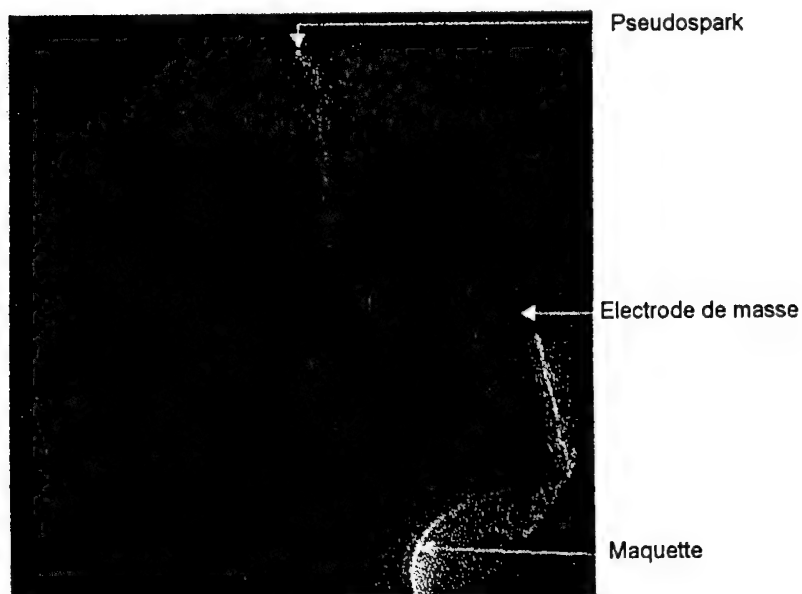

Fig. 7. Schematic of the EBF velocimetry.

Fig. 8. EBF image using a 60 kV pseudo-spark gun (top, on the edge of the circular field); exposure time 0.3 µs; circular field of view diameter: 40 cm; model is an 8 cm-dia sphere.
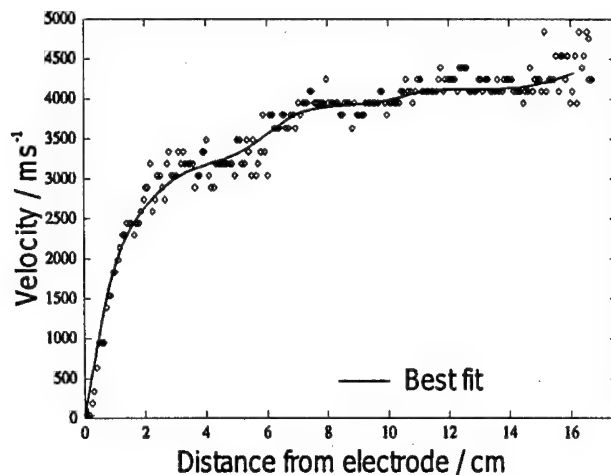
Fig. 9. Velocity profile derived from the data of Fig. 8.

the DLAS results. Note that an essential element of success here was to maintain a bias between the pseudo spark and the electrode, so that the electrons remaining in the convected plasma column kept exciting the ions to sustain the luminescence over the 5 μs. Some small problems still need attention. The thin ground electrode aligned along the flow and used to collect the charges is causing some light disturbance in its vicinity; thus the method is not fully non intrusive. Further, the penetration depth is only 20 cm for the moment. Progress in this area is to be expected.

CONCLUSION

Several promising techniques have been tested in hypersonic facilities and have entered active service, particularly the DLAS method. CARS is very promising but it is delicate and may need a year or two of progress to become usable in high enthalpy facilities. The key is the development of reliable tunable OPO sources that deliver short pulses at the diffraction limit. EBF can be employed for visualisation of a convected plasma column burned into the flow by a pseudospark gun. This is an elegant approach to extract velocity profiles from the most luminous streams.

REFERENCES

1   Mohamed A., Henry D., Faléni J.P., Sagnier P., Soutadé J., Beck W. and Martinez Schramm J. Infrared diode laser absorption spectroscopy measurements in the S4MA, F4 and HEG hypersonic flows. Intern. Symp. on Atmospheric Reentry vehicles and Systems, Arcachon, 1999. March 16-18.
2   Druet S.A.J. and Taran J.P. CARS spectroscopy. Prog. Quant. Elec. 1981. Vol. 7. P 1-72.
3   Lefebvre M., Péalat M. and Strempel J. Single shot time-domain CARS: application to temperature and velocity measurement in supersonic flows. Opt. Letters. 1992. Vol. 17. P 1806-1808.
4   Lefebvre M., Scherrer B., Bouchardy P. and Pot T. Transient Grating Induced by Single-Shot Time-Domain Coherent anti-Stokes Raman Scattering: Application to Velocity Measurements in Hypersonic flows. JOSA B. 1996. Vol. 13. P 514-20
5   Larigaldie S., Ory M., Bize D., Soutadé J., Mohamed A. and Taran J.-P. Velocity Measurement in Hypersonic Flows using Electron-beam-assisted Glow Discharge. AIAA J. 1998. Vol. 36. P. 1061-1064.

STUDY OF HYPERSONIC BOUNDARY LAYER STABILITY ON A CONE USING ARTIFICIAL DISTURBANCES

A.A.Maslov, A.N.Shiplyuk, A.A.Sidorenko

Institute of Theoretical and Applied Mechanics SB RAS,
630090, Institutskaya, 4/1, Novosibirsk, Russia

Introduction

The research of laminar-turbulent transition in a boundary layer at hypersonic velocities is of great importance in terms of calculation of heat loadings and aircraft drag. In the course of experimental study of turbulence generation mechanisms in a hypersonic boundary layer, the emphasis is the on study of its stability relative to what is called natural disturbances, i.e., the disturbances which are initially present in the stream of the wind tunnel. Using this method, at the moment quite a few experimental data has been obtained [1, 2]. At the same time, the potential of this method is reasonably limited. It is connected primarily to the impossibility of obtaining phase information about the disturbances studied. Some extra information may be gleaned though use of correlation measurements [3].

At the present time, the method of artificial disturbances gains more and more acceptance for investigations of this type, because it allows one to extract more detailed information about wave processes in the boundary layer. Such researches in compressible flows were originated by Laufer and Vrebalovich [4], who used a mechanical generator of pulsations. The first researches of stability in a hypersonic boundary layer with the help of artificially generated disturbances were made by Kendall [8]. To excite disturbances, he used a linear electrical glow discharge on the surface of a flat plate. In a supersonic boundary layer, the researches of this kind were carried out by Maslov and Kosinov [5], Schneider [6], Corke [7]. Point and linear electric-discharge sources were applied in works [9, 10] at free stream Mach number $M_\infty = 5.92$.

This paper deals with research of hypersonic boundary layer stability on a sharp cone at zero angle of attack. In spite of the fact that such researches were realized, there is no yet clarity in the question, the development of what special disturbances causes laminar-turbulent transition at wind tunnel investigations. Besides, as long as second mode disturbances are considered to be responsible for transition at hypersonic velocities, the research of their wave characteristics is demanded.

Experimental apparatus

The experiments were carried out in the hypersonic wind tunnel T-326 ITAM SB RAS at $M_\infty = 5.92$. T-326 is a blow–down wind tunnel of the ejector type with exhaust to atmosphere. The run time is determined by the regime and for $M_\infty \approx 6$ it reaches 20 minutes. Models are placed in an open jet test section with flow core diameter of 180 mm. To avoid condensation of air, heating is realized with the help of an electrical heater. The Mach number flow field non-uniformity does not exceed 0.7% for $M_\infty = 5.92$. In the course of each run, the pressure P_0 and temperature T_0 in settling chamber were measured and kept constant with accuracy of 0.5 %. The level of mass flow fluctuations under experimental conditions ($M_\infty = 5.92$, $T_0 = 390$ K,
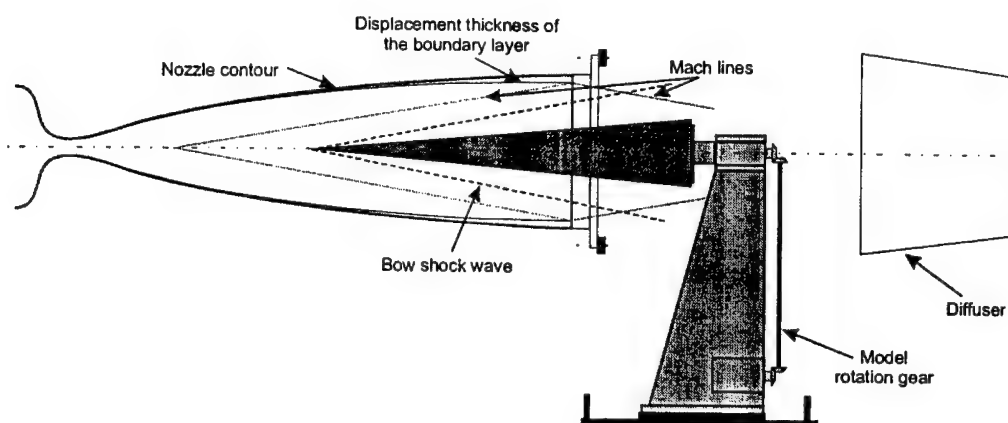
Figure 1. The scheme of the model disposition in T-326.

$P_0 = 1.01$ MPa, $Re_1 = 12.5 \cdot 10^6$ m^{-1}) makes approximately 1 %; this is typical of conventional wind tunnels.

The wind tunnel T-326 is equipped with a three-component traversing gear which provides an accuracy of 0.1 mm for the movement along the longitudinal coordinate x and 0.01 mm for the movement along the normal coordinate y. Besides, for model rotation around the longitudinal axis, a rotation gear is used, which provides a rotation accuracy of 0.1°, and the model nose wobble does not exceed 0.25 mm (Fig. 1).

The experiments were conducted on a sharp cone 500 mm long with a half-angle of 7°. The nose radius does not exceed 0.1 mm. The model is made of steel and consists of three parts (Fig. 2). Model parts are joined one to another by a threaded fastener with the use of a seal curtain; part dimensions are given in the figure. After the model assembling, it was grinned and polished that minimize the joint influence on boundary layer flow.

The changeable noses with various radii of bluntness were produced for the purpose of further use of this model to study boundary layer stability on a blunt cone. The middle part of the model is hollow to ensure its fast heating up when the wind tunnel is started. On this part, a source of artificial disturbances is mounted and also a thermocouple which is intended for the control of the model temperature regime.
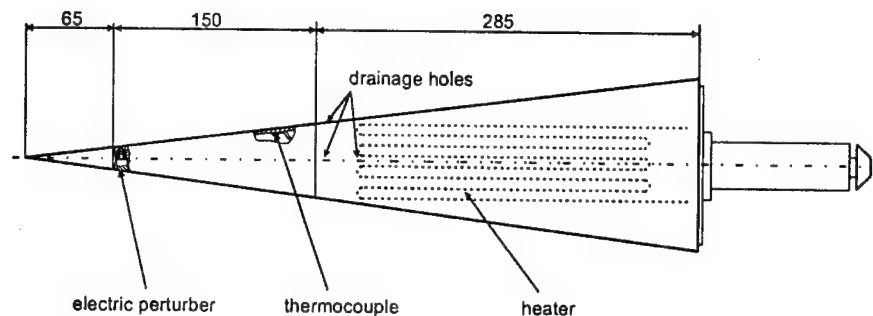
Figure 2. Sketch of the test model.

The tail part of the model is also hollow and has orifices for measurement of pressure distribution on the model surface and for ensuring model installation at zero angle of attack. Ten pressure taps are situated along the generatrix of the cone and four orifices – in one section in diametrically opposite locations. At model installing, it was necessary to ensure the equality of pressure on the surface in these four points. In addition, the tail part was equipped with a heater and it allowed one to sustain the necessary model temperature in the intervening periods from one wind tunnel run to another and to achieve faster the required temperature conditions during the run. During the measurements, the model walls were under adiabatic conditions.

Artificial disturbances were generated with a point electric glow discharge source, similar to that used in [5, 9]. The disturbance source was situated 70 mm from the model nose. The source chamber was connected to the model surface through a hole 0.5 mm in diameter. The source was supplied from a high-voltage impulse generator producing impulses of 1.5 kV voltage and duration of 1 μs. Negative voltage was supplied to the central source electrode, and the model body operating as the second electrode was grounded.

The frequencies of generated pulsations were chosen basing on calculation of boundary layer stability (Linear Stability Theory, LST) and also basing on the data of investigations of natural disturbance development on this model. The chosen frequencies corresponded to ones of the most unstable disturbances of the first and second modes ($f = 78.125$ kHz, $F = 2\pi f/(\mathrm{Re}_1 U_e) = 38 \cdot 10^{-6}$ and $f = 269$ kHz, $F = 129.4 \cdot 10^{-6}$ respectively).

To measure pulsations, a constant temperature hot-wire anemometer (CTA) was used. Wire probes 1 mm long made of 5–μm tungsten wire were applied. It ensured the frequency range of measurements up to 500 kHz. During the experiment, alternative and direct electric signals from the CTA were converted by two 12-bit ADC and were stored in a personal computer. To exclude random fluctuations and reveal artificial disturbances, a phase-locked ensemble averaging of time series was used. For this purpose, the recorded time-series of 1024 samples were summed 256 times. The recording was synchronized with ignition of an electric discharge. By this means, noncorrelated natural noise was eliminated, and the signal from the artificial disturbance was found despite of it's small amplitude.

Results

A hot-wire probe was moved in longitudinal and vertical directions, at the same time the model was rotated. As a result, three-dimensional distributions of pulsations were obtained and decomposed into a Fourier series. Besides, investigation of natural disturbances in the boundary layer was executed in the ordinary manner.

The measured cross distributions of natural and artificial disturbance amplitudes on the sharp cone are typical for a laminar hypersonic boundary layer. Figure 3 shows the distribution of pulsations of the mass flow rate for natural disturbances (integral over all the frequency range) across the boundary layer and also the distribution of the artificial disturbance amplitude and the results of calculation. The artificial disturbance amplitude distributions (as well as the results of calculations) were obtained for the first mode frequency $f = 78.125$ kHz. For all frequencies, the fluctuation amplitude maxima are grouped in a narrow layer approximately at $0.75 \div 0.8\delta$. The distribution of the artificial disturbance amplitude agrees with the natural one and LST calculations.

As the value of the longitudinal phase velocity C_x weakly depends on the wave inclination angle χ, the measurements of C_x were realized in the center of the wave packet in the maximum fluctuation layer. The measured phase velocity is equal to 0.89 and 0.9 for the first and seconds mode respectively. Spatial amplitude distributions and phases of artificial disturbances were also obtained in the layer of maximum pulsations.
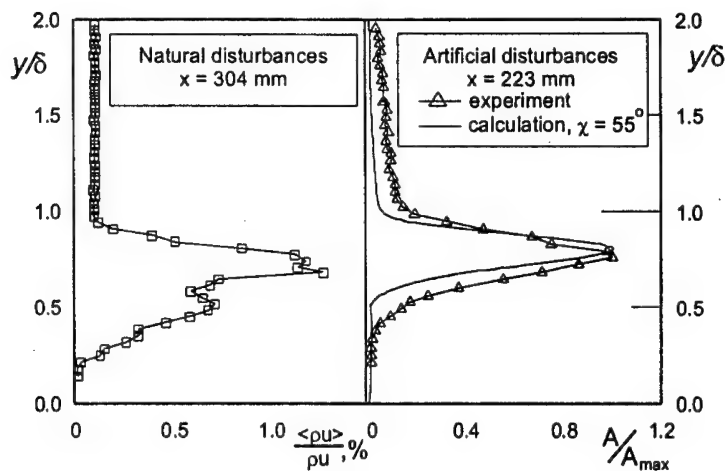
Figure 3. Cross distribution of disturbance amplitude.

Figure 4 shows the examples of distributions of the amplitude A and phase Φ of artificial disturbances in the maximum pulsation layer versus the angle of model rotation θ. For the distributions corresponding to the first mode disturbances, the presence of two strong peaks of the amplitude is typical and also a great change of Φ by θ. The transverse distributions of A and Φ obtained are similar for all studied sections. Small asymmetry caused by the source was found in each x section. For the second mode, disturbances one wide peak and a weak change of the phase across the wave packet were found.

Spatial transversal amplitude spectra were obtained after Fourier decomposition in the standard manner [10] and presented in Fig. 5. In this case, the model rotation angle θ was chosen as a spatial coordinate so that the spanwise wavenumber β had the scale rad/(deg of θ). It is seen that the spectra for all sections are similar and two peaks with $\beta \approx 28$ rad/deg are distinguished in the spectra for the first mode (Fig. 5a). Since the flow considered is a conic one, this value of β corresponds to waves with various χ in dependence on the coordinate x. As x increases, wave packet expansion occurs, and the peaks in the spectrum correspond to waves with smaller inclination angles. Depending on the position of the section, the peaks correspond to a pair of inclined waves with $\chi = 40 \div 49°$ which predominate in the wave packet.

In spatial spectra obtained for disturbances of the second–mode frequency, there is one peak with $\beta = 0$. Because the source generates a wave packet consisting of waves with various inclination angles, these waves are found in transversal spectra of sections which are distant quite far from the source. But as the packet recedes from the source, the share of inclined waves at the second–mode frequency decreases, and the two-dimensional wave ($\beta = 0$) begins to dominate in the wave packet (Fig. 5b).

Amplification rates $-\alpha_i = \dfrac{1}{2A}\dfrac{\partial A}{\partial R}$ of inclined waves of the first mode obtained from spectra are in the range $-\alpha_i = 0.9 \div 1.7 \cdot 10^{-3}$. Calculation in terms of LST for this range of $R = Re^{1/2}$ yield $-\alpha_i = 1.6 \cdot 10^{-3}$ for the most unstable waves of $\chi = 57°$. The measured amplification rate for the second mode is $-\alpha_i = 3.4 \cdot 10^{-3}$ and the calculated value is $-\alpha_i = 2.1 \cdot 10^{-3}$.
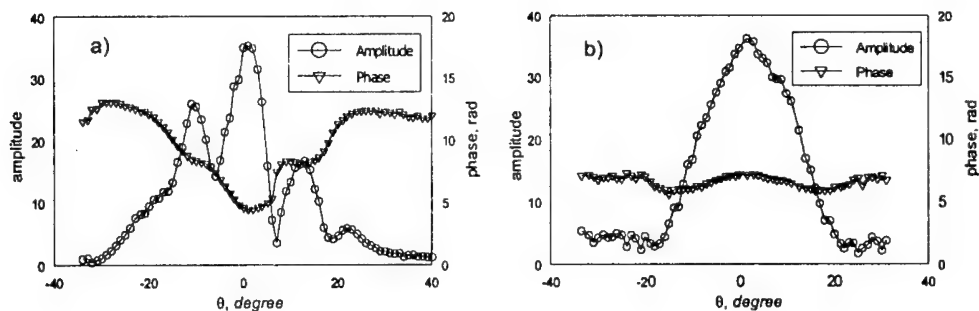
Figure 4. Transversal distribution of amplitude A and phase Φ for first ($R = Re^{1/2} = 1663$) (a); and second (b) mode ($R=2216$) disturbances.
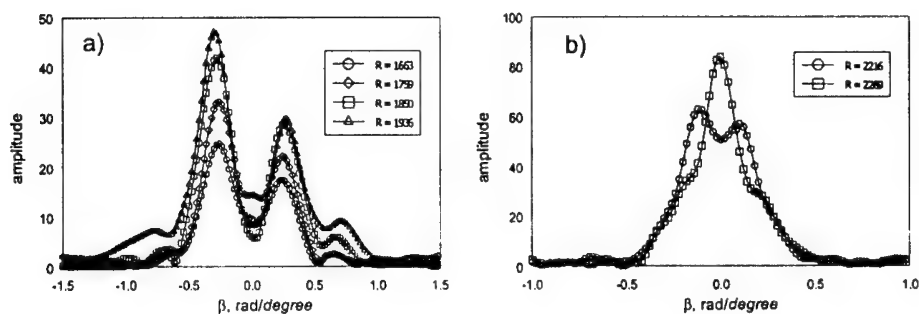
Figure 5. Transversal wave spectra of disturbance amplitude for first (a) and second (b) mode disturbances.

Thus, from the results obtained it follows that inclined disturbances are the most unstable at the frequency which corresponds to the first mode. The difference between experimentally obtained χ and $-\alpha_i$ and those calculated by locally parallel theory is related to the peculiarities of wave packet development in a conic flow, namely, to the turn of the plane wave front, as the longitude coordinate rises. At the same time, it is shown that plane waves are the most unstable at the second–mode frequency and their amplification rates exceed amplification rates of disturbances of the first–mode disturbance. This result agrees with the results of research of natural disturbance development [1,2] and theory predictions.

Acknowledgements

References

1. Reed H., Kimmel R., Schneider S., Arnal D. Drag prediction and transition in hypersonic flow. AIAA Paper –1997, No. 97-1818.
2. Stetson K., Kimmel R. On hypersonic boundary-layer stability. AIAA Paper –1992, No. 92-1737.

3. Kimmel R., Demetriades A., Donaldson J. Space-time corellation measurements in a hypersonic transitional boundary layer. AIAA Paper –1995, No. 95-2292.
4. Laufer J. Vrebalovich T. Stability of supersonic laminar boundary layer on an insulated flat plate // J. Fluid Mech –1960. –Vol. 9, P. 257-299.
5. Maslov A.A., Kosinov A.D., Shevelkov S.G. Experiments on the stability of supersonic laminar boundary layers // J. Fluid Mech., –1990. –Vol. 219, P.621-633.
6. Ladoon D. W., Schneider S. P. Measurements of controlled wave packets at Mach 4 on a cone at angle of attack. AIAA Paper –1998, No. 98-0436.
7. Corke T.C., Cavalieri D.A. Controlled experiments on instabilities and transition to turbulence in supersonic boundary layers. AIAA Paper –1997, No. 97-1817.
8. Kendall J. M. Jr. Supersonic boundary layer stability experiments. Air Force Report. –1967. –Vol. 2, No. BSD-TR-67-213.
9. Maslov A.A., Shiplyuk A.N., Sidorenko A.A., Tran Ph. Experimental investigation of the hypersonic boundary layer stability on a cone with a flare // Intern. Conf. on the Methods of Aerophysical Research: Proc. Pt 2.–Novosibirsk, 1998. P. 156-162.
10. Maslov A.A., Shiplyuk A.N., Sidorenko A.A., Arnal D.. Experimental investigation of the hypersonic boundary layer receptivity to acoustic disturbances // Izvestia RAS, Mekhanica zhidkosti i gaza. –1999. No.5, P. 89-95

REFLECTION OF AN OBLIQUE SHOCK WAVE IN A REACTING GAS WITH A FINITE LENGTH OF THE RELAXATION ZONE

A.E. Medvedev

Institute of Theoretical and Applied Mechanics SB RAS,
630090, Novosibirsk, Russia

Reflection of an oblique detonation wave was considered in [1] under the condition that the reaction takes place at the shock-wave front in an infinitely thin zone. Actual kinetics of chemical reactions has a finite (though often small) length of the relaxation zone. This assumption is valid in one-dimensional problems or problems with normal shock waves, particularly, if the detailed flow pattern in the vicinity of the shock wave is not of special interest. In the problems of reflection of detonation shocks, as is shown below, the relaxation zone length cannot be ignored.

In the present paper, we consider a model of a reacting gas with a characteristic ignition delay $\tau_i > 0$ and a characteristic time of reaction $\tau_r > 0$. Shock polars for an arbitrary level of completeness of the chemical reaction are built to analyze the reflection conditions of an oblique detonation wave. Based on the analysis of the shock polars, conditions of transition from regular to irregular (Mach) reflection are derived.

Relations on an oblique shock wave. We consider a plane steady flow of a reacting gas in the vicinity of a shock wave. The flow pattern is shown in Fig. 1.
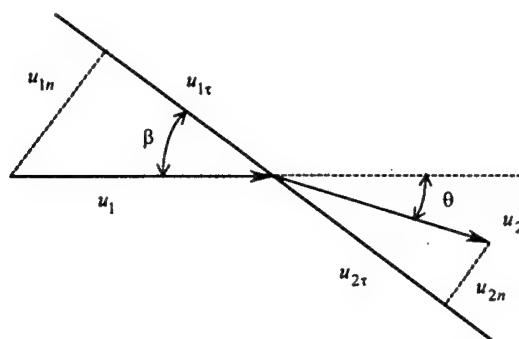
Fig. 1. Reflection of an oblique shock wave in a reacting gas.

The laws of conservation on the oblique shock wave (Fig. 1) have the form [2]

$$\rho_2 u_{2n} = \rho_1 u_{1n}, \tag{1}$$

$$\rho_2 u_{2n}^2 + p_2 = \rho_1 u_{1n}^2 + p_1, \tag{2}$$

$$q_2^2/2 + e_2 + p_2/\rho_2 = q_1^2/2 + e_1 + p_1/\rho_1, \tag{3}$$

$$u_{2\tau} = u_{1\tau}, \tag{4}$$

where ρ_i is the density, u_{in} is the normal component of velocity, $u_{i\tau}$ is the tangential component of velocity, p_i is the pressure, e_i is the specific internal energy, $q_i^2 = u_{in}^2 + u_{i\tau}^2$ is the squared modulus of velocity, $i = 1$ ahead of the shock wave, and $i = 2$ behind the shock wave.

The internal energy of the gas (for a polytropic gas) is determined by the relations

$$e_1 = p_1 V_1/(\gamma_1 - 1) + \kappa, \quad e_2 = p_2 V_2/(\gamma_2 - 1), \tag{5}$$

where γ_1 and γ_2 are the ratios of specific heats for the gas before and after the chemical reaction, respectively, $(1 < \gamma_2 \le \gamma_1)$; κ is the reaction heat per unit of the gas mass $(\kappa \ge 0)$; and $V_i = 1/\rho_i$.

From Eqs. (1)-(5), we obtain the relationship between the angles θ and β

$$\theta = \arctan\left[\cot\beta \frac{\gamma_1 M_1^2 \sin^2\beta - \gamma_2 + \sqrt{\Psi}}{(\gamma_2 + \cos^2\beta)\gamma_1 M_1^2 + \gamma_2 - \sqrt{\Psi}}\right] \equiv \Theta(\beta; M_1, \gamma_1, \gamma_2, \overline{\kappa}_1), \tag{6}$$

where $\Psi = \left(\gamma_1 M_1^2 \sin^2\beta + 1\right)^2 - \left(\gamma_2^2 - 1\right)\left[2\left(\frac{1}{\gamma_1 - 1} + \overline{\kappa}_1\right)\gamma_1 M_1^2 \sin^2\beta - 1\right]$, $\overline{\kappa}_1 = \kappa/(p_1 V_1)$. We denote the function inverse to (6) as

$$\beta = B(\theta; M_1, \gamma_1, \gamma_2, \overline{\kappa}_1). \tag{7}$$

The pressure on the oblique shock wave is given by the formula

$$J \equiv p_2/p_1 = (1 + \overline{\Omega} + \sqrt{\Omega})/(\gamma_2 + 1), \tag{8}$$

where $\overline{\Omega} = \gamma_1 M_1^2 \sin^2\beta$, $\Omega = \overline{\Omega}^2 - 2\frac{\gamma_2^2 - 1}{\gamma_1 - 1}\overline{\Omega} + \gamma_2^2 - 2(\gamma_2^2 - 1)\overline{\Omega}\overline{\kappa}_1$.

Equation of the shock polar. It is convenient to analyze the flow with oblique shock waves using shock polars [2]. For the case of a reacting gas with heat release and variable ratio of specific heats, the shock polars have not been constructed previously – this will be done below.

From the laws of conservation (1)-(5), we obtain the equation for the shock polar $J = J(\theta; M_1, \gamma_1, \gamma_2, \overline{\kappa}_1)$ in the form of an implicit equation

$$\tan\theta = \left[(J-1)\sqrt{F-1}\right]/\left[\gamma_1 M_1^2 - (J-1)\right], \tag{9}$$

where $F = \frac{2\gamma_1 M_1^2}{(\gamma_1 - 1)(J-1)} \frac{(\gamma_1 - \gamma_2) + (\gamma_1 - 1)\left[(J-1) - (\gamma_2 - 1)\overline{\kappa}_1\right]}{(\gamma_2 + 1)(J-1) + 2\gamma_2}$.

Shock polars (9) for nonreacting $\Lambda = \Lambda(\theta; M_1, \gamma_1, \gamma_1, 0)$ and reacting $\Lambda = \Lambda(\theta; M_1, \gamma_1, \gamma_2, \overline{\kappa}_1)$ gases are plotted in Fig. 2 (here $\Lambda = \ln J$).
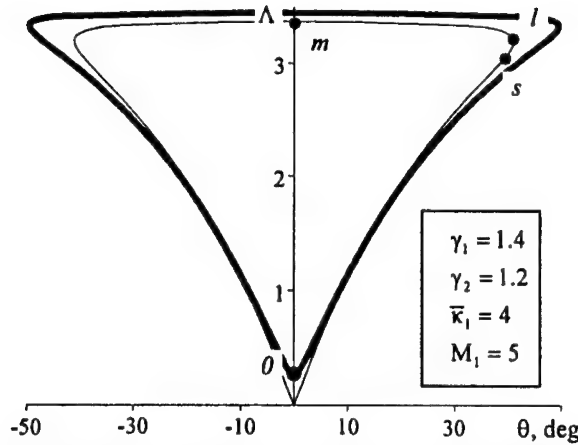
Fig. 2. Shock polars for nonreacting (thin curve) and reacting (bold curve) gases.

The shock polar $J = J\left(\theta; M_1, \gamma_1, \gamma_2, \overline{\kappa}_1\right)$ (Fig. 2) has four characteristic points: point 0 is the beginning of the shock polar, point m corresponds to the normal shock wave, point l refers to the limiting angle of flow turning behind the oblique shock wave (detachment criterion), and point s corresponds to the sonic shock wave.

The point l on the shock polar divides the shock waves into two families: weak family $(J < J_l)$ corresponding to shock waves attached to the wedge and strong family $(J > J_l)$ corresponding to the flow around the wedge in the presence of counterpressure or an opposite shock wave [3].

The point s on the shock polar (see Fig. 2) corresponds to a shock wave behind which the gas velocity equals the velocity of sound. For the shock-wave strength $J < J_s$, the flow is supersonic behind the shock; for $J > J_s$, the flow is subsonic. The point s is found from the condition $M_2\left(\theta_s; M_1, \gamma_1, \gamma_2, \overline{\kappa}_1\right) = 1$.

For the reacting gas $\left(\overline{\kappa}_1 > 0 \text{ or } \gamma_1 \neq \gamma_2\right)$, the shock polar begins at the point $J_0 > 1$:

$$J_0 = \left(\gamma_1 M_1^2 + 1 - \sqrt{\Delta_0}\right)\big/\left(\gamma_2 + 1\right), \tag{10}$$

where $\Delta_0 = \gamma_1^2 M_1^4 - 2\gamma_1 M_1^2\left[\dfrac{\gamma_2^2 - \gamma_1}{\gamma_1 - 1} + \left(\gamma_2^2 - 1\right)\overline{\kappa}_1\right] + \gamma_2^2$. Note that the shock polar for the nonreacting gas $\left(\overline{\kappa}_1 = 0 \text{ and } \gamma_1 = \gamma_2\right)$ begins at the point $J_0 = 1$ (or $\Lambda_0 = 0$).

Reflection of an oblique shock wave with the relaxation zone. The flow pattern of reflection of an oblique shock wave is shown in Fig. 3. The gas ignites downstream of the wedge apex (point A) at the point F_0. The distance between the point F_0 and the wedge apex equals

140

the length of the ignition induction zone. The ignition front $F_0 R_0$ generated a compression wave. In this compression wave, the ignition induction time decreases. The compression wave interacts with the incident shock wave, which leads to wave bending (section $H_0 R_0$). The ignition induction time vanishes, and a single detonation wave is formed. The structure of a bent shock wave and a compression wave is called a "λ-structure" [4]. The combustion zone $F_0 H_0 R_0 T T_* F_k$ is marked by gray color in Fig. 3.

Fig. 3. Reflection of an oblique shock wave with the relaxation zone.

The relationship between the angles β_1 and β_0 is found from the condition of equal slopes of the flow behind the shock waves $A H_0$ and $R_0 T$:

$$\Theta\left(\beta_1; M_1, \gamma_1, \gamma_2, \overline{\kappa}_1\right) = \Theta\left(\beta_0; M_1, \gamma_1, \gamma_1, 0\right),$$ wherefrom we obtain

$$\beta_1 = \overline{B}\left(\beta_0; M_1, \gamma_1, \gamma_2, \overline{\kappa}_1\right). \tag{11}$$

At the point T, the shock wave reflection for the nonreacting gas (the reaction has not begun yet) with an angle of inclination β_T occurs:

$$\beta_T = B\left(\overline{\theta}_0; M_2, \gamma_1, \gamma_1, 0\right) - \theta_0. \tag{12}$$

Here $\overline{\theta}_0 = \Theta\left(\beta_1; M_1, \gamma_1, \gamma_1, 0\right)$ is the inclination angle for the incoming flow in the nonreacting gas, which corresponds to an oblique shock wave with an angle of inclination β_1.

In the combustion zone (section $T Q_*$), the reflected shock wave becomes curved, and the angle of inclination after the end of the chemical reaction becomes equal to β_k

$$\beta_k = B\left(\theta_0; M_2, \gamma_1, \gamma_2, \overline{\kappa}_2\right) - \theta_0, \tag{13}$$

where $\overline{\kappa}_2 = \overline{\kappa}_1\left(p_1 V_1\right)/\left(p_2 V_2\right)$, M_2 is the Mach number, p_2 is the pressure, and V_2 is the specific volume behind the incident shock wave after the end of the chemical reaction.

Transition criteria between regular and Mach reflection. Regular reflection exists for angles of inclination of the incident shock wave $\beta \leq \beta_d\left(M_1\right)$ (detachment criterion [2]). The domain of regular reflection includes a subdomain with a subsonic flow behind the reflected shock wave, which is impossible without counterpressure [3]. Thus, we require the flow behind the reflected shock wave to be supersonic and denote the critical angle $\beta_M\left(M_1\right)$. It can be shown that we always have $\beta_M\left(M_1\right) < \beta_d\left(M_1\right)$. The difference between β_M and β_d is small, since the points "s" and "l" on the shock polar are close to each other (see Fig. 2).
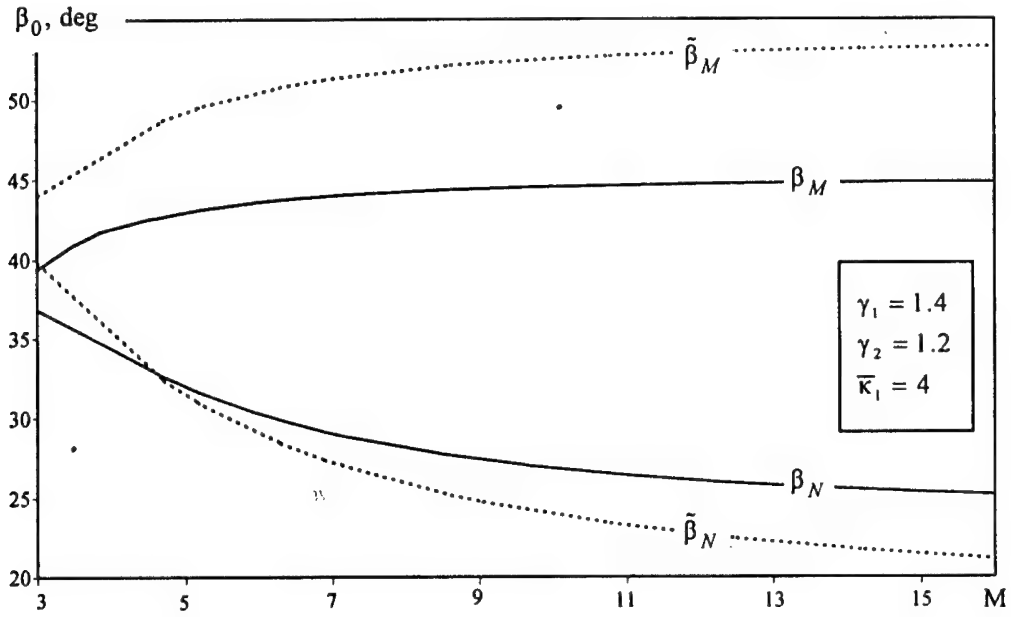
Fig. 4. Critical angles β_0 in the reacting gas. Curves β_N and β_D are given with account of the reaction zone length, curves $\tilde{\beta}_N$ and $\tilde{\beta}_D$ are plotted without the reaction zone.

For the reacting gas, the critical angles are calculated similarly to that described in [2], and the derivation is not given here. Since $\beta_T > \beta_k$ (Fig. 3), the critical angles β_0 calculated for the reflection at the point T ($\beta_0 = \beta_M$) are smaller than those calculated from the shock $Q_* E$ ($\beta_0 = \tilde{\beta}_M$). The critical angles β_0 are plotted in Fig. 4. Note that $\tilde{\beta}_M$ is the transition criterion without the account of the reaction zone.

142

Mach reflection exists until the angle $\beta \geq \beta_N(M_1)$ (von Neumann criterion [2]). Calculating the critical angle of the von Neumann criterion with account of the reaction zone length and with an infinitely thin reaction zone, we obtain two transition criteria: $\beta_N(M_1)$ and $\tilde{\beta}_N(M_1)$, respectively (Fig. 4).

It is seen from Fig. 4 that the criterion of transition from regular to Mach reflection (sonic criterion) is $\beta_M(M_1)$, since $\beta_M(M_1) < \tilde{\beta}_M(M_1)$ for all M_1. The situation is more complicated for the von Neumann criterion. For $M_1 \gtrsim 4,5$, we have $\beta_N(M_1) > \tilde{\beta}_N(M_1)$, and for $M_1 \lesssim 4,5$, we obtain $\beta_N(M_1) < \tilde{\beta}_N(M_1)$. The criteria $\beta_N(M_1)$ and $\tilde{\beta}_N(M_1)$ intersect at $M_1 \approx 3$.

Conclusion. Shock polars (Eq. (9) and Fig. (2)) are constructed for arbitrary heat release behind an oblique shock wave. Based on the analysis of the flow structure, the following criteria of transition from regular to Mach reflection and back are obtained. Regular reflection is possible (Fig. 4) for the angles of the incident shock wave

$$\beta_0 \leq \beta_M\left(M_1; \gamma_1, \gamma_2, \overline{\kappa}_1\right).$$

Mach reflection is possible (Fig. 4) for the incident shock angles

$$\beta_0 \geq \max\left[\beta_N\left(M_1; \gamma_1, \gamma_2, \overline{\kappa}_1\right), \tilde{\beta}_N\left(M_1; \gamma_1, \gamma_2, \overline{\kappa}_1\right)\right].$$

It is shown (Fig. 4) that the account of the relaxation zone length leads to a significant refinement of the transition criteria.

REFERENCES

1. **Li H., Ben-Dor G., Grönig H.** Analytical study of the oblique reflection of detonation waves // AIAA Journal. – 1997. – Vol.35. – No.11. – P.1712-1720.
2. **Courant R., Friedrichs K.** Supersonic flow and shock waves. – New York: Interscience, 1948.
3. **Rozhdestvenskii B.L.** Refinement of the theory of supersonic inviscid flow around a wedge // Matematicheskoe modelirovanie. – 1989. – Vol. 1. – No. 8. – P. 99-102.
4. **Vlasenko V.V., Sabel'nikov V.A.** Numerical simulation of inviscid flows with hydrogen combustion behind shock waves and in detonation waves // Combustion, Explosion, and Shock Waves – 1995. – Vol. 31. – No. 3. – P. 118-133.

FUEL SUPPLY SYSTEMS FOR INVESTIGATION OF COMBUSTION PROCESS IN HOT-SHOT WIND TUNNELS

A.A. Mishunin, R.V. Nestoulia, A.V. Starov

Institute of Theoretical and Applied Mechanics SB RAS, Novosibirsk, Russia

At the present time the researches of supersonic combustion in high-enthalpy facilities of short action are realised. These facilities provide stationarity of Mach number and have two operating regimes concerning to type of total pressure changing during operating regime. Operating regime with pressure multiplicator ensures quasi-stationarity of total pressure in free stream flow up to 80 ms. Operating regime without multiplicator is characterised by falling of total pressure during the whole experiment (more than three times). Thus one of urgent methodical problems of researches in impulse wind tunnels is provision of constant (given) fuel equivalence ratio during the whole experiment at tests of engine (ramjet/scramjet) model with combustion. At wind tunnel operation with or without multiplicator two various ways of fuel supply and calculation of its outflow should be used.

The determining parameters at provision of constant given fuel equivalence ratio are: total area of critical cross section of injector nozzles, loading pressure (initial pressure) of fuel system tank, and the volume of fuel tank. To find out these parameters, a special equipment and software tools has been produced. At known dependence of air mass flow (in wind tunnel) versus time and given critical cross section of fuel nozzle, it allows one to determine the loading pressure of fuel tank and its volume, or with prescribed loading pressure it is possible to find out necessary area of injector cross section, i.e. to choose fuel flow rate.

The theoretical and experimental researches of scramjet confirm the necessity of application of high-boiling hydrocarbons up to flying velocities which correspond to Mach numbers $M = 7...8$. In spite of less calorific power and lower cold-resource (in comparison with hydrogen), hydrocarbons turn out to be more effective in acceleration zone because of less specific volume. But liquid hydrocarbons (kerosene for example) demand extra preparation to improve mixing and ignition. One of the basic methods of kerosene preparation is kerosene heating with transfer in gas phase. At this stage there is a number of problems which demand extra investigations, partly, for realisation of experiments in high-enthalpy facilities of short action. That is why two fuel systems were elaborated to supply low-boiling (hydrogen) and high-boiling (kerosene) fuels.

The system for gaseous fuels has two independent channels with separate fuel supply through main and additional injectors. The difficulty of elaboration problem was that measurements of forces acting on injecting device during fuel outflow and combustion were necessary to be ensured. In fact the fuel tank (Fig. 1) was established on balance together with injector section. As a consequence, it was demanded to assure their force separation. So, manufacturing of two separate tanks was eliminated. The hydrogen fuel tank was made as two-sectional one. Each section of the tank has a mobile light piston inside. At the operation with multiplicator this piston separates fuel and displacing gas (air). The law of pushing pressure changing must be agreed with pressure changing in wind tunnel prechamber. At the operation without multiplicator this piston permits to regulate the volume of tank section with the help of special fixed support. The tank has a special "discharging" system of mounting, to decrease force, which acting on the balance to a minimum.

Each section of the fuel tank is intended for supplying of main injectors and additional distributed injecting, thus it has separate systems: fast-acting valve, connecting manifold and a
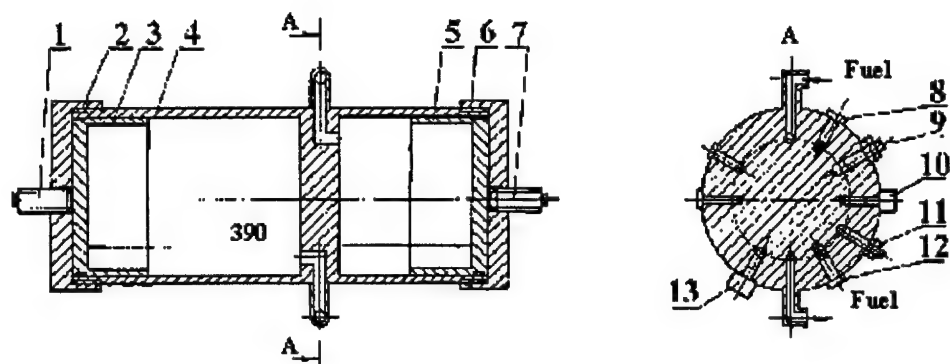
Fig. 1. The two-sectional tank for gaseous fuels.
1, 7 – support; 2, 6 – cap nut; 3, 5 – mobile piston; 4 – tank body; 8, 12 – thermocouple; 9, 11 –
charging fitting; 10, 13 – pressure gage.

measuring block. The fast-acting valve presents a device for diaphragm breakthrough with the help of pyrocartridge with electric control. The electric impulse is generated in Rogovsky coil at the moment of discharge in the prechamber and, with necessary delay (or without it) it explodes the removable valve pyrocartridge. Powder gases push a cylindrical knife with big pressure, the knife cuts off a metallic or lavsan diaphragm (it depends on pressure value). Such a scheme of fast-acting valve allows one to get operate time not more than 2 ms. It is confirmed by the results of experimental tests (Fig. 2).

The measuring block includes a pressure gage and a thermocouple. It permits to measure initial loading pressure, pressure and temperature changing in the fuel tank at fuel outflow. On these evidence a choice and calculation of necessary fuel equivalence ratio in the experiment with combustion is possible. The connecting manifold has big length and complicate configuration inside the injector section and thereby it is impossible to obviate pressure losses in manifold from the tank to critical cross section of fuel nozzles. So, the pressure in injector device was measured further (for each part of fuel system) near the critical section.
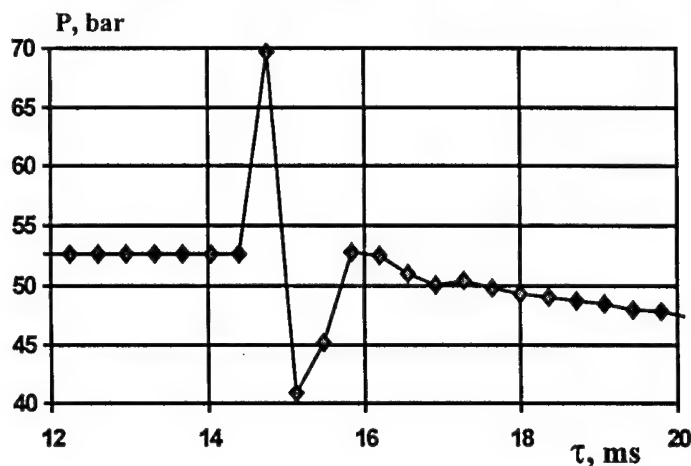
Fig. 2. The fast-acting valve opening from 14 ms up to 16 ms.

145
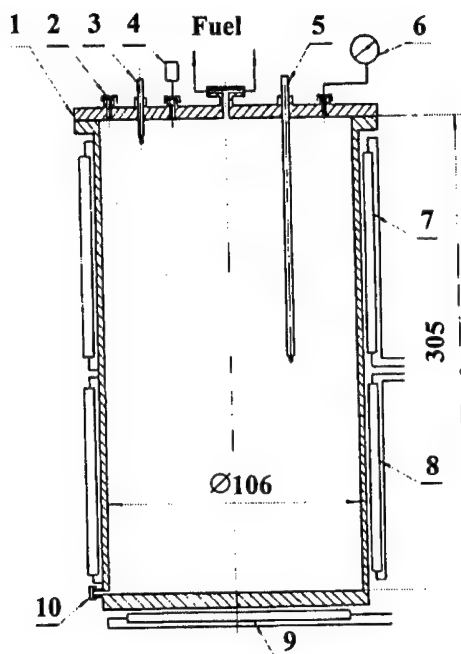
Fig. 3. The kerosene tank with heater. 1 – tank body; 2 – charging fitting; 3, 5 – thermocouple; 6 – manometer; 7, 8 – side ohmic heater; 9 – main ohmic heater; 10 — unloading fitting.

The fuel tank for kerosene (Fig. 3) presents a container of 6.2 litres volume. It was calculated for pressure of $P = 25$ bar when temperature is $T < 450$ °C. The assemble presents a stainless steel cylinder with flange head. Container bottom is made as one-piece and equipped with ohmic heater of 1 kW. On the side surface there are two additional ohmic heaters of 1.1 kW power. All tank surfaces beyond the heaters are protected with heat-insulating materials including supplying manifolds up to fast-acting valves. In the bottom part of the assembly there is a unloading fitting. On tank head there are various fittings for kerosene charging, for connection with pressure gages, with pressure-relief valve, etc. The kerosene tank has two thermocouples, which are situated in its top and bottom parts of tank.

To determine parameters of fuel system an algorithm was developed and a software of calculation was created. Calculation algorithm is based on assumption concerning adiabatic outflow of gaseous fuel from constant volume through sonic nozzle with known values of critical cross sections of the injector nozzles or maximum initial pressure of fuel. To define the law of change of fuel flow rate in time an iterative process is used. The program works under Windows-95 operation system and has friendly user- interface. The software allows one to calculate the fuel tank volume and loading pressure with known air mass flow distribution to provide constant in time required value of fuel/air equivalence ratio.

The realised calibrating tests and the major series of main tests have shown (Fig. 4), that difference in configuration of these channels on final zones inside the injector section. The
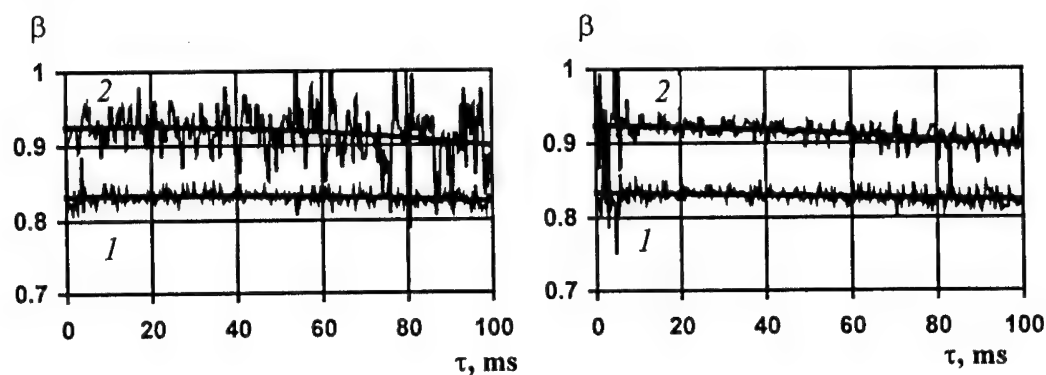
Fig. 4. The pressure losses in the manifolds for main (1, 3) and additional (2, 4) injection at different loading pressure (1 – 90 bar, 2 – 10 bar, 3 – 40 bar, 4 – 39 bar).

146
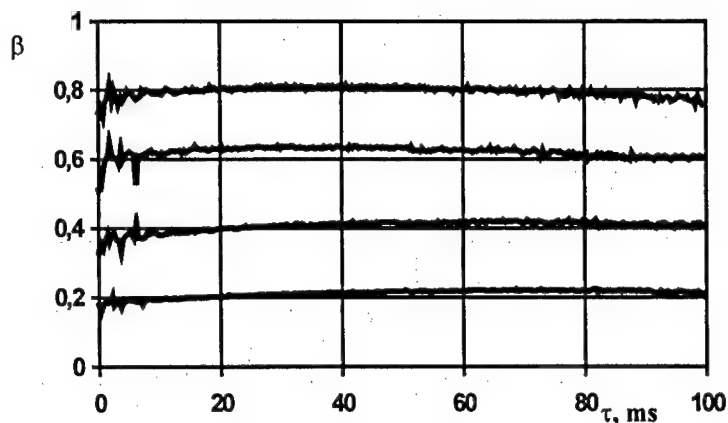
Fig. 5. Fuel – air equivalence ratios for two channels of hydrogen supply at different runs.

counting of pressure losses in supplying manifolds have raised the accuracy of fuel flow rate definition. At given total fuel equivalence ratio, the system of gaseous fuel supply permits to obtain various ratios for the main and additional channels (Fig. 5).

Also the calibrating tests of the tank were carried out with kerosene heating and transfer into gas phase with further outflow in atmosphere without wind tunnel start. The results are obtained for different mass of kerosene and different levels of pressure and temperature. Fig. 6 is shown a result of 175 gram of kerosene heating up to 420°. It is seen that heating up to 300° causes increase of kerosene vapour pressure and reaches 9.5bar at temperature maximum. Result analysis of calibrations with kerosene heating has shown that it is possible to use offered design tank, to provide demanded fuel-air equivalence ratio during the operation with wind tunnel IT-302M.

The developed equipment and program have allowed to realise a big series of experimental researches of supersonic combustion processes. The laws of hydrogen pressure change at its outflow through main and additional injectors are defined with the help of program and coincide successfully with experimental results (Fig. 7). It has permitted to specify tank
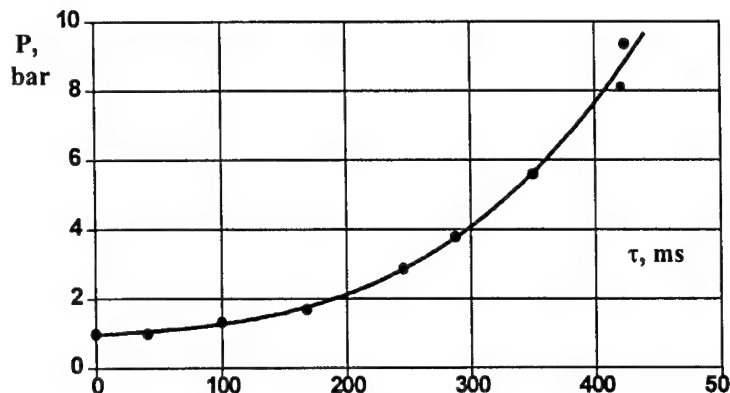
Fig. 6. The results of kerosene heating up to 420°.

147
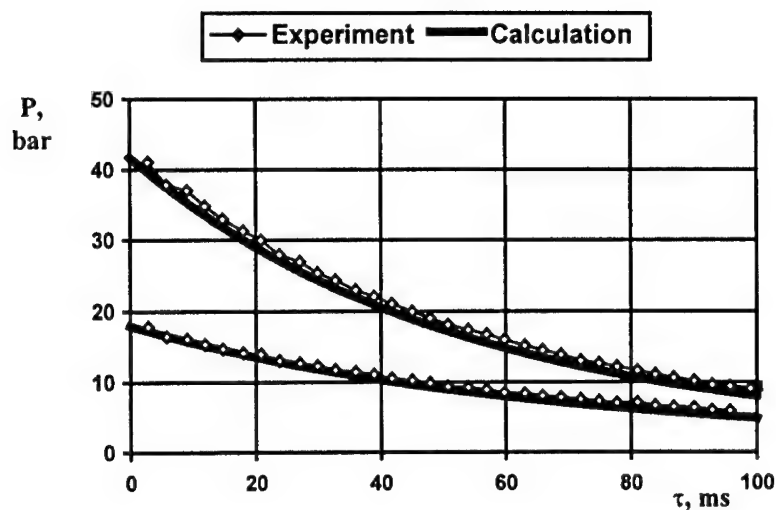
Fig. 7. Experimental and calculation data at hydrogen outflow.

volumes and loading pressure to achieve various fuel–air equivalence ratio. Besides, loading pressure and fuel tank volumes which are defined theoretically, ensure constancy of fuel equivalence ratio (both total and in each supplying channel) during the whole operating regime of the impulse wind tunnel at various air mass flow rates .

So, the produced equipment and software tools allow to calculate the parameters of fuel system to ensure given fuel equivalence ratio when the impulse wind tunnel operations with or without multiplicator at various laws of air mass flow rate changing. The experimental testing of developed system efficiency has allowed to obtain that with the help of this method one succeeds in obtaining temporal constant fuel equivalence ratio of ±2 % accuracy.

SPARK TRACER METHOD FOR SUPERSONIC VELOCITY MEASUREMENTS

A. P. Petrov and D. G. Nalivaicheko
Institute of Theoretical and Applied Mechanics SB RAS,
630090, Novosibirsk, Russia

Practical realization of the spark tracer method in a pulsed supersonic jet is described. The results of direct measurements of velocity in a gasdynamic setup with a short operational period are given.

To visualize flow pattern and measure velocity in various gas flows, including supersonic ones, the spark discharge technique method was used [1]. In the same work, the shape and stability of the first spark, aerodynamic disturbances introduced by the spark discharge into the flow, and random and systematic deviation of the tracer from the predicted trajectory were addressed. The spark tracer method, in combination with shadow visualization performed in [2] for the case of a hypersonic flow, facilitates interpreting tracer trajectories and, simultaneously, enables determination of Mach number from measurements of shock inclination angle.

To further develop this technique, intended for direct measurements of a velocity field in a supersonic flow, experiments on a pilot gasdynamic setup "Transit", of ITAM, have been performed [3]. This setup is a small-sized shock tube with a fast-operating gate having been employed instead of usually used blowout membrane. Repeated tests showed good reproducibility of experimental conditions realized, and the main characteristics of the flow were found to agree well with the values predicted by the model of quasi-steady flow. The latter allows using this setup for an independent testing of results previously obtained direct measurements of flow velocity.
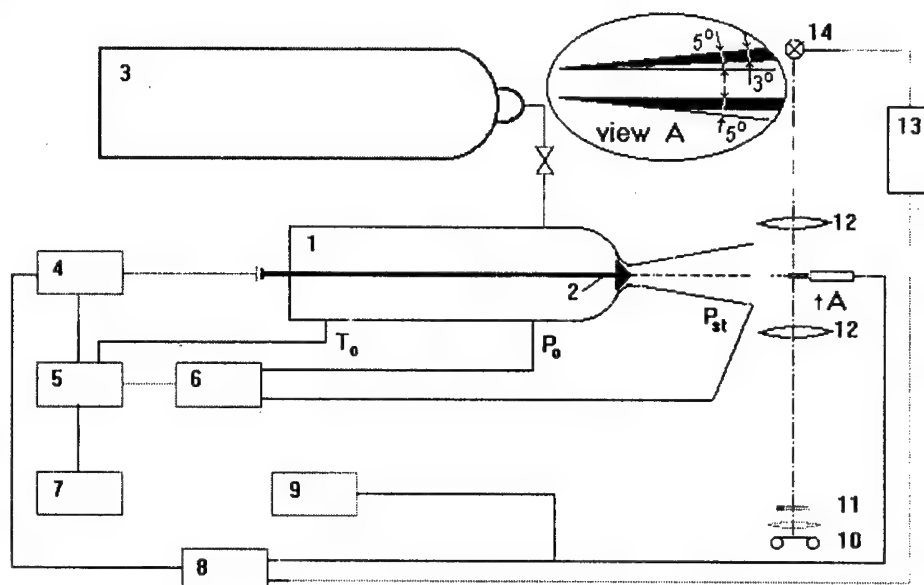
Fig. 1. Schematic diagram of the setup and measurement equipment.

The schematic diagram of the setup and measurement equipment is shown in Fig. 1. Air was fed into the prechamber (1) from a gas bottle (3). The gate was used to rapidly open the nozzle and, moving, closed contacts and initiated a two-channeled pulse generator G5-26 (4). The signal from the first channel triggered the recording system that registered the static pressure at the nozzle exit P_{st}, temperature T_o and pressure P_o into the prechamber. The pressure was measured by magneto-induction pressure transducers, the signals from which, passing through carrier frequency facility (6) and a CAMAC interface (5), arrived at a computer (7). The second channel of the generator with a time lag preset by the testing program, initiated a multi-channel high-voltage pulse generator (8) [4]. It gave out a series of sparks, which followed at a required frequency in the test zone near the nozzle exit. The spark current was monitored with the help of an oscilloscope C8-17 (9).

The shadow visualization system used in this study consisted of two lens objectives Uran-12 (12), a spark source of light with a duration of a light flash of $\tau=1$ μsec (14), a visualizing diaphragm (11) and a photographing device (photographic camera or video-camera) (10). The flash was synchronized with a series of sparks generated by generator (8) with the help of a power supply unit (13).

Registering the displacement of tracers in the spark gap permits to determine of the gas velocity along the electrodes. The presence of a sidewise velocity can be distinguished by performing experiments with another orientation of the spark gap. Using a mirror, one can do with only one photographic camera. Such an experimental scheme is most appropriate for the photographing from large distances, when the depth of focus exceeds the difference in the optical paths at direct observation and observation through a mirror. To eliminate this difference, a lens L was additionally introduced into the shorter path (Fig. 2a). It carried the spark probe image A_1 and K_1 over a certain distance to equalize the optical path lengths. On the photograph taken in this manner (Fig. 2b), spark tracks along two directions are seen, but with different magnification. The dashed line shows the nozzle exit and boundaries of the mirror. The image recorded through an additional lens is separated out by a light line and shown in the upper part of the photograph. A needle immersed into the flow in a streamwise position served as an electrode A (Fig. 2a). The electrode K was a wire 0.2 mm in diameter that stretched from the lower boundary of the nozzle at a small angle to the flow boundary. The spark tracks, in viewing through the mirror, lie in one straight line. This shows that they fall in a plane normal to the observation line and provide indication for the absence of an appreciable side velocity. For this reason, the photographs in subsequent experiments were taken along one direction.
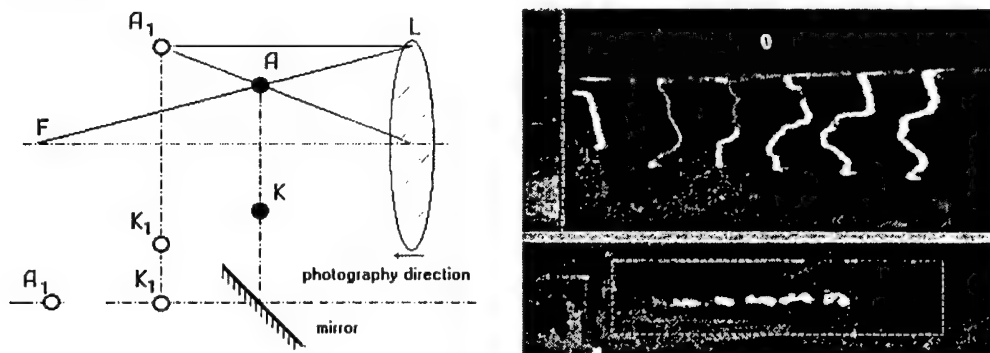
Fig. 2. Diagram of photographing from two directions.

The spark-generating unit (a spark probe) consisted of two 45 mm-long tungsten electrodes 2 mm in diameter. These electrodes were electrically insulated from each other and, on a special support, were introduced into the gas flow under study. One electrode was disposed in a streamwise position and had a nose part sharpened at the angle 5°. The second electrode was sharpened at the angle 3° and inclined at 2° to the first one, as shown in Fig.1 (view A). Shadow photographs show that such a layout of electrodes practically does not disturb the flow pattern inside the spark gap.

Experiments were carried out for the following parameters of the setup: prechamber volume – 7 dm³, conic nozzle for Mach number 4, initial pressure $P_o=10$ MPa, exhaust into atmosphere. Figure 3 shows the time dependence of P_0 and P_{st}, as well as that of the calculated flow velocity at the nozzle exit in a working cycle in one experiment. The curve for the velocity V' is calculated under the assumption of adiabatic gas expansion, and that for V'' using the temperature T_0 measured by a chromel-copel thermocouple. The overshoot on the pressure curves corresponds to the moment of initiation of the spark-generation high-voltage pulses. The flow velocity determined experimentally fall between the two curves in the graph (for the test under consideration, this value is shown with the circle. In fact, the temperature inside the prechamber falls off more slowly that in an adiabatic process, and the gas velocity should be higher than V'. The calculation based on the indications of the thermocouple gives an overestimated value of the velocity V''. The thermocouple (wire diameter 0.3 mm) has a finite response time; therefore, it shows a more gently sloping relaxation curve for the gas temperature in the prechamber compared with reality. It can be concluded that the experimental data agree well with the calculation results.

Fig. 3. Time dependences of P_0 and P_{st}, and that of flow velocity in one run of the setup.

Depending on the disposition of the spark probe with respect to the nozzle exit, different track patterns can be observed. To adequately reveal the reasons causing track curvature, onto the same photograph the shadow flow pattern was recorded at the thirtieth microsecond after the series of sparks was initiated. Such photographs are shown in Fig. 4. In these experiments, the probe was introduced into the central zone of the flow. This zone corresponded to the characteristic rhombus, where the flow was expected to be uniform.

The generator produced a series of sparks followed at a repetition frequency 200 kHz (i.e., with a time period of 5 μsec), t μsec's after the nozzle was opened. The photographs are taken in different runs. It can be clearly seen (Fig. 4) that subsequent tracers follows the trajectory of the first spark, which is indicative of the good uniformity of the velocity field. Last tracks are strongly bent. The shadow pattern (Fig. 4), in combination with spark

trajectories, furnishes explanation of their bending as resulting from the change in the flow velocity as the gas passes the oblique shock arising in the wave jet structure.
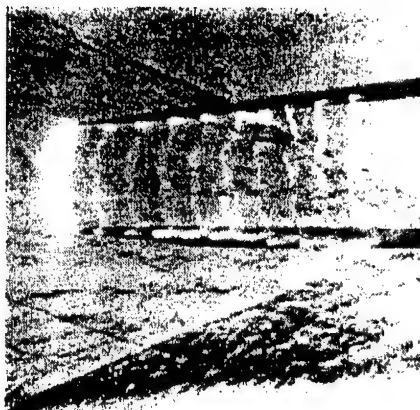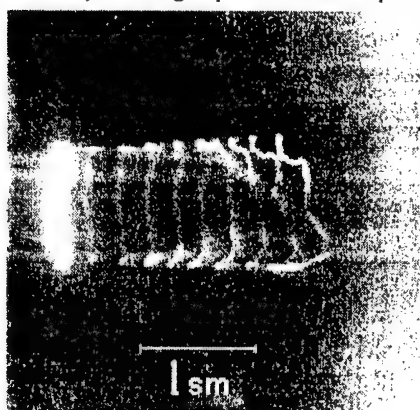
Fig. 4. Photographs of discharge tracks in the spark probe.

The first spark is the brightest one because, at the first discharge, the gap resistance is the highest and, across it, the main energy of the discharge contour is released. Subsequent discharges follow the ionic trace, whose resistance is appreciably lower; therefore, a smaller portion of the energy is being released. They become more blurred, resemble a diffuse discharge, their brightness diminishing. Besides, not only the difference in brightness between different sparks but also that along the length of one spark is observed. The shadow photograph shows that the manifestation of the above phenomena depends on the jet section, in which the spark trace is situated. The pressure in the characteristic rhombus at the nozzle exit is lower that that behind the oblique shock. Here, the gas is more rarefied, and the track look dimmer.

The estimated error of an individual velocity measurement did not exceed 5%. For higher flow velocities, the time interval between sparks should be shortened for the mean velocity to be close to the instantaneous velocity, and in this case this interval becomes comparable with the duration of one discharge. The leakage inductance in the high-voltage contour increases the duration of the current pulse in the discharge gap (determined from the pulse base) to 1 μsec. Accordingly, the glow time of a spark increases, and smearing of the streamer becomes more pronounced owing to the carrying-away of the spark by the flow for this time. The latter worsens the measurement accuracy. The situation can be better when the measurements are performed in extended regions with a constant flow velocity, for example, in the characteristic rhombus at the nozzle outlet. In this case, in order to reduce the measurement error, the measurement base can be made larger.

References

1. Bomelburg H.J., Herzog J., and Weske J. R. The elrctric spark method for quantative measurement in flowing gases // Z. Flugniss. – 1959. – Vol. 7. – P. 322.
2. Rychkov V.N. and Topchiyan M E. Direct measurements of hypersonic flow velocity by electric-discharge tracing // Thermophysics and Aeromechanics. –1999. – Vol. 6, No. 2. – P. 173-180.
3. Zvegintsev V.I. Application of pulsed wind tunnels at M = 8 // Izv. SO AN SSSR, Ser. Tekknicheskaya. – 1990. – Vyp. 5. – P.129 – 134
4. Yu. V. Afonin and A. P. Petrov, High-voltage pulse generator for velocity measurements in gas flows by spark tracer method // Intern. Conf. on the Methods of Aerophys. Research: Proc. Pt 2. Novosibirsk, 1998. – P. 10 – 13.

INVESTIGATION OF THE SEPARATION FLOW
IN THE VICINITY OF MULTI-BEAM PRISMATIC STRUCTURES

S. D. Salenko, A. D. Obukhovsky, and R. A. Gorban'

Novosibirsk State Technical University
Novosibirsk, Russia

Gaining better insight into unsteady flows aimed at improvement of aerodynamic stability of members of bridgework and other structures is of great interest. At present, the lengthwise sliding technology has gained widespread utility in bridgework erection. In this technology, it is required first to dismount floor plates from the leading part of the bridge framework to reduce it weight. As a result, the wind streamlines one by one several ordered beams of rectangular cross section, which gives rise to a vortex structure resembling a Karman vortex street or a more intricate coherent structure. This, in turn, can bring the cantilever of the sliding framework into intense vibrational motion [1].

Aeroelastic studies of multi-beam structures revealed that, for them, unlike the case of an isolated beam, there are several intervals of the approach stream velocity in which intense vibrations of the whole structure can be excited [2].

In this connection, a detailed experimental and numerical study of an airflow pattern around a multi-beam prismatic structure would be of considerable interest. Flow visualization studies permit comprehensive analysis of the whole unsteady flow pattern of interest and elucidation of its most important details. They can add much to our understanding of various mechanism of generation of aeroelastic vibrations and solving the problem of their damping.

Available literature data show that a good deal of works have been devoted to separation-flow studies in the vicinity of isolated cylinders both of circular and rectangular cross sections. At the same time, flows around an ordered sequence of prisms are studied poorly.

In this work, flows around single-beam and three-beam models oriented in a cross-wind direction were examined (Fig. 1). The cross sections of the beams had a rectangular shape with the height $H = 60$ mm and width $B = 40$ mm along the windstream direction, i. e., the relative beam width was $B/H = 2/3$. It is these cross-sectional proportions that are typical of real bridgework beams. The separation L between the beams was varied in the range $L/H = 4...9$. The cross-wind length of the beams was 600 mm, which is equivalent to the aspect ratio 10. To ensure a planar flow near the model, end plates were attached to beam ends. Flow visualization studies were carried out in the symmetry plane of the models, where the flow could be regarded two-dimensional.

The model was disposed in the working part of a wind tunnel being suspended on elastic hangers which allowed the model to execute vibrations with an amplitude running into half the height of the beam cross-sectional area. The frequency of the vibrations varied in the range $12...16$ Hz. The Reynolds number calculated from the beam height was $0.1 \cdot 10^5$ to $0.5 \cdot 10^5$.

The aerodynamic bench was installed in the T-503 wind tunnel of the Laboratory of Industrial Aerodynamics, NSTU. The tunnel T-503 is a closed-type wind tunnel with an open working part. Its main characteristics are the following: airstream velocity up to 60 m/s, turbulence level ~0.5 %, working-section diameter 1.2 m, working-section length ~2 m.

Vibrational characteristics of the models were measured with the help of strain gauges provided in branches of the model elastic suspension. The signals from the strain gauges, after
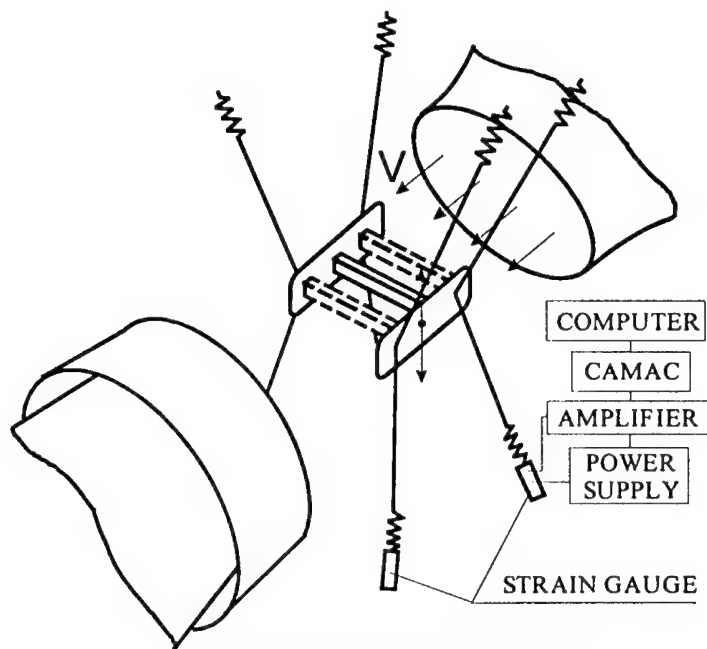
Fig. 1. Scheme of the experimental stand.

amplification, were converted into a digital code to be subsequently processed in a computer. To register the phase of the vibrations at the moment of flow pattern visualization, we designed an electron-optical device, whose indications provided information about the instantaneous phase of model vibrations. The device was installed against the part of the flow to be registered by a video camera working in an uninterrupted mode. The error in determining the phase of the oscillations did not exceed 2°. The photographing was performed by a digital video camera with the frequency 50 frame per minute and exposure times 1/500...1/2000 s. To reveal the phase-alternation pattern with a short sampling interval, we performed a series of experiments at the fundamental frequency of the model 1.5...2 Hz, the flow velocity in this case being of the order of 1 m/s.

For subsonic-flow visualization, non-optical methods are usually used based on the introduction into the flow of visible particles-tracers. In our visualization studies, we tried out several methods: silk-thread one, flow dusting, smoking-wire and smoke-jet methods. Experiments showed that the silk-thread method and flow dusting cannot ensure good visualization quality. The reason for this is that silk threads and particles-tracers should be light and small enough to adequately follow the direction of the unsteady flow, in this case, however, they being poorly detectable on the photograph.

The smoke and similar finely dispersed substances (steam, smog, etc.), perhaps, satisfy better the above requirements. The smoke can be introduced into the flow out of holes in the model or from an outside source, e. g., from an isolated smoke tube or tube comb. In order to produce discrete trajectories of smoke particles, the smoking-wire method can be also used which was devised in early sixties and was further developed in [4, 5].

Experiments showed that each of the above methods has its own merits and disadvantages. Some fragments of the flow pattern around sectional models are shown in Figs. 2-6. In these figures, negative photographs are shown. The introduction of a smoke out of a tube comb permits elucidation of the large-scale flow structure and to trace its development far
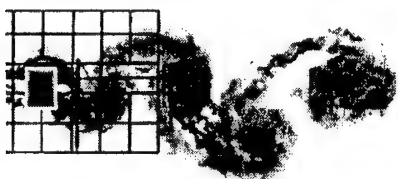
Fig.2. Smoke-flow visualization
(isolated beam, $Sh{\approx}0.12$, $A/H{=}0$).
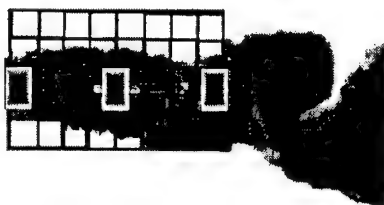
Fig.3. Smoke-flow visualization (three beams,
$Sh{\approx}0.095$, $A/H{=}0$).
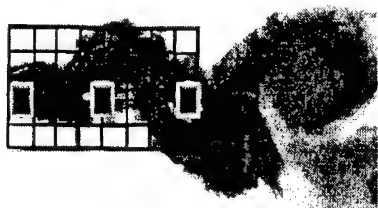
Fig.4. Smoke-flow visualization (three beams,
$Sh{\approx}0.12$, $A/H{\sim}0.3$).
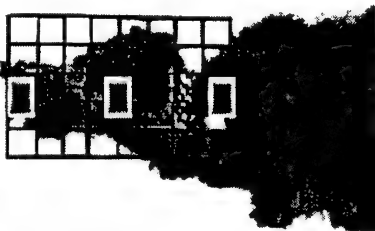
Fig.5. Smoke-flow visualization (three beams,
$Sh{\approx}0.95$, $A/H{\sim}0.3$).
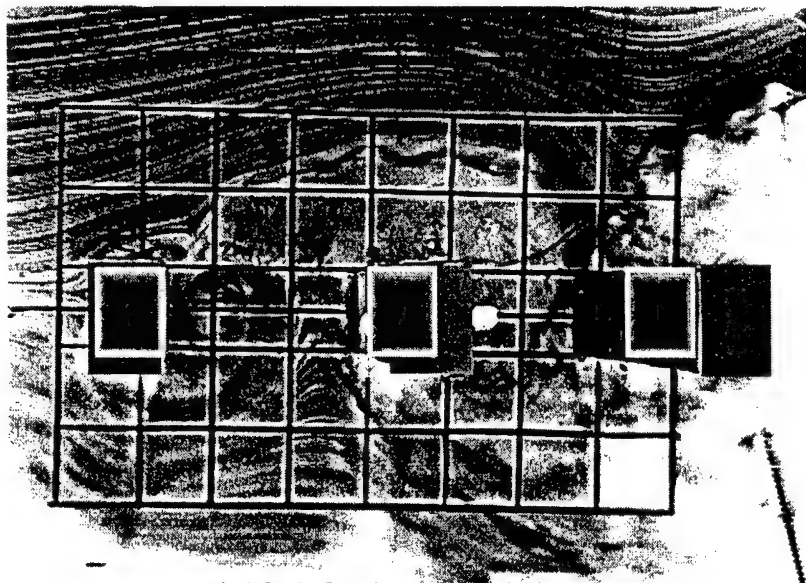
Fig.6. Smoke-flow visualization by smoking-wire method
($Sh{\sim}0.95$, $A/H{\sim}0.3$).

downstream of the body (Fig. 2-5). The smoking-wire method is capable of providing good results for the flow regions outside the separation zones, and also reveals well the fine structure of the flow (Fig. 6). However, in separation regions and at a distance downstream of the wire, the smoke jets get smeared and they cannot provide a distinct image. In addition, there are some restrictions in this method imposed on the approach flow velocity.

The interpreting of the images obtained and clear representation of visualization results remain most difficult problems in separation-flown studies. The smoke jets on photos should be identified with trajectories of particles-tracers. Other representation methods of the revealed flow structure can be used as well: streamlines (taken in different coordinate systems: those attached to the body, to the approaching stream, to a Karman vortex street, etc.); positions of the centers of discrete vortices (in numerical studies); vector diagrams of the field of instantaneous velocity.

Experimental realization of the majority of these methods is extremely difficult; therefore, different methods of flow-structure representation in this work were analyzed using numerical modeling. In the modeling, the well-known discrete-eddy method was used [6]. The obtained numerical results are shown in Fig. 7.

For comparison, Fig. 2 shows the result of smoke-assisted visualization of the flow structure around an isolated beam. A distinct vortex flow structure is seen. Experiments showed that a stable Karman vortex street downstream of the beam of a rectangular cross-section is observed both downstream of a stationary model and downstream of a model executing vibrations with relative amplitudes as high as 0.5 at Strouhal numbers Sh = 0.12 – 0.14. Comparison with numerical results shows a good agreement between two flow patterns.

Comparison of different methods of representation of visualization data (Fig. 7) shows that the trajectories are less suited for adequate reconstruction of the flow structure (Fig. 7d): each of them has its own individual character and does not reflect the flow pattern as a whole. Streamlines in the coordinate system attached to the body (Fig. 7c) give an insight into the flow structure as having a wave rather than a vortex character. Perhaps, this representation may prove useful in determining forces that act on the beams located downstream of the first beam. Streamlines in the coordinate system attached to the wake past the body (Fig. 7e) provide a clear idea of the flow structure but they are too difficult to be found experimentally.

Thus, depending on the manner of representation of the structure of unsteady flows, one can obtain drastically differing looks of one and the same flow.

Figures 3 – 6 show the flow structure around three-beam models. The presence of another two beams downstream of the first one prevents formation of a stable Karman vortex street. For small inter-beam separations, $L/H < 3$, and small amplitudes of vibrations, $A/H < 0...0.05$, separated stagnant regions originate in the gaps between the beams. In this case the system of beams is being streamlined as an entity, and the vortex street starts forming behind it. For medium inter-beam separations, $L/H \sim 3$, stagnant zones form only between the first and the second beam (Fig. 3). Comparison between the widths of the vortex wakes past the three-beam and single-beam models shows that, due to the above effect, the vortices originating downstream of the stationary three-beam model are less intense than those appearing downstream of the stationary single-beam model.

For vibration amplitudes $A/H{\sim}0.05$ of the three-beam model and some flow conditions, an intermittent bistable flow mode arises: one flow structure, after several periods of existence, transforms spontaneously into another, and, after a while, emerges again. In some cases, to observe the above behavior of the flow, it is required to introduce an additional disturbance into the upstream region of beams.

156

a) Vector diagrams of velocity field

b) Positions of discrete vortex centres

c) Streamlines in laboratory coordinate systems

d) Particle trajectories

e) Streamlines in vortex street –based moving coordinate system

f) Chosen particle lines
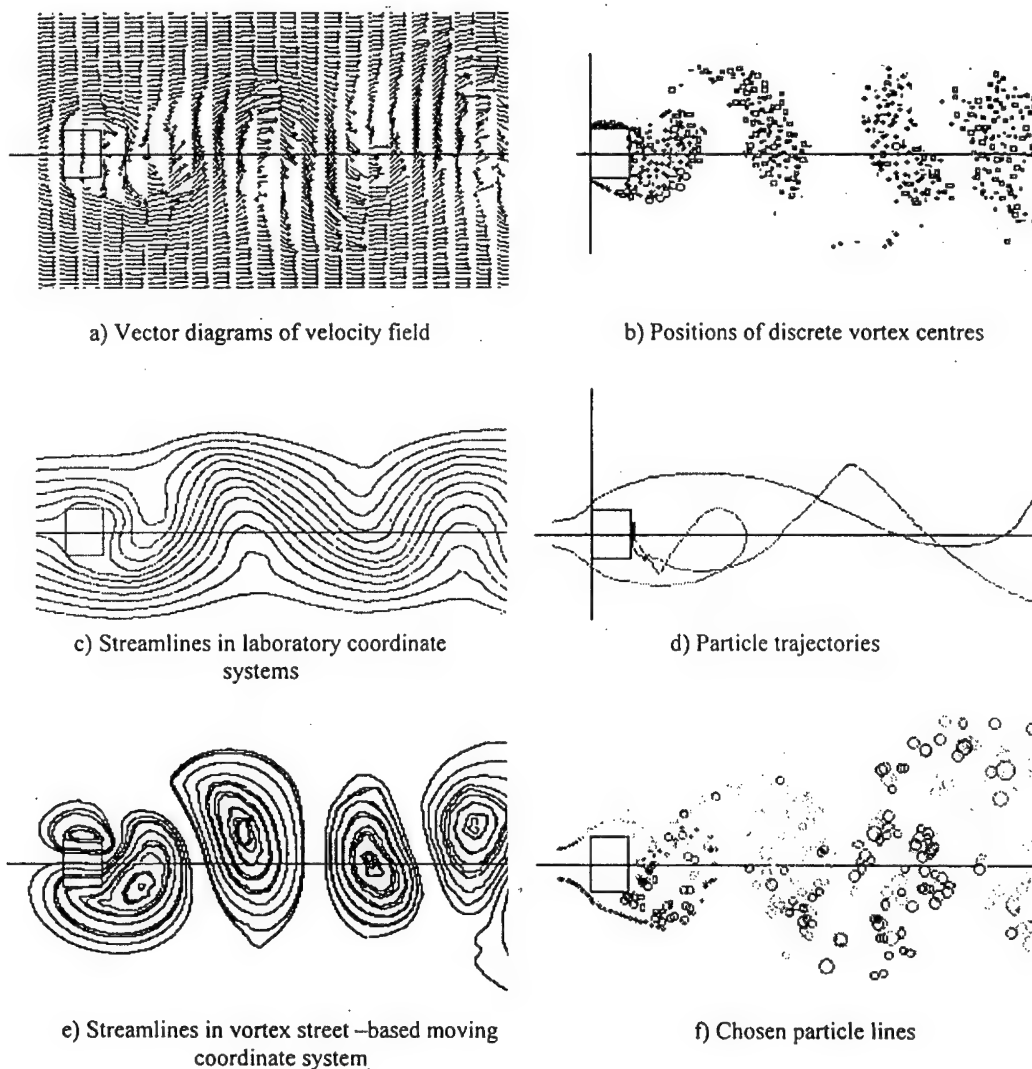
Fig. 7. Flow structures around an isolated beam (numerical results)

For large vibration amplitudes ($A/H > 0.1$), a number of vortex structures can be observed in the vicinity of three-beam structures which appear to be dependent on the dimensionless vibration frequency.

One flow mode is related to the frequency of vortex stall off an isolated beam: the first beam generates a Karman vortex street, which, as experiments show, possesses the highest stability At Strouhal numbers Sh ~ 0.12, it appears to be rather intensive. The interaction of this vortex street with subsequent beams may result in either its amplification or diminution depending on the value of the inter-beam separation and amplitude of the vibrations (Fig. 4).

This interaction can also slightly change the Strouhal number but, for all inter-beam separations, a resonant flow mode is observed, approximately at identical Strouhal numbers [3].

Another resonant flow mode arise due to that, when the model vibrates, the upstream beam generates a vortex street with a frequency of vortex stall equal to that of the vibrations. It can be supposed that, for a stable vortex street to originate in the vicinity of other beams, the inter-beam separation must constitute a multiple of the dimensionless flow velocity $V/fH =$ $= l/$Sh. In this case, the vortices that stall from the upstream beam can propagate over other beams with equal oscillation phases such that the interaction between the vortices will result in their intensification (Fig. 5). This conclusion agrees well with the results of a parametric study [3]: for one of the oscillation modes, an almost linear relation between the normalized velocities which correspond to highest amplitudes, and the normalized inter-beam separation is observed.

Thus, the experiments showed that there are at least two intervals of the Strouhal number in which the interaction between beams results in a formation of vortex structures near vibrating multi-beam models. For the Strouhal numbers beyond these intervals, the vortex system proved to be unstable even at a forced excitations of the vibrations, and the vibrational motion rapidly vanishes. Apparently, other flow structures of different stability can arise in the flow around multi-bulk structures. Further studies are required to gain more information about them.

REFERENCES

1. . Salenko S.D, Kuraev A.A., Akopov V.I., and Kunnikov A.B. Dampers of aeroelastic vibrations of bridgework cantilevers // Stroitel'stvo i rekonstruktsiya zheleznodorozhnykh i avtodorozhnykh mostov. 1996. No. 1. P. 53-58.
2. Salenko S.D. and Obukhovsky A.D. Parametric investigation of the multi-beam bridges // Intern. Conf. on Methods of Aerophys. Research: Proc. Pt 3. Novosibirsk, 1996. P. 241-246.
3. Ghad-el-Khack. Visualizing techniques for unsteady flows: an overview // Sovremennoe mashinostroenie, Ser. A. 1989. No. 5. P. 164-178.
4. Dovgal' A.V., Kozlov V.V., Nosyrev I.P., and Sarik V.S. A visualization method for boundary-layer flow structure: Preprint No. 37. Novosibirsk: ITAM, USSR Akad. Sci., Siberian Branch, 1981.
5. Adler J. N., Robinson M. C., Luttges M. W., Kennedy and D. A. Visualizing unsteady separated flows // Flow Visualization III / Ed. W. J. Yang, Hemisphere, Washington D. C., 1985. P. 342-347.
6. Belotserkovsky S. M. Mathematical Modeling of Planar Flows around Bodies. Moscow: Nauka, 1988.

ON JET – FLAT PLATE BOUNDARY LAYER INTERACTION

D.S. Sboev

Institute of Theoretical and Applied Mechanics SB RAS,
630090 Novosibirsk, Russia

Introduction. The basic feature of laminar-turbulent transition at high levels of free stream turbulence consists in occurrence of the so-called "streaky structures" in a boundary layer. The investigations of mechanisms of their occurrence and development is necessary for understanding the transition process as a whole. A series of model experiments has evidently demonstrated one of such mechanisms: occurrence of a "streaky structure" in interaction between a controlled localized free stream disturbance and incipient boundary layer on the leading edge of the model [1, 2]. However, these works have shown that the perturbation generated in such way decays in the boundary layer. It is in contrast with the results of investigations of laminar-turbulent transition in "natural" conditions, where the RMS-fluctuations inside layer grow as $X^{1/2}$. This fact forces to assume the existence of mechanisms of free stream turbulence influence along the boundary layer edge on occurrence and development of "streaky structures". Yet, the results of those model experiments, in which the boundary layer was exposed to external disturbances on its whole extent, also testify to the growth of disturbances inside the boundary layer [3].

It is possible to present two different scenarios of free stream turbulence influence on development of "streaky structures" in the boundary layer [1]. The first of them is based on a hypothesis about continuous forcing of external turbulence on disturbances arising directly on the leading edge. It can be caused by pulsations of pressure, produced by large vortices from an external flow, or these vortices themselves can penetrate directly into the boundary layer and interact with disturbances already existing in it. Another scenario bases on a hypothesis of occurrence of "streaky structures" in a fully developed boundary layer by-passing the leading edge. In this case, the higher Reynolds numbers allow the "streaks" to achieve larger transient growth, though the increase of the boundary layer thickness, as well as the decaying of free stream turbulence, will both reduce this effect. It is obvious, that for both scenarios the question about the interaction between localized free stream vortical disturbances and full-developed boundary layer is rather important. These reasons have served as the basic motivation for the present work.

Experimental set-up. The experiments were performed on a flat plate in the MT-324 wind tunnel at the ITAM SB RAS. The free stream velocity (U_{∞}) was equal to 6,6 m/s. The disturbance source (a pipe with a profiled cross-section) was mounted above the boundary layer at height $H = 8$ mm from the plate and at Reynolds number (R) based on displacement thickness equal 476 (Fig. 1). The pipe was connected to a loudspeaker, which was driven with a pulse signal from a function generator. The pipe installation has resulted in occurrence of local pressure gradients, however, it disappeared in all directions at a distance of the order of the distance from the pipe to the plate (Fig. 2). Downstream from this region, mean velocity profiles were relaxed to the Blasius ones. These pressure gradients can be interpreted as simulating the influence of large-scale vortices from the external flow. In spite of the fact that the pipe had a special profile, a turbulent wake was observed behind it. Thus, the boundary layer was exposed to the influence of an impinging short duration jet, local pressure gradients and turbulent wake behind the pipe (Fig. 1).

The streamwise velocity components were measured with a constant-temperature hot wire. Ensemble averaging of approximately 150 realizations was carried out.

Results. In Fig. 3 growth of RMS-fluctuations for various values of the coordinate Z is shown. After initial attenuation (receptivity phase) the disturbances grow proportionally to R (or $X^{1/2}$). Owing to three-dimensionality of the disturbances, the growth rates are different for different values of Z. The growth of RMS-fluctuations is rather quickly replaced by a nonlinear phase of saturation and disturbances transformation into turbulent spots at $R \approx 650$ (in Fig. 3 the oscilloscope traces containing turbulent spots were sorted out).

Figure 4 shows, in the (Z, t)-plane, the disturbance development in the boundary layer. Fast formation of disturbances, which have an inner structure similar to the "puff" [1, 2], is visible. For example, at $X = 223$ mm ($R = 541$) the forward part of the disturbance (15 ms $< t$ < 25 ms) consists of three alternating regions of defect and excess of the instantaneous velocity above its local mean value. This part of the disturbance is elongated as it travel downstream. Its duration at $X = 223$ mm takes 10 ms in comparison with 20 ms at $X = 273$ mm. Further downstream, a strong growth of oblique waves is observed, and the general view disturbance acquires reminds the Λ-structure.
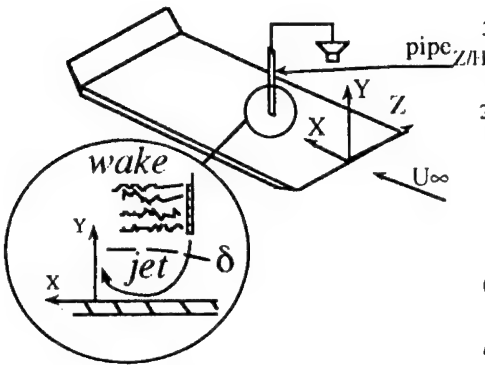
Fig. 1. Outline of experimental set-up.
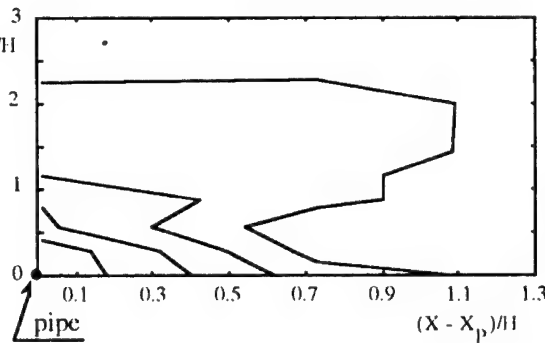
Fig. 2. Mean flow with extracted U_x at $Y.H = 0.85$. Contour spacing: $0.025U_x$.
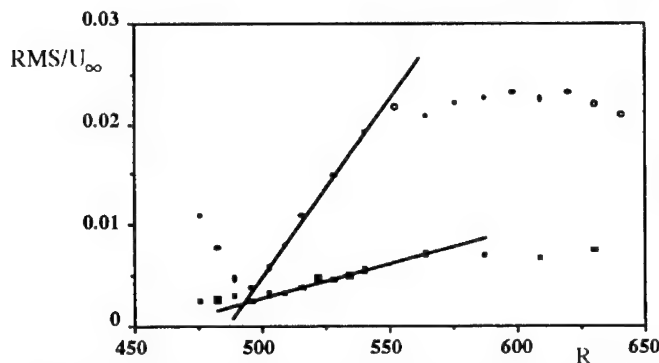
Fig. 3. Growth of RMS-fluctuations for some values of the coordinate Z.

It is possible to assume that the basic mechanism of disturbances formation is the *lift-up* effect. However, in such case, at first sight, one can expect the occurrence of disturbances with the central region of positive pulsations (instead of the negative ones, as seen from Fig. 4),

as the initial jet results in the movement of an accelerated liquid to the wall. The measurements have shown that near the disturbances source such situation validly occurs, however, downstream of the source there intensive lift-up of the liquid upwards from the wall, that results in formation of a region of strong defect longitudinal velocity components (see the bottom left diagram in Fig. 4). The initial disturbance decays in the boundary layer at subcritical Reynolds numbers. The general picture of perturbed motion near the source reminds flow visualization [4] of localized vortex interactions with a boundary layer on a flat plate. The high intensity of initial perturbations in [4], however, has resulted in much faster turbulent spot formation. Similarly to processes observed in [1, 2], the "petals" of positive fluctuations develop on the sides from the central defect region as the disturbance propagates further downstream. Thus, the concept of the *lift-up* effect can describe disturbance occurrence in the boundary layer in the case considered. It is necessary also to notice that, as R increases, the initial disturbance enters the area of instability (from linear theory point of view) and begins to grow, becoming visible in oscilloscope traces (rear part of the structure at $X = 223$ and 273 mm in Fig. 4).
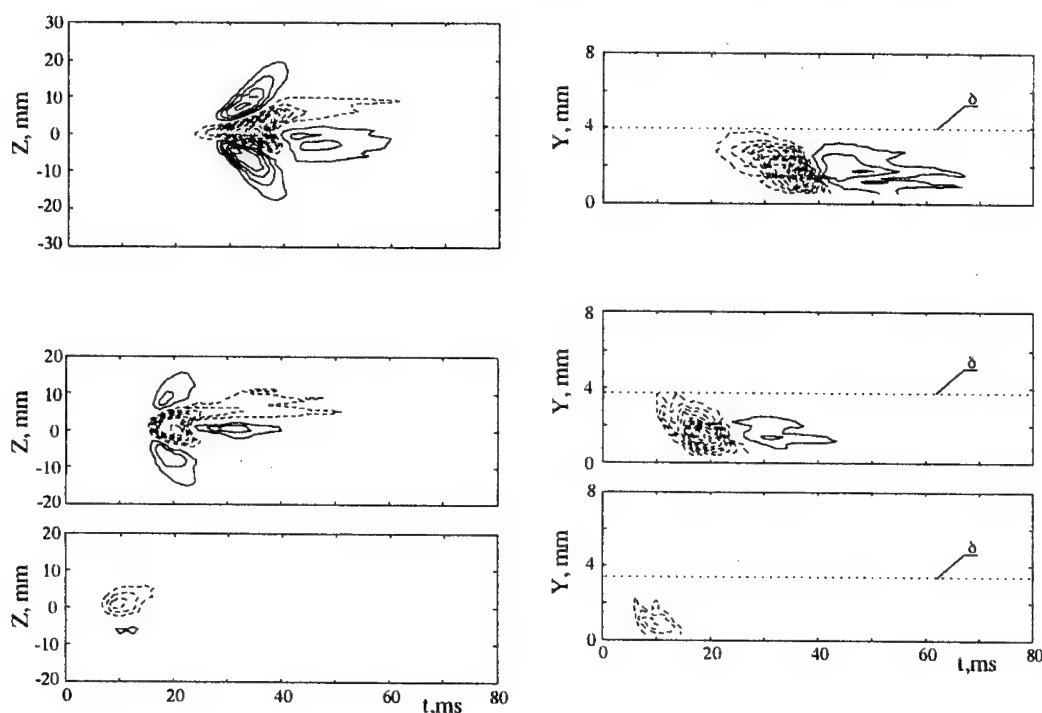
Fig. 4. Isocontours of the streamwise perturbation velocity of the disturbances in the horizontal plane at $Y/\delta_1 = 1,1$ (left) and vertical plane at $Z = 0$ mm (right). Solid and dashed lines represent positive and negative contours, respectively. The X – positions are from bottom to top 193, 223, 273 mm ($R = 503, 541, 598$). Contour spacing: $0,01U_\infty$.

In the right column of Fig. 4, the disturbance development in the vertical plane is shown. Inclination of the disturbance with respect to the wall is clearly seen. The maximum of pulsations lays in the middle of the boundary layer. The growth of the initial disturbance in the region of instability results in shear layer formation in the vertical plane. The propagation velocity of the front interface of the disturbance is about $0,8U_\infty$, at the same time, the

161

maximums of fluctuations propagate with a velocity of about $0.4U_{x_0}$, which is a typical value for Tollmien – Schlichting wave packets. This reduction of the propagation velocity is consistent with the disturbances transformation in a nonlinear wave packet observed.
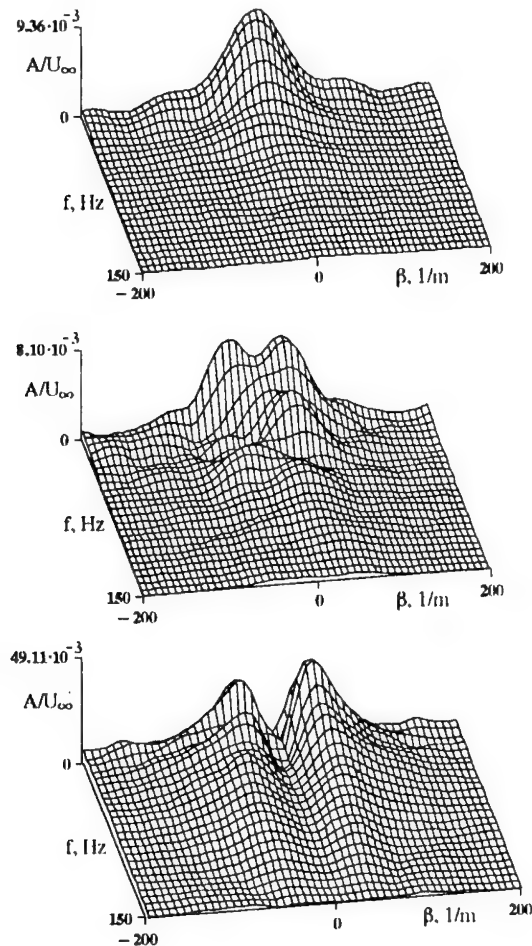
Fig. 5. Spectral decomposition (f,β) for some spanwise distributions.
The X – positions are from top to bottom 173, 183, 273 mm($R = 476$, 490, 598).

The disturbance development in the Fourier-space is illustrated in Fig. 6. Dominant in the initial disturbance, 2D waves decay at subcritical Reynolds numbers. At the same time, an intensive growth of oblique waves at a very low frequency ($f \approx 0$) is observed. With an increase in R, the growth of the low-frequency component in the spectra is slowed down, and most growing waves appear at 25 Hz $< f <$ 150 Hz. The spanwise wave length corresponding to most energetic harmonics in the spectra is greater than for disturbances generated on the flat

162

plate leading edge in [1, 2]. The measurements have shown, that the height of pipe installation above the plate has not direct influence on the spanwise scale of the disturbances. However, the measurements at U_∞ = 10 m/s allow us to conclude that the spanwise scale of the disturbances is determined by the local boundary layer thickness in the region of disturbance generation.

Conclusions. The interaction of a pulse impinging jet with a flat plate boundary layer results in the occurrence of localized boundary layer disturbances, which grow linearly with the Reynolds number. Disturbance transformation into nonlinear wave packets and turbulent spots was observed further downstream. Thus, the laminar-turbulent transition actually could be influenced by free stream turbulence through interactions of localized external vortices with a fully developed boundary layer. However, within the framework of the given experiment, a more detailed discussion of localized pressure gradient effects and continuous forcing from free stream turbulence is impossible and will be a subject of the future experiments.

This work is supported by SB RAS as part of its Young Scientists Project.

References

1. Westin K.J.A., Bakchinov A.A., Kozlov V.V., Alfredsson P.H. Experiments on localized disturbances in flat plate boundary layer. Part 1: Receptivity and evolution of a localized free stream disturbance // Eur. J. Mech. B/Fluids. - 1998. - Vol.17, № 6. - P. 823-846.
2. Sboev D.S., Grek G.R., Kozlov V.V. Experimental study of boundary layer receptivity to localized perturbations of the external flow // Thermophysics and Aeromechanics. - 1999. - Vol.6, № 1. - P. 1-13.
3. Bertolotti F.P., Kendall J.M. Response of the Blasius boundary layer to controlled free-stream vortices of axial form // AIAA Paper. - № 97-2018.
4. Maekawa H., Tacami H., Nishioka T. "Vortex dynamics" of a vortex ring introduced into laminar boundary layer // Laminar-Turbulent Transition, IUTAM Symp. / Ed. R. Kobayashi, Berlin et al.: Springer-Verlag, 1995. P. 221-228.

THE PROBLEM OF SCHEME OSCILLATIONS IN COMPUTATIONAL FLUID DYNAMICS AND THE WAYS TO ELIMINATE THEM

B.Yu. Scobelev and E.V. Vorozhtsov

Institute of Theoretical and Applied mechanics SB RAS,
Novosibirsk 630090, Russia

INTRODUCTION

The problem of the suppression of scheme oscillations is of great importance especially in those fluid dynamics problems, in which there are instabilities and bifurcations of the solutions. One of the practically important problems of such kind is the problem of laminar/turbulent transition. As was noted in [1], besides the well-known distortion of the velocity field by scheme viscosity, a new unpleasant phenomenon was revealed: the appearance of spurious oscillations in flow. At the direct numerical modeling of laminar/turbulent transition, this effect is the main effect, and it unfortunately resists to control. The appearance of spurious oscillations is especially dangerous at a rapid, "explosive" character of turbulence onset, as this takes place, for example, in a plane channel. This leads to a significant error in the determination of the time and location of turbulence onset and also distorts significantly the turbulent velocity field. It is noted in [1] that the small-scale distortions inevitably give rise to large-scale distortions.

Another class of problems, where the scheme oscillations may distort the solution significantly, is the gas dynamics problems with stagnation regions. The stagnation zone may serve a generator of scheme oscillations. Since the flow in the stagnation zone itself and its neighborhood is subsonic, the scheme oscillations propagate along the characteristics throughout the computational region and may distort the solution substantially. The spurious oscillations may give rise to certain difficulties also at the numerical solution of stationary problems by the pseudo-unsteady method [2].

We show in the present work that the difference scheme stability defined in conventional sense dos not ensure the absence of scheme oscillations in time domain. In this connection, we propose a new definition for stability of difference schemes, namely the uniform stability. A feature of uniformly stable difference schemes is that the powers of the corresponding amplification matrix decrease with increasing number of time steps. Consequently, the uniform stability ensures the absence of scheme oscillations in time.

The constructive criteria have been proposed for uniform stability, which give the possibility of constructing the new uniformly stable difference schemes for the aerodynamics problems.

UNIFORM STABILITY OF DIFFERENCE SCHEMES

Definition. We shall say that the difference scheme is uniformly stable in some region of the parameters $\kappa \in D$, if:

1) the step operator $S(\kappa)$ is uniformly bounded: $\|S(\kappa)\| \leq M$, $\kappa \in D$;

2) there is a natural number n_0 such that at all values of the wave vector ξ, the amplification matrix $G(\kappa, \xi)$ satisfies the condition:

$$||G^{n+1}(\kappa, \xi)|| \leq ||G^n(\kappa, \xi)|| \quad \text{at} \quad n \geq n_0, \quad \kappa \in D. \tag{1}$$

Remark. It is easy to show that a uniformly stable difference scheme is stable in the conventional sense. Let us take $\max_\xi$ of the both sides of equality (1). We obtain the following inequality for the transition operator $C_{n,0}$: $||C_{n+1,0}|| \leq ||C_{n,0}||$ at $n \geq n_0$. Since the step operator is bounded, then $||C_{n_0,0}|| \leq ||S||^{n_0} \leq M^{n_0}$. Hence, $||C_{n,0}|| \leq M^{n_0}$ for all $n \geq 1$.

Let us now elucidate the question of the conditions which a difference scheme should satisfy in order to be uniformly stable. Consider a difference scheme with constant coefficients whose amplification matrix $G(\kappa, \xi)$ is normal and the von Neumann condition $\max_\xi |\lambda_i(\kappa, \xi)| \leq 1$, $\kappa \in D$ is satisfied. Such a difference scheme will obviously be stable. Since matrix $G(\kappa, \xi)$ is normal then it follows from relation

$$||G(\kappa, \xi)|| = \max_\xi |\lambda_i(\kappa, \xi)|$$

and the von Neumann condition that

$$||G(\kappa, \xi)|| = \max_i |\lambda_i(\kappa, \xi)| \leq 1 \quad \text{for all} \ \xi; \ \ \kappa \in D.$$

Then we have the following relation for the powers of the matrix $G(\kappa, \xi)$:

$$||G^{n+1}(\kappa, \xi)|| \leq ||G^n(\kappa, \xi)|| \ ||G(\kappa, \xi)|| = \max_i |\lambda_i(\kappa, \xi)| \ ||G^n(\kappa, \xi)|| \leq ||G^n(\kappa, \xi)||,$$
$$\kappa \in D, \quad n = 0, 1, 2, \ldots .$$

That is the norm of the nth degree of the amplification matrix $G(\kappa, \xi)$ is a nonincreasing function of the exponent n. Consequently, the difference schemes with the normal amplification matrix will be uniformly stable according to the above Definition.

More general criteria for uniform stability of difference schemes are given by the following theorem (we omit its proof for the purpose of brevity).

Theorem. The difference scheme is uniformly stable in the region $\kappa \in D$, if any of the following criteria for the amplification matrix $G(\kappa, \xi)$ is satisfied.

Criterion 1. The eigenvalues $\gamma_i(\kappa, \xi)$ of matrix $G^*(\kappa, \xi) G(\kappa, \xi)$ satisfy the condition:
$$\max_\xi |\gamma_i(\kappa, \xi)| \leq 1, \kappa \in D.$$

Criterion 2.

1. *Criterion 1 is satisfied in a subregion $\xi \in \Omega_1(\kappa)$ of the periodicity region of the amplification matrix G.*

2. *The following conditions are satisfied in the complement of the set Ω_1 in the set Ω ($\xi \in \Omega \backslash \Omega_1$):*

    a) *the matrix $G(\kappa, \xi)$ is uniformly diagonalizable;*

    b) *there is a unique maximum eigenvalue $|\lambda_1(\kappa, \xi)|$ of matrix G so that for all eigenvalues λ_i*

$$|\lambda_i(\kappa, \xi)| < |\lambda_1(\kappa, \xi)|, \quad \text{if} \quad i \neq 1, \quad \max_{i \neq 1} \max_{\xi \in \Omega \backslash \Omega_1} \frac{|\lambda_i(\kappa, \xi)|}{|\lambda_1(\kappa, \xi)|} < 1 - \delta_1, \kappa \in D;$$

    c)
$$\max_{\xi \in \Omega \backslash \Omega_1} |\lambda_1(\kappa, \xi)| < 1 - \delta_2, \quad \kappa \in D,$$

where $\delta_1 > 0$, $\delta_2 > 0$ are some constants.

Remark. If the first criterion is satisfied then one can set $n_0 = 1$ in the above Definition.

Let us illustrate the uniform stability concept and the application of the above theorem at a number of examples.

Example 1. Consider the system of two-dimensional acoustics equations [3]

$$\frac{\partial w}{\partial t} + A \frac{\partial w}{\partial x} + B \frac{\partial w}{\partial y} = 0, \qquad (2)$$

where

$$w = \begin{pmatrix} u \\ v \\ p \end{pmatrix}, \quad A = \begin{pmatrix} 0 & 0 & \frac{1}{\rho_0} \\ 0 & 0 & 0 \\ \rho_0 c_0^2 & 0 & 0 \end{pmatrix}, \quad B = \begin{pmatrix} 0 & 0 & 0 \\ 0 & 0 & \frac{1}{\rho_0} \\ 0 & \rho_0 c_0^2 & 0 \end{pmatrix}. \qquad (3)$$

Here ρ_0 is the gas density, p is the pressure, c_0 is the sound velocity, u, v are the components of the gas velocity vector along the x, y axes, respectively. Let us approximate system (2) with the aid of the following three-stage scheme of the Runge-Kutta type [4]:

$$w^{(0)} = w^n, \quad w^{(1)} = w^{(0)} - \alpha_1 \tau P_h w^{(0)}, \quad w^{(2)} = w^{(0)} - \alpha_2 \tau P_h w^{(1)},$$
$$w^{(3)} = w^{(0)} - \tau P_h w^{(2)}, \quad w^{n+1} = w^{(3)}. \qquad (4)$$

Here $P_h w$ is the difference operator of spatial differentiation in (2):

$$P_h w_{jk} = A\,(w_{j+1,k} - w_{j-1,k})/(2h_1) + B\,(w_{j,k+1} - w_{j,k-1})/(2h_2),$$

h_1, h_2 are the steps of a uniform grid along the x- and y-axes, respectively; τ is the time step. The quantities α_1 and α_2 in (4) are the weight parameters; one can take, in particular, $\alpha_1 = \alpha_2 = 0.5$. The amplification matrix G corresponding to scheme (4) is

$$G = I - i Z - \alpha_2 Z^2 + i \alpha_1 \alpha_2 Z^3, \qquad (5)$$

where $i = \sqrt{-1}$, Z is the result of the Fourier transformation of operator τP_h, $Z = d_1 A + d_2 B$, $d_\alpha = (\tau/h_\alpha) \sin \xi_\alpha$, $\alpha = 1, 2, I$ is the 3×3 identity matrix. At $\alpha_1 = \alpha_2 = 0.5$ the von Neumann criterion for scheme (4) has the form $\sqrt{\kappa_1^2 + \kappa_2^2} \leq 2$, where $\kappa_1 = c_0\tau/h_1$, $\kappa_2 = c_0\tau/h_2$. One can show that this condition is sufficient for stability of scheme (4).
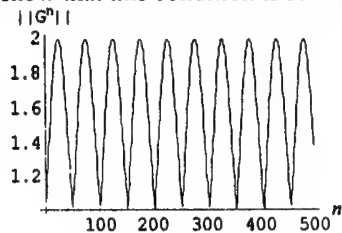
The amplification matrix of scheme (4) does, however, not satisfy the conditions of the above theorem, and this scheme is not uniformly stable, which is illustrated by the results of the computation of the quantity $\|G^n\|$ presented in Fig. 1.

Fig. 1. $\kappa_1 = 1.7,\ \kappa_2 = 1.0,\ \xi_1 = \xi_2 = 0.99\pi,\ \rho_0 c_0 = 2$

166

Example 2. We again consider the acoustics equations (2). It is well known that the system (2) can be symmetrized by introducing a new vector of dependent variables U by formula $U = Lw$, where $L = \text{diag}(\sqrt{\rho_0}, \sqrt{\rho_0}, (c_0\sqrt{\rho_0})^{-1})$. We obtain from (2) for U the system

$$\frac{\partial U}{\partial t} + A_1 \frac{\partial U}{\partial x} + B_1 \frac{\partial U}{\partial y} = 0, \tag{6}$$

where

$$A_1 = LAL^{-1} = \begin{pmatrix} 0 & 0 & c_0 \\ 0 & 0 & 0 \\ c_0 & 0 & 0 \end{pmatrix}, \quad B_1 = LBL^{-1} = \begin{pmatrix} 0 & 0 & 0 \\ 0 & 0 & c_0 \\ 0 & c_0 & 0 \end{pmatrix},$$

thus, matrices A_1 and B_1 are symmetric. Let us approximate (6) by the same scheme (4). The stability condition for this scheme coincides with the stability condition of the scheme from the foregoing example.

Matrix Z in the expression for the amplification matrix (5) is now a real symmetric matrix, therefore, matrix G is a normal matrix. Consequently, under the satisfaction of the von Neumann criterion the scheme under consideration is uniformly stable. The example of the behavior of $\|G^n\|$ is presented in Fig. 2.
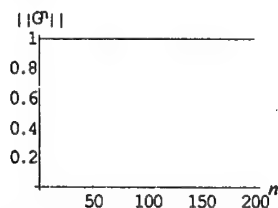
Fig. 2. The Runge-Kutta scheme for the symmetrized acoustics equations (6). The graph of $\|G^n\|$ as a function of the number n of time steps for $\kappa_1 = 1.7$, $\kappa_2 = 1.0$, $\xi_1 = \xi_2 = 0.99\pi$.

The behavior of $\|G^n\|$ is the same at other values of κ_1, κ_2, ξ_1, ξ_2.

UNIFORMLY STABLE DIFFERENCE SCHEME
FOR THE SOLUTION OF GAS DYNAMICS PROBLEMS

Consider the problem of one-dimensional flow of barotropic gas in a channel with constant cross-section. The constant values of the density ρ and velocity u were specified at the channel inlet, and they corresponded to the Mach number $M = 1$. At the channel exit, the value $M > 1$ was specified at $t = 0$, and at $t > 0$, the values of the density and velocity at the right boundary were determined by extrapolation from the nearest internal grid node.

We have at first carried out the computation by the Lax-Wendroff scheme [3] in terms of the variables u and ρ. The numerical results are presented in Fig. 3, where R_n is the maximum residual error at $t = t_n$, $R_n = \max_j |\rho_j^{n+1} - \rho_j^n|/\tau$, and M is the Mach number. It turns out that at $n \cong 1250$, the R_n begins to grow, and at $n \cong 2500$, the solution destabilizes, there is a blow-up in its magnitude. Before the time of this blow-up, the difference solution begins to oscillate (see Fig. 3, (b)), and these oscillations correspond to the oscillations of $\|G^n\|$.

We have then constructed an uniformly stable difference scheme by symmetrizing the original equations. The symmetrization of the equations governing the one-dimensional flow of compressible barotropic gas may be carried out in several ways. We have used, in particular, the following governing symmetric system of equations, which has a comparatively simple form:

$$\frac{\partial U}{\partial t} + S \frac{\partial U}{\partial x} = 0, \tag{7}$$

where

$$U = \begin{pmatrix} U_1 \\ U_2 \end{pmatrix}, \quad S = \begin{pmatrix} u & c \\ c & u \end{pmatrix}, \quad U_1 = \frac{\sqrt{2}}{\gamma - 1} c, \quad U_2 = \frac{1}{\sqrt{2}} u. \tag{8}$$

Here u is the fluid velocity and c is the sound velocity; γ is the ratio of the gas specific heats. Note that the new variables U_1 and U_2 are related to the Riemann invariants r and s via the formulas

$$r = \sqrt{2}\,(U_2 + U_1) = u + \frac{2}{\gamma - 1} c, \quad s = \sqrt{2}\,(U_2 - U_1) = u - \frac{2}{\gamma - 1} c.$$

The Lax-Wendroff scheme approximating the symmetrized equations (7) is as follows:

$$U_{\alpha j}^{n+1} = U_{\alpha j}^n - \tau\, s_{\alpha\beta}(U_j^n)(U_{\beta,j+1}^n - U_{\beta,j-1}^n)/(2h) +$$

$$\frac{\tau^2}{2h^2} s_{\alpha\beta}\left[s_{\beta k}(U_{j+1/2}^n)\left(U_{k,j+1}^n - U_{k,j}^n\right) - s_{\beta k}\left(U_{j-1/2}^n\right)\left(U_{k,j}^n - U_{k,j-1}^n\right)\right] + \frac{\tau^2}{2} Q_{\alpha,j}^n, \quad \alpha = 1,2, \tag{9}$$

where $U_{\alpha,j}^n = U_\alpha(jh, t_n)$, $\alpha = 1, 2$, h is the step of uniform grid on the x-axis, τ is the time step, $s_{\alpha\beta}$, $\alpha, \beta = 1, 2$, are the entries of matrix S in (8),

$$Q_{1,j}^n = \left(\frac{\gamma - 1}{\sqrt{2}} s_{1l} \frac{\partial U_l}{\partial x} \frac{\partial U_2}{\partial x} + \sqrt{2}\, s_{2l} \frac{\partial U_l}{\partial x} \frac{\partial U_1}{\partial x} \right)_j^n,$$

$$\tag{10}$$

$$Q_{2,j}^n = \left(\frac{\gamma - 1}{\sqrt{2}} s_{1l} \frac{\partial U_l}{\partial x} \frac{\partial U_1}{\partial x} + \sqrt{2}\, s_{2l} \frac{\partial U_l}{\partial x} \frac{\partial U_2}{\partial x} \right)_j^n.$$

In the difference scheme (9) and difference operators (10), the summation is carried out from 1 to 2 over the repeating indices.

(a)   (b)
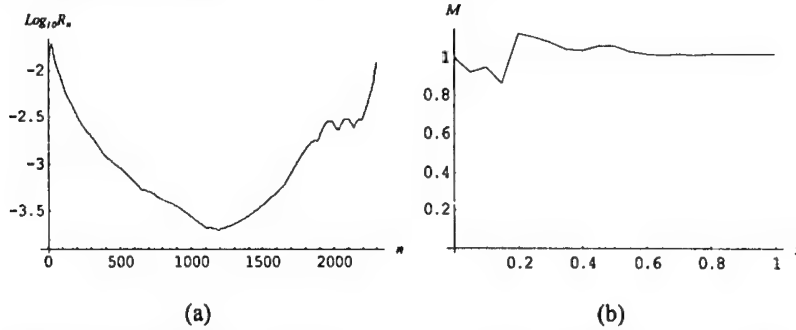
Fig. 3. The Lax-Wendroff scheme in variables ρ, u The Courant number $\kappa = 0.9$. (a) the graph of the maximum residual $log_{10}R_n$ as a function of the number of time steps n; (b) the Mach number $M = M(x, t)$ at $n = 2300$.
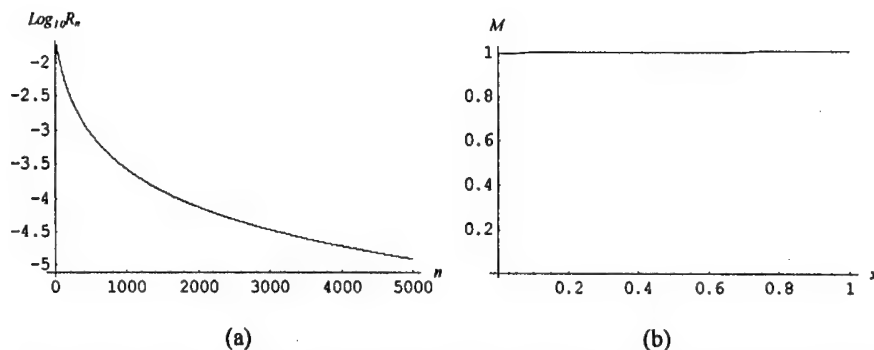
Fig. 4. The Lax-Wendroff scheme in new dependent variables. The Courant number $\kappa = 0.9$. (a) the graph of the maximum residual $log_{10}R_n$ as a function of the number of time steps n; (b) the Mach number $M = M(x, t)$ at $n = 5000$.

    The computational results are presented in Fig. 4. It may be seen that the quantity R_n (see Fig. 4, (a)) monotonously diminishes even at 5000 time steps. The Mach number profile (Fig. 4, (b)) is a monotonous function of x.

    In this problem, we have considered the case of very poor initial conditions, at which the stationary solution represents a flow, which is sonic in the overall spatial interval. This follows from the fact that at $u = c$, the quantity $\|G^n\|$ for the Lax-Wendroff scheme in variables u, ρ has oscillations with a non-decaying finite amplitude. Therefore, despite the linear stability of the Lax-Wendroff scheme at the Courant number $\kappa = 0.9$, the solution blows up because of nonlinear instability.

    The above example shows that it is desirable to use the uniformly stable difference schemes for a reliable computation of gas dynamics problems in the presence of the sonic flow subregions. Similar situations may arise at the computation of flow problems in which there are the stagnation zones.

REFERENCES

1. Zang T.A., Krist S.E., and Hussaini M.Y. Resolution requirements for numerical simulations of transition. Lecture Notes in Engineering. – 1988 – No. 3. – P. 508-525.
2. Darmofal D.L., Siu K. A robust multigrid algorithm for the Euler equations with local preconditioning and semi-coarsening. J. Comput. Phys. – 1999. – Vol. 151. – No. 2. – P. 728-756.
3. Richtmyer R.D., Morton K.W. Difference Methods for Initial-Value Problems. – New York: Wiley-Interscience, 1967.
4. Jameson A., Schmidt W. Some recent developments in numerical methods for transonic flow. Computer Methods in Appl. Mech. and Engineering. – 1985. – Vol. 51. – Nos. 1-3. – P. 467-493.

HEAT AND MASS TRANSFER IN A LAMINAR STEAM-AIR-DROPLET FLOW

V.I. Terekhov
S.S. Kutateladze Institute of Thermophysics SB RAS, 630090, Novosibirsk, Russia.
A.V. Chichindaev, M.A. Pakhomov
Novosibirsk State Technical University, Novosibirsk, Russia.

Introduction. A wealth of theoretical and experimental studies were devoted to the problem of heat and mass transfer and particle dynamics in dispersed flows (see, e. g., [1-8]). The heat transfer in a two-phase flow with no liquid film on the wall [1] takes place under conditions in which liquid droplets vaporize completely until they reach the wall or just on their deposition onto it [3-8].

Physical model and main assumption. In this paper, we consider a 2D anisothermic unsteady steam-droplet flow in a tube with allowance for liquid droplet vaporization. The conductive heat transfer caused by immediate contacting between a droplet and the wall is negligible compared to the convective heat transfer from the steam flow to the wall. The radiative heat transfer was also ignored [3].

The flow and droplet temperatures at the tube inlet are assumed equal, and all droplets are of the same size here. The Biot criterion for the explored range of droplet diameters ($d_{1d} \leq 100$ μm) does not exceed $Bi = \alpha_p / d_{d1} \lambda_L < 0,1$; hence, according to [9], we may ignore the effects caused by heat conduction in each droplet and assume both the droplet surface and core to have the same temperature.

In the steam-gas flow, the droplets take part of a distributed heat drain and a steam source. The mixture gives up heat to liquid droplets, and the released steam takes on the temperature of the main steam-air flow. The liquid phase acts as a set of local heat drains and local mass (steam) sources. Each droplet is assumed to retain its spherical shape. By virtue of low droplet concentration, the inter-particle collisions are ignored. The flow-carrier is described within the Eulerian approach, while the droplet dynamics is considered within the Lagrangian approximation, which permits tracing the dynamic properties of each individual particle along its trajectory [1].

On the whole, the problem statement is similar to those of [3,4], but, unlike them, it permits investigation of more complex air-steam flows with contained droplets, for which there arises a necessity in solving the system of energy and diffusion equations for a gas-steam mixture. In the given activity the main attention is given to the analysis of the thermal and diffusive tasks, and the flow is supposed hydrodynamics stabilized with a developed profile for a laminar flow. The slip of phases also as a first approximation is not taken into account, which essentially simplified all further analysis.

System of equations. With allowance for the above assumptions, the heat transfer and hydrodynamics of the air-steam-droplet flow is given by the following system of equations. The energy equation for the mixture of interest is [3,4,10]:

$$\rho C_p U \frac{\partial T}{\partial x} = \frac{1}{r} \frac{\partial}{\partial r}\left(r\lambda \frac{\partial T}{\partial r}\right) - \alpha \pi n d_d^2 (T - T_{1L}) + \rho D_{V-A} \frac{\partial K_V}{\partial r}(C_{pV} - C_{pA})\frac{\partial T}{\partial r}. \tag{1}$$

The diffusion equation for steam in air is [10]:

$$\rho U \frac{\partial K_V}{\partial x} = \frac{\rho}{r} \frac{\partial}{\partial r}\left(r D_{V-A} \frac{\partial K_V}{\partial r}\right) + j \pi n d_d^2. \tag{2}$$

The energy and diffusion equations include source (drain) terms, which allow for the heat transfer from the gas phase and steam mass supply caused be droplet evaporation. These are the second terms in the right side of Eqs. (1) and (2). The third term in the right part of the energy equation (3) describes the diffusional heat transfer in the steam-gas phase.

Equations (1) an (2) are supplemented by the heat-transfer equation for the interface between phases:

$$C_{pL}\rho_L \frac{\pi d_d^3}{6}\frac{dT_L}{d\tau} = \alpha\pi d_d^2(T-T_L) - j\pi d_d^2\left[L + C_{pV}(T-T_L)\right].$$

(3)

The equation of mass conservation on the droplet surface includes the convective and diffusional components [10]:

$$j = jK_{VS} - \rho_V D_{1-2}\left(\frac{\partial K_V}{\partial r}\right)_S.$$

(4)

The balance equation for a binary steam-air mixture has the form

$$K_V + K_A = 1.$$

(5)

For a triple steam-gas-liquid mixture, this equation can be written as

$$C_A + C_V + C_L = 1.$$

(6)

The mass concentrations K_i и C_i are related by the equation

$$K_V = \frac{C_V}{C_V + C_A}; \quad K_A = \frac{C_A}{C_V + C_A} = 1 - K_V.$$

(7)

Boundary conditions. The inlet mixture and particle temperatures, as well as the inlet steam, gas and droplet concentrations were assumed uniform across the tube:

$$T = T_1, \quad d_K = d_{1K}, \quad K_{A1} = 1 - K_{V1}, \quad C_L = C_{L1} \text{ at } x = 0.$$

(8)

At the tube axis, the symmetry condition holds:

$$\frac{\partial T}{\partial r} = \frac{\partial K_V}{\partial r} = \frac{\partial U}{\partial r} = 0 \quad \text{at } r=0.$$

(9)

The boundary conditions at the wall surface are

$$\lambda\frac{\partial T}{\partial r} = q_W, \frac{\partial K_V}{\partial r} = U = 0 \quad \text{at } r=R_0.$$

(10)

The local Nusselt number for a constant wall heat-flux density was found from the difference between the wall temperature and the mean-mass temperature of the gas-steam mixture:

$$\mathrm{Nu} = \frac{q_w 2R_0}{\lambda_\Sigma\left(T_w - T_m\right)}$$

(11)

The man-mass temperature in (19) was found by integration of the temperature field over the tube cross section:

$$T_m = \frac{4}{R_0^2}\int_0^{R_0} T\left(1 - \left(\frac{r}{R_0}\right)^2\right) r\,dr.$$

(12)

In the same manner, the mean-mass concentrations of all components in both phases were determined.

171

Thus, relations (1)-(10) constitute a closed system of equations, which describes the heat-transfer processes in the steam-gas-droplet flow and permits determination of all desired quantities, i. e., temperatures, enthalpies and concentrations of the phases and each of their components. In addition, the system of equation allows one to trace evolution of particle sizes and elucidate the degree of heat transfer enhancement by evaporation processes.

Calculation procedure. The above equations supplemented with the indicated boundary conditions were solved numerically by the finite-difference method. The stability of the calculation procedure was ensured by using an explicit absolutely stable sweep scheme. The resultant matrix was solved by the Thomas algorithm [11]. The steps along the streamwise and crossflow coordinates were one caliber and one-hundred of the caliber. The length of the tube and its inside diameter were 2 m and 2 cm, respectively. The thermophysical properties were calculated using the formula reported in [12].

The explored range of parameters and validation of results for adequacy. Numerical studies were performs for the standard physical conditions of laminar flow in the following range of initial parameters: the mixture temperature T_1 varied from 373 to 450 K, the Reynolds number of the flow Re_D from 100 to 2000, the droplet diameter d_{1d} from 1 to 100 μm, and the mass concentrations of droplets and air C_{L1} and C_{A1} from 0 to 0.1 and from 0 to 0.8, respectively.

In the absence of the liquid phase and air, the numerical solution was found to be in agreement (within 2 %) with the analytical data of [13]. For comparison purposes, data of the numerical analysis of [3] for the two-phase flow were invoked. In this case, the errors turned out to be more substantial, running into 5-7 % for some flow conditions.

Numerical results, their discussion and comparison with the experiment. The primary emphasis in this study was placed to the stable flow mode.

The profiles of the air, steam and liquid mass concentrations across and along the tube for various droplet diameters and identical inlet concentrational and temperature conditions (d_{1d}=30 μm, q_w=0,2 kW/m^2, T_1=373 K и T_{1L}=283 K) are shown in Figs. 1a-1c, respectively.

The heat and mass transfer between the liquid phase and the steam-gas mixture and the heat exchange with the wall surface are obviously inter-related processes. To gain a better insight into them, it is required to study the concentration profiles along the tube both for the liquid phase and for each of the steam-gas mixture components. These date are shown in Fig. 1. The mass content of the liquid phase (Fig. 1a) decreases monotonically with the distance along the tube length, and the released steam (Fig. 1b) results in a growth of the steam concentration, which, for the conditions under study (C_{L1}=C_{V1}=0,1) increases by a factor of two as $x/D\to10$.

The mass concentration of air varies non-monotonically along the tube radius (Fig. 1c). In the zones with the most intensive evaporation, local minima of the air concentration forms, which, as the mixture moves downstream, becomes less pronounced and moves closer to the tube axis.

The calculated dimensionless enthalpy profiles $\eta = (h - h_W)/(h_0 - h_W)$ over several cross sections of the channel at different distances from its inlet are shown in Fig. 2. The enthalpy h was determined from the following formula for a
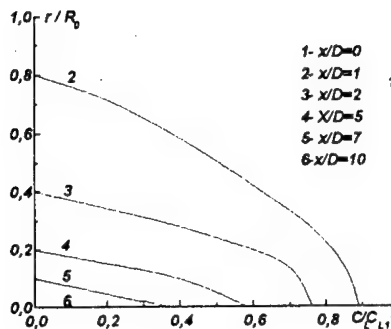
Fig. 1a. Liquid-phase distribution.

gas-steam $h = (C_{PA}C_A + C_{PV}C_V)T + C_{PL}C_LT_L + LC_V$, where L is the latent heat of the phase transition.
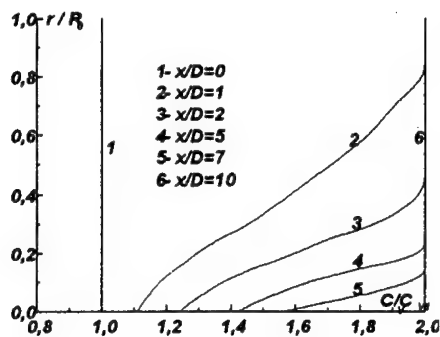
Fig. 1b. Steam concentration profiles.
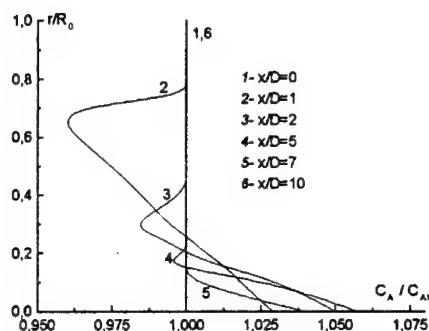
Fig. 1c. Variation of the air concentration
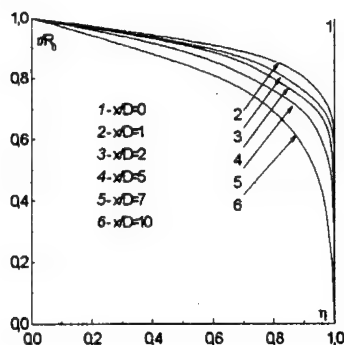
Fig. 2. Distribution of the relative enthalpy h over the tube radius.

The Reynolds number built on the inlet parameters was kept unchanged in this calculation. The obtained flow pattern, however, turned out to be typical of cases with other flow and concentrational conditions at the tube inlet.

The above peculiarities of thermal and concentrational fields in the two-phase steam-gas flow are embodied in the heat transfer enhancement parameter defined as the ratio Nu/Nu_0, where Nu_0 is the Nusselt number in a single-phase steam flow with a fixed inlet Reynolds number. These results are shown in Fig. 3. For a single-component steam-droplet flow ($C_{A1} = 0$, curve 1) the heat transfer is enhanced in a lest degree ($Nu/Nu_0 < 1.5$). As the air concentration increases, the heat transfer enhancement becomes more pronounced, the zone of the enhanced heat transfer however shrinking along the channel length.

It should be noted that the data of Fig. 3 are presented here only to demonstrate a typical situation since the process under study is in fact a multi-parametric one, the enhanced heat transfer depends on a multitude of parameters. It is beyond the scope of this article to give the detailed analysis of their influence.

Analysis of available literature data on the heat transfer in channeled two-phase flows showed that these data are few in number.

For comparison purposes, we used the experimental data of [8] on the heat transfer in a water-air aerosol flow in a low-bulk heat exchanger. To be compared are immediately measured quantities, namely, the heat transfer enhancement ratio, being the ratio of heat transfer coefficients in the two-phase gas-droplet flow and in a single-phase air flow. The working section parameters were the following: length $L = 0,24$ m, equivalent tube diameter $D = 2,67$ mm and $x/D = 0 \div 80$, maximum Reynolds number $Re_D = 8 \cdot 10^3$, mass concentration of droplets $C_{L1} = 0 \div 0.03$, and their diameter $d_{1d} = 1 \div 2$ μm. In the experiments, the wall heat flux was kept unchanged ($q_W = $ const).

173
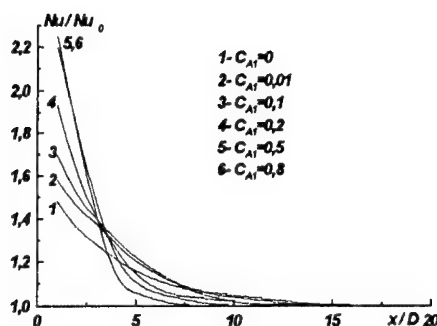
Fig. 3. Heat-transfer enhancement in a channeled steam-gas-droplet flow.
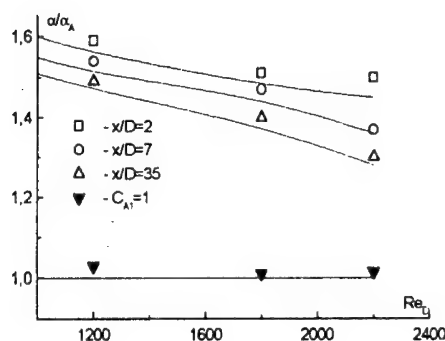
Fig. 4. Comparison with the experimental data [8]. Curves – calculation results.

The comparison between the numerical results of this study and the experimental data of [8] is presented in Fig. 4, where the ratio of the heat transfer coefficients α/α_A is shown as a function of the lengthwise coordinate for several Reynolds numbers Re_D, where α_A is the heat-transfer coefficient for the single-phaseair flow.

From the figure, it follows that the predicted values agree well with the experimental data. Both sets of values show a gradual decrease of the efficiency parameter of the heat-transfer intensification as the free stream velocity increases

Thus, Figure 4 shows that the advanced model provides a good qualitative and quantitative description of the heat and mass transfer in a two-component two-phase flow with a phase transition. At the same time this model cannot be regarded as an exhaustive one which gives full and adequate description of all involved phenomena. To devise such a model, more theoretical and experimental studies are required.

Conclusions

1. A physical model of the combined heat and mass transfer in a developed laminar channeled flow of a gas-steam-droplet mixture is proposed. The liquid phase is considered as a set of local heat drains and steam mass sources. A closed system of transfer equations is given.

2. Heat- and mass-transfer processes in the laminar air-droplet flow are studied. An increase in the air content of the mixture enhances the heat transfer in comparison with a single-component steam-droplet flow. The performed comparison between the numerical and experimental data shows good qualitative and quantitative agreement between them.

Nomenclature

α – heat-transfer coefficient, d – droplet diameter or differential sign, λ – heat-conduction coefficient, ρ – density, μ – dynamic viscosity, C_P – specific heat, T – temperature, n – number of droplets per unit volume of the mixture, D_{1-2} – steam diffusivity in the gas, K – concentration of a component in the binary steam-air mixture, C – concentration of a component in the steam-gas-droplet mixture, j – crossflow steam flux at the droplet surface, x – longitudinal coordinate, r – transverse coordinate, L – length of the heat-exchanging channel, D – tube diameter, R_0 – tube radius, U –lengthwise velocity.

Subscripts

P – non-vaporizing particle, d – droplet, L – liquid phase, A – air, V – steam, S – parameter taken along the saturation curve, W – wall, m – mean-mass value, 0 – tube axis, 1 – inlet value of a parameter, D – parameter built on the tube diameter.

References

1. Nigmatulin R.I. Dynamics of multiphase media. Vol. 1, 2. N. Y.: Hemisphere, 1990. 505 p.
2. Soo S.L. Fluid dynamics of multiphase systems. Toronto: Blaisdell Publ. Co., 1967. 525 p.
3. Yao S.-C., Rane A.G. Heat transfer of laminar mist flow in tubes // J. of Heat Transfer. 1980. Vol. 102, No. 3. P. 678-683.
4. Terekhov V.I., Pakhomov M.A., Chichindaev A.V. Heat transfer at laminar developed flow of a steam/drops flow in a pipe // Thermophysics and Aeromechanics. 2000. Vol. 7 (in press).
5. Hishida K., Maeda M., Ikai S. Heat transfer from a flat plate in two-component mist flow // J. of Heat Transfer.-1980.-Vol. 102, No.3. P. 513-518.
6. Mashayek F. Direct numerical of evaporating droplet dispersion in forced low Mach number turbulence // Int. J. of Heat Mass Transfer. 1998. Vol. 41, №17. P. 2501 -2619.
7. Crowe C.T., Sharma M.P., Stock D.E. The Particle-Source-In Cell (PSI-Cell) model for gas-droplet flow // J. of Fluid Eng. 1977. Vol. 99, №2. P. 325-332.
8. Chichindaev A.V. Research of heat transfer to a cold flow of a water aerosol: Ph. D. dissertation / Novosibirsk State Technical University, 1998. (in Russian)
9. Luikov A.V. Theory of heat conduction. Moscow: Vysshaya shkola, 1967. 600 p. (in Russian)
10. Issaev S.I. and al. Theory heat- and mass transfer / Ed. A.I. Leontiev. Moskow: MSTU, 1997. 538 p. (in Russian)
11. Shi Tien-mo Numerical heat transfer. Berlin et al.: Springer-Verlag, 1984. 535 p.
12. Fujii T. Theory of laminar film condensation. N. Y. et al.: Springer-Verlag, 1991. 213 p.
13. Kutateladze S.S. Fundamentals of heat transfer. N. Y.: Academic Press, 1965. 563 p.

THE SEPARATED FLOW BY VARYING DEGREE OF EXTERNAL TURBULENCE

V.I. Terekhov, N.I. Yarygina, R.F. Zhdanov

Institute of Thermophysics SB RAS,
630090, Novosibirsk Russia

1. Introduction

The study of separated flows behind obstacles is of great importance for high-power elements of various apparatus, civil-engineering constructions, and in many other applications. In most cases, the vortices in separated flows are unsteady, and their experimental study is difficult. In spite of the considerable influence of the initial flow turbulence on the dynamics and heat transfer in such flows, the energy exchange in them has not yet received the attention it deserves.

The flow over a downward step is a classical separation flow; therefore, when studying the effect of the approach-flow turbulence, it can be used for comparison with other types of separation flows. In [1], it was shown that the free-flow turbulence brings about a more intense pulsational motion of the shear layer just behind the flow detachment point and results in higher Reynolds stresses throughout the layer. Irrespective of the manner in which the flow separation is organised (step, blunt plate, rib, etc.), with increasing outside turbulence, the flow reattachment regions moves closer to the obstacle; hence, the recirculation zone becomes shorter. For instance, in [1] the flow reattachment point behind a rib was found to move half the initial separation closer to the obstacle. The length of the recirculation region behind a step was decreased by a factor of 1.6 [2]. Another peculiarity of the separated flows established in [2] is a rise in the recirculation flow velocity by 15 % under the action of the outside turbulence. In many works, an increase in the heat-transfer rate caused by the outside turbulence was reported. For example, in [2] the heat-transfer coefficient appeared to be increased by about 15 %. However, there are other reported data. For instance, the authors [2] showed that, behind a step, both the flow pulsation frequency and the heat-transfer rate turned out to be practically independent of the initial flow turbulence. They also established that an increase in the mainstream turbulence level exerts only a weak effect on the intensity of velocity pulsations in the flow recirculation region.

In view of the contradictions both in model concepts used for interpreting the complex structure of separated flows and in numerical estimates of relevant characteristics of heat-transfer processes, it becomes clear that only combined studies can shed light on the evolved dependence of separation-flow parameters on the free-flow conditions. The present work continues our previous studies [4]. It describes some new results on the dynamics of separation flows and on the heat transfer behind a downward step and a crossflow rib as a function of obstacle geometry, obstacle height (3÷30 mm) and initial tunnel turbulence ($Tu_0 \approx 1 \div 15$ %).

2. Experimental setup and procedure

The experiments were carried out in one of the wind tunnels of the Institute of Thermophysics. The cross-sectional flow area of the tunnel was 200×200 mm². The length of the tunnel was 600 mm, the flow velocity over the obstacle being ~20 m/s ($Re_x = xU_0/v \approx 1 \cdot 10^3 \div 5 \cdot 10^5$). In the present study, several models were employed. In heat-transfer studies, we used a textolite model. Its length, width and thickness were 500, 200 and 13 mm, respectively. To ensure tem-

perature measurements, 40 Chromel-Copel thermocouples were chalked into the plate. The horizontal surface of the plate was heated by a ribbon foil heater, with a spatially uniform heat flux supplied (q = const). The total area of the heater was about 150×400 mm². The heat leaks caused by heat conduction were estimated from the measured temperature difference across the model. The dynamic losses behind obstacles were measured by sampling static pressure along a similar plate through taps 0.3 mm in diameter. The soot-oil visualization studies of the separation flow were performed using another model whose upper part was made transparent. The thermographic visualization of the working model covered with a current-conducting 120×315 mm² graphite-epoxy coating was performed with the help of an IR imager. Digital representation of the measured images was ensured by 15 Chromel-Alumel thermocouples, which measured local temperatures at points equally spaced along the symmetry axis of the plate. Another two such thermocouples were installed on the lower surface of the model.

In the experiments, the step height (Fig. 1, a) varied from 6 to 30 mm. This variation was ensured by displacement of the model along the vertical line. A 230 mm-long foam-plastic fairing with a uniform thickness $H^* = 58$ mm ensured identical outside conditions for the flow-separation studies with steps of different heights. The rib installed on the model (Fig.1, b) was made from organic glass. The rib heights were H = 3, 6, 10, 20, and 30 mm. The rib length and thickness were fixed (200 mm and ~3 mm, respectively).
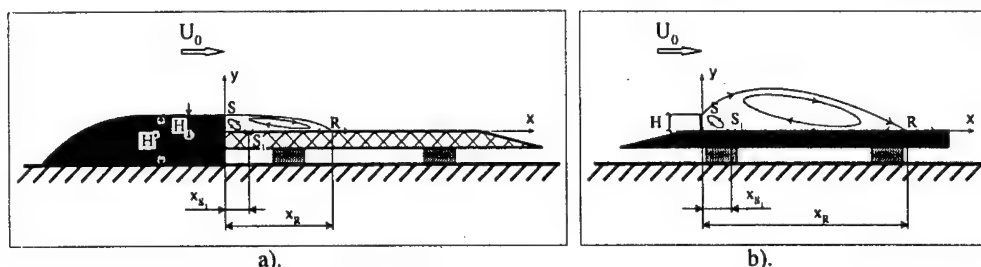
Fig.1. Experimental model with a downward step (a) and a rib (b).
Notations and coordinates: S – flow detachment point; R – flow reattachment point; x_R – distance to the reattachment point; S_1 – point of the second flow detachment; x_{S_1} – coordinate of the flow detachment at the model surface, the secondary–vortex region; H – rib/step height; H^* – step fairing height.

Forced turbulization of the tunnel flow was ensured by a passive turbulence generator "perforated plate", the perforated portion of the total surface being about 64 %. The generator was made in the form of a screen with 81 holes 20 mm in diameter. The axes of neighboring holes were spaced 22 mm apart. A flag-type turbulence generator was also employed made in the form of the above-described screen with flags fastened to nodal points. The flags were about 100 mm long and 10 mm wide. Each turbulence generator totally spanned the cross-sectional area of the working channel, being installed 330 mm upstream from the obstacle.

3. Experimental results

3.1. Flow separation dynamics. The soot-oil visualization studies revealed a substantial difference in the formation of the separated flow behind the step and the rib. This difference was especially pronounced in the secondary-vortex region. Behind the 20-mm-high step, the turbulent tunnel flow without additional turbulization (Fig.2, I, a) gave rise to quite a symmetrical flow pattern over the model surface. The time-averaged reattachment line was situated at the

distance ~4.8·x/H from the step. In the corner zones, two vortices were observed which executed rotational motion, moving from corner towards the flow reattachment region and, then towards the step. In the central region of the secondary vortex, a mushroom-like structure formed.

In the tunnel with installed flag-type turbulence generator, the recirculation region behind the step of the same height (Fig.2, I, b) was found to be shorter by eight tenth parts of the gage. The flow reattachment line was perfectly straight, while the flow in the step corner was asymmetric. The asymmetry of the secondary vortex was observed not only at the center near the step: the sidewall vortex could disintegrate into two smaller vortices whose directions of rotation coincided with that of the initial solitary vortex.

In the low-turbulent flow, the time-averaged reattachment region behind the 10-mm-high step was situated at the distance $x_R/H \approx 5.5$ downstream (Fig.2, II, a). The corner flow structure
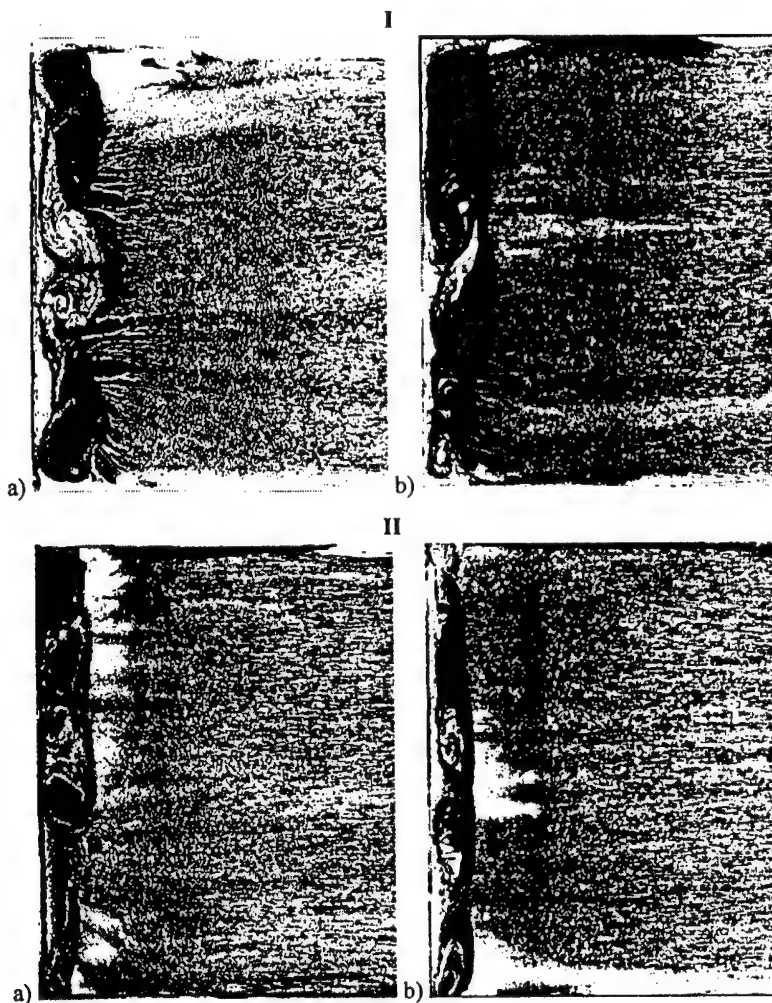
Fig.2. Soot-oil visualization of the separated flow downstream of the step of height H = 20 mm (I) and 10 mm (II) at $Tu_0 \to 0$ (a) and $Tu_0 > 10$ % (b). Top view. Flow direction: from the left to the right.

178
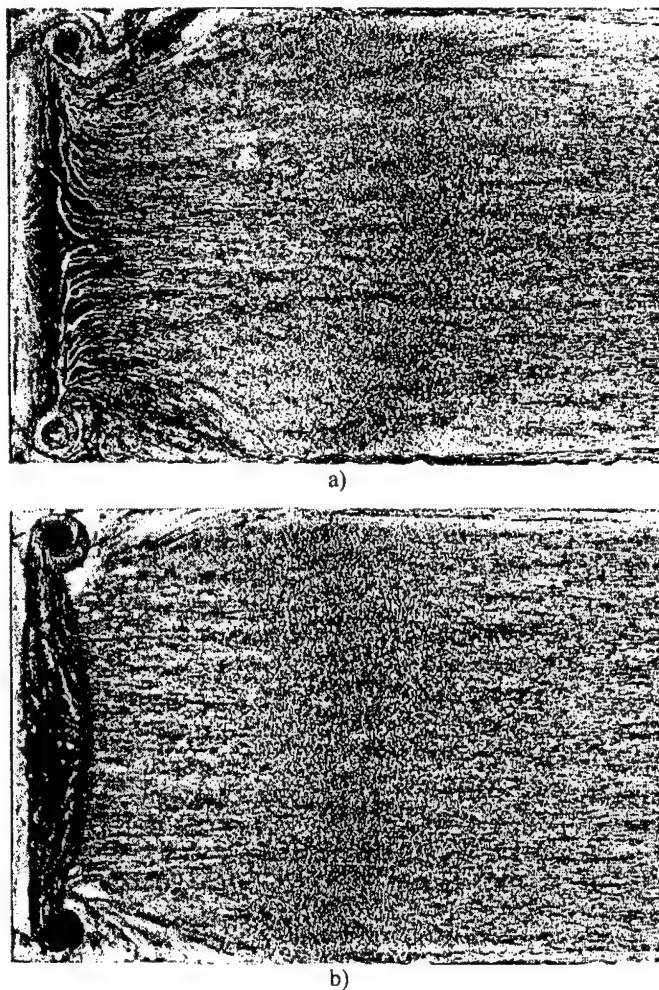
Fig. 3. Soot-oil visualization of the separated flow dowstream of the rib of height 10 mm at $Tu_0 \rightarrow 0$ (a) and $Tu_0 > 10\%$ (b). Top view. Flow direction: from the left to the right.

in this case was clearly asymmetric. The high-turbulent flow (Fig.2, II, b) makes the recirculation region to contract $(4.7 \cdot x/H)$ and changes the structure of the secondary vortex.

Thus, a rise in the free-flow turbulence results in a contraction of the flow separation region behind a step, straightens the time-averaged flow reattachment line and substantially deforms the secondary-vortex region. A decrease in the step height results in a larger ratio between the recirculation-region length and the step height. The high-turbulent flow ensures uniform displacement of the flow reattachment line upstream irrespective of the step height (10 or 20 mm) compared with the conditions of natural turbulence in the tunnel.

Behind the rib of height 10 mm, in the case of the natural turbulence (Fig.3, a), two large-scale structures originate. Their origination is supported by thermovisualization data and observations reported in [5]. The time-averaged flow reattachment region is situated at the distance $x_R/H = 18.5$ downstream along the plate central line. The higher turbulence of the approaching stream, provided by the flag generator (Fig.3, b), makes the flow separation region shorter ($x_R/H = 15$). The curvature of the reattachment line in this case is diminished. Behind the rib of height $H = 20$ mm, the turbulence-induced displacement of the flow reattachment region towards the rib amounts to 3.3 gages.

Comparative visualization studies of the flows over the step and the rib of equal heights reveal the following drastic difference between the structures of the two separated flows: in the central part, just near the step, new vortices appear additional to corner sidewall ones. At the same time, behind the rib only corner large-eddy structures appear. The reattachment line in this case is more curved than behind the step.

The high free-stream turbulence has different effects on the separation-flow structure behind the rib and the step. Behind the rib of heights 10 and 20 mm, a higher free-stream turbulence

Fig. 4. Distribution of the maximum reverse-flow velocity
normalized to the mainstream velocity.
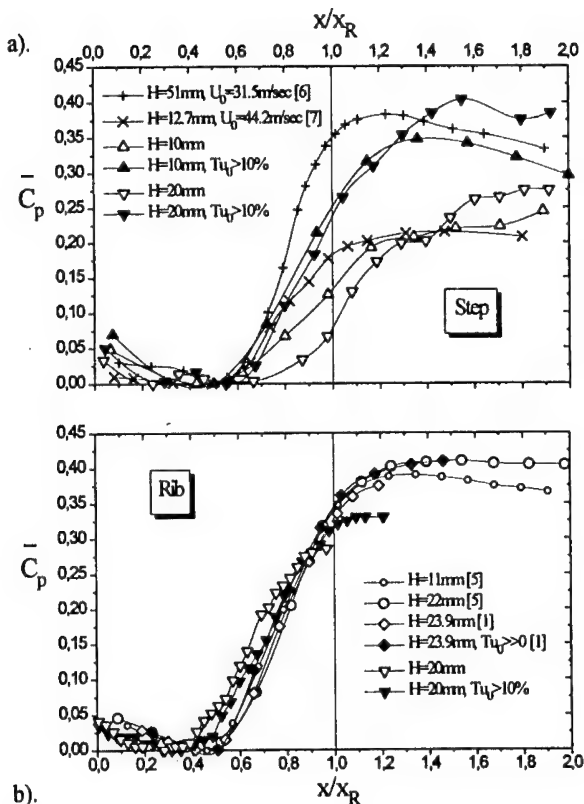
Fig. 5. Distribution of pressure behind steps (a) and ribs (b)
of various heights.

results in a contraction of the entire flow-separation region by three gages, whereas behind the step of the same height the similar contraction does not exceed one gage, which, after normalization, is also lesser. The high-turbulent flow cause no appreciable deformation of the secondary-vortex structure behind the rib, whereas the flow behind the step suffers more pronounced changes. The main reason for the observed contraction of the flow separation region is, presumably, the increased thickness of the mixing layer. It is the flow pre-history upstream the obstacle which is responsible for the more substantial contraction of the recirculation flow behind the rib compared to the case of step.

The corner vortex structure is caused by fluid ejection from the main reverse flow. The highest velocity in the reverse flow behind the step does not exceed 30 % of the free-stream velocity (Fig.4), whereas behind the rib it may reach 40 %. The smaller obstacle height results in a lower maximum velocity of the reverse flow. The high free-stream turbulence accelerates the recirculation flow.

For convenience sake, the dynamic losses behind the obstacles of various heights can be compared by considering the relative pressure coefficient

$$\overline{C}_p = (C_p - C_{p\,min})/(1 - C_{p\,min}),$$

where $C_p = 2 \cdot (P_i - P_0)/\rho U_0^2$ and P_i is the static pressure at the flow separation line. Figure 5, a shows the pressure distribution behind the steps of heights 10 and 20 mm for two levels of free-stream turbulence. The static pressure profiles upstream from the flow reattachment region show

that the reattached stream is accelerated by pressure gradient and the bottom-pressure coefficient decreases gradually up to the point $x/x_R \approx 0.5 \div 0.6$. Farther upstream, the pressure gradient changes its sign, which results in flow separation from the surface and gives rise to the corner vortex, the separation of the flow taking place after passing the highest $\overline{C}_p$, i.e., $x_{\overline{C}_{p\,min}} > x_{S_l}$. The displacement of the $\overline{C}_p$ maximum towards the step in a high-turbulent flow correlates well with the observed shrinkage of the flow separation region. Variation of the step height reveals a considerable difference between the pressure profiles, whose maximum scatter is observed in the flow reattachment region. Here, the higher obstacle, the higher $\overline{C}_p$. Behind the rib (Fig. 5, b), the scatter of relative pressure coefficients is insignificant and becomes notable father downstream from the reattachment region. For example, the twofold change in the rib height [5] exerts a profound influence on the $\overline{C}_p$ profile only for $x/x_R > 1.2$.

The performed comparison of the profiles of the relative pressure coefficient behind the obstacles under study illustrates the weak sensitivity of the separation flow behind the rib to the free-flow turbulence compared to the case of step. This effect can be understood as stemming from the experienced flow pre-history.

Fig.6. Distribution of Stanton number in the ralaxation (a) and recirculation (b) regions behind the step and the rib. The coordinate x is reckoned in the downstream (a) and upstream (b) direction from the place with the most intense heat transfer. Symbols without connecting lines – numbers based on the outside–flow parameters. Symbols with connecting lines – numbers based on the flow parameters at the edge of the new
wall boundary layer.

3.2. Heat transfer in separation flows. It worth considering the obtained data on the convective heat transfer behind the step and the rib of various heights at different levels of free-stream turbulence in two regions, those lying upstream and downstream from the flow reattachment region. In the relaxation region (Fig. 6, a), both behind the rib and behind the step the development of the new boundary layer follows the dependence being valid for the turbulent boundary layer over a plate $St_{turb.} = 0.0306 \cdot Re_x^{-0.2} \cdot Pr^{-0.6}$.

The appreciable difference in velocity levels and temperature profiles at the edge of the new boundary layer in recirculation region and in the main stream is responsible for the Stanton number (St) profiles behind rib and especially behind step (symbols without connecting lines in Fig.6, b) which differ from the profile for the turbulent boundary layer over a plate. The same dependences for the Stanton and Reynolds numbers built on the highest velocity in the reverse flow and on the temperature in the near-wall region is also shown in Fig.6, b (symbols with connecting lines). The above representations of the experimental data permits gaining a better insight into the character of the flow as it moves farther from the reattachment region towards the reattachment point. The presence of large-scale vortex structures in the corner region obviously affects the convective heat transfer. Hence, it necessitates more detailed analysis of the data in the secondary-vortex zone. In the recirculation region behind the rib of height 20 mm, the initial section of the flow which develops behind the flow reattachment point is of clearly pronounced turbulent character. Then, the boundary layer moves upstream and detaches from the surface. Simultaneously, the power exponent at Re_x in the dependence for the Stanton number assumes the value -0.3. For the shorter rib (H=10 mm), the "turbulent character" is retained farther upstream, up to the region of the secondary flow separation. The high-turbulent free stream exerts a profound influence on the development of the new boundary layer in the flow recirculation region. In this case, the dependence $St = f(Re_x)$ behind the rib of height H=20 mm preserves its turbulent character until the secondary flow separation happens. Under natural turbulence level in the tunnel, the wall boundary layer in the flow behind the step obeys the laminar law $St_{lam.} = 0.47 \cdot Re_x^{-0.5} \cdot Pr^{-2/3}$. The latter is evidenced by the experimental data of [8].

Thus, changing the geometry of the separated flow, the obstacle height, and the free-stream turbulence, one can effectively control the dynamics and heat transfer in separated flows.

Conclusions

1. Pressure distributions in flows over a step and a rib show drastic differences. Variation of the obstacle height results in a considerable scatter of the relative pressure coefficients behind the step, the maximum scatter being observed in the flow reattachment region. At the same time, the scatter behind the rib is insignificant: it was observed only in the region past the reattachment region.

2. A highly turbulent external gives rise to more pronounced contraction of the flow separation region. This contraction runs into more than three gages behind ribs of heights 10 and 20 mm, but does not exceed one gage in the case of steps of the same heights. The enhanced mainstream turbulence accelerates the recirculation flow and causes only slight deformation of the secondary-vortex region behind the rib compared to the case of step.

3. The heat transfer rate in the relaxation region follows general regularities inherent to the boundary-layer turbulent transfer.

4. With outside-flow parameters used as determining ones, the experimental data on the heat transfer in the recirculation region cannot be fitted by the laws of laminar and turbulent heat exchange on a plate. With local flow parameters at the edge of the wall boundary layer used for the fitting, the variation of the heat-transfer coefficients inside the recirculation region shows an intricate behaviour. However, the heat-transfer law near the flow reattachment point is turbulent, which is especially the case for the rib, although the correlation dependence itself, because of the occurrence of intense turbulent pulsations here, lies higher than that for a plate.

References

1. Castro I.P., Haque A. The structure of a shear layer bounding a separation region. Part 2. Effects of free-stream turbulence // J. Fluid Mech. 1988.Vol. 192. P. 577-595.

2. Alemasov V.E., Glebov G.A., and Kozlov A.P. Thermoanemometry methods for investigation of separation flows. Kazan: KAI, 1990. 178 p.

3. Dyban E.P., Epik E.Ya., and Yushina L.E. Heat transfer on the surface of longitudinally streamlined bodies in the presence of closed separation and external flow turbulization // Proc. Tenth Int. Heat Transfer Conf. Vol. 3. Brighton (UK). P. 25-30.

4. Terekhov V.I., Yarygina N.I., and Zhdanov R.F. The structure of the separated flow behind obstacles at high external turbulence // Intern. Conf. on the Methods of Aerophys. Research: Proc. Pt 1. Novosibirsk, 1998. P. 220-227.

5. Ruderich R. and Fernholz H.H. An experimental investigation of a turbulent shear flow with separation, reverse flow, and reattachment // J. Fluid Mech. 1986. Vol. 163. P. 283-322.

6. Chandrsuda C. and Bradshaw P. Turbulence structure of a reattaching mixing layer // J. Fluid Mech. 1981. Vol. 110. P. 171-194.

7. Driver D.M., Seegmiller H.L., and Marvin J.G. Time-dependent behavior of a reattaching shear layer // AIAA J. 1987. Vol. 25, No. 7. P. 914-919.

8. Vogel C.J. and. Eaton J.K Combined heat transfer and fluid dynamic measurements downstream of a backward-facing step // Trans. ASME, J. Heat Transfer. 1985. Vol. 107, No. 4. P. 922-929.

APPLICATION OF AN OPTICAL PULSATED DISCHARGE FOR STABILIZATION OF THE HYDROGEN/AIR FLAME

P.K. Tretyakov, S.S. Vorontsov, A.F. Garanin, A.V. Tupikin, V.I. Yakovlev

Institute of Theoretical and Applied Mechanics SB RAS
630090, Novosibirsk, Russia

G.N. Grachov, V.B. Shulyat'ev

Institute of Laser Physics SB RAS
630090, Novosibirsk, Russia

Introduction. Nowadays research of the optical pulsated discharge (OPD) in supersonic gas flow [1–3] shows the possibility to apply new methods of stabilizing the flame and control the combustion in gaseous flows. OPD formation in the reactive flow can cause new effects conditioned by the influence of the gasdynamic and kinetic factors on this flow. Non-stationary gasdynamic disturbances appear at optical breakdown which forms quasi-stationary wave structure consisting of a shock wave and thermal wake under certain conditions [3]. Besides, an optical breakdown plasma, emitting in a wide spectral range can considerably change pre-flame processes in the reactive medium, leading mechanisms of kinetic processes, respectively, the rate of heat release in the flow till ultimate determining the explosive character of the process.

In present paper the possibility of application of the optical pulsated discharge for flame initiating and stabilization in homogeneous hydrogen/air flow was studied for the first time. To provide the radiation power density above medium's breakdown threshold the argon was injected into the focused laser beam region along the axis of the main flow. The breakdown threshold is several times lower in inert gases than in the used mixture. However, this additional factor of the optical discharge stabilization (by argon injection) is not important and can be excluded when the laser power is increased several times.

Experimental set-up and registration methods. Gas-dynamic section of the set-up (Fig. 1) provides the formation of subsonic jet of the working mixture by the confuser (with the outlet diameter 8 mm) and the argon wake (through the hole of 3 mm) along the flow axis. Air and hydrogen are mixed in the working chamber *1*, argon is supplied from the plenum chamber *2*. Laser radiation is focused by the lens *3* in the argon jet at a distance of 10 mm from the outlet section and blocked up by absorber *4*. The pulse-periodic CO_2-laser LOK-3MSI developed in ILP SB RAS and applied in the previous our experiments was used.

Optical scheme of flow visualization is presented in Fig. 1 too. The flow region with OPD *5* was lighted using He-Ne – laser *6*. The spherical wave front (converging beam) with the demanded aperture of the object under investigation was formed by micro-lens *7* and large focusing distance (450 mm) lens *8*. The application of the spherical wave front allowed one to use interferometer 9 with the inlet aperture 16 mm, which is less than the visualization field's dimention (50 mm). Interferometer was set up at a certain distance from the object. The applied scheme of interferometer with the separated regulation of the fringe's width and sensitivity allowed one to determine reliably the boundaries of the turbulent combustion zone. Information was registered through light filter *10* and objective *12* by television camera of technical vision *11* with the exposure time 0,1 ms. It was recorded by video-player *13* and displayed by monitor *14* during process in study. After experiment the selected frames were numbered and processed by the standard graphic methods.
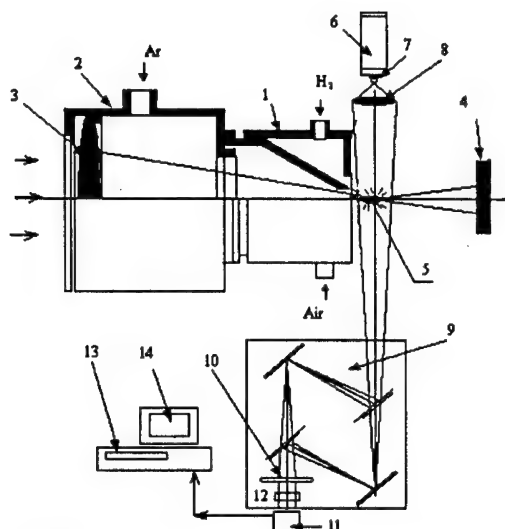
Fig. 1. Experimental set-up and optical scheme.

Parameters and conditions of the experiments. All experiments were conducted with the homogeneous mixture hydrogen/air jet at subsonic exhaustion into ambient atmosphere. The range of air consumption varied within $1,5 - 8$ g/s, hydrogen $0,045 - 0,1$ g/s. Argon consumption varied little and made up $2,3 - 2,5$ g/s. The velocities of the mixture flow and argon were determined by the data about gas consumptions and throat areas of the outlet holes. Equivalence ratios was determined by the relation of air and hydrogen consumptions taking into account stechiometric coefficient, equal to 34,5.

Experiments were performed in two stages. At the first stage without supply of laser power (OPD) and argon supply two regimes of combustion were established: (1) – "attached" flame stabilized at the outlet confuser hole, which at increasing of the flow velocity was transferred into (2) – "detached" from the hole's edge flame with the following it's breakdown. Argon supply decreases the breakdown parameters, this effect depends on the argon consumption. In average according to the total measurements conducted in the range of the argon velocities $150 - 210$ m/s the characteristics of breakdown were: mixture velocity $60 - 70$ m/s and equivalence ratio $0.6 - 0.8$. Thus, the first regime of combustion was realized at argon supply without OPD.

The second stage of the experiments was performed with the OPD formation in the flow. Argon exhaustion velocity was 190 m/s. This parameter determines the choice of pulse repetition frequency f of the laser. As it is shown in [3] the upper limit of this parameter is determined by the value $f = u / l$ (where l is the optical break-down plasma extension), which is not more than 30 kHz for the conditions of the experiment. The experiments were performed also for the frequency of 8 kHz.

Experimental results. Typical results of combustion visualization (at the limited width of fringes) are presented in Fig. 2, $a - c$. The first (Fig. 2, a) shows the argon jet with the OPD without reactive mixture, the next one shows it with the mixture. OPD plasma is registered as the great lighting region showing the length $8 - 10$ mm and diameter two times smaller, whereas the diameter of the focused laser beam was not more than 0,3 mm. Figure 2, c shows the combustion in the same homogeneous flow without OPD (radiation is blocked). These data

185
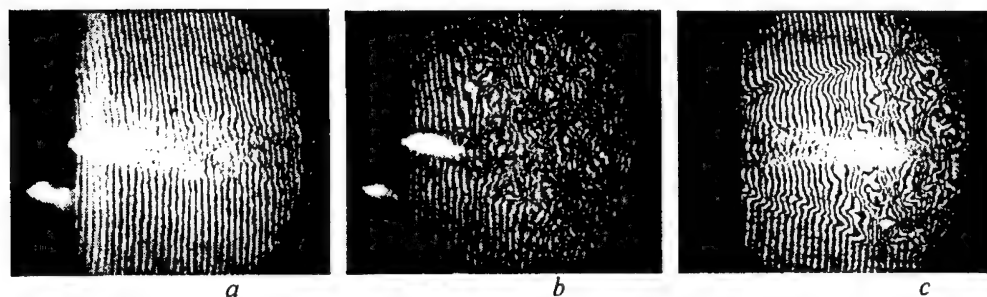
Fig. 2. The results of combustion visualization (at the limited width of fringes).

show that at chosen sensitivity of the interferometer cold flows of argon and mixture are not registered practically. The fringe's shift is not considerable even in the wake behind OPD plasma. Only at combustion the interference picture is changed considerably according to which the boundaries of the combustion zone and the characteristic scale of density fluctuations can be registered.

Figure 3, *b–f* shows the results of visualization of hydrogen/air mixture combustion supported by OPD when the flow velocity (from 79 m/s till 175 m/s) and equivalence ratio (from 0,6 till 1,9) increase. Interferometer is adjusted to the fringes of the unlimited width. Figure 3, *a* shows mixture combustion flow without OPD at low velocity and equivalence ratio values (60 m/s and 0,5 respectively) and argon supply, i.e. in the regime of the "attached" flame. Argon jet in the axis part of the flow is traced poorly. The feature of this flow is that the interference fringes vary regularly at a distance not less than two diameters of the confuser. Density and other parameters in the considered flow vary regularly, that characterizes the laminar flow and combustion process. Downstream parameters vary not regularly which indicates transition to the turbulent regime. Therefore the determination of the Reynolds numbers range at which the experiments were performed is of particular importance. This
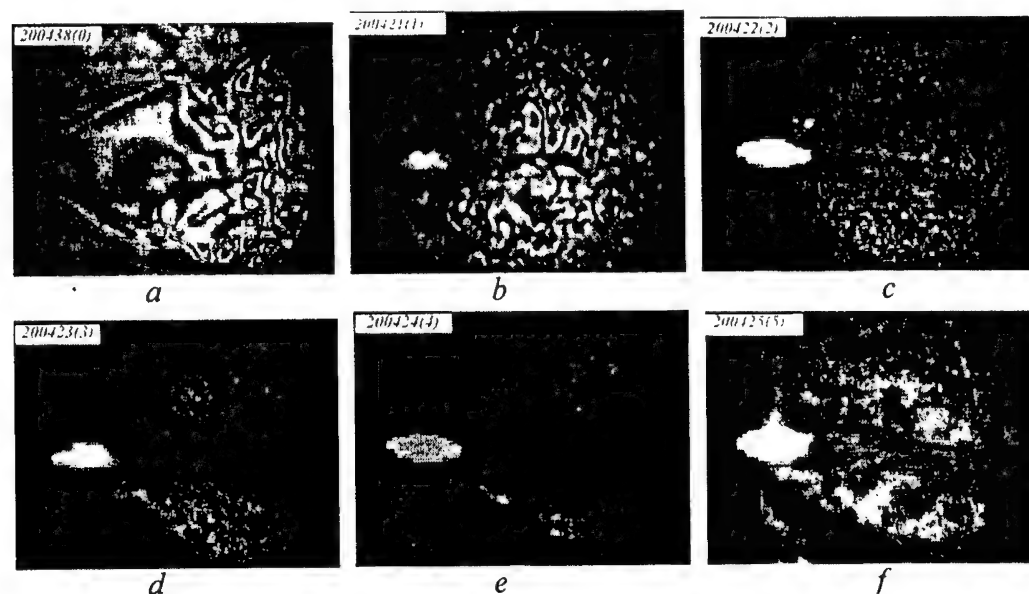
Fig. 3. The results of hydrogen/air combustion visualization.

parameter varied in the range of Re = $(0,5 - 3) \cdot 10^4$ (at $\alpha \gg 1$, i.e. pure air flow) considering the characteristic scale of 2 mm – the circular slot which forms the mixture flow. At fixed α Re number depends on the flow velocity only.

Thus, the optical pulsated discharge effects considerably the reactive flow and stabilizes the flame near the place of radiation focusing. The variation of the parameters of the flow at combustion in the whole range of the Reynolds numbers corresponds to the turbulent one even at low Re (see Fig. 3, a and 3, b). Besides, combustion was performed even at the highest flow velocities. The ultimate values of the parameters of it's breakdown were not reached. Figure 3, b in which there is not plasma lighting should be paid attention to. It is caused by the fact that at the given laser's pulses repetition frequency of 8 kHz the time interval between them (0,12 ms with the frame frequency 25 s^{-1}) exceeds a little the exposition time (0,10 ms). That is why in some (not frequent) cases the optical breakdown is not registered (when the opening of the lock is during the time interval between pulses). Poor lighting is conditioned by after lighting of the discharged plasma. Nevertheless the combustion process is registered which shows that it is sustained even during the period between pulses. The angle of inclination of the flame decreases monotonously when the velocity and the equivalence ratio increase. Thus, one can make a conclusion that quasi-stationary process of combustion is formed by pulsated optical discharge at used frequencies of radiation 8 and 30 kHz.

Propagation velocity of the turbulent flame. Measured flame velocities u_T in the reactive flow hydrogen/air is considerably greater than the velocity of the laminar flame propagation whose quantity does not exceed 2,6 m/s. Consequently, the turbulent regime of combustion is realized in the experiments.

The experimental data obtained at various flow velocities (60 – 220 m/s) and equivalence ratios (0,45 – 2,52) are divided into three groups with average values of turbulent flame propagation velocity: u_T = 32 m/s, 64 m/s and 84 m/s. To use maximum results of measurements in the whole range of parameters variation these data are selected in the certain intervals: ±4 m/s for u_T =32 m/s, –4 and +8 m/s for u_T = 64 m/s, –9 and +11 m/s for u_T = 84 m/s, so that their relative deviations from the selected average values of u_T does not exceed ±12 %. The parameters corresponding to these average values of the turbulent velocity are presented (Fig. 4) in the coordinate axis: the flow velocity u (or the Reynolds number), the equivalence ratio α. These data are marked by the corresponding lines 1, 2, 3 (in the increasing order) taking into consideration the laser pulse repetition frequency. The range of the Reynolds numbers is shown for the case of pure air flow ($\alpha \gg 1$). For other α it varies in accordance with the variation of the coefficient of mixture viscosity.
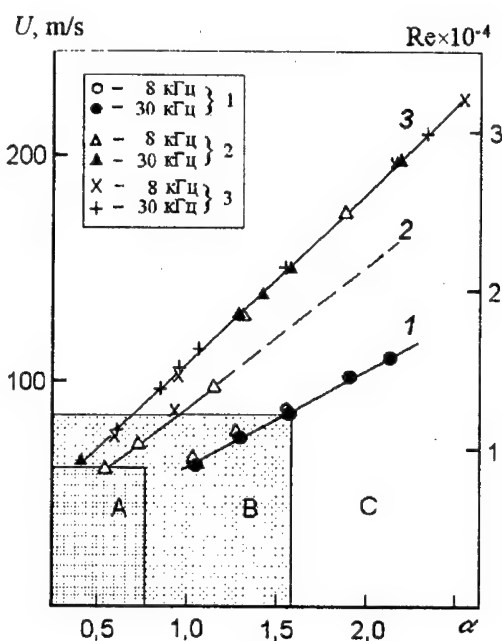
Fig. 4. The experimental data of hydrogen/air combustion.

187

The combustion regimes with u_T = 32 and 84 m/s were obtained in the great part at frequency 30 kHz at which the average power is two times higher than at 8 kHz. All measurement results (except one point) are well approximated by the straight lines *1* and *3*, respectively. Regimes with u = 64 m/s were obtained at both frequencies.

The spread of the experimental points is observed which can be caused by a number of reasons. The instability of the regime, i.e. the variation of u_T between laser pulses is possible. In this case the great flow velocity u at smaller u_T means that not the greatest angle of inclination of the flame front was measured. The moment of registration was not controlled in the experiments. Besides, not fixed values of u_T were used but a certain range of values. So, it can lead to data spread taking into consideration the error of determining of both parameters (u and u_T).

The obtained isolines (three selected values u_T = 32, 64, 84 m/s) shows obviously the tendencies of turbulent flame propagation velocity variation from the main parameters of the experiment: the flow velocity (Reynolds numbers) and the equivalence ratio. Fixing one of them the change of u_T from another parameter is determined. The qualitative dependence of turbulent velocity variation (the value of the partial derivative) on the respective parameter is obtained in measurements. At fixed flow velocity the turbulent flame velocity decreases with the equivalence ratio increasing. This effect is stronger marked at decreased flow velocity. At fixed α and Reynolds number increasing the velocity of the turbulent flame propagation increases. Since the relative variation of the Re number corresponds to the flow velocity variation one can determine that the turbulent velocity is proportional to Re number in power, close to value 0,5, i. e. $u_T \sim \mathrm{Re}^{1/2}$.

The revealed tendencies in the range of great α qualitatively agree with the data on the combustion without optical discharge. However, with OPD the combustion is sustained at greater parameters at which the flame breaks down in case of its absence. The boundary values of the parameters of the "rich" break-down with argon (region A) and without it (region B) are shown in the same Fig. 4. In the conducted experiments with OPD (region C, including A and B) the ultimate values of the parameters of break-down were not reached.

Conclusions. The results of the conducted experiments on the initiation of the combustion of the homogeneous hydrogen/air mixture by the optical pulsated discharge showed that OPD effects considerably the reactive flow. Measurements in the transition range of the Reynolds numbers proved that the stable combustion is performed in a wider range of the initial conditions, the scale of density fluctuations vary considerably. High values of the flame propagation velocity indicate the development of the turbulent combustion.

References

1. Tretyakov P.K., Garanin A.F. et al. Control over the supersonic flow around applying powerful optical pulsated discharge // Dokl. Akad. Nauk. – 1996. – Vol. 329, № 3. – P. 329 – 332.
2. Tretyakov P.K., Yakovlev V.I. Formation of the quasi-stationary supersonic flow with the pulsated – periodic plasma heat source // Pis'ma v ZhTF. – 1998. – Vol. 24, Iss. 6. – P. 8 – 12 (in Russian).
3. Tretyakov P.K., Yakovlev V.I. Wave structure in supersonic flow with laser energy supply // Dokl. Akad. Nauk. – 1999. – Vol. 365, № 1. – P. 58 – 60.

COMPUTATIONAL STUDY OF SUPERSONIC FLOW OVER THE WINGS AT HIGH ANGLES OF ATTACK AND SIDESLIP IN THE FRAMEWORK OF EULER EQUATIONS

V.F. Volkov, M.S. Loginov
Institute of Theoretical and Applied Mechanics SB RAS,
630090 Novosibirsk, Russia

The absence of full investigations on the flow around the wings at incidence of attack with slip makes it necessary to continue the studies. The paper [1] refers to the few experimental researches of these spatial flows. In this paper, there are results of flow visualization by the «laser sheet» technique. The data of this paper illustrate the configuration of shock waves over the wing and the scales of vortex structures. They are, however, qualitative. The paper [2] is a theoretical one in which the aerodynamic characteristics of the delta wing at small slip angles are studied in approximation of the thin body. Complete information about the gas-dynamic structure of the flow in the disturbed region near the body, local and integral loads can be obtained by numerical calculations. The reliability of the numerical results should be tested by comparison with the experimental data and the results of the authoritative numerical research.

In the present paper, the problems of the spatial flow around the bodies of an arbitrary form within the Euler equations are considered. The flow in the disturbed region is supersonic everywhere in the streamwise direction. A wing-fixed coordinate system with the origin at the top of the wing was used, where the x axis is streamwise, the y axis is normal to the wing surface and the z axis is along the left half-wing. The components of the free-stream velocity vector in the wing-fixed coordinate system are determined by the following way:

$$\vec{W}_\infty(\cos\alpha \cdot \cos\beta, \sin\alpha \cdot \cos\beta, \sin\beta)$$

where α is the angle of attack and β is the slip angle.

The algorithm suggested earlier [3] is applied to solve these problems. The boundary condition of symmetry is substituted by the condition of «matching» the solution at $\varphi = 0$ and 2π along the radial coordinate in each section $x = \text{const}$. At $\varphi = 0$ and 2π, the values of flow parameters and radial coordinates $g_{i,j}$ are determined by the relations $g_{j,2} = g_{j,N} = (g_{j,2}+g_{j,N})/2$, where i is the number of the point along the radius and j is the number of the point along the azimuthal coordinate. The values $g_{j,1} = g_{j,N-1}$; $g_{j,N+1} = g_{j,3}$ are assigned to $g_{i,j}$ in fiction points to the left and right of the matching line.

It is difficult to determine the location of the outer boundary under the condition of flow around at high angles of attack. Therefore it is useful to perform a calculation with bow shock wave capturing.

The accepted condition of matching was tested by the calculation of flow around the a circular cone with a half angle $\theta = 10°$ for a free-stream Mach number $M_\infty = 3$. For the assigned angles of attack $\alpha = 5; 3.54; 0°$, the slip angle is $\beta = 0; 3.54; 5°$. The flow is equivalent to the flow around the cone with an angle of attack $\alpha_0 = 5°$ for these angles of attack and slip. A comparison of the solutions obtained for these angles of attack and slip showed their good agreement in terms of the flow parameters in the disturbed region and the location of the bow shock wave (Fig. 1, a), as well as the pressure distribution along φ on the body surface (Fig. 1, b). The divergence of the solution obtained with the results tabulated in [4] does not exceed 5 % for the bow shock location as well as for surface pressure distribution. The adopted condition of matching is well grounded by the correspondence of pressure distribution for the mentioned α and β (Fig. 1, b).
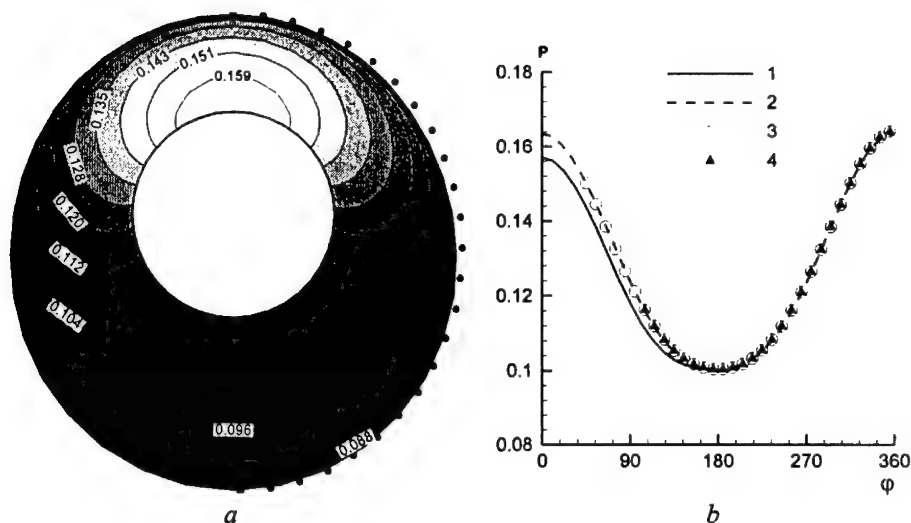
Fig. 1. Pressure distribution for $\alpha_0 = 5°$.

a) at the section x = const: points mark the location of the bow shock wave according to [4];
b) on the body: 1 — data [4], 2 — calculated data for $\alpha = 5°$, $\beta = 0$; 3 — $\alpha = 3.54°$, $\beta = 3.54°$;
4 — $\alpha = 0$, $\beta = 5°$.

To make a comparison with the experimental data [1] (Fig. 2, a, j), of the flow around the delta wing with a sweepback angle $\chi = 75°$ at a free stream Mach number $M_\infty = 3$, an angle of attack $\alpha = 20°$ and slip angles $\beta = 0$; 2.5; 5; 10° was calculated. The wing with sharp leading edges has a flat leeward surface, its thickness is 3 % of the root chord length (see Fig. 3). The location of the bow shock wave was determined during the solution, as in the previous case. The regime of flow around the leading edges of the right and left half wing is determined by the component of the Mach number normal to them:

$$M_N = M_\infty \sqrt{1 - \left(\cos\alpha \cdot \cos\beta \cdot \sin\chi \pm \sin\beta \cdot \cos\chi\right)^2} \ , \tag{1}$$

where the left wing edge is taken with the sign «–» and the right one with — «+». For all flow regimes considered the normal Mach number value was $M_N > 1$. However, taking into consideration that the windward surface angle α_N (determined as the sum of the aperture angle of the edge and the angle of attack) in the considered plane for the considered M_N values exceeded the critical angle of flow deviation for an attached shock wave, the flow with a detached bow shock wave was realized.

Vortex structures on the leeward wing surface are an important feature of the flows under consideration. Their evolution depending on the slip angle can be observed in Figs. 2, 3. Intensive rarefaction regions are formed on the leeward surface in the vicinity of the leading edges in the flow over the wing under the angle of attack, which are clearly observed in the calculated density fields presented in Fig. 2, b–e. The darker color corresponds to the regions with lower density. It should be noted, that for $\beta = 0°$ (Fig. 2, b), these regions are located symmetrically to the symmetry plane of the wing and agree qualitatively with the data of flow visualization [1] (Fig. 2, a). In the paper mentioned, this picture is connected with the presence of vortex flows (1) on the leeward side. Besides, the zones of accelerating cross-flow (or rarefaction zone (2)) over the mentioned vortices are observed. At the end of zones (2), there are internal shock waves (3). The flow oriented to the
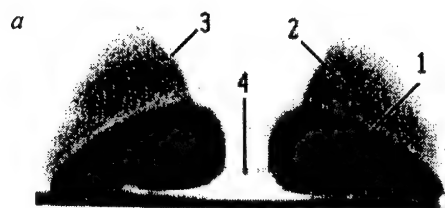
$M_\infty = 3$, $\alpha = 20°$, $\chi = 75°$
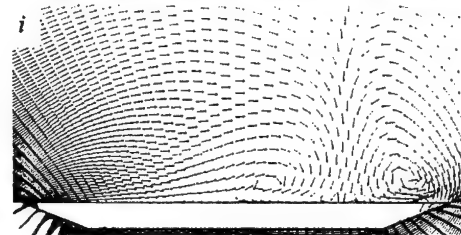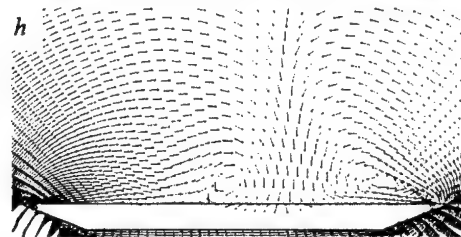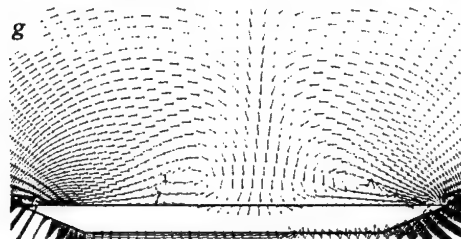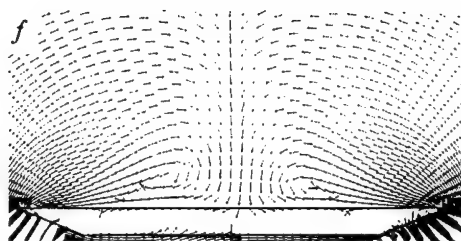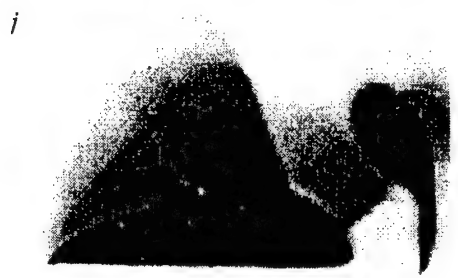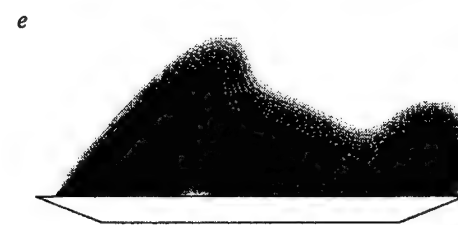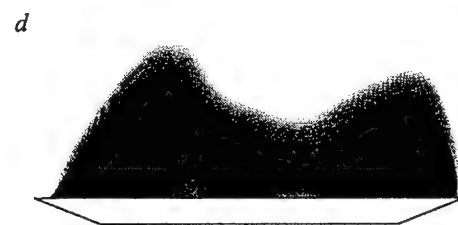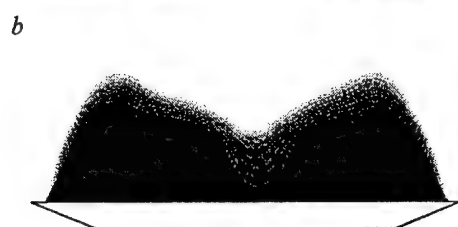
Fig. 2. Density distribution and velocity field
on the leeward side of the wing.
a) experiment [1], $\beta = 0$
b, *f*) calculation, $\beta = 0$
c, *g*) calculation, $\beta = 2.5°$
d, *h*) calculation, $\beta = 5°$
e, *i*) calculation, $\beta = 10°$
j) experiment [1], $\beta = 10°$

wing surface between the vortices is accelerated and decelerated in the centerline shock (4). Shock waves (3) in the calculation are displayed but they are rather smeared. Central shock wave (4) was not displayed in the calculations, which indicates the necessity of further improvement of the considered method of calculation.

The development of vortex structures depending on the slip angle β at the fixed angle of attack α is well observed (Fig. 2, f–i) in the conic velocity $\vec{W}_c$ calculations determined in accordance with [5] as well as in the density fields (Fig. 2, b–e). Their analysis shows that the counter cross flows directed to the symmetry plane of the wing are formed near the edges. The interaction of these flows at $\beta = 0$ (Fig. 2, f) leads to the formation of symmetrically located large-scale vortices. In the vicinity of the symmetry plane, the flow directed to the wing surface is observed. This flow divides vortex formations over the right and left half wings. The
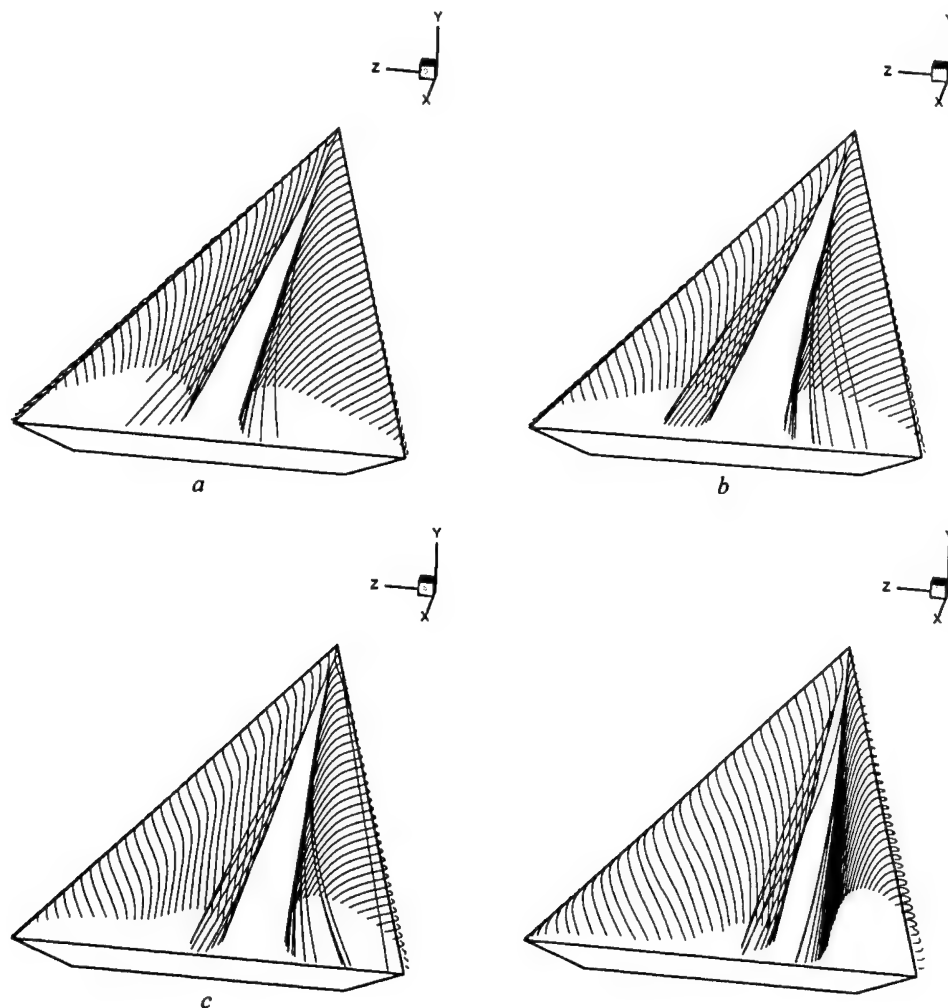
Fig. 3. The shape of the vortex sheet at $M_\infty = 3$; $\chi = 75°$; $\alpha = 20°$:
$\beta = 0$ (a); $\beta = 2.5°$ (b); $\beta = 5°$ (c); $\beta = 10°$ (d)

divergence line is formed on the surface. According to the calculated data, the flow directed to the surface does not reach the conically supersonic speed. The vortex sheet shedding from the leading edges is shown in Fig. 3, *a*. It is constructed on the basis of the spatial velocity field $\vec{W}$.

The asymmetry of flow around the wing is greatly displayed in the regime of flow around with slip at the increase in the angle β (Fig. 2, *g–i*). The region dividing vortex flows over the right and left half wings and the divergence line on the wing surface are shifted to the right edge. The vortex structures are extended on the left half wing, and their compression occurs on the right half wing. These structures are gradually displaced to the right edge. It is obviously shown
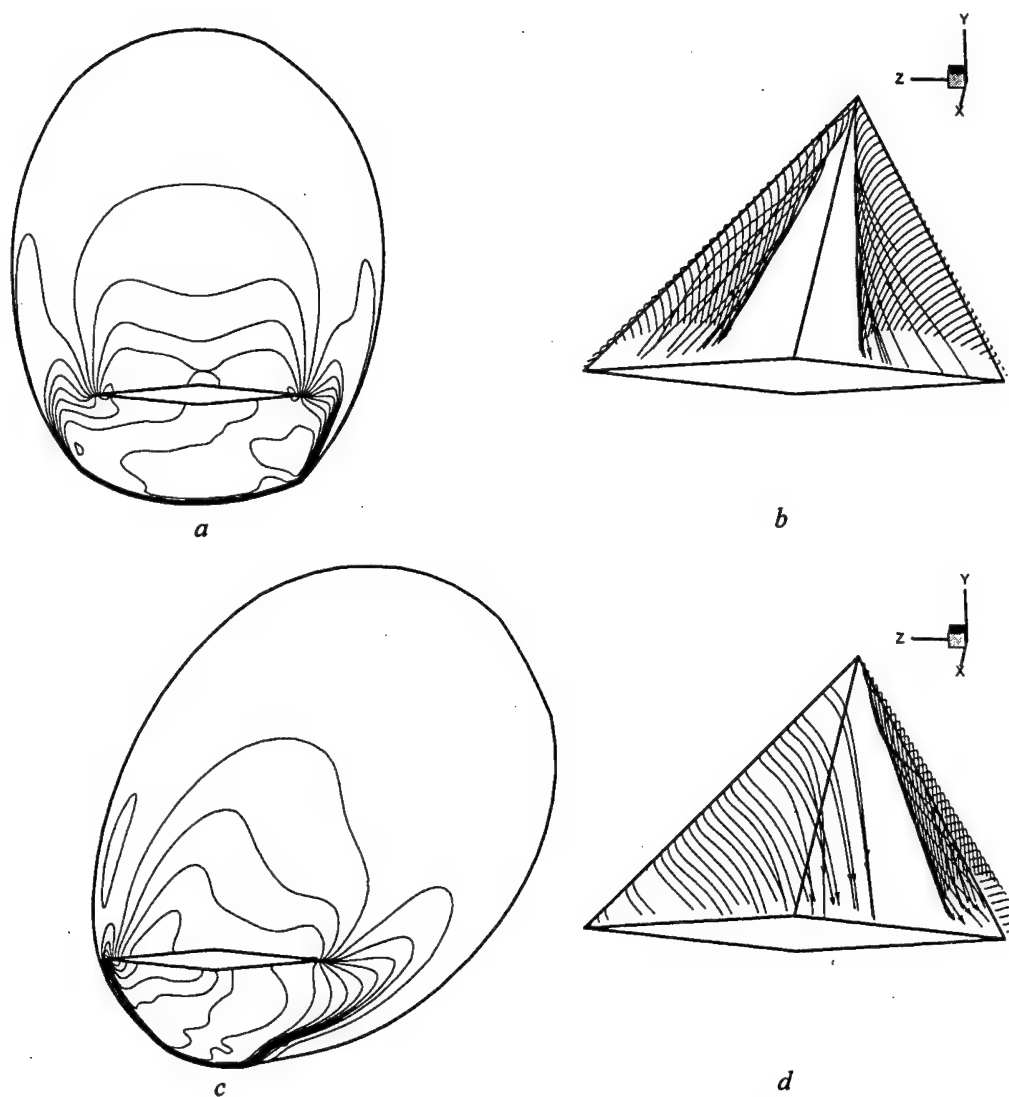
Fig. 4. Pressure contours and the shape of the vortex sheet at
$M_\infty = 2$; $\chi = 70°$; $\alpha = 20°$; $\beta = 0$ *(a, b)*; $\beta = 15°$ *(c, d)*

in Fig. 3. When the slip angle grows, the deformation effect increases, and at $\beta = 10°$ (Fig. 3, d) the vortex sheet spreading on the wing surface in the left part is observed, which swings into a vortex in the symmetry plane. It is separated along the right leading edge, and an intensive vortex is formed. The features of flow around at $\beta = 10°$ discovered in the calculations (Fig. 2, e, i; 3, d) correspond qualitatively to the visualization results in the experiment [1] (Fig. 2, j). Alongside with the similarity of the configuration of asymmetric vortex structures, shock waves (3, 4) are also displayed, though the regions of their existence are smeared in Fig. 2, e.

The evolution of the bow shock wave and the static pressure fields in the disturbed region depending on the slip angle is well observed in the calculation of the flow around the delta wing with sweepback angle $\chi = 70°$ for a free-stream Mach number $M_\infty = 2$, an angle of attack $\alpha = 20°$ and a slip angle $\beta = 0$ and $15°$ (Fig. 4). The wing has sharp leading edges and a double-wedge cross section with the maximum thickness of 3 % of the root chord length. According to relation (1), at $\beta = 0$ both edges are subsonic, and in the case $\beta = 15°$ one is subsonic and the other is supersonic.

At $\beta = 0$, the bow shock wave has the shape of a symmetric ellipsis whose major axis is in the symmetry plane of the wing (Fig. 4, a). At $\beta = 15°$ the bow shock wave is deformed with axis inclination to the right side (Fig. 4, c). The shock wave is attached to the leading edge on the left half wing, and it is detached on the right one. The corresponding evolution of the vortex sheet over the wing is shown in Fig. 4, b, d. When β increases, the vortex is degenerated near the left edge, and the streamlines shed from the edge spread along the surface. The vortex sheet shed from the right edge acquires the shape of a conic vortex core (Fig. 4, d).

Thus, the numerical results obtained broaden considerably the conceptions about gas-dynamic features of the flow in the region disturbed by the wing under the flight conditions with slip and supplement the experimental data.

References

1. Borovoi V.Ya., Brazhko V.N., and Maikapar G.I. Leeward separated supersonic flows // Separated flows and jets: IUTAM–Simp. Novosibirsk, USSR July 9–13, 1990 / Eds. V.V. Kozlov, A.V. Dovgal. Berlin et al.: Springer-Verlag, 1991. P. 311 – 317.
2. Gorenbukh P.I., Nikolaev V.S. Numerical experimental studies of the aerodynamic characteristics of the delta wing at the slip angle under high supersonic speed // Uchenye Zapiski TsAGI. 1991. Vol. 22, No. 1. P. 32 – 38.
3. Volkov. V.F., Mazhul I.I., Shcherbic D.V. Calculation of the supersonic flow around the spatial configurations with the sharp leading edges by the inviscid gas // Thermophys. and Aeromech. 1995. Vol. 2, No. 3. P. 245 – 252.
4. Babenko K.I., Voskresensky G.P., Lyubimov A.I., Rusanov V.V. Spatial flow around the smooth bodies by the ideal gas. Moscow: Nauka, 1964.
5. Brodetsky M.D., Shevchenko A.M. Experimental study of the supersonic flow on the leeward side of the delta wing // Thermophys. and Aeromech. 1998. Vol. 5, No. 3. P. 307 – 318.

EXPERIMENTAL AND NUMERICAL INVESTIGATION OF 3D ACOUSTIC RECEPTIVITY DUE TO LOCALIZED WALL ROUGHNESS

W. Würz[1], S. Herr[1], A. Wörner[1], U. Rist[1], S. Wagner[1] and Y.S. Kachanov[2]

[1] Institut für Aerodynamik und Gasdynamik Universität Stuttgart,
70550 Stuttgart, Germany
[2] Institute of Theoretical and Applied Mechanics SB RAS,
630090 Novosibirsk, Russia

Introduction

The problem of boundary layer transition from laminar to turbulent flow still attracts much attention because of its fundamental and practical importance. It has three main aspects. First, there is the laminar flow receptivity to external perturbations. The second aspect is the linear development of boundary layer instabilities according to linear stability theory and finally there is the nonlinear flow breakdown to turbulence. This paper is devoted to experimental and numerical investigations of the linear 3D acoustic receptivity of a two-dimensional laminar boundary layer in the presence of a localized (in streamwise and spanwise direction) quasi steady surface non-uniformity.

This problem is poorly studied, so far. Most of the previous experiments in this field were devoted to two-dimensional receptivity problems (see e.g. [1, 2]). The quantitative receptivity characteristics of the 2D (Blasius) boundary layer to 3D surface vibrations were studied experimentally in [3]. The only available experimental investigation of the 3D vibrational acoustic receptivity was carried out in a swept-wing boundary layer and was devoted to the generation of cross-flow instability modes [4]. Recently, the acoustic receptivity due to stationary, localized 3D roughness was studied qualitatively in [5]. The first quantitative evaluation of the complex 3D acoustic receptivity function was performed in [6] for quasi stationary 3D roughness and a single acoustic frequency.

In general, the amplitude part of the acoustic receptivity coefficient is defined by the ratio of the initial (i. e. at the surface non-uniformity) instability wave amplitude, generated in the boundary layer, to the amplitude of the external acoustic perturbation and the amplitude of the involved surface non-uniformity (see e. g. [7, 8, 4]). More exactly, all these amplitudes must be determined for every single (normal) mode of the corresponding frequency-wavenumber spectra, i. e. the spectra of the instability waves, surface non-uniformities and acoustic perturbations.

Experimental Investigation

The experiments were carried out in the Laminar Wind Tunnel (LWT) of the IAG. The LWT is an open return tunnel with a turbulence level less than $Tu = 2 \cdot 10^{-4}$. The boundary layer measurements were performed on a symmetrical airfoil section at zero angle of attack and at a Reynolds number of $1.2 \cdot 10^{6}$ based on the arclength $s_{max} = 0.615$ m measured from the leading edge (Fig. 1). A plane acoustic wave with fixed frequency was chosen as the external perturbation. In extension to [6], three different acoustic
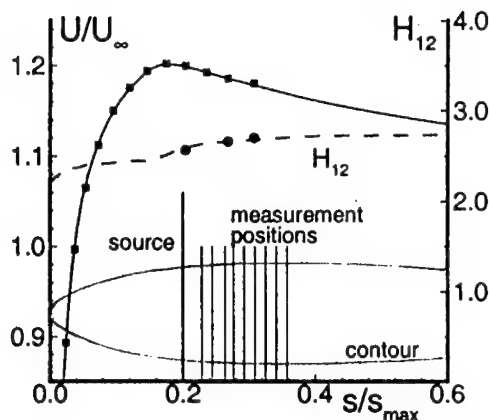
Fig. 1. Velocity Distribution and development of the shape factor.
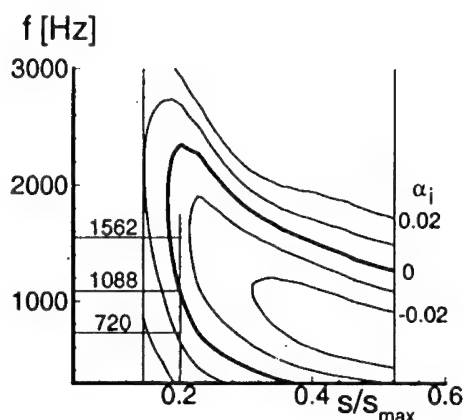
Fig. 2. Stability diagram, roughness element at 0.2 s/s_{max}.

frequencies (f_{ac} = 720 / 1088 / 1562 Hz) were used to cover a significant part of the unstable TS- frequency range for the selected boundary layer properties. The middle frequency f_{ac} = 1088 Hz is close to the most unstable TS-frequency for 2D TS-waves (with respect to the amplitude reached at the last measurement station). The acoustic wave was generated by a loudspeaker at the centerline downstream of the test section. The position of the localized 3D roughness element was selected to lie on branch I for a 2D wave with f= 1088 Hz (Fig. 2).

When studying 3D roughness acoustic receptivity, the data analysis represents a very complicated problem because of difficulties to distinguish signals measured at the same (acoustic) frequency but having different physical nature. The signal consists of a mixture of: (i) the instability wave generated by the acoustics (that is relatively weak initially), (ii) vibrations of the hot-wire probe and the model surface, and (iii) the acoustic field itself including the Stokes layer in the near-wall region. These experimental problems have been solved in [4] by means of arranging an unsteady surface non-uniformity (vibrating source) oscillating with a very low frequency and providing a quasi-steady scattering of the acoustic wave. A similar method has been applied in the present investigation. The vibrating source is driven at the frequency f_v = 1/64 f_{ac} which leads to an amplitude modulation of the generated 3D TS-wave in time. This corresponds to distinct combination modes in the frequency spectrum of the hot-wire signal at frequencies $f_{1,2} = f_{ac} \pm f_v$. In contrast to the signal observed at the acoustic frequency, the combination harmonics correspond to the instability waves *only*, excited by acoustic on the vibrator *only*. The spatial behavior of these combination modes has been studied in detail.

The 3D roughness element was modeled by the inflection of the membrane of a circular surface vibrator. The active diameter (d = 6 mm) was chosen to be approximately one half of the TS-wavelength (at f_{ac} = 1088 Hz). The body of the source was set up flush-mounted with the model surface. The vinyl membrane was driven by a
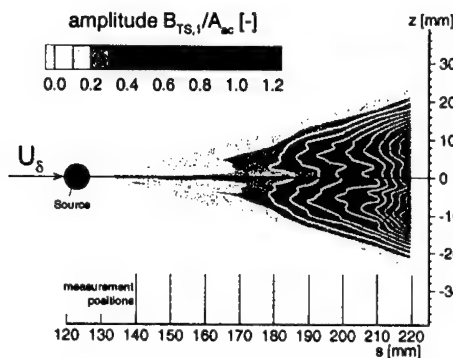
Fig. 3. Amplitude part of the wave train (left combination mode, f_{ac}=1088 Hz).

loudspeaker and the shape of the inflection of the membrane was measured with a laser triangulation device.

An acoustic amplitude of 100 dB was used together with a vibrational amplitude of 29.7 μm_{RMS} in order to be in the linear regime of receptivity and linear development of boundary layer instabilities. The linearity of both has been carefully checked.

The acoustic frequency as well as the vibrational frequency and the sampling trigger were generated strictly phase locked by a single time source. The ratios between the frequencies were chosen as integer powers of two ($f_v : f_{ac} : f_{sample} = 1:64:8$) which gave the possibility to represent each of them with single Fourier coefficients after a FFT.

The initial amplitudes (which are necessary for determining the receptivity coefficients) of the most unstable TS-waves can not be measured directly in the flow because in the near-field of the source a mixture of different other perturbations such as continuous-spectrum instability modes and forced (bounded) fluctuations is present. Therefore, similar to some previous receptivity experiments (see e. g. [3]), we used the boundary layer as a selective amplifier of the most unstable (discrete-spectrum) modes and, simultaneously, an attenuator of the continuous-spectrum modes and the forced oscillations. The distributions of the TS amplitudes and phases were measured downstream of the surface non-uniformity. In contrast to [3] the linear stability theory was then used for extrapolation of the data to the position of the surface non-uniformity.

The hot-wire measurements were performed in 8 to 9 spanwise scans covering the whole width of the wave train. A constant, non-dimensional wall distance of $y/\delta_2 = 2.2$ was used in order to be close to the maximum of the TS-eigenfunction for different propagation angles. This procedure yields a good compromise for $f_{ac} = 720$ Hz and $f_{ac} = 1088$ Hz but obviously underpredicts (by up to 10 %) the receptivity for $f_{ac} = 1562$ Hz at propagation angles close to zero. This has to be taken into account for the comparison of receptivity coefficients for small propagation angles.

The time signals at every measurement point were analyzed with an FFT and the amplitude and phase of the perturbations obtained at the combination frequencies $f_{1,2}$ were used for further data processing. The amplitudes were normalized by the local free-stream velocity $U_\delta = 36$ m/s and the length with the displacement thickness $\delta_{1ref} = 0.356$ mm (H_{12}=2.57) at the position of the source. The resulting spatial field of the disturbance amplitude for the "left" combination mode $f_1 = f_{ac} - f_v$ is shown in Fig. 3.

Experimental Results

The complex values of the wave train in physical space were mapped for each spanwise cut to spanwise wavenumber spectra. After this the downstream development of waves with different spanwise wavenumbers were investigated separately. The measured

Fig. 4. Comparison of amplitude development f_{ac}=1088 Hz.

Fig. 5. Dispersion characteristic at the position of the source (f_{ac}=1088 Hz).

amplitudes (Fig. 4, symbols) for the combination modes are found to be consistent with the linear stability theory (Fig. 4, lines). This allows their upstream extrapolation to the position of the receptivity element. The associated phases could easily be fit by a straight line. The gradient of this line is the streamwise wavenumber α_r. By this procedure the dispersion characteristic $\alpha_r = \alpha_r(\beta)$ is determined, for each fixed frequency, that gives a dispersion relationship between the streamwise and spanwise wavenumbers (Fig. 5). From the double Fourier decomposition of the shape of the membrane oscillation the complex wavenumber spectrum of the surface vibration is obtained. From this spectrum the amplitudes of the "resonant" vibrational modes, that have the same wavenumbers as the TS-waves generated by them, can be found with the help of the dispersion function. Thus, the complex receptivity function $\widetilde{G}_{avl,2}(\alpha_r, \beta)$ can be evaluated by calculating its amplitude part and its phase part separately according to the following definition:

$$\widetilde{G}_{avl,2}(\alpha_r, \beta) = G_{avl,2}(\alpha_r, \beta) \cdot e^{i\phi_{avl,2}(\alpha_r,\beta)} = \frac{\widetilde{B}_{inTS1,2}(\alpha_r, \beta)}{\widetilde{A}_{ac} \cdot \widetilde{A}_v(\alpha_r, \beta)}$$

where $\widetilde{B}_{inTS}$ is the complex initial spectrum of TS-waves excited by the acoustics on the vibrator, $\widetilde{A}_{ac}$ is the complex acoustic amplitude, and $\widetilde{A}_v(\alpha_r, \beta)$ is the complex spectrum of the resonant vibrational modes. Figure 6 to 8 show the amplitude and phase parts of the complex receptivity function, for the three investigated frequencies, in dependence of the propagation angle $\theta(\beta) = \arctan(\beta/\alpha_r)$ of the generated TS-wave. The results obtained in every regime are plotted for the two combination frequencies.

Comparison with Direct Numerical Simulations

The DNS are based on the vorticity-velocity formulation of the complete Navier — Stokes equations using a uniformly spaced grid in streamwise and wall-normal direction and a spectral representation in spanwise direction, c. f. [9]. The sound wave in the free stream is prescribed as a solution of the second Stokes' problem at inflow, and a novel wall model has been implemented and compared with standard first-order formulations that consider only a no-slip condition in wall-parallel directions. The use of
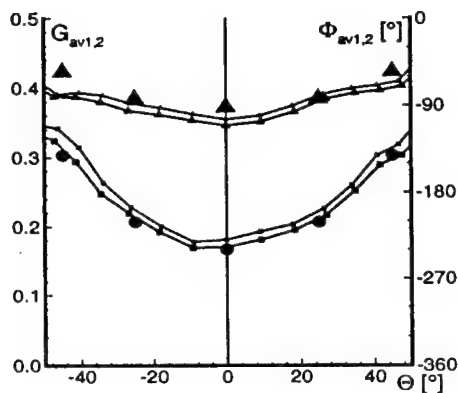
Fig. 6. Amplitude and phase part
of the receptivity function
(f_{ac}=1088 Hz, Symbols: DNS).

Fig. 7. Amplitude and phase part of
the receptivity function (f_{ac}=720 Hz,
Symbols: DNS).

a body-fitted coordinate system is avoided and the typically small surface roughness is simulated by non-zero velocity at the lowest row of grid points which are extrapolated from the field in such a way as to fulfill the no-slip condition on the surface of the roughness. Here, this is done using high-order polynomials which are consistent to the finite-difference representation of the flow field. However, the main difference between the new model and models found in literature is that it takes into account the no-slip condition for the wall-normal velocity on the roughness, as well. Thus, at least for higher surface roughness, this novel formulation should lead to more accurate results.

Fig.8. Amplitude and phase part of
the receptivity function (f_{ac}=1562 Hz,
Symbols: DNS)

The Blasius boundary layer is assumed at the position of the roughness element and the receptivity coefficients are evaluated for the same nondimensional wall distance as in the experiment. The DNS were performed for steady roughness, three acoustic frequencies and three discrete spanwise wavenumbers which correspond to propagation angles of 0°, 25° and 45°, respectively. All modes show good quantitative agreement with the experimental receptivity functions (c. f. Fig. 6 – 8)

Conclusions

The linear 3D acoustic receptivity due to a localized quasi stationary roughness element was studied experimentally and theoretically for three different acoustic frequencies in the range of the most unstable TS-frequencies. The obtained results

199

demonstrate that the scattering of the acoustic wave is significantly more effective for 3D surface non-uniformities rather than for 2D ones. Similar to the vibrational receptivity [3] the acoustic receptivity coefficients for all propagation angles increase with the acoustic wave frequency. The most significant frequency dependence is observed for strongly 3D modes. The phase delays of the generated TS-waves depend only weakly on the spanwise wavenumber and the frequency.

Acknowledgment

References

1. Kosorygin V.S., Levchenko V.Y., Polyakov N.F. On generation and evolution of waves in laminar boundary layer // Laminar-Turbulent Transition / Ed. V.V. Kozlov. Berlin et al.: Springer Verlag, 1985. P. 233-242.

2. Saric W.S., Hoos J.A., Kohama Y. Boundary-layer receptivity: Pt 1. Freestream sound and 2D roughness strips: Report CEAS-CR-R-90191. Arizona State University, College of Engineering and Applied Sciences, 1990.

3. Ivanov A.V., Kachanov Y.S., Obolentseva T.G., Michalke A. Receptivity of the Blasius boundary layer to surface vibrations. Comparison of theory and experiment // Intern. Conf. on Methods of Aerophysical Research: Proc. Pt I. – Novosibirsk,1998. P.93-98.

4. Ivanov A.V., Kachanov Y.S., Koptsev D. An experimental investigation of instability wave excitation in 3D boundary layer at acoustic scattering on a vibrator // Thermophysics and Aeromechanics. 1997. Vol. 4, No. 4.

5. Cullen L.M., Horton H.P. Acoustic receptivity in boundary layers with surface roughness // Laminar-Turbulent Transition: Proc. IUTAM Symp. / Eds. H. Fasel, W. Saric. Berlin et al.: Springer-Verlag, 1999.

6. Würz W., Herr S., Wörner A., Rist U., Wagner S., Kachanov Y.S. Study of 3D Wall Roughness Acoustic Receptivity on an Airfoil // Ibid.

7. Choudhari M., Streett C.L. A finite Reynolds-number approach for the prediction of boundary-layer receptivity in localized regions // Physics in Fluids. 1992. Vol. 11. P. 2495-2514.

8. Crouch J.D. Receptivity of three dimensional boundary layers. AIAA Paper 93-0074, 1993.

9. Rist U., Fasel H. Direct numerical simulation of controlled transition in a flat-plate boundary layer // J. Fluid Mech. 1995. Vol. 298. P. 211-248.

THE MODELING OF THE DYNAMICS OF
AN AEROELASTIC STRIP IN AXIAL FLOW

Y. Yadykin, V. Tenetov, D. Levin

Faculty of Aerospace Engineering, Israel Institute of Technology, Israel

Introduction

The research interest lies in the aeroelastic behavior of a non-stretching strip of finite dimensions. The phenomenon of the instability of such a configuration can easily be demonstrated by blowing a strip of a paper in a vertical wind tunnel [1]. The air stream flows vertically from top to bottom at the test section. As the wind speed increases, a stable response is observed until a certain critical speed beyond which the strip bends and embarks on violent vibrations. By "bend" we mean that some parts of the strip are deflected in opposite directions and the whole length becomes wavy [2]. The "violent" vibrations settle down to a limit cycle with a tip amplitude of the order of half the strip length. Further details regarding the history of this problem have been published in ref [3].

Instabilities of strips subjected to flow directed parallel to their surface are usually labeled as "panel flutter" [4]. Under the combination of an airstream and axial loading due to weight, strips exhibit a variety of nonlinear behavior, such as several types of flutter and transitions among them.[1] In this aspect the strip's flutter problem is a useful model of an essentially non-conservative, nonlinear system allowing to study the onset and spatiotemporal evolution of flutter in like aeroelastic structures [4].

Earlier studies of post-critical behavior of flexible strips in flow were performed mainly by experimental methods [1, 5, 6] and to a lesser degree using analytical methods of the classical nonlinear mechanics [7]. The application of analytical methods to continuous systems is based on the assumption that their response after the bifurcation is close to that observed immediately at the bifurcation. However, analytical methods become inapplicable in remote post-critical domains dealing with a secondary or multiple bifurcation [4]. Our primary interest is both in the initial stage of the instability and the *post-critical dynamics* of the elastic strip. The questions we want to raise are: a) what affects the onset of the instability, b) in what spatiotemporal form does the strip oscillate on the very infant stage of the instability, and in the remote post-critical domains, c) are there any more bifurcation in the post critical domains in addition to the fundamental bifurcation. The reason why these questions, regarding such an obvious phenomena, have not been answered previously, is essentially because the aeroelastic response of the strip, fixed at one edge, can only be investigated when the mathematical model of the strip's motion in the airstream is nonlinear. Numerical experiment becomes the main tool to study the post-critical behavior of fluttering strips, especially when spatiotemporal transitions are expected.

Derivation of the equation

The current derivation generalizes the planar linear equations of Datta *et al.* [8] and the planar nonlinear equation of Lundgren *et al.* [9] for a strip hanging vertically in an axial flow.

The basic assumption are as follows: (a) the strip has a rectangular planform with length l, width H, constant mass per unit area m and flexural rigidity D; (b) the strip is long compared to its thickness a and its width H, (c) the center plane of the strip is not elongated; (d) the strip is elastic and initially straight; (e) A plane section before the deformation remains a plane during
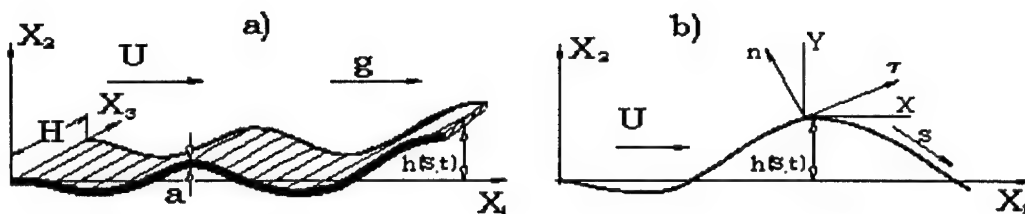
Fig. 1. System model(a) and coordinate system used (b).

the deformation; (f) the effects of the internal dissipation of the strip material are neglected; (g) the motion is planar and the deflections of the strip $h(s,t)$ are large, but the strains are small; (h) the strip is clamped at the upstream edge and is free at the downstream one; (i) the fluid is incompressible; (j) the incoming flow is uniform and of a constant velocity U.

In the undeformed state the strip extends along the X_1-axis of the Cartesian coordinate system $(X_1X_2X_3)$ in the direction of gravity and oscillates in the (X_1X_2) plane (Fig. 1(*a*)). Let (X_1, X_2, X_3) represent the position of a material point O in its original state, and (x, y, z) the position of the same material point in the deformed state. The displacement of that material point is defined as $v = x - X_1$; $h = y - X_2$; $w = z - X_3$.

The strip, in its initially undeformed state lies along the X_1-axis, and when undergoing motions in the (X_1, X_2) plane, retains $X_2 = 0$, so that y is identical to the displacement $h(s, t)$, since the strip is not stretching. Thus, all the other physical quantities and the final governing equation can be expressed in terms of (s, t). The strip planform is given by $0 \leq s \leq l$; $0 \leq z \leq H$.

Let us introduce the orthogonal system of coordinates n, τ connected to the strip (Fig. 1(*b*)). The n, τ- axis are the normal and tangent to the center-plane of the strip respectively.

The equations of motion in the v-and h-direction have been derived by Lundgren *et al.* [9]. When the aerodynamic drag force, as given by Hoerner [11] is added, the equations of motion become:

$$m\ddot{v} + Dv''' - \left(\left(T - Dk^2\right)v'\right)' - m^*g - \left(\Delta p + F_n\right)h' - F_\tau v' = 0$$

$$m\ddot{h} + Dh''' - \left(\left(T - Dk^2\right)h'\right)' + \left(\Delta p + F_n\right)v' - F_\tau h' = 0, \qquad (1)$$

where k-curvature, $m = \rho_0 a$, $m^* = (\rho_0 - \rho)a$. The dot and the prime denote the derivatives with respect to time t, and to the curvilinear coordinate s respectively.

The pressure difference across the strip Δp was postulated in accordance with the slender-wing theory by Jones [10]

$$\Delta p = M\left(\ddot{h}(s,t) + 2U\dot{h}'(s,t) + U^2 h''(s,t)\right) \qquad (2)$$

An additional equation is provided by the constraint on the length of the center line

$$(v')^2 + (h')^2 = 1;$$

the boundary conditions :

$$h = h' = 0 \text{ at } s = 0; \quad h'' = h''' = 0 \text{ at } s = l.$$

In equations (1)-(2) $M = \rho \pi H/4$ is the "added mass" of a cross section of the strip per unit area [8]. The values ρ_0, ρ being the densities of the material strip and fluid respectively; g is the

202

gravity; T is the tension force. The terms F_n, F_τ are the normal and tangential aerodynamic forces acting on the strip. The normal aerodynamic force per unit area of the strip is defined, as proposed by Hoerner [11] and Triantafyllou [7]

$$F_n = q(C_n U_R |U_R| + \pi A U_R/2),$$

where $q = \rho U^2/2$ is the dynamic pressure; $A = H/l$ is the aspect ratio of the strip and U_R is the cross flow component of the velocity. The notation $U_R|U_R|$ was used in order to assure that the resulting force is in the direction of the cross flow velocity [7].

The nondimensional cross-flow component of the velocity is given by

$$U_R = (\dot{h} + Uh')/U .$$

The value of C_n is not known for the case of hydroelastic problem. To a first – and rather crude – approximation, C_n can be considered equal to that of a rigid low-aspect ratio wing inclined to the flow. In the case of rigid wings, the values of C_n is independent of the Reynolds number of the cross flow, and depends only on the aspect ratio of the wing [11]. For the case of an infinitely long wing, i.e. zero aspect ratio, C_n is equal to the drag coefficient of a flat plate, which is equal to two. As the aspect ratio increases, the value of C_n decreases and approaches zero, as the aspect ratio approaches infinity. Experimental values for C_n has been presented by Hoerner [11], Triantafyllou [7] and others for various aspect ratios. These values can be quantitatively estimated by the expression $C_n = C_0 \exp(-A/2)$, where $C_0 = 2$, $A < 1.0$.

The tangential aerodynamic force per unit area of the strip is [8] $F_\tau = qC_\tau$, where the drag force coefficient C_τ, for a laminar flow, is given by Blasius [12] $-C_\tau = 1.328 \mathrm{Re}^{-1/2}$ and for a turbulent flow by White [12] $-C_\tau = 0.054 \mathrm{Re}_s^{-1/7}$. Here $\mathrm{Re}_s = Us/\upsilon$ is the Reynolds number, s is a curvilinear coordinate along the strip, υ is the kinematic viscosity of the fluid.

For planar motions the transversal displacement is assumed to be "small" relative to the length of the strip, i. e. $h \approx O(\varepsilon)$, where $\varepsilon \ll 1$. Small but finite strip rotations imply that $(h')^2$ cannot be neglected compared to unity, whereas $(h')^4$ and higher order terms can.

In this way the general equation of the strip motion (1) may be written in a nondimensional form as follows:

$$\ddot{\eta} + \eta''' + \left[\eta'(\eta'\eta')' \right] + \left(\delta(\ddot{\eta} + 2V\dot{\eta}' + V^2\eta'') + \gamma\eta' \right) \left(1 + \frac{\eta'^2}{2} \right) + \eta' \int_0^s (\dot{\eta}'^2 + \eta'\ddot{\eta}') d\xi +$$

$$+ \sigma \left[V C_c (\dot{\eta} + V\eta') + C_n (\dot{\eta} + V\eta')|\dot{\eta} + V\eta'| \right] \left(1 + \frac{\eta'^2}{2} \right) - T\eta'' + O(\varepsilon^5) = 0,$$

$$T = \sigma \left(1 + \frac{3}{2}\eta'^2 \right) \int_\xi^1 \left(\frac{\gamma}{\sigma} + V^2 C_\tau \right) d\xi + \delta \int_\xi^1 (\ddot{\eta} + 2V\dot{\eta}' + V^2\eta'')\eta' d\xi +$$

$$+ \sigma \int_\xi^1 \left\{ V C_c (\dot{\eta} + V\eta') + C_n (\dot{\eta} + V\eta')|\dot{\eta} + V\eta'| \right\} \eta' d\xi + \int_\xi^1 \int_0^\xi (\dot{\eta}'^2 + \eta'\ddot{\eta}') d\xi d\xi + O(\varepsilon^4),$$

(3)

where

$$\xi = \frac{s}{l}; \quad \eta = \frac{h}{l}; \quad \tilde{\tau} = t\sqrt{D/(ml^4)}; \quad V = U\sqrt{ml^2/D}; \quad \sigma = \frac{\rho l}{2m}; \quad \gamma = \frac{m^* g l^3}{D}; \quad \delta = \sigma C_c; \quad C_c = \frac{\pi A}{2}$$

The total aerodynamic drag force coefficient C_D, per unit area of the wetted surface, may be obtained from (3) for $\xi = 0$:

$$C_D = \frac{T}{2\sigma V^2} - \left(1 + \frac{3(\eta')^2}{2}\right)\frac{\gamma}{2\sigma V^2} + O\left(\varepsilon^4\right).$$ (4)

Now (3) is to be solved, subject to the following boundary conditions

$$\eta = \eta' = 0 \quad \text{at } \xi = 0; \qquad \eta'' = \eta''' = 0 \quad \text{at } \xi = 1.$$ (5)

Method of Solution

We applied the standard method, based on Galerkin's method, for the numerical solution of equation (3). The solution is presented as the series

$$\eta(\tilde{\tau}, \xi) = \sum_{j=1}^{N} Q_j(\tilde{\tau})\Phi_j(\xi)$$ (6)

where η was expanded in terms of the eigenfunctions of the equation $\Phi'''' - \lambda^4 \Phi = 0$, satisfying the boundary conditions (5). For further information about this approach see ref [3].

The selection of the required value for N, is a complex problem, and is a theme for investigation. It was determined that for the non-linear case, 8 modes gave an adequate convergence [3]. The practical implementation of the numerical study has indicated that an oscillation's period of 16 seconds was sufficient for the development of the flutter process. The results shown below are being obtained during one second of oscillations, usually between the 11th and 12th seconds. There exists enough data about the process within one second to acquire confidence in the nature of the process.

Numerical Results and Discussion

The system parameters for the strip in question are chosen as follows: the density of air $\rho = 1.07$ kg/m^3; the density of the strip $\rho_0 = 3900$ kg/m^3; the flexural rigidity of the strip $D = 323a^3$ MN/m^2; the kinematic viscosity of the air $\upsilon = 0.15$ cm^2/s; the thickness of the strip $a = 0.05$ mm; the length of the strip $l = 0.25$ m; the width $H = 0.025$ m and the flow velocity U is being gradually increased. All the results have been obtained for the following initial conditions

$$h_1(0) = 0.05 \text{ mm}; \quad h_j(0) = 0;$$

$$\dot{h}_j(0) = 0; \quad j = 2, 3, ..., 8.$$

In Fig. 2 some sets of calculated parameters for the Hopf bifurcation are presented vs. the mass ratio σ under the constant strip width. There are the "critical" values of the flow velocity U (m/s), the Reynolds number Re and the nondimensionless frequency S_r (Strouhal number). The behavior of the U-curve are attributable to the different contribution of the bending stiffness
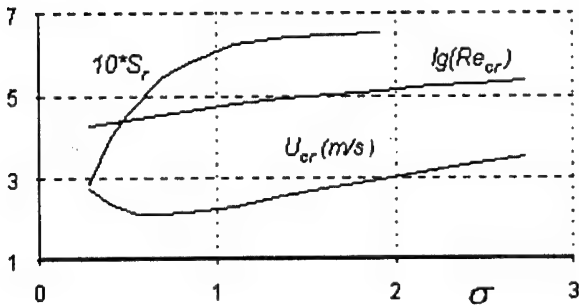
Fig. 2. The critical parameters: U_{cr}, lgRe$_{cr}$ and S_r for the Hopf bifurcation vs. the mass ratio σ for the strip' slength $l = 0.1$–1.0 m.

204

a)   b)
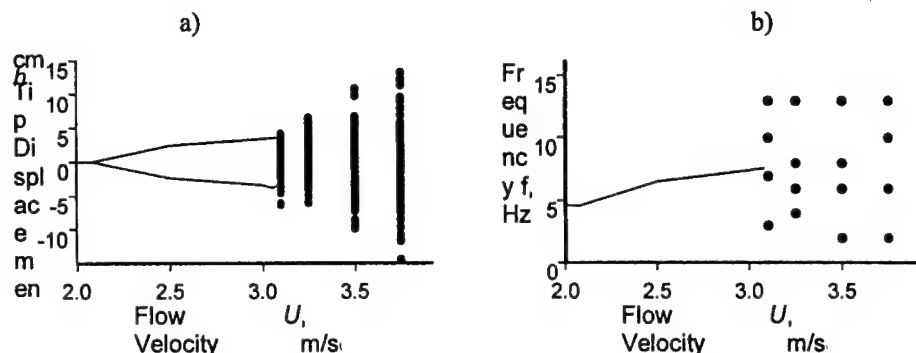
Fig. 3. Dependence for the calculated parameters of the fluttering strip $a) - h$, $b) - f$ upon the flow velocity, U

D and the strip's mass. In general, for σ below 0.7 the bending stiffness is the dominant parameter. At $\sigma = 0.7$ a balance between the effect of the stiffness and the mass ratio is achieved. For higher mass ratios rhe effect of the stiffness vanishes. This interpretation is confirmed by the behavior of Re and S_r curves.

In Fig. 3 some sets of calculated parameters are presented *vs.* the flow velocity. The parameters are: the tip displacement h and the frequency f of the free edge of the fluttering strip.

The results shown in Fig. 3 show that four distinct types of solution may occur:

1. Solutions converging to a stable equilibrium for subcritical air velocity ($U < 2.$ 1 m/s);
2. Periodic solutions corresponding to regular oscillations, whose above-mentioned parameters increase slowly with increasing air velocity from 2.1 m/s to 2.38 m/s. The amplitude variation along the strip has a shape of the standing wave in the third mode.
3. Periodic solutions corresponding to regular oscillations at higher amplitude and frequency. This type of a solution occurs at flow velocities between $U = 2.38$ m/s and $U = 3.08$ m/s. The amplitude of the oscillation variation along the strip, is once again a standing wave, but its order is higher.
4. Irregular oscillations occur at air velocities higher than $U = 3.08$ m/s. The solution assumes the shape of travelling waves along the strip, in the direction of the trailing edge. Note, that FFT analysis detailed fourth predominant frequencies of the flutter in the travelling-wave range at flow velocity straight off beyond $U = 3.08$ m/s (Fig. 3(b)).

The results for the paths 1 and 2 are presented in Fig. 4 as a function of flow velocity path. There are the upper and lower envelopes of the amplitude in Fig 4(a) and the frequency of oscillations in Fig. 4(b). The arrows show the velocity variance direction by path.

The small hysteresis can be observed in the case of the backward variance of flow velocity U near the point of the second bifurcation $U = 2.38$ m/s. As shown in Fig. 4 the realization of one state or another is a function of paths by flow velocity variance as a continuous process.

Figures 5, 6 demonstrate various patterns of the transitions between the standing wave oscillations and the travelling wave oscillations of the fluttering strip. The transition are presented for time interval sequence (a, b, c) of the oscillation process at the critical velocities $U = 2.38$ m/s and $U=3.08$ m/s, respectively. The time intervals in Fig. 5 are: $t = 5 \div 6$ s (a); $6.5 \div 7.5$ s (b); $8 \div 9$ s (c); in Fig. 6: $t = 3 \div 4$ s (a); $4 \div 5$ s (b); $5 \div 6$ s (c).
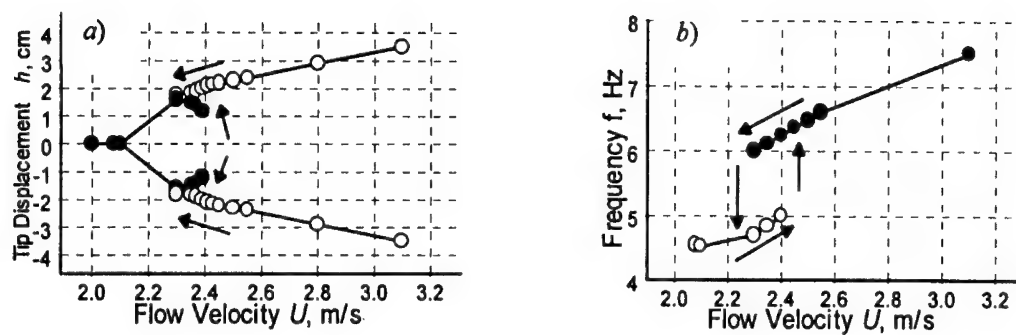
Fig.4 The histeretic phenomena on the bifurcation paths in the flutter domain
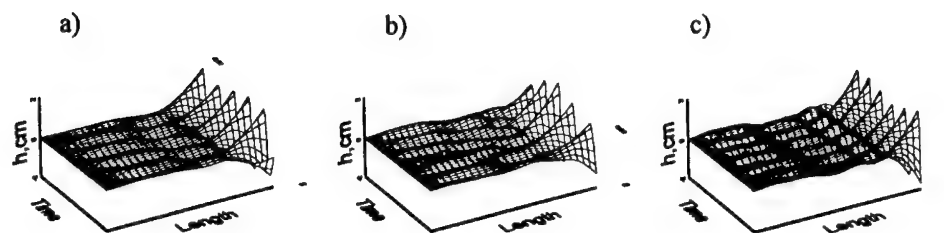
Fig. 5. The space-time wave structure of the fluttering strip for time intervals sequence
(a-b-c) of the oscillation's process at critical velocity U = 2.38 m/s.
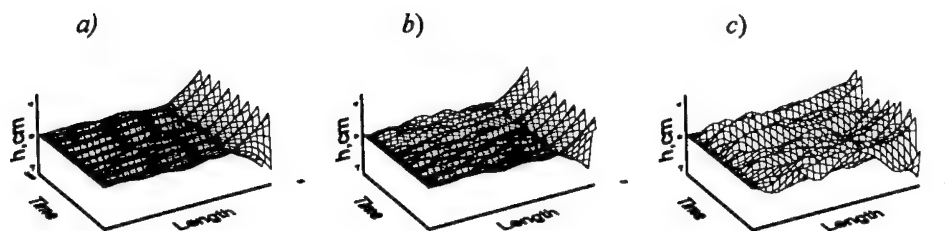
Fig. 6. The space-time wave structure of the fluttering strip for time intervals sequence
(a-b-c) of the oscillation's process at critical velocity U = 3.08 m/s.

At $U < 2.1$ m/s the strip's state is stable and the Hopf bifurcation appears at $U = 2.1$ m/s, corresponding to Reynolds number of $3.5 \cdot 10^4$. With a further increase of the flow velocity the regular flutter appears in the standing wave form (Fig. 5(a)). The strip's shape resembles the shape obtained when the strip oscillates in the third *in vacuo* mode. This shape is kept until the neighborhood of the flow velocity of $U = 2.38$ m/s, corresponding to Reynolds number of $3.97 \cdot 10^4$, where the curves jump (Fig. 4). This effect is connected to the transition of the oscillation's shape – from a third to a fourth *in vacuo* mode (Figs. 5(b), 5(c)). The estimations for the amplitude and frequency jumps are given below for increasing velocity :

$$U = 2.38 \text{ m/s; } h = 1 \text{ cm; } f = 5 \text{ Hz; } U = 2.4 \text{ m/s; } h = 2 \text{ cm; } f = 6.2 \text{ Hz}$$

The following bifurcation point is in the neighborhood of flow velocity of $U = 3.0\ 8$ m/s, corresponding to Reynolds number of $5.13 \cdot 10^4$, where the standing wave oscillations change into travelling wave ones (Fig. 6). Later the strip's motion becomes irregular.

Summary and Conclusions

A nonlinear mathematical model has been developed in order to study the evolution of disturbances in a finite, flexible strip hanging vertically and subjected to a uniform parallel flow. A series of numerical experiments has been conducted for the linear/non-linear model for various strip lengths. The study was focused on the range of flow velocities at which, small initial disturbances, begin to develop aeroelastic instability, that eventually, for the non-linear model of the strip's dynamics, lead to a limit-cycle of the oscillations. In the range of the fluid-structure parameters that were studied, eight modes should be employed to gain a quantitative accuracy.

The main conclusions obtained by the present study are as follows:

For small flow velocities corresponding to Reynolds number of $3.5 \cdot 10^4$ the strip does not flutter at all. As the flow velocity is increased the trailing edge of strip begins a regular flapping motion with small amplitudes. The strip oscillates regularly with a standing wave shaped motion. A further increase of the flow velocity, corresponding to Reynolds number of $3.97 \cdot 10^4$, leads to a steep jump of the parameters of the strips flapping motion.. However it continues to flap regularly, in this range, with a standing wave shaped oscillations. At a higher flow velocity, corresponding to Reynolds number $5.13 \cdot 10^4$, a second jump in the parameters of the motion occurs. However, in this velocity the nature of the fluctuation changes into non-regular, travelling wave in the direction of the trailing edge. No further steep change in the strip response at higher flow velocities corresponding to Reynolds number up to $6.25 \cdot 10^4$ has been observed.

The present numerical study predicts the onset and the evolution of the flutter of the strip in good agreement with earlier experimental works. Although the present simulations provide mainly a solution in the time domain, the comprehensive model of the strip's motion in the flow also allows to study the wave structure.

References

1. Taneda S. Waving Motions of Flag J. Physical Society of Japan. 1968. Vol. 24. P. 393-401.
2. Huang L. Flutter of Cantilevered Plates in Axial Flow. J. Fluids and Struct. 1995. Vol. 9. P. 127-147.

3. Yadykin Y., Tenetov V., Levin D. The Flow-Induced Vibration of a Flexible Strip Hanging in a Parallel Flow // Emerging Technologies in Fluids, Structures, and Fluid/Structure Interactions: Proc. ASME Press. Vessels and Piping Conf., Boston, MA,1999. Vol. 396. P. 321-332.
4. Bolotin, V.V., Grishko A.A., Kounadis A.N., Gantes C.J. Non-Linear Panel Flutter in Remote Post-Critical Domains // J. Non-Linear Mechanics. 1998. Vol. 33, No. 5. P. 753-764.
5. Jordan P.F. The Physical Nature of Panel Flatter // Aero. Digest. 1956. No.72-73. P. 34-38.
6. Stearman R. Small Aspect ratio Membrane Flutter. CALTEC Rep. AFOSR-TR 1, 1959. 59-45.
7. Triantafyllou G.S. An evolution of the hydroelastic behavior of membranes in parallel-flow. Mineral-Collect. Syst.: Ph. D., MIT, Depart. of ocean engin., 1983.
8. Datta S.K., Gottenberg W.G. Instability of an elastic strip hanging in an airstream // J. Applied Mechanics. 1975. Vol. 3. P. 195-198.
9. Lundgren T.S., Sethna P.R., Bajaj A.K. Stability Boundaries for Flow Induced Motions of Tubes with an Induced Terminal Nozzle // J. Sound and Vibration. 1979. Vol. 64. P. 553-571.
10. Katz J., Plotkin A. Low-Speed Aerodynamics. New York: McGraw-Hill, 1991.
11. Hoerner S. F. Fluid dynamic lift. Published by L.A. Hoerner, 1975.
12. White F.M. Viscous Fluid Flow. New York: McGraw-Hill, 1991.

STREAMWISE VORTICES IN A INITIAL REGION OF THE SUPERSONIC NONISOBARIC JET SHEAR LAYER

V.I. Zapryagaev

Institute of Theoretical and Applied Mechanics SB RAS
630090 Novosibirsk, RUSSIA

The efficiency of prediction of mixing characteristics and the possibility of controlling the mixing process are defined by understanding of physical phenomena that occur in a turbulent shear layer. A great number of factors should be taken into account while describing turbulent mixing even in case of the absence of chemical reactions [1]. The axial gradients of pressure, vorticity, density stratification and other factors complicate the description of turbulent mixing.

It was established comparatively recently that streamwise vortex structures are formed and developed at the boundary of a supersonic underexpanded axisymmetric jet exhausted in the ambient space [2]. The appearance of vortex structures in the initial region of the mixing layer of a supersonic jet is associated with the development of flow instability of the Taylor-Goertler type, which is caused by the curvature of streamlines and the appearance of centrifugal forces. The 3-D flow structure in the initial part of the shear layer of a supersonic underexpanded jet at high Reynolds numbers was investigated in [3-5]. The 3-D structure of flow in the mixing layer of a supersonic underexpanded jet is connected with the presence of a stationary streamwise Goetler vortices. Nevertheless, the conditions of appearance and the characteristics of development of the Taylor-Goertler vortices in a compressible mixing layer have not been adequately studied yet. The evolution of small disturbances in a curved mixing layer have been analyzed in [6] by using linear theory of hydrodynamic stability.

The results of an experimental study of the Taylor-Goertler disturbances in a curved shear layer of a supersonic nonisobaric jet are described. Radial and azimuthal distributions of the Pitot pressure were measured in various cross-sections of the initial region of the jet. A spectral analysis of stationary azimuthal nonuniformities in the shear layer of a supersonic underexpanded jet was performed. The data on the spectral composition of a stationary three dimension disturbances in the jet shear layer have made possible to calculate the spatial growth rates of disturbances for different wavenumbers.

Object and method of investigation

The characteristics of development of steady disturbances in the initial region of the mixing layer have been experimentally studied in a supersonic jet exhausted from an axisymmetric nozzle. The experiments were conducted in a jet facility of ITAM SB RAS using a data acquisition system connected to a personal computer. The measurement system allowed a simultaneous registration of pressure and temperature in the plenum chamber (P_o and T_o); the total pressure and the azimuthal angle corresponding to the Pitot tube position with respect to the jet axis. The experimental procedure involved the obtaining of the total pressure dependence both on the azimuthal angle and on the radius for various cross sections of the jet, i.e., $P_i(x, r, \varphi)$. The jet facility had a nozzle rotation mechanism that was computer-controlled with a special code.

A jet of cold air with the stagnation temperature T_o=273 K exhausted from a convergent nozzle into the ambient space with atmospheric pressure P_h and temperature T_h=293 K. Two identical convergent nozzles were used for this experiments. The exit diameter was equal to 20 mm. The main series of the experiments was performed with steel nozzle. The inner surface roughness of the steel nozzle was less than 1 micron. Special measurements of the surface roughness were not performed.

In this paper, data are presented for one gasdynamic regime of the jet flow. The dimensionless stagnation pressure in the receiver of the jet facility was P_o/P_h=5.02. The Reynolds number based on the nozzle exit diameter and the flow parameters in the exit cross-section of the nozzle was Re_d=1.71*10^6. M_j=1.71 is the Mach number corresponding to isentropic expansion of the flow in an underexpanded jet from the nozzle exit pressure P_a to the ambient pressure P_h (n_p=P_a/P_h=2.65 is the jet pressure ratio).

Results

Figure 1 shows the distribution of the dimensionless Pitot pressure P_i/P_0 measured by a Pitot probe ($\varnothing$0.6 mm) as a function of the radial distance. The data are presented for one cross section of a supersonic underexpanded jet. The letters BS mark the barrel shock wave. The shear layer thickness δ is shown at the plot for one cross-section (x/R_a=2.5). The letters PPL mark the Pitot pressure location for measuring of the pressure $P_i(\varphi)$ vs the azimuthal angle.

The dependence of the measured dimensionless thickness of the shear layer at the jet boundary δ/R_a on the dimensionless distance x/R_a for the examined regime can be represented by a single approximating formula (x/Ra< 8) :

$$\delta/R_a = 0.157 x/R_a + 0.048.$$
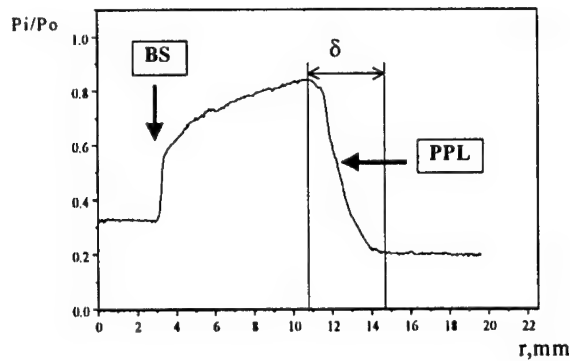
Fig. 1. Pitot pressure P_i/P_0 vs. the radial distance r/Ra for the cross sections of a supersonic underexpanded jet, x/Ra=2.5.

The dependence of the measured pressure $P_i(\varphi)$ on the azimuthal angle for six various cross-sections of the jet for steel nozzle are shown in Fig. 2. The presented plots $P_i(\varphi)$ are obtained for a radius corresponding to the middle of the shear layer, $r = r_{0.5}$, where $P_i(r_{0.5}) \sim 0.5 * Pi(r_m)$, r_m is the radius corresponding to the internal boundary of the mixing layer of the jet.

It is seen that the Pitot pressure distribution is significantly nonuniform in the azimuthal

direction, which is attributed to a three-dimensional structure of the flow caused by the presence of streamwise vortex structures in the mixing layer of the jet. To increase the reliability of the measured data, the dependence $P_i(\varphi)$ was obtained for two rounds of nozzle rotation around the axis $0 < \varphi < 720°$. Polar plots $P_i(\varphi)$ show a significant transformation of azimuthal nonuniformities with increasing longitudinal distance. An analysis of this transformation was performed using a spectral method.

The spectral analysis of the dependence P_i/P_0 on the angle φ was performed using the fast Fourier transform with a rectangular window using of the natural period for these nonuniformities 360 degrees. In the paper, the amplitude wave spectra of disturbances $P_s(n)$ in various cross-sections of the jet are presented, n is the azimuthal wavenumber. Typical amplitude spectra P_s versus azimuthal wavenumber are presented in Fig. 3 (a, c, e).

It is reasonable to represent the Taylor-Goertler disturbances in accordance with the form used in calculation works where the hydrodynamic flow stability is studied under the condition of curved streamlines [6]:

$$ p = A(r) \cdot \exp(i\alpha'x) \cdot \cos(n \cdot \varphi); \quad \alpha' = \alpha'_r + i \cdot \alpha'_i. $$

Here α'_i is the spatial growth rate in the streamwise direction, α'_r is the streamwise wavenumber, A is the amplitude of disturbances.

Dimensionless spatial growth rates $(\alpha_i = \alpha'_i \cdot R_a)$ of Taylor-Goertler disturbances were determined from the formula

$$ \alpha_i(n) = \frac{R_a}{x_2 - x_1} \ln \frac{P_{s1}(n)}{P_{s2}(n)}, $$

where x_1 and x_2 are the coordinates of the measurement cross-sections, $P_{s1}(n)$ and $P_{s2}(n)$ are the spectra amplitudes of disturbances for the first and second cross-sections for the same wavenumber n, respectively, $x_1 < x_2$. The calculated growth rate was connected with the longitudinal distance $x = (x_1 + x_2)/2$. This value is shown on the plot $\alpha_i(n)$, Fig. 3 (b, d, f).

The dependences $\alpha_i(n)$ and their approximation are presented in Fig. 3. Only the greatest values of the spectra amplitudes (the peaks in the dependences $P_s(n)$) were selected for determination of the dependence of the growth rate $\alpha_i(n)$.

It is seen (Fig. 3) that for $0 \le n \le 8$ and $n \ge 25$ the disturbances amplitudes are decreasing $(x/R_a = 2.25)$. But for $8 < n < 25$ the disturbances increase $(\alpha_i < 0)$ and the flow is unstable to this type of disturbances. The maximum values of $(-\alpha_i)$ are equal to 0.8-0.9 and are registered for $x/R_a = 1.25$. A comparison of these growth rates with available calculation results [6] demonstrates reasonable agreement.

The disturbance decrease $(\alpha_i > 0)$ for small wavenumbers $(0 < n < 10)$ is caused by the large initial amplitude of this kind of disturbances, namely, for shear layer conditions. This fact is in good conformity with the data [3] obtained for the development of spectral components of stationary Taylor-Goertler type disturbances with the artificial surface roughness. The development of stationary streamwise disturbances in a compressible curved shear layer is determined by an additional parameter: streamline curvature $\mathfrak{R}$. This parameter is additional to well-known parameters: Mach number, shear layer thickness and density gradient.

The dependence of neutral disturbances $(\alpha_i = 0)$ on the longitudinal distance is presented in Fig. 4. The interval of unstable wavenumbers decreases with increasing distance. Probably,

this effect can be associated with the growth of the shear layer thickness δ and the decrease in the streamline curvature ℜ.
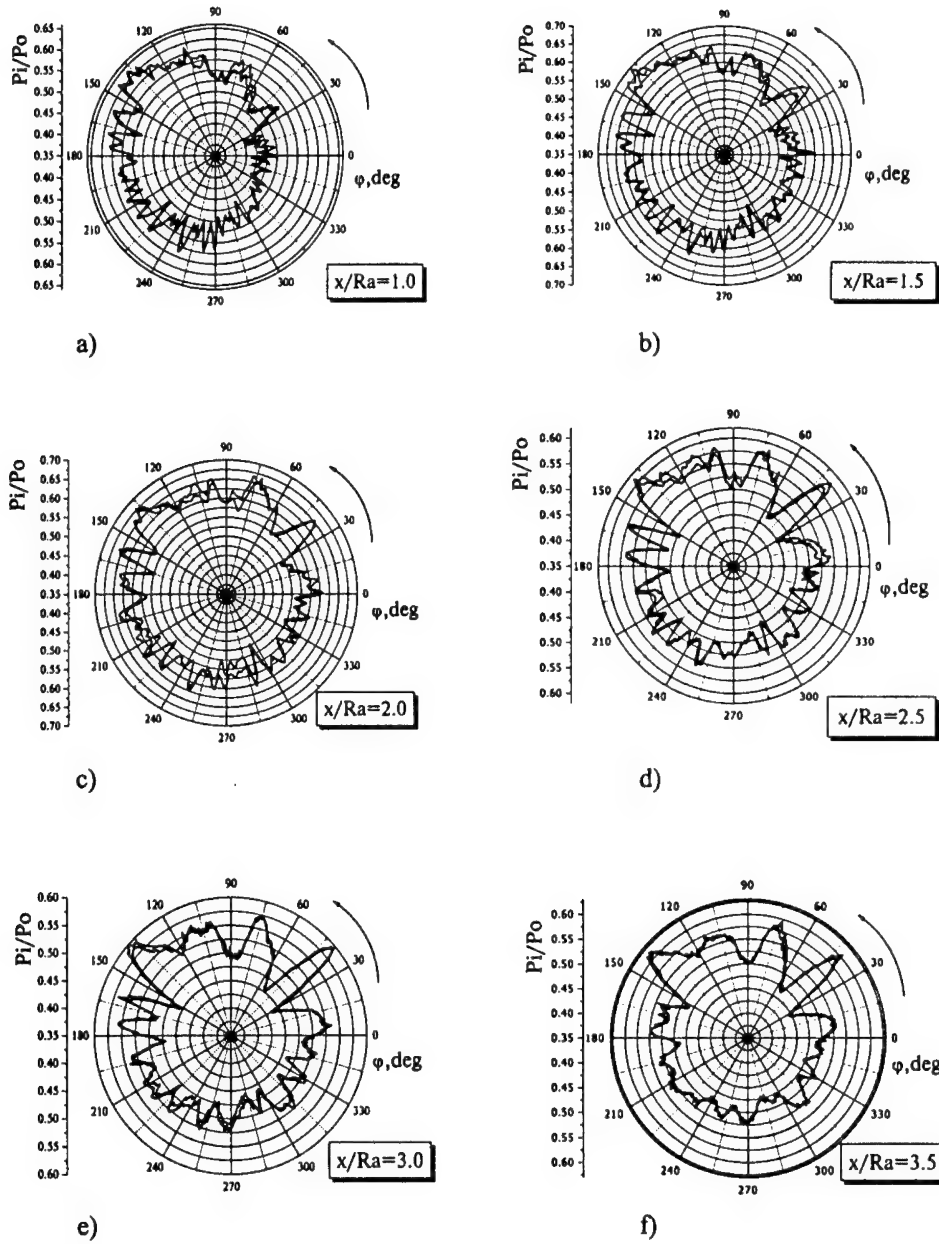
Fig. 2. Pitot pressure Pi/Po versus the azimuthal angle for various jet cross sections x/R_a=1.0; 1.5; 2.0; 2.5; 3.0 and 3.5 (steel nozzle).
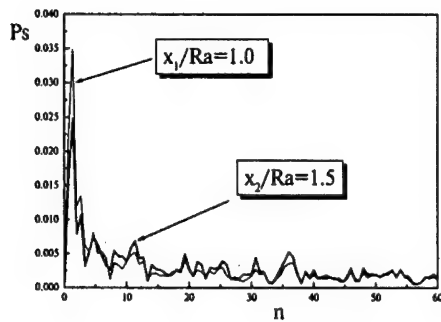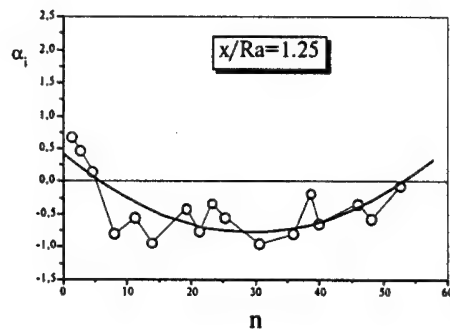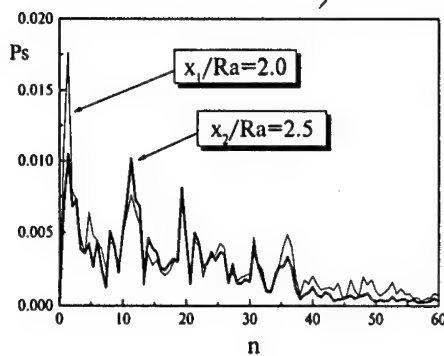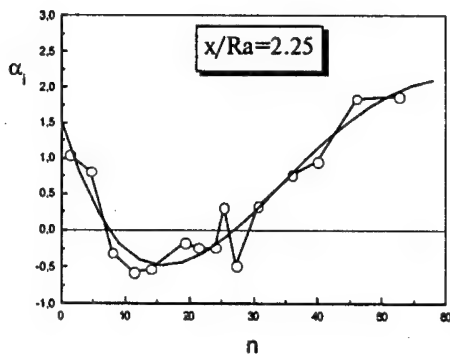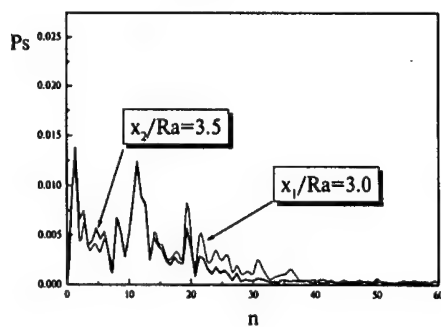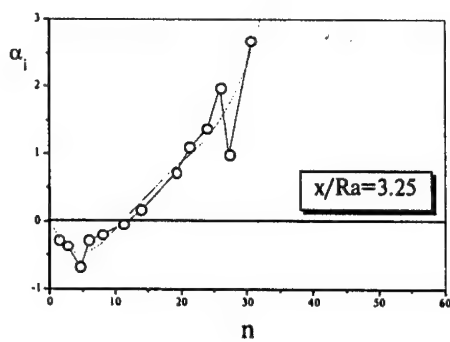
Fig. 3. Amplitude spectra of a dimensionless Pitot pressure P_a vs. the azimuthal wavenumbers for different longitudinal cross sections x/R_a and a corresponding growth rates $\alpha_i(n)$ vs. wavenumber n (steel nozzle).
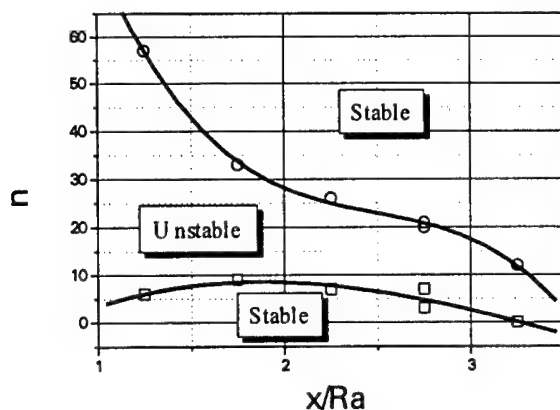
Fig. 4. Azimuthal wavenumbers n as functions of the longitudinal distance x/Ra for the neutral disturbances ($\alpha_i = 0$) in the shear layer of a supersonic underexpanded jet. Unstable region ($\alpha_i < 0$). Stable regions – ($\alpha_i > 0$). $M_j = 1.71$; $n_p = P_a/P_h = 2.65$; Re=1.71· 10^6.

Conclusion

The measured data for spatial growth rates of steady disturbances of the Taylor-Goertler type in various cross-sections of the initial region of a supersonic underexpanded jet are presented. The spatial growth rates are more generalized experimental data about the character of development of stationary streamwise vortices. It was observed that the wavenumber interval with negative spatial growth rates (unstable disturbances) is decreasing with the distance from the nozzle exit.

This work was supported by the Russian Foundation for Basic Research (grant No. 00-01-00847).

References

1. Schetz J.A. Injection and mixing in turbulent flow // Progress in astronautics and aeronautics. Vol. 128. New York, 1980.
2. Zapryagaev V.I., Solotchin, A.V. Spatial structure of flow in the initial section of a supersonic underexpanded jet: Preprint No.23-88. Novosibirsk, ITAM, 1988.
3. Zapryagaev V.I., Solotchin A.V. Evolution of streamwise vortices at the initial part of a supersonic nonisobaric jet in the presence of microroughnesses of the internal surface of the nozzle // Fluid Dynamic. 1997. Vol. 32, No.3. P. 465-469.
4. Krothopalli A., Strykowski P.J., King C.J. Origin of streamwise vortices in supersonic jet // AIAA J. 1998. Vol.36, No.5. P. 869-872.
5. Arnette S.A., Sammimy M., Elliott G.S. On streamwise vortices in high Reynolds number supersonic axisymmetric jets // Phys. Fluids A. 1993. Vol 5, No.1. P.187-202.
6. Terekhova N.M. Streamwise vortices in axisymmetric jets // J. Appl. Mech. Tech. Phys. 1996. Vol. 37, No. 3. P. 339-349.

VISUALIZATION OF 3D SEPARATED FLOWS
BY LIQUID CRYSTAL COATINGS

G.M. Zharkova, A.V. Dovgal, V.N. Kovrizhina, B.Yu. Zanin
Institute of Theoretical and Applied Mechanics SB RAS
630090 Novosibirsk, Russia

Introduction

An aerodynamic problem of wings operation is boundary layer separation which may have much effect upon lift, drag and local flow characteristics. Extensive studies are being carried out in order to develop reliable methods for prediction and control of the phenomenon. As a result, some of fundamental features of separated flows are captured by their fairly simple 2D models which have been elaborated. However, flow physics in separation regions is more complex than it can be expected from the 2D approximation. What it does not take into account is three-dimensionality inherent to separated flows. A great deal of research data on the problem indicates 3D vortical motion occurring at separation in low and high aspect ratio configurations. This was revealed in wind-tunnel tests by different visualization techniques, including smoke injection and by covering test surfaces with oil films and tufts [1 – 3, 6, 7]. Spatial separated flow structure in an incompressible fluid is the topic of present contribution. The aim of experiments is examination of surface flow patterns on a low aspect ratio wing, varying basic aerodynamic parameters. The method used for this purpose is visualization by liquid-crystal (LC) coatings. In previous studies, beginning from [5], this nonintrusive technique proved to be an effective tool of aerodynamic researches, providing both panoramic snapshots and resolution of flow details. Earlier, liquid-crystal visualization was adapted to experimental work in subsonic wind tunnels of the Institute of Theoretical and Applied Mechanics in [4, 8].

Experimental arrangement

The experiments were carried out in the subsonic wind tunnel MT-324 of the Institute of Theoretical and Applied Mechanics, Novosibirsk. The experimental model made of wood was a symmetric profile with 228 mm chord, 198 mm span and 16 % maximum thickness placed in the open test section of the facility with the nozzle 200 × 200 mm, at the free-stream turbulence level close to 0.1 %. (Fig. 1).

The wing's surface was covered by a thermosensitive coating, i. e., a mixture of cholesteric LC and polymer with selective reflection bandwidth between 30 and 34 °C at ambient temperature of about 20.0 °C. Before starting visualization under low subsonic conditions without natural temperature gradients, the test surface was artificially overheated above the selective reflection bandwidth of the coating. At aerodynamic cooling of the model color variations of the LC film were recorded by a video system. Then, temperature distributions on the surface were reconstructed through further processing of the initial data, see in [8]. Low thermal conductivity of the experimental model provided heat flux mainly from the surface to the flow. Small thickness of the coating making 25 microns had negligible effect upon heat transfer and results of visualization.
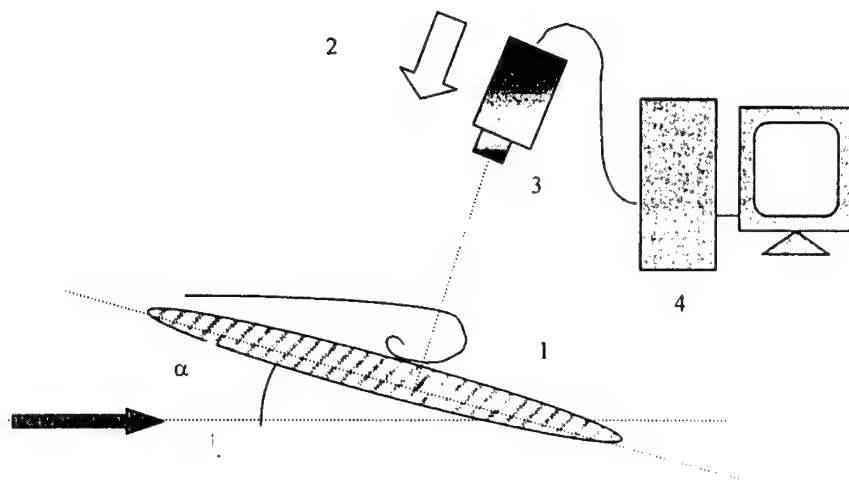
Fig. 1. Scheme of the experiment.
1 – model, 2 – light source, 3 – camera, 4-PC.

Two sets of experiments were carried out. First, visualization was performed at one and the same chord Reynolds number $Re_c = U_\infty c/v = 97\,000$, varying incidence of the wing. Second, angle of attack was kept constant and the flow visualized at Reynolds numbers, ranging from 84000 to 162000.

Results

In the first series of visualization the results were obtained, increasing angle of attack in small steps from its zero value. Some of data for basic flow regimes which were observed are shown by temperature fields on the test surface in Figs. 2–3. Each of them gives two snapshots "a" and "b" taken one by one in single experimental runs, which focus different flow details while surface temperature falling down. The free-stream direction in the figures is from top to bottom.

At low angles of attack, $\alpha \leq 3°$, the flow is attached to the wing, Fig. 2. In its central sections the boundary layer grows with the streamwise distance. As a result, aerodynamic cooling gets smaller and wall temperature increases. On both sides of the model the flow is affected by tip vortices (1) which enhance heat transfer and induce a pair of disturbances (2) in the rear part of the wing almost symmetric to the centreplane. At a low incidence one may also expect separation near the trailing edge, however, it can not be definitely judged because of perturbation produced by the vortices, converging towards this region.

Flow separation in the mid-chord section of the wing is detected beginning from $\alpha = 6°$. In the range of $6 \leq \alpha \leq 18°$ one can observe a closed circulation region (3) with relatively slow motion near the wall and the reattaching flow (4) where mixing of fluid goes up. As angle of attack increases the streamwise extent of separation bubble is reduced and it moves against the flow, coming close to the leading edge at $\alpha = 18°$. At this stage internal three- dimensionality of the separation region becomes apparent as temperature spots (5) spaced in the transverse direction. This spanwise structure which is associated with quasi-stationary vortices, rotating in the wing plane, looks very similar to that found at global leading-edge separation on low aspect ratio wings in previous studies. In the present experiments the flow separates globally, without reattaching back to the surface, at $\alpha \geq 21°$.

216
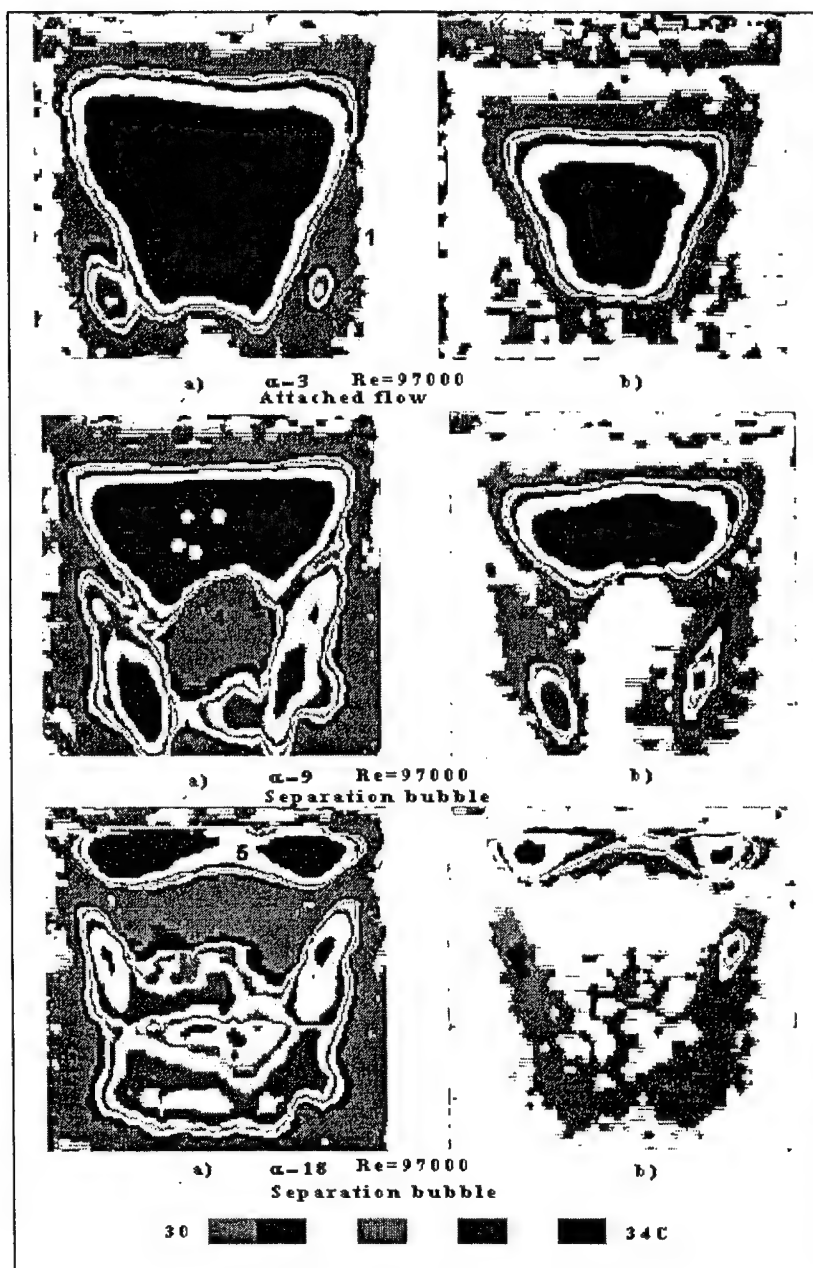
Fig. 2.

Results of visualization under poststall conditions are shown in Fig. 3 at $\alpha=24°$ where the region of reattachment is no longer observed and the 3D flow pattern is dominated by the large-scale symmetric vortex motion.

a) α–24   Re=97000   b)
Global separation

Fig. 3.

a) α–21   Re=99000   b)
Leading-edge separation

a) α–21   Re=152000   b)
Leading-edge separation

30   34C
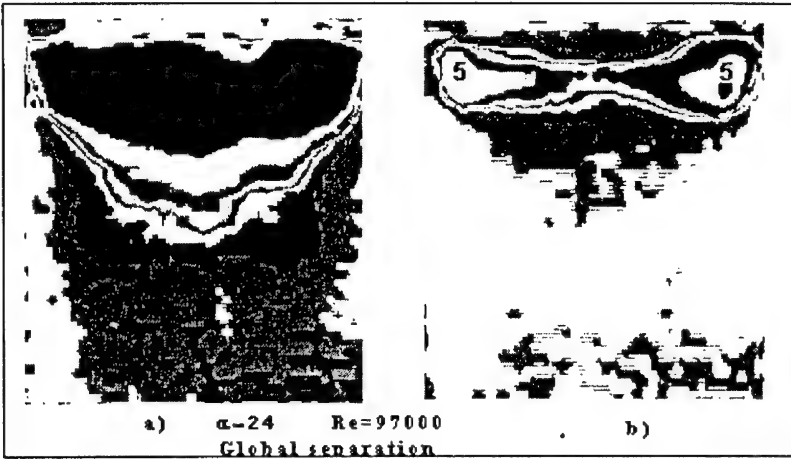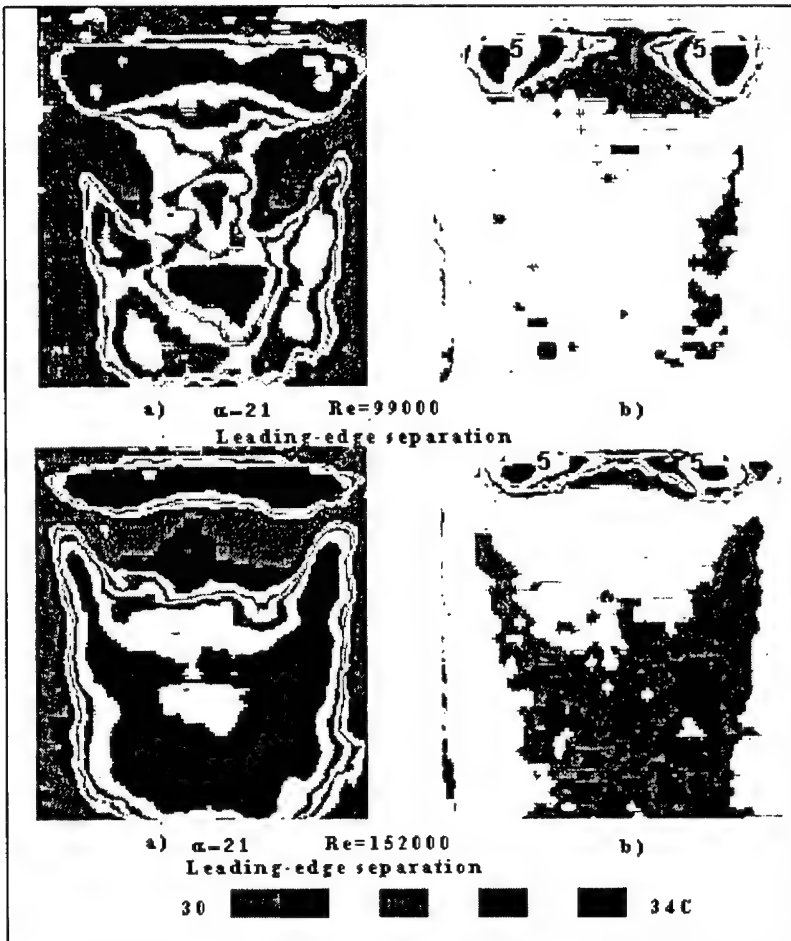
Fig. 4.

The second series of visualization was performed at $\alpha = 21°$ close to the critical angle of attack for different oncoming-flow velocities. In this case, the LC-technique gives time-averaged data on the leading-edge separation, being essentially unsteady process at the critical incidence. The effect of Reynolds number is illustrated in Fig. 4. The tendency observed with its growth is earlier reattachment of the separated layer. Thus, the separation region is progressively reduced until the leading-edge bubble occurs. All over the present range of Re-numbers there is no much variation in the vortical near-wall structure which remains qualitatively the same as that shown in above for high angles of attack.

Conclusion

In the present study visualization by liquid crystal coatings was used for investigation of flow separation on a low aspect ratio wing. As a result, systematic variation of the 3D surface flow pattern with Reynolds number and angle of attack was obtained. In particular, similarity of its spanwise structure is found when the flow separates globally under poststall conditions and locally at angles of attack just before the critical one.

References

1. Bastedo Jr.W.G., Mueller T J. Spanwise variation of laminar separation bubbles on wings at low Reynolds numbers // J. of Aircraft .1986. Vol. 23, No. 9. P. 687-694.
2. Bippes H. Experimental investigation of topological structures in three-dimensional separated flow // Boundary-Layer Separation / Eds. F.T. Smith, S.N. Brown. Berlin et al.: Springer Verlag, 1987. P. 379-381.
3. Boiko A.V., Dovgal A.V., Zanin B.Yu., Kozlov V.V. Three-dimensional structure of separated flows on wings (review) // Thermophysics and Aeromechanics. 1996. Vol. 3, No. 1. P. 1-13.
4. Dovgal A.V., Kozlov V.V., Kovrizhina V.N., Zharkova G.M. (1995) Liquid-crystals visualization of the boundary layer in incompressible gas flow // Flow Visualization VII / Ed. J.P.Crowder. New York: Begell House, Inc. P. 532-537.
5. Klein E.J. Application of liquid crystals to boundary-layer visualization. AIAA Pap. 68-376. 1968.
6. Neyland V.Ya., Stolyarov G.I. A type of flow separation on a rectangular wing // Sci. Notes of TsAGI. 1982. Vol. 13, No. 1. P. 83-89 (in Russian).
7. Winkelmann A.E., Barlow J.B. Flowfield model for a rectangular planform wing beyond stall // AIAA J. 1980. Vol. 18, No. 8. P. 1006-1008.
8. Zharkova G.M., Dovgal A.V., Kovrizhina V.N., Zanin B.Yu. Flow visualization on a low aspect ratio wing by liquid crystal coatings // 8th Intern. Symp. on Flow Visualization: CD Rom Proceedings, 1998 / Eds. G.M. Carlomagno, I. Grant. ISBN 0 9533991 0 9.

TEXTURAL TRANSITION IN CHOLESTERIC LIQUID CRYSTALS AND ITS APPLICATION IN SHEAR STRESS VISUALIZATION STUDIES

G. M. Zharkova, V. N. Kovrizhina, and V. M. Khachaturyan
Institute of Theoretical and Applied Mechanics SB RAS
630090 Novosibirsk, Russia

Introduction

The problem of heat transfer intensification in various technical apparatus is a most important one from the practical viewpoint [1–3]. The proper choice of heat transfer intensification strategy (or, which is equivalent, that of an optimal shape of the heat-exchanging surface most appropriate for the particular application area) can be made only with due regard for the actual flow structure and flow conditions in the channel. In many cases, most suitable surfaces have intricate shapes, for which no accurate analytical calculations are possible. The great complexity and variety of heat-exchanging surfaces and channels they form necessitate further experimental flow-structure studies.

Visualization and measurement of surface distributions of skin friction, heat flux, pulsational flow characteristics and other parameters allow the researchers to establish physical mechanisms that govern the flow. On the other hand, they provide engineers with various data required for developing and testing new numerical procedures. For these reasons, further development of panoramic optical methods for registering gas-dynamic parameters over streamlined surfaces is an important problem of modern aerodynamics.

In recent years, methods based on the use of liquid-crystal (LC) coatings for panoramic visualization of temperature and skin friction fields have gained widespread utility. A thin layer of an LC introduces no disturbances into the boundary layer, and the optical response of the LC to various distortions of the field of interest allows the researcher to employ the coating in aerodynamic studies [4, 5]. For instance, using some polymer-LC compositions of the cholesteric type, one can visualize the temperature field on the surface of the model under study. On the other hand, making the proper choice of the LC mix components, one can prepare materials insensitive to temperature but changing their properties under mechanical deforming, which is used for shear stress visualization. The shear stress is a physical parameter more sensitive to the flow pattern than temperature. The combined use of LC thermography and LC coatings responding exclusively to shear stress allows one to reveal peculiarities of the flow structure on models of complex geometries.

The textural transition in cholesteric LCs insensitive to temperature is a physical phenomenon that can be used to visualize shear stress (Fig. 1). Normally, when such a coating is sprayed onto a surface, the so-called focal-conic (confocal) texture forms. In this texture, LC molecules are situated at random, and, when being illuminated with a white light, this coating scatters light and looks colorless. Under mechanical deforming, the LC layer suffers the transition from the focal-conic to the so-called Granjean texture, where the LC molecules are aligned in a predominant direction, which results in a selective reflection of light. In this case the color variation displays the shear stress distribution on the wall.
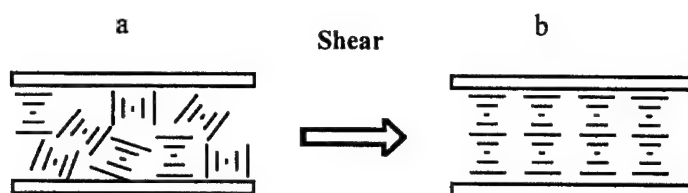
Fig.1. Textural transition in cholesterics.
Confocal texture (a) and Granjean (b).

In the present work, some results are described of application of a textural transition in LCs to flow-structure studies in channels formed by the so-called structured packings [6, 7]. The aim of this work was to study the effect of channel geometry on the topology of the near-wall turbulent flow.

Experimental conditions and procedure

The experiments were performed on a subsonic wind tunnel with a closed working section 15×80×250 mm in size (Fig. 2). The structure under study was a structured packing formed by two corrugated surfaces closely brought together and held against the walls of the working section of the wind tunnel. The ribs of plates were crossed to form cell structure (Fig. 3). The character and peculiarities of the flow in such channels, and hence, heat transfer and hydraulic losses in them depends both on the flow conditions and channel geometry. The corrugation angle θ, the doubled angle between the inlet flow direction and the rib direction, is a most important geometric parameter of the model of interest. The aim of this experiment was to examine the effect of the corrugation angle on the flow structure. We performed visualization of the flow in three models, with corrugation angles $\theta = 50, 90$, and $130°$, with the angle at the rib crest $\varphi = 90°$ and the hydraulic diameter $D_h = ph/s = 8.19$ mm.

It is known that in structured packings, depending on the Reynolds number and geometry, two or more types of flow of the working medium can be observed: along the channel wall valleys ($\theta > 90°$) or along the channel ($\theta < 30°$). At $\theta = (30-90°)$, the flow turns out to be a combinations of these flow modes, which results in origination of recirculation regions in the cells. In these recirculation regions, the shear stresses are rather low, and hence, more sensitive LC indicator is required to visualize them.
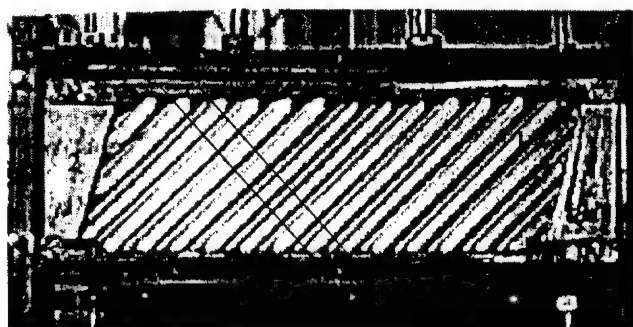
Fig.2. Working part of the experimental setup
1-corrugated plate, 2-connecting tie.
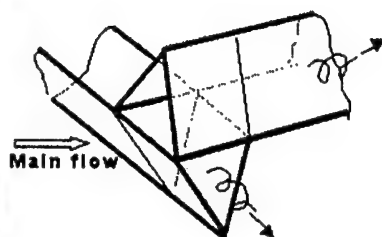
Fig.3.Sketch of the elementary cell.

In this study, we used a composition prepared from holesterol esters. To visualize shear stress, the coating-indicator was applied onto the blackened model surface by spraying. After a certain time interval, the working part was dismounted, and the resultant image was registered with a video-camera. The obtained image was colored, the result being dependent on the exposure time. In view of the above, the application of LC coatings-indicators seems to be most effective for the case of outside flows and when a visual access to the coating is available. For the case of an internal flow, the choice of the exposure time can be made by cut-and-try method with successively increasing duration of the exposure. For a fixed exposure duration, a non-reversible image is registered which corresponds to the maximum shear stress value happened to occur at the given point of the surface for the exposure time. The time which is required for visualization the shear stress in the most strained parts of the surface is shorter than that for parts with comparatively lower stresses. The image obtained permits elucidation of surface areas differing in the shear stress level realized.

The experiments were carried out for the Reynolds number calculated from the hydraulic model diameter $Re_{Dh} = 1.3 \cdot 10^4$.

Experimental results

Below, visualization results are presented for the shear stress caused by the turbulent flow structure in the near-wall region of the model under study. Figure 4 shows the 3D cellular flow structure which was observed on the lee and on the windward side of the model and its evolution with distance from the channel inlet. The exposure time of the LC coating was 5 min.

The dark (colorless) regions in the figure are the regions with the shear stress level below the threshold value for the given LC mixture and exposure time, where the confocal texture was undisturbed. The colored regions (in the black-and-white representation, regions with different shades of gray) show the parts of the surface with an enhanced skin friction.

The data obtained represent the structure of a complex vortex flow, whose structure, and hence, heat transfer in the near-wall parts of the lee and windward sides differ markedly. In addition, the image is seen to change both with the distance from the channel inlet and along the rib length. On the lee side of the model, the bottom part of the rib face is occupied by the image of a longitudinal structure D. Dimensions of this structure slowly vary along the rib length. Near the crest of the channel wall, this side shows a periodic image composed of semi-circular wakes of cellular vortices SV, which originate when the flows in the channels of the upper and lower walls merge together. These images visualize the boundaries of flow separation regions formed in the flow over the rib crest and contact points of the walls. On the windward side, diverging streamlines are noteworthy (R ≈ 2–3 mm from the rib crest throughout the entire lengths of the rib and the working section), as well as the flow separation line S. The zone of lowered (zero) skin friction below this line becomes wider downstream along the rib length.

The above specific features observed in the flow over both sides of ribs allowed us to deduce the flow diagram shown in Fig. 5.

In what follows, we consider the effect of the corrugation angle on the flow structure. Figure 6 presents visualization data for corrugation angles ranging from 50° to 130°. As the corrugation angle decreases, the characteristic structure change their positions and dimensions.
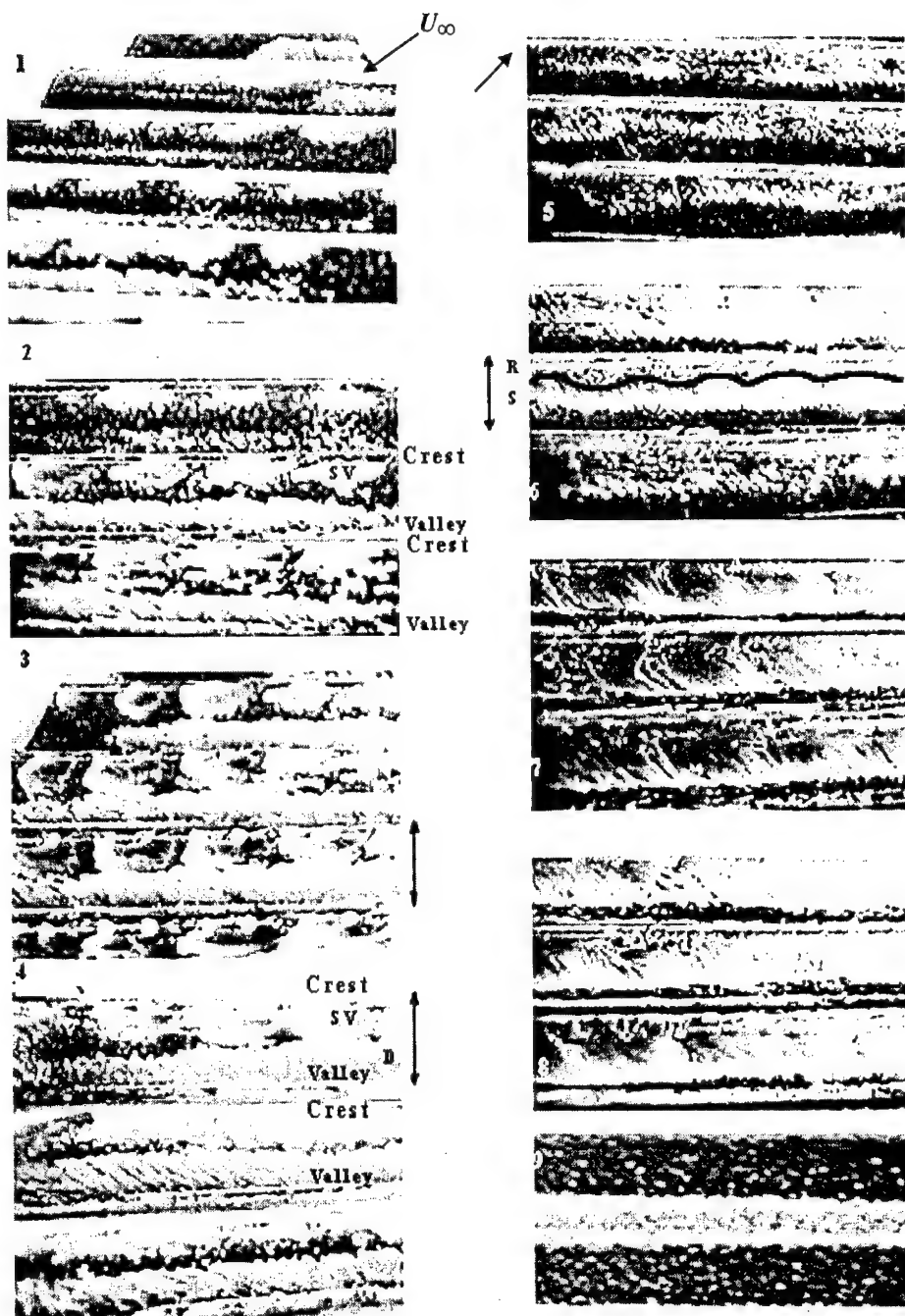
Fig. 4. Visualization of shear stress on the model surface with the corrugation angle 90°
(1–4) - view of the lee side of the ribbed surface for increasing distance from the inlet section;
(5–8) – view of the windward side; 9 – image of the working surface prior to its exposure to the
flow. The arrows show the width of the side surface of a rib.
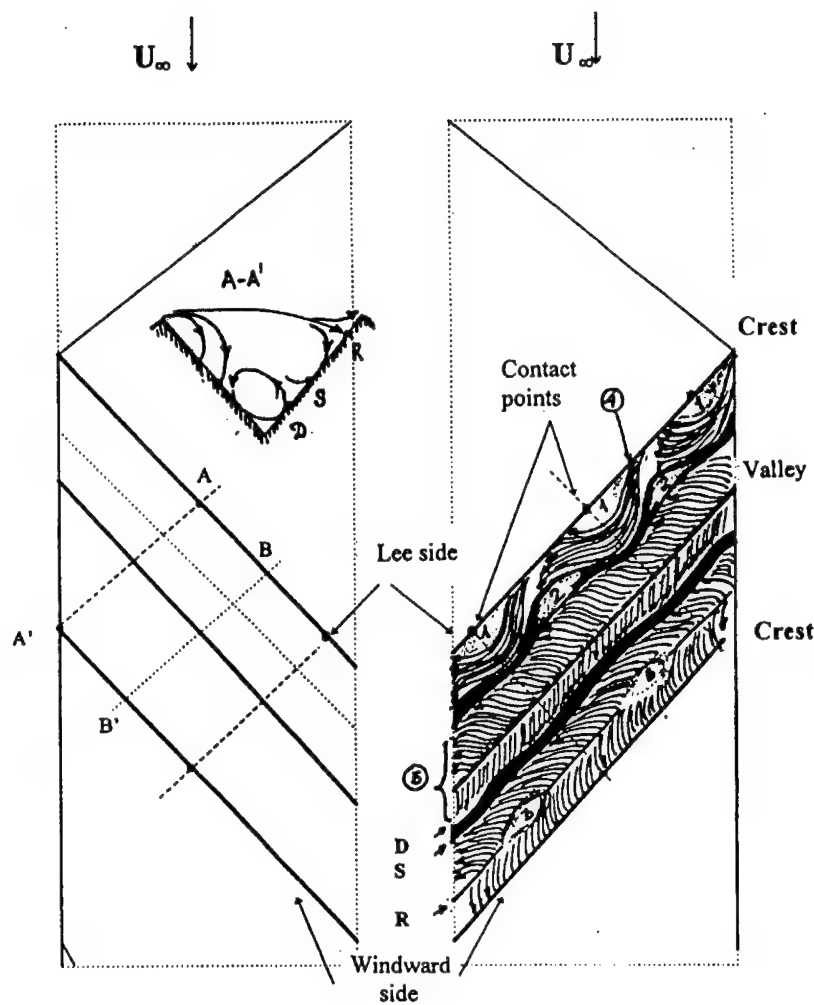
Fig. 5. Flow structure over the surface of a rib of the corrugated channel wall (not to scale).
1, 2, 3 – regions with decreased (or zero) shear stresses; 4 – regions of local cellular vortices;
5 – region of a longitudinal vortex with an increased skin friction.

For instance, on the lee side the boundary of the longitudinal vortex D descends from the middle of the rib face (θ =130°) down to the point $\approx 0.3S$ (θ =50°); the image of vortex SV change its shape from a semicircular one to one elongated along the rib (θ = 50 °).

On the windward side, as the corrugation angle decreases, flow separation line S moves upward up to the point $\approx 0.6S$ from the rib crest (θ = 50°), and line D descends down to the lowest point. At the same time, th]]e position of line R turns out to be insensitive to the corrugation angle.
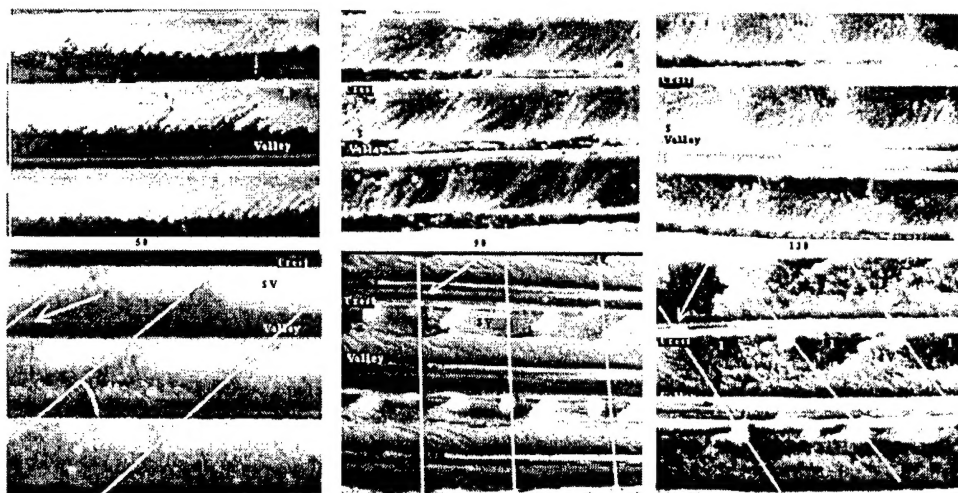
Fig. 6. Flow visualization data of the surface of a ribbed heat exchanger with corrugation angles $\theta = 50$, 90, and 130°. View of the windward (on the top) and lee (on the bottom) sides of the rib. The arrows show the direction of the free stream velocity U_∞.

Conclusions

In the present paper, results of visualization studies of the flow in structured packings are presented. The studies employ the textural transition in an LC coating covering the model surface. For low subsonic flow velocities and, hence, low temperature gradients on the model surface, visualization of shear stress permit reconstruction of the flow structure.

Aknowledgements

References

1. Kays W.M. and London A.L. Compact Heat Exchangers. New York: McGraw-Hill, 1984.
2. Kern D. and Krause A. Highly Developed Heat-Exchanging Surfaces. M.: Energiya, 1977. 464 p.
3. Svetlov Yu.V, Usyukin I.P., and Elukhin N.K. Effect of corrugation angle and disc height on the efficiency of disc packings of regenerators // Apparatus and Units of Oxygen and Cryogenic Setups: Proceedings of Vniicryogenmash. Vyp. 13. M., 1971.
4. Zharkova G. M., Khachaturyan V.M., Vostokov L.A., Alekseev N.M. Study of Liquid Crystal. Advances in Liquid Crystal, Research and Applications / Ed. by Bata, Budapest: Pergamon Press, Oxford, Acad. Kiado, 1980. P. 1221-1239.
5. Zharkova G.M., Sonin A.S. Liquid-Crystal Composites. M.: Nauka, 1994.
6. Stasiek J., Collins M.W., Ciofallo V., Chew P.E. Investigation of flow and heat transfer in corrugated passages-I. Experimental results/ Int. J. Heat Mass Transfer. 1996. Vol.39, No.1. P.149-164.
7. Gaiser G. Flow and transport processes in corrugated structures: Diss. Inst. For Chemical Process Engineering, University of Stuttgart, 1990.

Contents

Contents 226